



**Politecnico  
di Torino**

**ScuDo**

Scuola di Dottorato - Doctoral School  
WHAT YOU ARE, TAKES YOU FAR

Doctoral Dissertation

Doctoral Program in Civil and Environmental Engineering (35<sup>th</sup> cycle)

# **Design and Properties of Cementitious Materials Substituted by Recycled Waste Aggregates**

**Beibei Xiong**

\*\*\*\*\*

**Supervisors:**

Prof. Giuseppe Carlo Marano, Supervisor

Prof. Fabio Di Trapani, Co-Supervisor

Prof. Cristoforo Demartino, Zhejiang University-  
University of Illinois at Urbana Champaign Institute,  
External Advisor

**Doctoral Examination Committee:**

Politecnico di Torino  
2023

## **Declaration**

I hereby declare that, the contents and organization of this dissertation constitute my own original work and does not compromise in any way the rights of third parties, including those relating to the security of personal data.

Beibei Xiong  
2023

\* This dissertation is presented in partial fulfillment of the requirements for **Ph.D. degree** in the Graduate School of Politecnico di Torino (ScuDo).

## **Acknowledgements**

I would like to take this chance to express my sincere gratitude to my principal supervisor Prof. Giuseppe Carlo Marano, for his invaluable guidance, strong support, and meticulous care throughout my Ph.D. study in polito. The experiences in polito I have significantly promoted my professional growth, and meantime awarded me with the abilities, skills, and characteristics that are essential for an independent and mature academic researcher.

The second and foremost person I would like to acknowledge is my co-supervisor, A/Prof. Cristoforo Demartino. He supports my research on dynamic experimental research on concrete and followed me in each stage of my investigation. From my study for master's degree to Ph.D.'s degree, he always plays as a mature leader, patient, precise and dedicated and he can spend a whole day in the lab with students to discuss and solve problems. I thank him for teaching me how to think logically and rigorously, and for the good custom to double-check everything during the process of the experiment. All of these reshape me into a better researcher.

I also thank A/Prof. Devid Falliano for his kind help with my tests in polito. His suggestion greatly improved my ability to perform tests. During my mortar and concrete tests, he not only helped me cast the specimens but also assisted me to negotiate with the technicians. During the epidemic period, he made me feel Italian concern and care, the role he plays includes both my supervisor teacher, and friend in Italy. Other thanks from A/Prof. Luciana Restuccia, A/Prof. Fabio Di Trapani for their kind discussion and useful suggestion for tests and publication choice. Other thanks in the field of academic activity should be given to my friends Dr. Isabella Cosentino, Dr. Giovanni Anglani and Prof. Paola Antonaci in polito, and Dr. Dade Lai and Prof. Yan Xiao from ZJUI for their help during tests and complete this dissertation. Finally, I would like to extend my love and gratitude to my parents and my husband. They spare no effort to love and support me.

Once again, I offer my best regards and grateful thanks to all of those who supported me in any respect during the completion of this thesis.



## **Abstract**

Concrete is a widely used material in structural engineering applications characterized by technical/economic convenience and end-products. Globalization and the growth of population have accelerated the dynamics of the urbanization process, however, it has made the management of the construction and demolition waste (CDW) a significant issue and big challenge to all over the world. Recycled aggregate concrete is a type of concrete that recycled aggregate, especially recycled aggregate from CDW is utilized to replace the virgin aggregate like fine and coarse aggregate. Recycled CDW aggregate concrete offers a valuable method for recycling industrial by-products and reducing greenhouse gas emissions and thus produces a novel green concrete. The superior merits of recycled CDW aggregate concrete include avoiding over-exploitation of natural aggregate, reducing landfills of CDW and diminishing existing wastes. In this dissertation, plastics, recycled crushed concrete aggregate (RCA) and recycled clay brick aggregate (RBA) were selected as the representative recycled CDW aggregates in the meanwhile, plastics consist of PET powder and Mix-plastic granules. The novel green are developed and evaluated.

Before conducting the concrete tests under high strain rate, the design and calibration of a large-scale 155-mm Split-Hopkinson Pressure Bar (SHPB) is required. The design and construction of the apparatus are described and its data processing, including wave pulse dispersion correction, is assessed to ensure accurate representation of stress and deformation conditions. The apparatus is validated through experiments on both brittle (confined concrete) and ductile (copper) specimens. The results demonstrate the ability of SHPB to characterize the dynamic properties of large-scale specimens and to correct dispersed signals in the bar, allowing for the accurate determination of specimen surface pulses. The validity of the results is confirmed through 1D, 2D, and 3D wave analyses. Therefore, the 155 mm diameter SHPB setup has shown excellent performance in deriving the dynamic properties of large-diameter specimens.

Existing studies have validated that the quasi-static compressive behavior of concrete made with different levels of substitution and types of coarse aggregate by RCA and RBA was widely investigated. Thus, herein, only the high strain rate compressive behavior of Recycled Aggregate Concrete (RAC) and Recycled clay Bricks Concrete (RBC) were in-depth investigated by a SHPB apparatus with a large bar diameter of 155 mm. Specimens were divided into 9 groups with different levels of substitution and types of coarse aggregate ranging from 0% (Natural Aggregate Concrete, NAC) up to 100% (full substitution with recycled crushed concrete or clay bricks). Tests were executed up to a strain rate of around  $100\text{s}^{-1}$ .

Subsequently, difference exists in PET powder and mix-plastic granules adopted in this dissertation with previous literature, thus, in-depth investigation were conducted from mortar level. In detail, the physical and mechanical characteristics of a novel mortar that uses recycled PET powder as a replacement of the natural sand were examined. To create five distinct mortar mixes, recycled PET powder was substituted in varying proportions (0–30% by volume of the sand). The investigation focuses on the physical and mechanical characteristics of the material, including density, slump, water absorption, ultrasonic pulse velocity, flexural and compressive strength, and micro-structural and interface characterization. Then, a step further, PET powder and recycled mixed plastic granules were adopted to substitute fine and coarse aggregates. Two different substitution strategies are employed. In the first one, the PET powder is used to substitute the fine sand by volume. In the second one, the PET powder is used to substitute the fine sand while the recycled mixed plastic granules are used to substitute the coarse sand and fine coarse aggregates by volume (50% for PET powder and 50% for recycled mixed plastic granules). Four total replacement levels (5%, 10%, 20%, and 30%) by volume were considered. The fresh concrete properties (slump and density), compressive and flexural behavior, toughness, and permeability are investigated. Finally, a micro-scale characterization of the plastic-paste interface is provided. Later, the comparative experiments were conducted on the study on the characterization of the high-strain rate compressive behavior of the concrete with two different substituted recycled plastic aggregates. Tests were performed using conventional quasi-static loading with a compressive testing machine and high-strain rate tests with a diameter of 80-mm SHPB for strain rates up to  $100\text{s}^{-1}$ . Moreover, stress-strain curves, and energy absorption capacity and data-driven model are proposed for all kinds of tests in this dissertation.

Overall, this dissertation could support the producers of CDW to gain considerable interest by applying the CDW aggregate into concrete and can be a promising material to be employed for protective techniques against impact and blast loads.

# Contents

<b>List of Figures</b>	<b>xiv</b>
<b>List of Tables</b>	<b>xxii</b>
<b>1 Introduction</b>	<b>1</b>
1.1 Background and problem statement . . . . .	1
1.1.1 Plastics . . . . .	3
1.1.2 Recycled bricks and recycled crushed concrete aggregate . . . . .	6
1.2 Dynamic apparatus . . . . .	7
1.3 Objectives . . . . .	9
1.4 Outline of the thesis . . . . .	10
<b>2 Literature review</b>	<b>12</b>
2.1 Quasi-static tests on recycling and reusing plastics in cementitious materials . . . . .	12
2.2 High-strain rate compressive behavior of concrete made with substituted recycled crushed concrete and clay bricks aggregates . . . . .	22
2.3 High-strain rate compressive behavior of green concrete made with substituted plastic aggregates . . . . .	29
<b>3 Design and calibration of 155-mm Split-Hopkinson Pressure Bar</b>	<b>32</b>
3.1 Working principle of large scale 155-mm SHPB . . . . .	32

---

3.2	SHPB primary design and construction . . . . .	33
3.2.1	SHPB data acquisition system . . . . .	34
3.2.2	Geometric characteristics of the specimens . . . . .	36
3.2.3	Characteristics of the bars . . . . .	36
3.2.4	SHPB loading device . . . . .	37
3.2.5	SHPB trapping device . . . . .	39
3.3	Data processing: validation and test acceptance conditions . . . . .	40
3.3.1	SHPB impedance mismatch . . . . .	40
3.3.2	SHPB transmission coefficient . . . . .	41
3.3.3	Strain rate limits . . . . .	42
3.3.4	SHPB calibration . . . . .	44
3.3.5	Test validation . . . . .	44
3.4	Dispersion correction . . . . .	46
3.4.1	Theory of wave propagation . . . . .	46
3.4.2	Dispersion correction in the frequency domain . . . . .	48
3.4.3	Dispersion correction about radial non-uniform distribution . . . . .	49
3.4.4	Dispersion correction procedure . . . . .	50
3.5	Results and discussion . . . . .	51
3.5.1	Brittle material: concrete . . . . .	51
3.5.2	Ductile material: copper . . . . .	54
3.6	Conclusions . . . . .	56
<b>4</b>	<b>Compressive behavior of concrete made with recycled crushed concrete and recycled clay bricks under different strain rate</b>	<b>59</b>
4.1	Materials and methods . . . . .	59
4.1.1	Materials . . . . .	59
4.1.2	Test specimens: mix design and casting . . . . .	60

---

4.2	Quasi-static test program . . . . .	62
4.3	High-strain rate tests program . . . . .	63
4.3.1	Large diameter SHPB: apparatus and working principle . . .	63
4.3.2	Test matrix and protocol . . . . .	64
4.3.3	Validation of the tests . . . . .	65
4.4	Experimental results of quasi-static compressive behavior . . . . .	66
4.4.1	Compressive strength . . . . .	66
4.4.2	Failure modes . . . . .	67
4.5	Experimental results of high-strain rate compressive behavior . . . . .	68
4.5.1	Stress and strain relationship and dynamic strength . . . . .	68
4.5.2	Energy absorption density . . . . .	71
4.5.3	Failure modes . . . . .	73
4.6	Discussions . . . . .	75
4.6.1	Dynamic increase factor . . . . .	75
4.6.2	Predictive equations for RAC . . . . .	78
4.6.3	Predictive equations for RBC . . . . .	79
4.7	Conclusions . . . . .	80
<b>5</b>	<b>Quasi-static physical and mechanical properties of mortar with substituted recycled PET powder</b>	<b>83</b>
5.1	Materials and methods . . . . .	83
5.1.1	Materials and specimens . . . . .	83
5.2	Test program . . . . .	86
5.2.1	Density . . . . .	86
5.2.2	Slump . . . . .	87
5.2.3	Ultrasonic Pulse Velocity tests . . . . .	87
5.2.4	Flexural tests . . . . .	88

---

5.2.5	Compressive tests . . . . .	89
5.3	Experimental results . . . . .	89
5.3.1	Density and slump . . . . .	89
5.3.2	Ultrasonic Pulse velocity (UPV) . . . . .	90
5.3.3	Flexural behavior . . . . .	91
5.3.4	Compressive strength . . . . .	94
5.4	Discussion . . . . .	96
5.4.1	Fracture energy . . . . .	96
5.4.2	Critical stress intensity factor . . . . .	97
5.4.3	Data-driven predictive models . . . . .	98
5.5	Conclusions . . . . .	103
<b>6</b>	<b>Physical and mechanical properties of concrete with two different substituted recycled plastic aggregates</b>	<b>105</b>
6.1	Materials and methods . . . . .	105
6.1.1	Materials . . . . .	105
6.1.2	Concrete mixture proportion and specimens preparation . . .	107
6.2	Test program . . . . .	110
6.2.1	Fresh concrete properties . . . . .	110
6.2.2	Compressive tests . . . . .	111
6.2.3	Flexural tests . . . . .	111
6.2.4	Water-penetration tests . . . . .	113
6.2.5	Micro-scale characterization . . . . .	114
6.3	Experimental Results . . . . .	114
6.3.1	Fresh concrete properties . . . . .	114
6.3.2	Compressive behavior . . . . .	116
6.3.3	Flexural behavior . . . . .	119

---

6.3.4	Water-penetration tests . . . . .	122
6.3.5	Micro-scale characterization . . . . .	123
6.4	Discussion . . . . .	127
6.5	Conclusions . . . . .	130
<b>7</b>	<b>Dynamic mechanical properties of concrete with two different substituted recycled plastic aggregates</b>	<b>134</b>
7.1	Materials and method . . . . .	134
7.1.1	Materials . . . . .	134
7.1.2	Test specimens: mix design and cast . . . . .	134
7.2	Quasi-static test program . . . . .	136
7.2.1	Ultrasonic pulse velocity (UPV) test . . . . .	136
7.2.2	Quasi-static compressive test program . . . . .	136
7.2.3	Micro-scale characterization . . . . .	137
7.3	High-strain rate test program . . . . .	138
7.3.1	Apparatus and working principle . . . . .	138
7.3.2	Calibration for the SHPB system . . . . .	140
7.3.3	Test matrix and protocol . . . . .	141
7.3.4	Validation of the tests . . . . .	141
7.3.5	Selection of pulse shaper . . . . .	143
7.4	Results . . . . .	144
7.4.1	Fresh state properties . . . . .	144
7.4.2	UPV . . . . .	146
7.4.3	Quasi-static compressive behavior . . . . .	147
7.4.4	High-strain rate compressive behavior . . . . .	153
7.4.5	Micro-scale characterization . . . . .	157
7.5	Discussion . . . . .	159



---

7.5.1	Dynamic increase factor . . . . .	159
7.5.2	Image-based waveform analysis of SHPB tests . . . . .	163
7.6	Conclusion . . . . .	168
<b>8</b>	<b>Conclusions and future perspectives</b>	<b>179</b>
8.1	Conclusions . . . . .	179
8.2	Future perspectives . . . . .	182
	<b>Bibliography</b>	<b>184</b>

# List of Figures

1.1	The volume of various construction and demolition waste (CDW) (modified from [1]). . . . .	2
1.2	Toward zero carbon building . . . . .	2
1.3	Global life-cycle GHG emissions of conventional plastics in by life-cycle stage and plastic type (modified from [2]). . . . .	5
1.4	The technical roadmap in this thesis . . . . .	11
2.1	Plastic and recycling code according to ASTM D7611 / D7611M [3]	13
2.2	Typical process to obtain recycled plastic aggregates to be employed in cementitious material . . . . .	14
2.3	Literature review for plastic aggregate substituted concrete of <i>SRF</i> as a function $r$ for partial or full substitution of fine, coarse, or both fine and coarse aggregates. . . . .	18
2.4	Classification and evaluation of particle shape (adapted from Ulusoy [4]) . . . . .	20
2.5	Comparison of experimental points and predictive equations of <i>DIF</i> as a function of $\dot{\epsilon}$ for different values of $r$ . Data taken from: CEB-FIP Model Code formula [5], Xiao et al. [6], Lu et al. [7], and Guo et al. [8]. Note that the colors inside the squares in the legend are indicating the substitution level of aggregate, $r$ , associated to the different lines and markers in the figure. . . . .	27
3.1	Schematic and photos of the main parts of the large diameter SHPB. After Xiong et al. [9]. . . . .	35

3.2	Gas gun (left) and air compressor (right). . . . .	37
3.3	Relationship between the pressure and impact velocity with the empirical fitting curve reported in Eq. 3.6. After Xiong et al. [9]. . . . .	38
3.4	Transmission coefficient and reflection coefficient vs. impedance mismatch. . . . .	42
3.5	Collection of the incident waves adopted for the calibration (a). The gray rectangle indicate the time range ( $700 \mu s \leq t \leq 1000 \mu s$ ) used for the calculation of the mean of the measured incident wave. Comparison of the predicted and measured amplitude of the incident wave (b). After Xiong et al. [9]. . . . .	45
3.6	Phase velocity: exact numerical solutions, $\nu = 0.25$ and $0.30$ (a) and relative uncertainties generated by the fitting curves (b). . . . .	48
3.7	Correction factors for $M1$ with $\nu = 0.25, 0.27, 0.30, 0.32, 0.35$ (a) and $M2/E$ (b). . . . .	50
3.8	Bridge output at the incident and transmitted bars for confined concrete specimen (a) incident (b) transmitted. . . . .	52
3.9	Delimitation and correction of the dispersion for confined specimens: $P_g = 1.0 \text{ MPa}$ (a) and stress-strain diagram (b). . . . .	53
3.10	Bridge output of the incident bar for copper at $P_g = 0.6 \text{ MPa}$ . . . . .	55
3.11	Delimitation and correction of the dispersion for copper test (a) and stress-strain diagram for copper under $ASR = 54 \text{ s}^{-1}$ (b). . . . .	56
4.1	Signals obtained for a specimen RAC40 tested at a pressure of $P_g = 0.3 \text{ MPa}$ : typical waveforms from the incident and transmission bars and the three identified waves ( $\epsilon_i(t)$ , $\epsilon_r(t)$ and $\epsilon_t(t)$ ) (a); stress-strain curve with averaged axial stress (Eq. 4.7c), front and back stresses (Eqs. 4.7a and 4.7b), their difference (Eq. 3.18), and acceptance condition $R(t) = 0.05$ (b). . . . .	66
4.2	Quasi static-strength and $SRF$ at 28 days, $f_c(r = 0\%, \dot{\epsilon} \rightarrow 0 \text{ s}^{-1})$ , as a function of $r$ for RAC (a) and RBC (b). . . . .	67
4.3	Typical failure modes under static loading of standard cylinder specimens for NAC, RAC and RBC with different $r$ . . . . .	68

- 
- 4.4 Stress-strain curves for different dynamic tests: RAC (a) and RBC (b). For each gun pressure ( $P_g$ ), the three thin lines are the results of the three repetition tests while the thick line is their average across the axial strain. . . . . 70
- 4.5 Dynamic strength,  $f_c(r, \dot{\epsilon})$ , as a function of the strain rate,  $\dot{\epsilon}$ , for the different tests: RAC (a) and RBC (b). . . . . 72
- 4.6 Typical failure modes of NAC, RAC and RBC specimens with different  $r$  after SHPB tests. . . . . 74
- 4.7  $DIF$  as a function of the strain rate,  $\dot{\epsilon}$ , for the different tests: RAC (a) and RBC (b). The blue continuous and dashed lines indicate the CEB-FIP Model Code specification recommendation formula [5], see Eq. 2.5. . . . . 76
- 4.8 Comparison of experimental points of  $DIF$  as a function of  $\dot{\epsilon}$  for different values of  $r$ . Data taken from: CEB-FIP Model Code formula [5] (cyan thick continuous line), Xiao et al. [6] (cross points), Guo et al. [8] (hollow circles) and this study (full circles). Note that the colors inside the squares in the legend are indicating the substitution level of aggregate,  $r$ , associated to the different lines and markers in the figure. . . . . 79
- 4.9 Fitted predictive equations of the  $DIF$  as a function of  $\dot{\epsilon}$  (see Eq. 4.10) for different values of  $r$  for RAC. The fitting is reported using different sets of experimental: this study (continuous thick lines), this study and Guo et al. [8] (dashed thick lines), and Xiao et al. [6] (dotted thin lines). The cyan thick continuous line is the CEB-FIP Model Code formula [5] valid for NAC. Note that the colors inside the squares in the legend are indicating the substitution level of aggregate,  $r$ , associated to the different lines and markers in the figure. 80

4.10	Fitted predictive equations of the <i>DIF</i> as a function of $\dot{\epsilon}$ (see Eq. 4.10) for different values of $r$ for RBC. The continuous thick lines are the fitting according to Eq. 4.10. The cyan thick continuous line is the CEB-FIP Model Code formula [5] valid for NAC. Note that the colors inside the squares in the legend are indicating the substitution level of aggregate, $r$ , associated to the different lines and markers in the figure. . . . .	81
5.1	Recycled PET aggregate (a) and micro-photo (b) . . . . .	84
5.2	Particle size distribution of natural sand and recycled PET powder . . . . .	85
5.3	Notched specimen (left) and flexural test setup (right) . . . . .	88
5.4	Photo of the compressive test apparatus and specimen . . . . .	89
5.5	Relationship between UPV and $r$ . . . . .	91
5.6	Flexural load vs CMOD curves at 7 days (a) and 28 days (b). Note that x axis has different scale . . . . .	92
5.7	Average flexural strength at 7 and 28 days calculated using Eq. 5.6. The standard deviation values are shown with error bars . . . . .	93
5.8	Typical failure modes (lateral view, split specimen, crack surface, and micro-photo of crack surface) for flexural tests at 28 days with different $r$ . . . . .	95
5.9	Average compressive strength at 7 and 28 days. The standard deviation values are shown with error bars . . . . .	96
5.10	Fracture energy of mortar with different $r$ at 7 and 28 days . . . . .	97
5.11	<i>FSRF</i> (a) and <i>CSRF</i> (b) as a function of $r$ at 7 and 28 days of mortar containing substituted PET aggregates from this study and literature [10–13]. . . . .	100
5.12	Comparison between the measured and predicted <i>FSRF</i> (a) and <i>CSRF</i> (b) based on proposed model in Table 5.5 at 7 and 28 days. Data from this study and literature [10, 11, 14, 12, 13] . . . . .	102
6.1	Grain-size distribution of adopted materials. The mix-plastic granules are not re-sieved since their granulometry is almost constant . . . . .	107

6.2	Micro-photo of recycled PET powder (a), mix-plastic granules (b), and details of the concave bases (c) . . . . .	108
6.3	Three point flexural test: test set-up (a), geometry and dimensions of notched beam specimen (b). . . . .	112
6.4	Water-penetration test setup: photo (a) and schematic of the specimen (b) . . . . .	113
6.5	Sample splitting apparatus: photo (a), schematic (b), and example of split face of a specimen (c) . . . . .	114
6.6	Mean compressive strength for different $r$ and substituted plastic aggregates. Standard deviation values are shown with error bars . .	117
6.7	Failure modes of compressive tests . . . . .	118
6.8	Flexural load-CMOD curves (a and b) and vertical displacement-load curves (c and d) for different $r$ . PET (a and c) and MIX (b and d) cases. Red lines are showing the results of the three repetitions while the black line is their average across CMOD . . . . .	120
6.9	Mean flexural strength (Eq. 5.6) for different $r$ and substituted plastic aggregates. Standard deviation values are shown with error bars . .	121
6.10	Failure modes of flexural tests . . . . .	122
6.11	SEM scans of: natural aggregate (a), PET powder (b), and MIX aggregate (c). The left scans are large view of the region of interest while right scans are close views of the region inside the rectangle reported on the left side. In MIX aggregate scan (c, left) the location of the spectrum analyses (Figure 6.12) are reported . . . . .	125
6.12	EDX elemental point analysis in terms of spectrum for: (spectrum 1) natural aggregates (a); (spectrum 2) PET powder (b), and (spectrum 3) mix-plastic granules (c). . . . .	126
6.13	$CSRF$ (a) and $FSRF$ (b) as a function of $r$ of concrete substituted by plastic aggregates from this study and literature [15–27]. Different colors indicate different studies and different markers and line style represents various factors, see Table 2.4 for details. For this study, the continuous black line refers to the PET case while the dashed black one to the MIX case . . . . .	129

6.14	Comparison between the measured and predicted <i>CSRF</i> (a) and <i>FSRF</i> (b) based on proposed model in Table 6.6. Data from this study and literature.[15–27] . . . . .	131
7.1	Quasi-static test apparatus . . . . .	137
7.2	Photo (a) and schematic (b) of 80mmdiameter SHPB apparatus . . . . .	139
7.3	Relationship between the gun pressure and impact velocity . . . . .	140
7.4	Three aligned waves ( $\epsilon_i$ ; $\epsilon_r$ and $\epsilon_t$ aligned and equilibrium condition checking (a); stress-strain curve with averaged axial stress, the stress on the back and forth faces of specimen, stress equilibrium condition and their difference (b). . . . .	143
7.5	Selection of pulse shaper . . . . .	145
7.6	Effect of recycled plastic aggregates with $r$ on UPV tests of different concrete . . . . .	147
7.7	Static stress-strain relationship curves . . . . .	148
7.8	Comparison of the elastic modulus calculated using ACI 318-05 [28] and CEB-FIP [29] models and experimental values of concrete from present study. . . . .	151
7.9	Typical failure modes under static loading of standard cylinder specimens for NAC, PET and MIX with different $r$ . . . . .	152
7.10	Stress–strain curves for different dynamic tests under each gun pressure	154
7.11	Energy absorption density as a function of the axial strain for NAC ( $r = 0\%$ ), PET and MIX tests. The circle mark is representing the point corresponding to the peak stress. . . . .	156
7.12	Failure modes of SHPB tests . . . . .	158
7.13	SEM scans of: natural aggregate (a), PET aggregate (b), and MIX plastic aggregate (c). The left scans are large view of the region of interest while right scans are close views of the region inside the rectangle reported on the left side. In MIX aggregate scan (c, left) the location of the spectrum analyses (Figure 6.12) are reported. . . . .	160

7.14	EDX elemental point analysis in terms of spectrum for: (spectrum 1) natural aggregates (a); (spectrum 2) PET powder (b), and (spectrum 3) mix-plastic granules (c). . . . .	161
7.15	DIF as a function of the strain rate, $\dot{\epsilon}$ , for different tests. The black continuous and red dashed lines indicate the CEB-FIP Model Code specification recommendation formula CEB [5, 30]. . . . .	163
7.16	Dynamic behavior of NAC in terms of characteristic points. Transmitted and reflected waveform curves (left); Stress–strain curve (right);	164
7.17	Dynamic behavior of PET5 in terms of characteristic points. Transmitted and reflected waveform curves (left); Stress–strain curve (right);	165
7.18	Dynamic behavior of PET10 in terms of characteristic points. Transmitted and reflected waveform curves (left); Stress–strain curve (right);	165
7.19	Dynamic behavior of PET20 in terms of characteristic points. Transmitted and reflected waveform curves (left); Stress–strain curve (right);	165
7.20	Dynamic behavior of PET30 in terms of characteristic points. Transmitted and reflected waveform curves (left); Stress–strain curve (right);	166
7.21	Dynamic behavior of MIX5 in terms of characteristic points. Transmitted and reflected waveform curves (left); Stress–strain curve (right);	166
7.22	Dynamic behavior of MIX10 in terms of characteristic points. Transmitted and reflected waveform curves (left); Stress–strain curve (right);	166
7.23	Dynamic behavior of MIX20 in terms of characteristic points. Transmitted and reflected waveform curves (left); Stress–strain curve (right);	167
7.24	Dynamic behavior of MIX30 in terms of characteristic points. Transmitted and reflected waveform curves (left); Stress–strain curve (right);	167
7.25	NAC: 0.3MPa (a); 0.45MPa (b); 0.6MPa (c) . . . . .	169
7.26	PET5: 0.3MPa (a); 0.45MPa (b); 0.6MPa (c) . . . . .	170
7.27	PET10: 0.3MPa (a); 0.45MPa (b); 0.6MPa (c) . . . . .	171
7.28	PET20: 0.3MPa (a); 0.45MPa (b); 0.6MPa (c) . . . . .	172
7.29	PET30: 0.3MPa (a); 0.45MPa (b); 0.6MPa (c) . . . . .	173
7.30	MIX5: 0.3MPa(a); 0.45MPa(b); 0.6MPa(c) . . . . .	174



---

7.31	MIX10: 0.3MPa (a); 0.45MPa (b); 0.6MPa (c) . . . . .	175
7.32	MIX20: 0.3MPa (a); 0.45MPa (b); 0.6MPa (c) . . . . .	176
7.33	MIX30: 0.3MPa (a); 0.45MPa (b); 0.6MPa (c) . . . . .	177

# List of Tables

2.1	Summary of physical and mechanical characteristics of plastics . . .	13
2.2	Plastic category and characteristic size range, adapted from [31] . . .	15
2.3	Overview of previous studies on mortars containing substituted plastic aggregates. $w$ : width; $t$ : thickness; $l$ : length; $r$ : substitution ratio; $D$ : Density; $CS$ : Compressive strength; $FS$ : Flexural strength; $STS$ : Splitting tensile strength; $EM$ : Elastic modulus; $PV$ : Pulse velocity; $TC$ : Thermal conductivity; $WA$ : Water absorption . . . . .	15
2.4	Literature review of quasi-static tests on plastic aggregate substituted concrete: granules (a) and fibers (b). . . . .	19
2.5	Coefficients $a$ and $b$ in Eq. 2.6 proposed by Lu et al. [7] and Xiao et al. [6]. $\dot{\epsilon}_t(r)$ is the critical strain rate for Lu et al. [7]. . . . .	26
3.1	Roots of the Pochhammer-Chree frequency equation (Eq. 3.20). . .	47
4.1	Physical properties and photos of the different coarse aggregates employed. . . . .	60
4.2	Mix proportion and dry density for concrete made with different levels of substitution and types of coarse aggregate tested in this study. Symbols are reported following Eq. 4.3. . . . .	61
4.3	Summary of the SHPB tests. . . . .	64
4.4	Energy absorption density at failure, $\hat{\omega}$ [MJ/m <sup>3</sup> ], for the different tests. The layout of the data in the cells is the following: $\tilde{\omega}(\hat{\omega}_1, \hat{\omega}_2, \hat{\omega}_3)$ , where $\hat{\omega}_1, \hat{\omega}_2, \hat{\omega}_3$ are the values of $\hat{\omega}$ for the three repetitions of tests and $\tilde{\omega}$ their average. . . . .	73

4.5	Comparison of the parent concrete mix design among this study, Guo et al. [8] and Xiao et al. [6]. . . . .	77
4.6	Coefficients $a$ and $b$ in Eq. 4.10 fitted using the experimental data for RAC of this study and this study and Guo et al. [8]. The fitted lines are shown in Figure 4.9. . . . .	79
4.7	Coefficients $a$ and $b$ in Eq. 4.10 fitted using the experimental data for RBC. The fitted lines are shown in Figure 4.10. . . . .	80
5.1	Mix proportion of the different mortars . . . . .	85
5.2	Fresh density, density after 24h of the mortar, water absorption, and slump. The reported values are the average of three repetitions and the values inside brackets are the standard deviation . . . . .	89
5.3	Critical stress intensity factor with different $r$ at 7 and 28 days. In the table, the average of $K_{IC}$ is followed by three numbers inside brackets corresponding to the first, second and third tests, respectively	98
5.4	Summary of ranges of input variables (dataset) adopted in the symbolic regression. Additional details are reported in Table 2.3 and Section 5.1.1. * of the reference mix, i.e., for $r = 0\%$ . . . . .	99
5.5	Data-driven predictive models for $FSRF$ and $CSRF$ at 7 and 28 days	101
6.1	Properties and photos of natural aggregates and plastic aggregates adopted in this study . . . . .	106
6.2	Mix proportion of the mix investigated. See Figure 6.1 for the definition of the granulometry . . . . .	110
6.3	Slump, slump flow, visual inspection of slump tests, and fresh density for the different concrete mixtures. . . . .	115
6.4	Cracking initiation load ( $P_{max}$ ), initial crack opening displacement ( $CMOD_c$ ), vertical displacement at peak load ( $D_v$ ), flexural elastic modulus ( $E_{fl}$ ), and fracture toughness ( $K_{IC}$ ). The three numbers are the results of the three tests while the average and standard deviation values are reported inside the parenthesis . . . . .	123

6.5	Maximum and average of water penetration depth. The three numbers are the results of the three tests while the average and standard deviation values are reported inside the parenthesis . . . . .	124
6.6	Data-driven predictive models for <i>CSRF</i> and <i>FSRF</i> . . . . .	130
7.1	Concrete mix proportion . . . . .	136
7.2	Slump values of concrete mixture . . . . .	146
7.3	Quasi-static compressive properties of different mixes. $f_c$ : the compressive strength; <i>SRF</i> : Strength Reduction Factor (see Eq. 5.13); $E_c$ : Elastic modulus (see Eq. 7.15); <i>ERF</i> : Elastic modulus Reduction Factor. The number reported in the table are the mean. When the variable is followed by the numbers inside the brackets, e.g., $f_c$ (1;2;3), indicates that the results refers to the first, second and third test, respectively. <i>SRF</i> and <i>ERF</i> are the mean of the three repetitions.	150
7.4	Energy absorption density at peak stress, $\tilde{\omega}$ (unit: MJ/m <sup>3</sup> ). When the variable is followed by the numbers inside the brackets, e.g., 0.33 (0.35; 0.31; 0.33), indicates that the results refers to the first, second and third test, respectively. . . . .	156

# Chapter 1

## Introduction

### 1.1 Background and problem statement

Globalization and the growth of population have accelerated the dynamics of the urbanization process in developing countries[32]. Especially, the uncontrolled growth of the population and advancement of modern technology in undeveloped or developing countries has made the management of the municipal solid waste (MSW) a significant issue and big challenge to all over the world. MSW consists of the waste coming from field of construction, businesses, educational institutions and hospitals and etc. The non-decaying and non-degrade wastes can remain in the environment for hundreds, perhaps thousands of years. Focus on the solid waste in construction sector, the types of construction and demolition waste (CDW) mainly include bricks and blocks, unused concrete metal such as aluminum and steel, gypsum, glass, which derives from demolition of buildings other wastes like wood, plastics and asphalts are also quite common in field of construction. Figure 1.1 shows the percentage of particular construction waste materials (data from [1]), it shows the more than 30% of constructional waste is contributed by brick and blocks, unused concrete and plastics.

Clearly, the way to limit the impact on the environment is by reducing the amount of waste that is generated [33]. In general, construction by nature is not an environment-friendly activity. Researchers have provided comprehensive reviews of the negative impacts caused by construction activities [34]. Until now, the balance

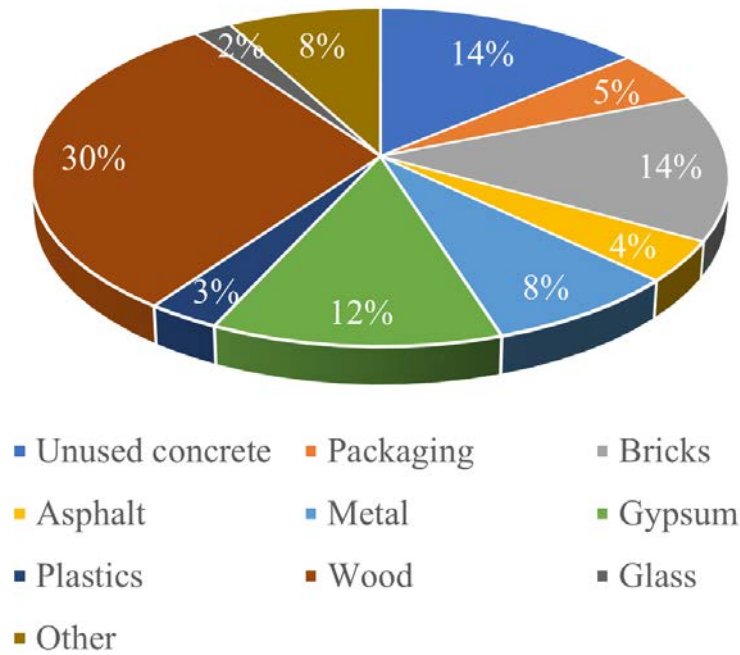


Figure 1.1 The volume of various construction and demolition waste (CDW) (modified from [1]).

between the needs to be struck is to reduce the overall environmental impact of the waste management system as far as possible within an acceptable cost limit [32].

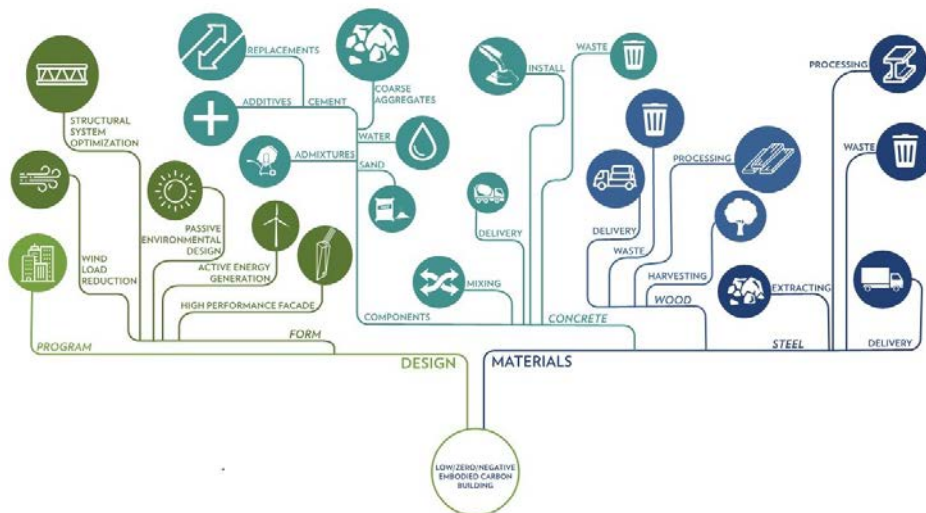


Figure 1.2 Toward zero carbon building

Figure 1.2 shows the possibility of realizing the low embodied carbon building. Generally, it can be realized by two main method approaches, namely, the low carbon design and low carbon materials. Regarding the low carbon design, it can be mostly involved with the design form, such as wind load reduction at outer-surface of building, structural system optimization, passive environmental design, active energy generation and high performance facade, etc. Another significant way to achieve the target of low carbon building is the low carbon materials. The constructional materials are mainly composed by concrete, wood and steel. Regarding low carbon materials, it can be realized by proper materials manufacturing. Considering steel and wood production process, during the delivery, waste disposal, processing and harvesting of wood and extracting of steel, which can be accompanied by low carbon activities. Similarly, regarding cementitious materials, the process of mixing, delivery, install and waste disposal can be finished by low carbon activities. Compared with wood and steel, concrete is a kind of composite material which composed of different materials, which can take more chances to realize low carbon material. For example, the traditional natural fine and coarse aggregates can be replaced by CDWs or other low carbon constructional materials, or the CDWs or low carbon constructional material can be used as addition or additives in the concrete. The details of materials which are beneficial to achieve the low carbon materials are introduced in the next contents.

### 1.1.1 Plastics

In detail, plastics are a wide range of synthetic or semi-synthetic materials that use polymers as the main ingredient [35]. Polymers exist organically or can be created synthetically, and consist of chains of joined individual molecules or monomers. The difference between polymers and plastics is that plastics are a type of polymer composed of chains of polymers that can be partially organic or fully synthetic. Thermoplastics encompass a wide range of materials, including polyethylene terephthalate (PET), polyethylene (PE), polystyrene (PS), polypropylene (PP), polyvinyl chloride (PVC), polyester, nylon, acrylonitrile butadiene styrene (ABS). These plastic types show quite different physical and mechanical properties thus their use and applications are wide depending on the product requirements.

Plastic materials have been widely applied in the consumer field since mass production in the 1930s-1940s. Over the last few decades, they have been vastly

used in a multitude of industries, with an alarmingly growing rate of production globally. Plastic materials have been widely applied in the consumer field since mass production in the 1930s-1940s. The cumulative global production of plastics has been approximately 8.3 billion tons since 1950, half of which was produced in the past 13 years (more than 300 million tons annually in recent years) [36]. At the beginning of the use of plastic materials, the very slow degradation capacity was neglected resulting in a negative effect on the human and wildlife and a great threat to plane. Strategies for controlling plastic waste include both waste management practices (e.g., recycling, landfilling, converting plastic to energy) and innovation (e.g., using biodegradable plastics) and all have shortcomings [37].

In contrast to the advantages of the application of plastics, more attention should be paid to the reduction of production [38], elongating of their life cycle [39], and development of solutions for the end of their life cycle (solid waste) [40]. The enormous quantity of plastic waste has raised the attention of all over the world. Globally plastic waste occupies more than 10% of MSW [41]. More than 12 million tons of plastic waste are generated every year [42], and more than 6.4 million tons are entering the marine environment which takes an irreversible threat to the ecosystem. The major disposed methods of plastic waste are landfill, combustion (incineration), and recycling including mechanical recycling and feed-stock recycling [43], although a few biodegradable methods are proposed nowadays [44]. Before the 1980s, recycling and combustion of plastic were negligible with almost 100% landfilled. From the 1980s, combustion became to be commonly used, and in the 1990s recycling started to be paid attention. Geyer et al. [45] predicted that by 2050, combustion rates would increase to 50 percent, recycling to 44 percent, and discarded waste would fall to 6 percent in which the concrete or mortar projections are not represented. Landfills are not ideal for degradation of the material and require very large land-space consumption thus implying high costs and low effectiveness in solving the plastic waste problem [46]. Air pollution and the by-products of combustion (i.e., converting plastic to energy) still need to be fully solved.

Another threat is that plastic produces a tremendous amount of CO<sub>2</sub>, which is opposite of the goal of carbon neutrality and even negative for achieving it. Figure 1.3 shows the Global life-cycle GHG emissions of conventional plastics by life-cycle stage and the corresponding plastic type, and the carbon credits generated by recycling are not included. Which depicted clearly that the method of recycling and landfill can reducing the carbon emission than incineration. Regarding landfill,



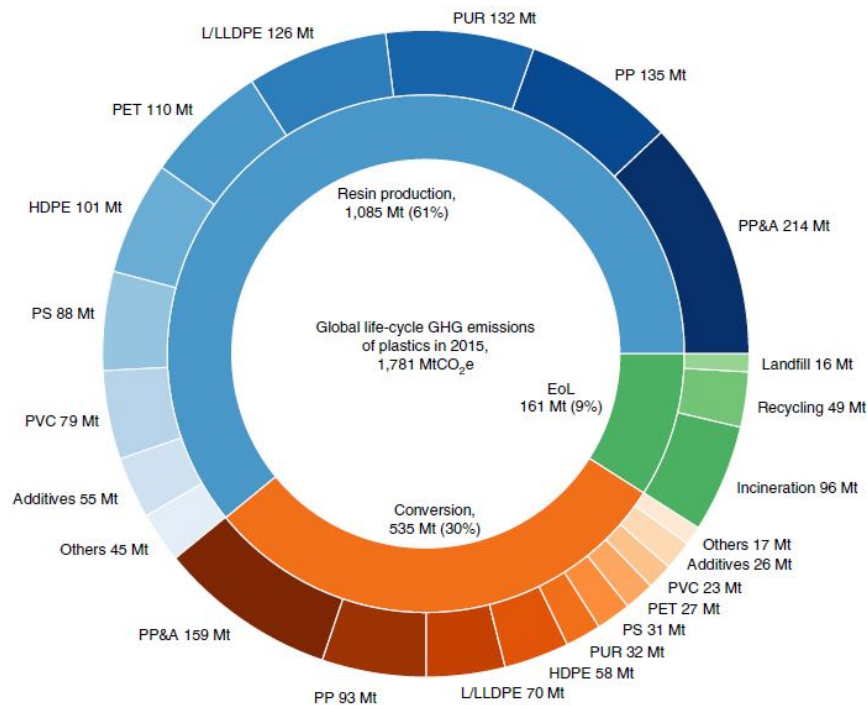


Figure 1.3 Global life-cycle GHG emissions of conventional plastics in by life-cycle stage and plastic type (modified from [2]).

especially for brick and blocks, unused concrete, the major types of constructional wastes. Owing to its non-combustible nature, construction waste normally ends at landfills, landfill has been the worldwide disposal way to solve them, for example, in UK, it is estimated more than 50% of the waste from constructional field deposited by landfill [47, 34], and the amount of the construction waste can be 70 million tons. In Australia, more than 14 million tons waste are land filled, which 44% of the waste is contributed by construction field. In USA, the percentage is about 22%. However, the waste in landfill takes new challenge on the extensive amount of air, water and soil pollution from anaerobic degradation and the harmful substance of the waste. However, Broitman et al. [48] has indicated that the landfill affected by the city size, population density and the restriction is relatively large by the development of city, especially the large demand of land contributed by urbanization.

### 1.1.2 Recycled bricks and recycled crushed concrete aggregate

On the other hand, the rapid growth of the global population and urbanization over the next several decades will create a vast demand for the construction of new buildings and accompanying infrastructure [49] and in turn for construction materials. Concrete is the second most used substance by mass after water [50]. Worldwide, over ten billion tons of concrete are being produced each year [51] corresponding to around 1 ton per person per year [52], and this demand has continued to grow [53]. Concrete is a composite material composed of fine and coarse aggregates bonded together with a mortar made of water and cement. Taking in all stages of production, concrete is said to be responsible for 4-8% of the world's CO<sub>2</sub> [54]. The production of concrete has two main detrimental effects on the environment: (i) a large CO<sub>2</sub> emission produced during the production of the main cement component, the clinker [55]; (ii) large exploitation of quarries for the production of the aggregates employed [6]. These are major threats to the sustainable development of concrete structures and infrastructures.

The most common natural coarse aggregate employed in the concrete is gravel. A typical concrete mix contains roughly 60 – 80% of sand and gravel with a dominant part made by the second one. Given the importance of the coarse aggregates in the mixture and their negative environmental impact, different researchers tried to substitute them with different recycled materials. A promising solution is the use of CDW materials. CDW materials also contribute a large fraction by mass to the waste stream. For example, about 850 million tons of CDW is generated in the European Union per year, representing 31% of the total waste generation [56]. Therefore, building strategies that maximize the use of existing materials in new constructions would yield significant results in reducing the environmental impact [57]. For instance, the use of crushed Recycled Concrete Aggregate (RCA) or crushed Brick Aggregate (BA) as coarse aggregates has been an object of research since the 1980s [e.g., 58–60]. Concrete, bricks, and tiles are widely used in residential construction accounting for a large proportion of CDW [60–64]. The proper disposal method for them also attracted attention from civil and infrastructure engineering.

## 1.2 Dynamic apparatus

The response of materials under large deformations applied in a very short time range can be quite different from the quasi-static case [65, 66]. In many fields, such as aeronautics, protective structures, military industries, and civil engineering, the design and structural checks requires knowledge about the variation of the material strengths under high rate loading [67, 68]. The study of the constitutive laws of materials under high-strain rates generally requires experimental testing performed using special apparatus.

Since the pioneering work of Hopkinson who performed a dynamic test with one slender bar [69], a variety of techniques were developed including the drop-weight machine, SHPB [70], Taylor impact [71], and plate impact [72]. This experimental apparatus attempts to describe the constitutive law of material accounting for an additional parameter called strain-rate describing the variation of the deformation as a function of time and generally expressed as the inverse of the time, i.e.,  $s^{-1}$ . All the experimental techniques previously described are based on the application of a rapidly varying load and differ in the range of strain rates achievable [9]. One of the most adopted apparatuses at high strain rates is the SHPB with strain rates ranging from  $10^2$  to  $10^4 s^{-1}$  [73, 74].

The SHPB bar system is mainly composed of three bars [75]: a striker, an incident (or input), and a transmission (or output) bar. The specimen is sandwiched between the incident and the transmission bars. The tests are generally performed by accelerating the striker and forcing a collision to one extremity of the incident bar generating the propagation of an elastic wave. This wave propagates along the incident bar until reaching the location of one end face of the specimen [76]. When reaching that face, the elastic wave is partially reflected and part of the compressive wave is transmitted to the specimen. A second reflection occurs at the second interface representing the contact between the specimen and the output bar. The reflection is due to the difference between the physical, and/or mechanical, and/or dimensional properties between the bars and the specimen, called impedance mismatch. If the specimen has a low impedance than the bar, the reflected wave at the first interface is a tensile wave whereas the wave reflected at the second interface is compressive [77]. Thus, the sample is uni-axially subjected to a compressive load. Strain gauges are used to measure the strains in the bars and the stress-strain curves could be constructed without consideration of the specimen by using

one (transmitted), two (incident and reflected), or three (incident, reflected, and transmitted) waves.

The majority of materials experience an increase in compressive strength positively correlated to the increase of the strain rate. This increase is generally expressed in terms of a non-dimensional factor called Dynamic Increase Factor (*DIF*). This factor represents the ratio between the dynamic and the quasi-static strength of the material. For example, the *DIF* of concrete at high strain rates under dynamic compressive and tensile loading could reach 3.5 and 9, respectively [78–80]. Metal materials exhibit similar trends, with lower *DIF* ranging around 1.3 – 1.9 changed with material strength and input strain rate [81].

As fine-grained materials are extensively studied under high strain rates [82], the development of the SHPB apparatus is largely dominated by small-diameter test setups. To test a specimen made of metal, the diameter of SHPB generally ranges from 10 to 20 mm [e.g., 83, 84]. However, the study of inhomogeneous materials such as concrete needs enlargement of the diameter of the bars and upgraded measurement techniques [85, 86]. A larger diameter SHPB apparatus brings several challenges, such as the design of the striking system because of the heavy striker, wave pulses dispersion more striking because of wave propagation in the larger bars, and the limitation of input strain rate because of large-size specimen characterization, etc. [87].

The design and calibration of large-scale SHPB setup are needed to study further in the case of the valid test on dynamic properties of concrete and composite materials, especially for the absence of the study on apparatus with a diameter more than 100 mm. For instance, the European Laboratory for Structural Assessment has a Large Hopkinson Bar Facility (ELSA-HopLab) facility with a very large 100 mm Hopkinson bar developed for testing brittle materials [88]. To the best authors' knowledge, this SHPB apparatus used in Chapter 4 has the largest diameter in the world. The system is custom designed to perform tests on both brittle and ductile materials. One of the main applications of such a large diameter bar is concrete where large specimens are needed to cope with homogenization issues.

Cementitious material is heterogeneous material and its mechanical behavior is strongly affected by the time and by environmental factors. The quasi-static mechanical behavior was mainly investigated by performing quasi-static tests with low values of the strain rates (i.e., change in strain with respect to time), namely

slower than  $10^{-3} s^{-1}$  and the quasi-static mechanical properties of concrete are nowadays well-known. However, the cementitious materials are sensitive to the strain rate, which represents that the response of cementitious materials can be quite different from its static properties under rapid varying dynamic loading. In fact, the rapid varying dynamic loading are common in Civil Engineering applications, since concrete, or more generally reinforced concrete structures, can be subjected to vehicular impacts (e.g., cars, trucks, trains, boats, railed, aircraft, etc.), to blasts or explosions and to other complex fast varying dynamic loads during their service life. And in the light of the relative researches on concrete containing CDWs under dynamic loading are deficient and the knowledge of the dynamic mechanical properties of concrete substituted by CDWs aggregates are urgently-needed.

### 1.3 Objectives

A generic approach for dealing with municipal solid waste (MSW) including CDW and plastics is proposed from a technical view, namely, using recycled aggregate for different concrete applications can help reduce, reuse and recycle construction waste and plastics effectively [34]. The application of the construction waste in producing new concrete has been proposed as a promising strategy. Regarding the construction waste, several types from them are selected to be representative materials adopting in producing novel green concrete.

Considering the amount, accessibility and price, in this thesis, unused concrete, clay bricks and different types of plastics, herein PET, mixed-plastic granules are selected to produce a novel concrete and conducted a deep investigation. The details of plastics and the recycled bricks aggregate and recycled concrete aggregate are introduced in Section 1.1.1 and Section 1.1.2. The details of each experiment are show in the next each Chapter. The experiments are divided into two parts, quasi-static and dynamic tests since the loading rate and loading method are different.

By conducting static and dynamic tests, it can evaluate the feasibility and suitability of the novel concrete applied in structural engineering. These tests can provide information about the mechanical properties, durability, and structural behavior of the concrete material. By combining the results of dynamic and static tests, it can achieve a comprehensive understanding of the behavior of the novel green concrete and assess its potential for use in structural engineering. The data obtained from

these tests will help inform design decisions and ensure the safety and reliability of structures built using the novel concrete.

## 1.4 Outline of the thesis

The thesis is divided into main 8 chapters, which are organized as follow and reflect the main objectives set in the previous section. The technical roadmap applied in this thesis is shown in Figure 1.4. The detailed content of each chapter can be summarized as follows:

Chapter 1: in this first introductory chapter, the motivations and objectives of the research were stated.

Chapter 2: this chapter contains a literature review on the CDW material in concrete and the mean quasi-static compressive strengths of the wrapped concrete specimens are and 82MPa. quasi-static and dynamic experimental researches.

Chapter 3 gives a basic introduce and calibration to the large diameter SHPB system and it is the foundation of Chapter 4.

Chapter 4: in this chapter, a literature review of the state-of-the-art on the development of recycled concrete substituted by crushed concrete and bricks is given, and the quasi-static and high-strain rate compressive behaviors of them are given.

Chapter 5: this chapter reports on the possibility of adopting PET powder in cementitious, especially in mortar, and physical and mechanical properties of mortar with substituted recycled PET powder are deeply investigated in this chapter.

Chapter 6: in order to apply the results in Chapter 5 (mortar scale) in plain concrete scale, some preliminary studies were conducted on concrete with two different substituted recycled plastic aggregates and the physical and mechanical properties of the concrete are in a deep investigation.

Chapter 7 continues to have a dynamic loading on the novel green concrete with two different substituted recycled plastic aggregates which offering the comparison with Chapter 1.

Chapter 8: to conclude, in this chapter the main research findings of the study are summarized and perspectives for further research are suggested.

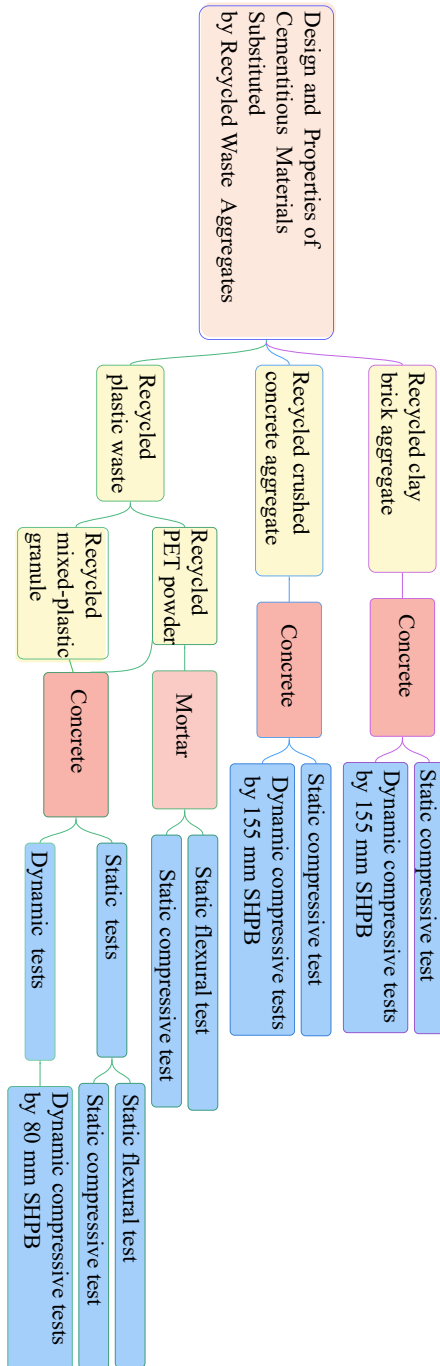


Figure 1.4 The technical roadmap in this thesis

# Chapter 2

## Literature review

### 2.1 Quasi-static tests on recycling and reusing plastics in cementitious materials

Nowadays, the disposal method of recycling plastic is growing in popularity. Recycling can be divided into feed-stock recycling and mechanical recycling [43]. The feed-stock recycling implies a change of chemical structure while the mechanical recycling implies no chemical change or in other words just reuse [89]. The mechanical recycling method implies processes like classification of the plastic categories, and change of plastic size or shape, without chemical change.

Therefore, a sustainable and eco-friendly method to manage plastic waste is an immediate requirement. In addition, reuse and recycling of plastic wastes have been found to be more effective when compared with landfill and incineration [43]. To this aim, notable actions have been taken to reduce the production of plastic and to increase its recycling rate. For instance, Figure 2.1 shows the common plastic and the corresponding recycling codes according to ASTM D7611 / D7611M [3] and based upon the system developed in 1988 by the Society of the Plastics Industry (SPI). This classification allows for rational waste sorting at urban and industrial levels.



## 2.1 Quasi-static tests on recycling and reusing plastics in cementitious materials 13

Table 2.1 Summary of physical and mechanical characteristics of plastics

Abbreviation	Name	Chemical formula	Density range	Elastic Modulus	Tensile Strength	Thermal Conductivity	Performance	Application
-	-	-	(g/cm <sup>3</sup> )	(GPa)	(MPa)	(W/mK)	-	-
PET	polyethylene terephthalate	(C <sub>10</sub> H <sub>8</sub> O <sub>4</sub> ) <sub>n</sub>	1.37-1.45	2.1-3.1	55-80	0.15	High strength and stiffness, excellent electrical insulating, transparent, Poor burning behavior	Bottles for drinks, microwavable containers, transparent films, etc.
PE	polyethylene	(C <sub>2</sub> H <sub>4</sub> ) <sub>n</sub>	0.91-0.97	0.6-1.4	18-30	0.33-0.52	Good impact resistance, low temperature resistance, abrasion resistance, chemical corrosion resistance, self-lubrication	Caps for food packaging, jerry cans, trays
PVC	polyvinyl chloride	(C <sub>2</sub> H <sub>3</sub> Cl) <sub>n</sub>	1.16-1.58	2.7-3.0	50-60	0.17-0.21	Lightweight, durable, good insulation, self-extinguishing and abrasion-resistant	Construction, packing, wires and cables, clothing and even medical
PP	polypropylene	(C <sub>3</sub> H <sub>6</sub> ) <sub>n</sub>	0.90-0.91	1.3-1.8	25-40	0.12	Good chemical resistance and weldability, high chemical and bacterial resistance	Food and consumer goods, medical application like disposable syringes
PS	polystyrene	(C <sub>8</sub> H <sub>8</sub> ) <sub>n</sub>	1.01-1.04	3.1-3.3	30-55	0.105	Transparent, glassy and brittle, excellent dimensional stability, good resistance to water and inorganic chemicals, low thermal conductivity, low moisture absorption and excellent cushioning properties	Office accessories, lightweight fill in road and railway construction, sports helmets, infant car seats, insulated panel systems for facades, walls, roofs and floors in buildings, as flotation material in the construction of marinas and pontoons
PC	polycarbonate	bisphenol A (C <sub>15</sub> H <sub>16</sub> O <sub>2</sub> ) + phosgene (COCl <sub>2</sub> )	1.20-1.22	2.2-2.5	55-77	0.21	Relatively high impact strength, high dimensional stability, good electrical insulation, lightweight and transparent, resistance to UV light	Eye-catching design, agricultural houses, manufacturing CDs/DVDs and sunglasses, refrigerators, air conditioners, coffee machines, etc.



Figure 2.1 Plastic and recycling code according to ASTM D7611 / D7611M [3]

As discussed in the upper part, the most common thermoplastics include Polyethylene (PE), Polypropylene (PP), Polystyrene (PS), Polyvinyl Chloride (PVC), Polyethylene Terephthalate (PET) and Polycarbonate (PC). The basic characteristics of the common plastics of daily life are shown in Table 2.1. The density of the thermoplastic is generally low and exhibits good and similar thermal conductivity performances while the mechanical properties of PET and PVC are the best in terms of elastic modulus and tensile strength.

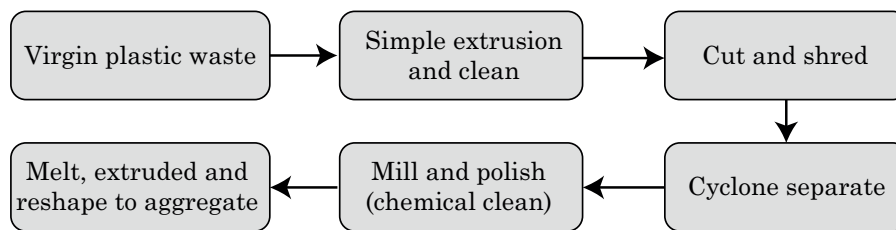


Figure 2.2 Typical process to obtain recycled plastic aggregates to be employed in cementitious material

One viable way to recycle plastic is its use as a constituent of construction material such as concrete and mortar [e.g., 90–95]. There are already pioneering researches and according to the best authors' knowledge, the first study proposing recycled plastic in cement-based materials dates 1997 [96]. Before being aggregates in the mixture, plastic wastes are processed to have a suitable shape and size distribution. Figure 2.2 showed a typical transformation process of plastic waste into plastic aggregate. First, simple extrusions and cleaning is performed followed by wastes cut and shredded into small pieces and fragments. Then, the pieces and fragments were put into the cyclone separator to remove the impurities such as dust and metal. Subsequently, plastic pieces and fragments were milled and polished with the application of the surfactants and alkaline substances to remove the chemical products, e.g., glue. Later the plastic pieces and fragments were melted, extruded, and reshapes to have a suitable shape and size distribution, e.g., fibers, granules of different sizes, etc.

Plastic particles can be grouped into different categories regarding their size especially by diameter (or characteristic size). Table 2.2 summarizes some standard ranges for a given particle category [31]. The plastic aggregates adopted in mortar are commonly from nanoplastics to large microplastics [10, 11, 97, 98]. In the last decades, many researchers have investigated the possibilities of the substitution of recycled plastic aggregates in mortar. In particular, Table 2.3 presents a state-of-art of previous studies on mortars containing substituted plastic aggregates in recent decades. From this table, it can be observed that the majority of researches uses large microplastics and mesoplastics. Only Aattache et al. [99] adopted small microplastics. Nanoplastics are seldom used having granulometry more similar to cement but being inert (not chemically reactive).

In this thesis, a primary research is focused specifically on mortar with substituted recycled PET powder. Patented by J. Rex Whinfield and James T. Dickson in 1941,

## 2.1 Quasi-static tests on recycling and reusing plastics in cementitious materials 15

Table 2.2 Plastic category and characteristic size range, adapted from [31]

Particle category	Characteristic size range
Nanoplastics	< 0.0001 mm (0.1 $\mu$ m)
Small microplastics	0.00001 – 1 mm
Large microplastics	1 – 4.75 mm
Mesoplastics	4.76 – 200 mm
Macroplastics	>200 mm

Table 2.3 Overview of previous studies on mortars containing substituted plastic aggregates. w: width; t: thickness; l: length; r: substitution ratio; D: Density; CS: Compressive strength; FS: Flexural strength; STS: Splitting tensile strength; EM: Elastic modulus; PV: Pulse velocity; TC: Thermal conductivity; WA: Water absorption

Reference	Year	Plastic type	Shape	Plastic size (mm)	r [%]	D	CS	FS	STS	EM	PV	TC	WA
Hannawi et al. [10]	2010	PET	Fiber	2-6.3	0; 3; 10; 20; 50	✓	✓	✓		✓			
Hannawi et al. [10]	2010	PC	Granules	3.15-5	0; 3; 10; 20; 50	✓	✓	✓		✓			
de Oliveira and Castro-Gomes [100]	2011	PET	Fiber	w: 2 t: 0.5 l: 35	0; 0.5; 1.0; 1.5	✓	✓	✓					✓
Wang and Meyer [101]	2012	HIPS	Granules	< 4	0; 10; 20; 50	✓	✓	✓		✓			✓
Ghernouti and Rabeih [102]	2012	NA	Granules	>1	0; 10; 20; 30; 40	✓	✓						
Hannawi et al. [14]	2013	PC; PET	PC: granules; PET: fiber	1-10	0; 3; 10; 20; 50	✓			✓				
Lucolano et al. [103]	2013	Mix (PP+PE)	Granules	0.5-1.5	0; 10; 15; 20; 25; 33; 50	✓	✓	✓					✓
Safi et al. [11]	2013	PET	Granules	1-5	0; 10; 20; 30; 50	✓	✓	✓			✓		✓
da Silva et al. [97]	2014	PP; PF	Granules	1-4	0; 5; 10; 15	✓	✓	✓		✓			✓
Hannawi and Prince-Agbodjan [104]	2015	PC	Granules	< 5	0; 3; 10; 20; 50	✓	✓				✓		✓
Al-Tulaian et al. [105]	2016	PVC	Fiber	w: 2 t: 20, 50	0; 0.5; 1.0; 1.5	✓		✓					
Coppola et al. [106]	2016	PP+PE	Granules	0.2-2	0; 10; 25	✓	✓	✓					
Aattache et al. [99]	2017	PE	Granules	0.08-0.5	0; 2; 4; 6	✓			✓				✓
Aciu et al. [107]	2018	PVC	Granules	< 8	n/a	✓	✓	✓					
Badache et al. [108]	2018	HDPE	Fiber and granules	< 3.15	0; 15; 30; 45; 60	✓	✓	✓		✓	✓		✓
Coppola et al. [109]	2018	PP+PE	Granules	0.2-2	0; 10; 25	✓							✓
Rubio-de Hita et al. [110]	2018	PP	Fiber	< 16	0; 5; 7.5; 10; 12.5; 15	✓	✓			✓	✓		✓
Senhadji et al. [111]	2019	PVC	Granules	0-4	0; 10; 30; 50; 70	✓	✓	✓			✓		✓
Ohemeng and Ekolu [112]	2019	LDPE	Granules	n/a	0; 5; 10; 20; 30; 40; 50; 60	✓	✓	✓					
Merlo et al. [98]	2020	PVC	Granules	0.5-3	0; 5; 10; 15; 20	✓	✓						
Kaur and Pavia [12]	2020	PC; PET	PC: granules; PET: fiber	2-5	0; 5; 15; 20	✓	✓	✓		✓			✓
Hacini et al. [13]	2021	PET	Fiber	w: 9-19 t: 0.5-1.1	0; 15; 30; 45; 60	✓	✓	✓		✓	✓		✓
Martínez-López et al. [113]	2021	PE; PP	Granules	< 2.8	0; 1; 2; 3 (by weight)	✓	✓			✓			
Górák et al. [114]	2021	PET	Fiber	< 8	0; 10; 25	✓	✓	✓					

PET is the most common thermoplastic polymer resin of the polyester family, with almost 70 million tons manufactured annually worldwide for use in textiles and packaging [45]. The density of PET is in the range of 1.37 – 1.45 g/cm<sup>3</sup>. PET is well known for its high strength and stiffness, excellent electrical insulating, and transparency. It is generally used as virgin plastic for soft drink and mineral water bottles, filling for sleeping bags and pillows, textile fibers and as recycled plastic, (multi-layer) detergent bottles, clear film for packaging, carpet fibers, fleecy jackets [90].

Several authors investigated mortar with substituted recycled PET powder (see Table 2.3). First, Hannawi et al. [10] studied the properties of mortar with PET and

PC granules with a large range substitution level. Results showed that the incorporation of plastic aggregates decreases mechanical strength and increases strain capacity and cracking resistance. de Oliveira and Castro-Gomes [100] investigated PET fiber reinforced mortar with a relatively low addition level and the results indicated that PET fibers significantly improve the flexural strength and toughness although the compressive strength decreases. Safi et al. [11] used PET as fine aggregate instead of sand in a large substitution range level by weight and the work presented shown that the mortars made with 50% of plastic waste aggregated are characterized by better results regarding density and the reduction of mechanical strength about 15 to 33%. da Silva et al. [97] also conducted some tests on mortar with substituted PET granules sand and results showed that incorporation of plastic aggregates led to worse performances in terms of mechanical properties but an improvement in water vapor permeability, impact resistance, and dimensional stability. Experiments on mortar with PET granules conducted by Kaur and Pavia [12] showed that when substitution level up to 15%, the flexural strength was enhanced. Hacini et al. [13] explored the possibility of using PET strapping bands in mortar, the tests results showed that the dynamic elastic modulus and ductility were improved and the reduced expansion due to the alkali-silica reaction (ASR) by adding PET strapping bands in mortar.

However, even though many studies have investigated the effect of substituted recycled PET aggregates into cementitious materials (see Table 2.3), the possibility of use of recycled PET powders (microplastic, see Table 2.2) into a cementitious material has never been investigated, whether for concrete or mortar. Besides, the majority of research focused on the hardened properties neglecting those at the fresh state. The latter properties can be quite important for the application of such materials where flowability is important. Accordingly, the knowledge of these characteristics opens interesting scenarios for the optimization of mortar with substituted recycled PET powder for 3D printing applications [115].

To this aim, the purpose of this investigation is to study the effects of the substitution of fine aggregates with recycled polyethylene terephthalate (PET) powder and curing time on the physical and mechanical properties of mortars with substituted recycled PET powders. The remainder of this thesis is divided into five sections. Section 5.1 presents the materials adopted and the experimental program comprising measurements of density, slump, water absorption, ultrasonic pulse velocity, flexural and compressive behavior, and micro-structural and interface characterization. Section 5.3 presents the experimental results. Section 5.4 reports a discussion focusing

## 2.1 Quasi-static tests on recycling and reusing plastics in cementitious materials 17

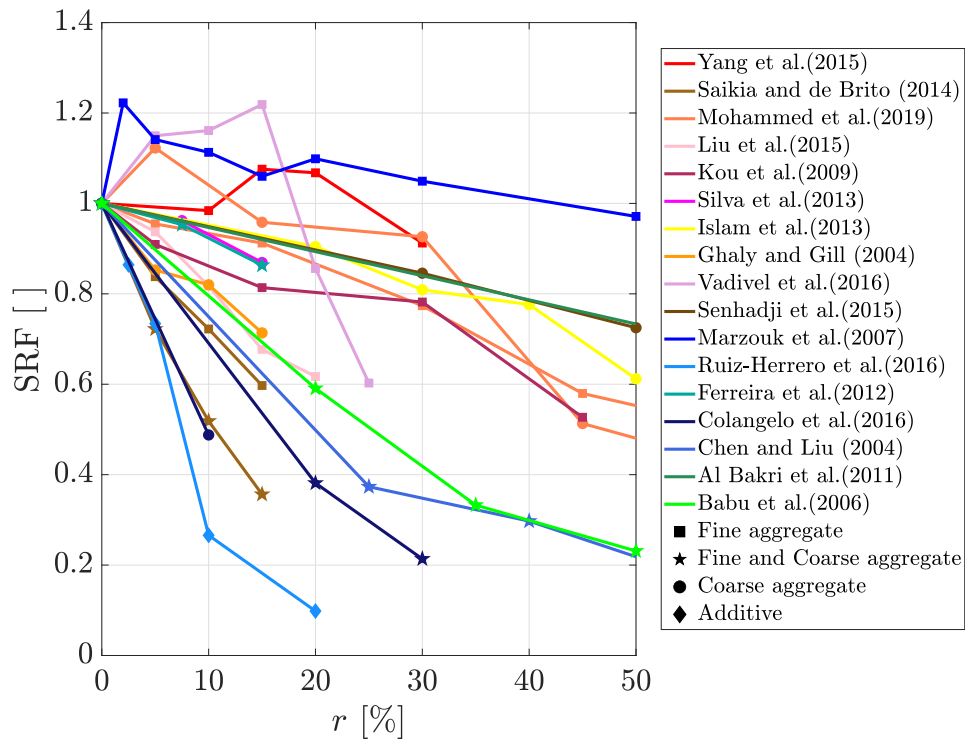
on the fracture energy, flexural fracture toughness factor and residual strength, and a proposed predictive equation for the strength compressive and flexural reduction factors based on the data taken from this study and the literature. Finally, some conclusions and perspectives were drawn (Section 5.5).

Besides recycling plastic in mortar, the most common approach is to substitute some of the main components of the concrete with recycled plastic trying to obtain a new mix with the same granulometric characteristics. This substitution is generally expressed as substitution ratios,  $r$ , defined as the ratio of amount (in terms of volume or mass) of recycled material to original aggregate (or of the original mix considered). The superior mechanical properties of plastics make it possible to used as a part of constructional materials and it has already attract growing interests of researchers, it can be reviewed in Figure 2.3 and Table 2.4. Considering the application of plastic in concrete, the influence of the compressive strength is attractive. In this thesis, the reduction ratio of compressive strength ( $SRF$ ) is represented as [73]:

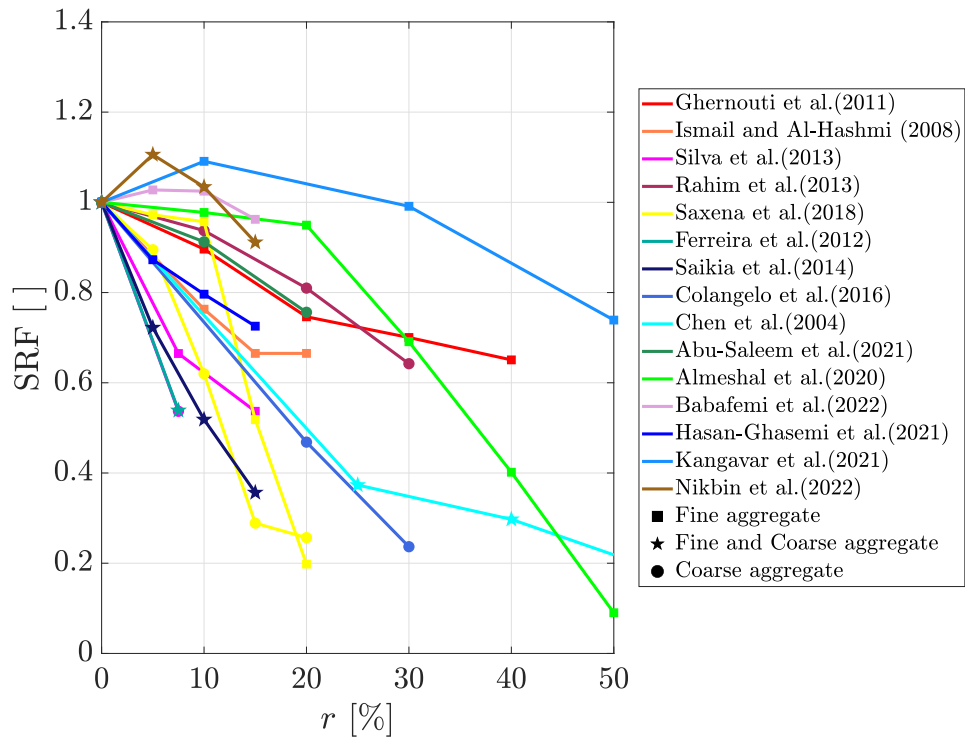
$$SRF(r) = \frac{f_c(r, \dot{\epsilon} \rightarrow 0)}{f_c(r = 0, \dot{\epsilon} \rightarrow 0)} \quad (2.1)$$

where the 2.1 is a non-dimensional form,  $r$  is the substitution level of the plastic aggregate,  $f_c(r, \dot{\epsilon} \rightarrow 0)$  and  $f_c(r = 0, \dot{\epsilon} \rightarrow 0)$  are the static compressive strength of concrete substituted by plastic aggregate (PA) with different substitution level ( $r$ ),  $\dot{\epsilon}$  is strain rate, is expressed as  $\dot{\epsilon} = \frac{\partial \epsilon}{\partial t}$ , means the change in strain (deformation) with respect to time. Figure 2.3 shows previous researches on the concrete replaced by plastic aggregate and the literature review for plastic aggregate concrete (PAC) of  $SRF$  as a function  $r$  for PAC with fine, coarse, and fine and coarse aggregate substitution. The figure shows that under a proper  $r$ , the reduction of the compressive strength is acceptable. However, regarding the effect factors on  $SRF$  of PAC, except the  $r$ , the morphology of plastic aggregates [116, 4, 117], like granule (particle) shape, fiber (flake, flyer) shape also influence results of  $SRF$ , other factors like water to cement ratio ( $w/c$ ), size of plastic aggregate, plastic type, and fine/ coarse to plastic aggregate ratio, additives like steel fiber, fly ash and special cement also are vital to the results of  $SRF$  of PAC. The above factors are also shown in the Table 2.4.

The Figure 2.3 and Table 2.4 show that there are a lot of researches on the application of plastic on granules and relatively less researches on the plastic fibers in concrete. It shows that the compressive strength can increase under low  $r$ , which



(a) Granules



(b) Fiber

Figure 2.3 Literature review for plastic aggregate substituted concrete of *SRF* as a function *r* for partial or full substitution of fine, coarse, or both fine and coarse aggregates.

## 2.1 Quasi-static tests on recycling and reusing plastics in cementitious materials 19

Table 2.4 Literature review of quasi-static tests on plastic aggregate substituted concrete: granules (a) and fibers (b).

(a)				(b)			
Granules				Fiber			
Previous studies	w/c	Plastic type	Plastic size	Previous studies	w/c	Plastic type	Plastic size: length, width
[-]	[-]	[-]	[mm]	[-]	[-]	[-]	[mm]
Babu et al. [118]	0.38; 0.36	PS	6.3-8	Chen and Liu [120]	0.37	PS	3; 8
Ghaly and Gill [119]	0.42	Not given	3-6	Ismail and Al-Hashmi [132]	0.53	MIX	0.15–12 mm, 0.15–4 mm
Chen and Liu [120]	0.37	Expanded PS	3 for type-A, 8 for type-B	Ghernouti et al. [23]	0.48	PET	1.4-5
Marzouk et al. [26]	0.5	PET	5;2;1	Ramadevi and Manju [133]	0.45	PET	Not given
Kou et al. [121]	0.32	PVC	<5	Ferreira et al. [123]	0.53; 0.6	PC; PF	PC: 20; PF:0.5
Al Bakri et al. [122]	0.5	MIX	14-20	Silva et al. [124]	0.54	PET	1-4
Ferreira et al. [123]	0.53	PP	3-4	Saikia and de Brito [125]	0.53-0.74	PC	4-8
Silva et al. [124]	0.54	PET	1-4	Rahim et al. [134]	0.55	HDPE	4.75-20
Saikia and de Brito [125]	0.53	PP;PC;PF	PC:4-11.2; PF:2-4; PP:2-4	Colangelo et al. [130]	0.6	MIX	6
Yang et al. [126]	0.25	PP	1.5-4	Saxena et al. [135]	0.45	PET	0-4.75; 4.75-20
Liu et al. [127]	0.36	PC	1.0-2.0	Abu-Saleem et al. [15]	0.7	PET; HDPE; PP	PET: 5-10; HDPE: 5-7; PP: 5-7
Senhadji et al. [128]	0.49	PVC	3-8	Almeshal et al. [16]	0.54	PET	0.075-4
Islam et al. [24]	0.42; 0.48; 0.57	PET	10-11	Hasan-Ghasemi and Nematzadeh [18]	0.47	PET	<6
Vadivel et al. [39]	0.38	Not given	<5	Babafemi et al. [17]	0.5	PET	Not given
Ruiz-Herrero et al. [129]	Not given	PVC; PE; PVC+PE	Not given	Kangavar et al. [19]	0.45	PET	<2
Colangelo et al. [130]	0.6	MIX	6	Nikbin et al. [21]	0.3	PET	<7
Batayneh et al. [1]	0.56	Not given	<4.75				
Mohammed et al. [131]	0.52	PVC	0.49-0.95				

is relatively clear in case concrete substituted by granules, e.g. [26, 39, 126, 131]. However, the research on plastic fiber is insufficient, and the size of the fiber is in the range of large microplastics which is 1 – 4.75 mm. Another limitation in previous researches is that a few of papers used plastic aggregate substituted both fine and coarse aggregate at the same time, [118, 123, 125, 130] substituted both fine and coarse aggregates at the same time with same tape of plastic aggregate just with different size, but in these studies, they just use plastic aggregate to replace fine and coarse aggregate, without considering the effect of different types of plastic and the morphology and size of fine and coarse aggregate.

Shapes and sizes of plastic aggregates have a significant influence on the behavior of the corresponding concrete. The shape of plastic used in concrete can be divided into two main classes: granule and fiber. Fibers have a very large ratio of length to width when compared with granules. Granules show a higher Specific Surface (SA) given the same volume when compared with fibers. Fibers highly affect the workability and flowability of the fresh mix [132, 128, 23, 126, 125, 136]. Granules have a round, angular, and irregular shapes whose classification is shown in Figure 2.4. Sphericity and roundness are two significant evaluations for granule shape. Rounded aggregates have lower water demand attributed to lower SA.



Figure 2.4 Classification and evaluation of particle shape (adapted from Ulusoy [4])

Regarding the particle size, Table 2.2 reports the main plastic categories in terms of characteristic size ranges. Nano and small micro-plastics can substitute the cement (normally with a size range of 0.007 – 0.2 mm [137]). For example, Aattache et al. [99] adopted PE powder ranging from 80  $\mu\text{m}$  to 0.5 mm to substitute cement by volume. Gesoglu et al. [138] used plastic waste powder with a mean diameter of 0.153 mm to replace cement in the mix proportions with  $r$  of 5, 10, 15, 20 and 25%. The small microplastics can also substitute fine aggregate, e.g., fine aggregate was substituted by PVC granules with size of 0.5 – 1 mm by volume with substitution levels from 5 to 85% by Mohammed et al. [131]. Large microplastics are quite fitting the size of fine aggregates like fine/coarse sand or very fine gravel and are the most common size adopted in the literature (Table 2.4). Mesoplastics can be employed as a substitution for coarse aggregates. For instance, Rahim et al. [134] used HDPE granules with a diameter in the range of 4.75-20 mm to substitute coarse aggregates with  $r$  of 10, 20, and 30%.

Another approach is to melt different types of plastic together. For instance, Ismail and Al-Hashmi [132] adopted mixed plastic fibers with a size range 0.3-4.75 mm to replace fine aggregate by volume. Ghaly and Gill [119] utilized mixed plastic granules with a size of 1.0-6.0 mm to replace coarse aggregate by mass. Ghernouti et al. [139] used plastic bag waste fibers with a length of 2.4 and 6 cm as additive in the concrete mix design.



## 2.1 Quasi-static tests on recycling and reusing plastics in cementitious materials 21

Due to the large quantity of wasted PE, PP, and PVC, the applications in concrete or mortar mix design are mainly focused on these three types of plastic. For instance, Thorneycroft et al. [140], Jacob-Vaillancourt and Sorelli [141] replaced fine aggregate with PE aggregate while Rahim et al. [134], Al Bakri et al. [122] use PE aggregate to substitute coarse aggregate with different values of  $r$ . Yang et al. [126], Saikia and de Brito [125], Jacob-Vaillancourt and Sorelli [141], Thorneycroft et al. [140] investigated the influence of PP aggregate on the properties of concrete and noted that most of all researchers used PP aggregate to substitute fine aggregate with different  $r$ . Several studies have focused on the application of PVC in mortar and concrete mix design, Kou et al. [121], Senhadji et al. [128], Ruiz-Herrero et al. [129], Jacob-Vaillancourt and Sorelli [141], Mohammed et al. [131] employed PVC granules to substitute fine or coarse aggregate in concrete.

PET is the fourth-most produced synthetic plastic. Islam et al. [24] utilized PET particles with a size larger than 2 mm to substitute coarse aggregate. Thorneycroft et al. [140], Rahim et al. [134], Jacob-Vaillancourt and Sorelli [141], Al Bakri et al. [122], Ruiz-Herrero et al. [129] adopted PET particles with a size in the range of 0.5-2.0 mm to substitute fine aggregate. Saxena et al. [135] used waste PET fibers with two sizes of 0-4.75 mm and 4.75-20 mm to substitute fine and coarse aggregate, respectively. Bui et al. [25] added PET fibers with a length of 50-60 mm, a width of 2-3.5 mm inside the concrete mix design. However, the relative researches on the small micro-plastic size of PET fiber are limited, actually, the PET fibers in the size range lower than 2 mm are very popular as the leftovers in the industry.

However, few studies investigated the use of both fine and coarse plastic aggregates substituted at the same time, and the available studies substituted both fine and coarse aggregates at the same time with only one type of plastic aggregate with different sizes [118, 123, 125, 130]. Therefore, more research is needed to understand the combined effects of different plastic aggregates substituted in the concrete for replacing fine and coarse aggregates. Further research to determine the effect of different morphology (e.g., fibrous and granular plastic aggregate) simultaneously substituted would be needed.

However, the availability of this data is crucial for the definition of constitutive laws accounting for the morphology effect and synergistic effect of various plastic aggregates substituted in the same concrete, which allows for the evaluation of the application of plastic waste in concrete and develops a kind of green concrete. In this

context, this study focused on the characterization of the physical and mechanical properties of concrete with two different substituted recycled plastic aggregates. First, the materials employed (Section 6.1.1), concrete mixture proportions and specimen preparation (Section 6.1.2), and test program (Section 6.2) are presented. A reference mix with an average compressive strength of around 60 MPa is considered. Recycled PET powder and recycled mixed plastic (PP and PE) granules were adopted to substitute fine and coarse aggregates. Two different substitution strategies are employed. In the first one, the PET powder is used to substitute the fine sand by volume. In the second one, the PET powder is used to substitute the fine sand while the recycled mixed plastic granules are used to substitute the coarse sand and fine coarse aggregates by volume (50% for PET powder and 50% for recycled mixed plastic granules). Four total replacement levels (5%, 15%, 20%, and 30%) by volume were considered. The results are presented in Section 6.3. The experimental tests are aimed to determine the fresh concrete properties (slump and density), compressive and flexural behavior, toughness, and permeability. Finally, a micro-scale characterization of the plastic-paste interface is provided (Section 6.2.5). An explanation and interpretation of the results of this study by comparing them with the results of previous studies are provided in Section 6.4. The database used herein refers to tests on concrete specimens with substituted aggregates made of PET. Two predictive equations for the compressive and flexural strength reduction factors are formulated based on symbolic regression. Finally, some conclusions and perspectives are drawn in Section 6.5. Moreover, Table 2.1 provides a summary of physical and mechanical characteristics of plastics while Table 2.3 gives a literature review on main studies adopting recycled plastic aggregates as substitute aggregate in the concrete mix design.

## **2.2 High-strain rate compressive behavior of concrete made with substituted recycled crushed concrete and clay bricks aggregates**

The use of CDW as aggregates in the new concrete mixture has been recognized as an attractive approach to conserve natural resources and to reduce the environmental impact of the construction industry [142]. De Brito and Saikia [143] reviewed

procedures and methods to substitute CDW to natural aggregated in concrete production. In this study, attention is paid to the use of RCA and BA as coarse aggregates with different levels of substitution. It is generally accepted that given a mix design of the parent concrete, the quasi-static compressive strength is mainly dependent on a non-dimensional parameter representing the substitution level of aggregate:

$$r = \frac{ra}{ca} [\%] \quad (2.2)$$

where  $r$  is the substitution coefficient,  $ra$  is the mass of recycled coarse aggregates while  $ca$  is the mass of coarse aggregates. Therefore,  $r = 0\%$  indicates a Natural Aggregate Concrete (NAC) and  $r = 100\%$  represents a concrete with full substitution of recycled coarse aggregates.

Here and in the following, quasi-static indicates low strain rates (the time rate of change on strain,  $\dot{\varepsilon} = \partial\varepsilon/\partial t$ ), normally the range is from  $\dot{\varepsilon} = 10^{-6}$  to  $10^{-3}$ . The variation of the strength for different levels of substitution is commonly expressed in a non-dimensional form as:

$$SRF(r) = \frac{f_c(r, \dot{\varepsilon} \rightarrow 0 \text{ s}^{-1})}{f_c(r = 0\%, \dot{\varepsilon} \rightarrow 0 \text{ s}^{-1})} \quad (2.3)$$

where  $SRF$  is the quasi-static compressive strength reduction ratio of a concrete with a certain level of substitution (RCA or BA),  $f_c(r, \dot{\varepsilon} \rightarrow 0 \text{ s}^{-1})$ , compared with equivalent NAC,  $f_c(r = 0\%, \dot{\varepsilon} \rightarrow 0 \text{ s}^{-1})$ .

Factors influencing  $SRF$  have been explored in several studies. The addition of RCA has slight detrimental effects on the strength due to inferior properties (low strength of adhered mortar and initial damage of micro-cracks) of recycled aggregates [e.g., 144, 142, 145–149]. However, a beneficial or detrimental effect on the strength was found by adding RCA depending on the mix design adopted generally due to the higher water adsorption of the recycled aggregates compared with natural ones [150]. The higher water absorption results from the higher water absorption rate of cement mortar attached to the aggregate particles [59, 151]. The common range of water absorption for RCAs and NAs is 3 – 12 % [152, 153, 144, 150] and 0.5 – 2 % [154–158], respectively. In other words, RCAs are characterized by a water absorption around 6 times larger than NA. There are two different strategies that can be adopted in the mix design of (Recycled Aggregate Concrete) RAC [145]: (i) Equivalent

Effective Water (EEW) method and (ii) Equivalent Total Water (ETW) method. The first aims at obtaining the same workability by adding water proportional to the water absorption increase in the substitute recycled aggregates [150, 159, 145]. In this way, the same effective water-to-cement ratio is guaranteed. Given the inferior properties of concrete, a reduction of the strength ( $SRF < 1$ ) is observed by increasing  $r$  [160–162]. The second method aims at obtaining the same water-to-cement ratio of the NAC. The reduction in the effective water-to-cement ratio leads in some cases to increase the strength ( $SRF > 1$ ). In the following, attention will be paid to the first method. Using this approach, values of  $SRF$  in the range of 0.75 – 0.8 were observed for  $r = 100\%$  [150]. Similar features were observed in Recycled Brick Concrete (RBC) [e.g., 163, 164, 62]. The main differences are the higher water absorption of BAs compared to RCAs and their lower density and strength. The common water absorption ratios of BA is in the range of 15 – 19% [165–167]. In other words, BAs are characterized by a water absorption around 13 times larger than NA.

As previously summarized, the quasi-static compressive behavior of concrete made with different levels of substitution and types of coarse aggregate was widely investigated. However, the high-strain rate compressive behavior lacks investigation. The high-strain rate compressive behavior of concrete can be quite different because of its strain rate sensitivity [e.g., 9]. In fact, concrete-based structures can be exposed during their service life to fast-varying loads such as those deriving from impacts (e.g., land or sea vehicles) and blasts [e.g., 168–170]. Different experimental techniques were developed to study the high-strain rate compressive behavior of materials, such as conventional and servo-controlled material testing systems, drop hammer and Split-Hopkinson Pressure Bar (SHPB) [171, 82, 172]. For high strain rates ( $\dot{\epsilon} > 10\text{s}^{-1}$ ), SHPB is the most adopted apparatus. The most common parameter influenced by strain rate effects is the strength. Usually, a non-dimensional form of the strength is provided in terms of Dynamic Increase Factor ( $DIF$ ) that is the ratio of the dynamic compressive strength,  $f_c(r, \dot{\epsilon})$ , to the quasi-static compressive strength,  $f_c(r, \dot{\epsilon} \rightarrow 0\text{s}^{-1})$ , expressed as:

$$DIF(r, \dot{\epsilon}) = \frac{f_c(r, \dot{\epsilon})}{f_c(r, \dot{\epsilon} \rightarrow 0\text{s}^{-1})} = \frac{f_c(r, \dot{\epsilon})}{SRF(r) \cdot f_c(r = 0\%, \dot{\epsilon} \rightarrow 0\text{s}^{-1})} \quad (2.4)$$

When  $DIF$  is larger than the unity, it corresponds to an increase of the dynamic compressive strength with respect to the quasi-static one while when smaller than

the unity is the opposite. Different Standards and Codes proposed *DIF* predictive equations valid for NAC. The most commonly used is the CEB-FIP Model Code specification recommendation formula [5]:

$$DIF(r = 0\%, \dot{\epsilon}) = \begin{cases} \left(\frac{\dot{\epsilon}}{\dot{\epsilon}_s}\right)^{1.026\alpha} & \dot{\epsilon} \leq 30s^{-1} \\ \gamma_s \left(\frac{\dot{\epsilon}}{\dot{\epsilon}_s}\right)^{1/3} & \dot{\epsilon} > 30s^{-1} \end{cases} \quad (2.5)$$

where  $\alpha = 1/(5 + 9 \cdot f_c(r = 0\%, \dot{\epsilon} \rightarrow 0s^{-1})/f_{c0})$  being  $f_{c0} = 10\text{MPa}$ ,  $\gamma_s = \exp(6.156\alpha - 2)$ ,  $\dot{\epsilon}_s$  is the static strain rate taken as  $30 \times 10^{-1} s^{-6}$ , and  $30s^{-1}$  is the sensitivity threshold. Kim et al. [173] recently investigated the effect of maximum coarse aggregate size on dynamic compressive strength of high-strength concrete. They concluded that to evaluate a realistic dynamic compressive strength of concrete using SHPB tests, it is recommended that concrete specimens should be cast using the same coarse aggregate as that used in the actual structure.

However, no Standards and Codes are available for the case of concrete made with different levels of substitution and types of coarse aggregate. Most studies on dynamic mechanical properties of high-strain rate compressive behavior of concrete focus only on one type of recycled aggregate and with a limited range of  $r$ .

Pioneering studies on the high-strain rate compressive behavior of RAC were carried out by Lu et al. [7] and Xiao et al. [6] using SHPB equipment up to  $\dot{\epsilon} = 100s^{-1}$ . The diameter of the bar was 100mm in Lu et al. [7] and 74mm in Xiao et al. [6]. Lu et al. [7] and Xiao et al. [6] proposed *DIF* linear (in the semi-logarithmic plan) predictive equations valid for RAC:

$$DIF(r, \dot{\epsilon}) = a(r, \dot{\epsilon}) + b(r, \dot{\epsilon}) \cdot \log(\dot{\epsilon}) \quad (2.6)$$

A summary of the coefficients ( $a$  and  $b$ ) of predictive equations valid for RAC proposed by Lu et al. [7] and Xiao et al. [6] is provided in Table 2.5. They tested similar values of  $r$ , namely  $r = \{0, 25, 50, 75, 100\}\%$  in Lu et al. [7] and  $r = \{0, 30, 50, 70, 100\}\%$  in Xiao et al. [6]. Similar to the the CEB-FIP Model Code formula [5] (see Eq. 2.5), Lu et al. [7] proposed a critical strain rate,  $\dot{\epsilon}_t(r)$ , function of  $r$  leading to a bi-linear function in the semi-logarithmic plan. Below the critical strain rate, a reduced strain rate sensitivity is considered. On the other hand, Xiao et al. [6] provided a single linear function valid only above the critical strain rate assumed as

Table 2.5 Coefficients  $a$  and  $b$  in Eq. 2.6 proposed by Lu et al. [7] and Xiao et al. [6].  $\dot{\epsilon}_t(r)$  is the critical strain rate for Lu et al. [7].

Eq. 2.6	Lu et al. [7]		Xiao et al. [6]	
	$10^{-5} s^{-1} \leq \dot{\epsilon} \leq \dot{\epsilon}_t(r)$	$\dot{\epsilon}_t(r) \leq \dot{\epsilon} \leq 100 s^{-1}$	$20 s^{-1} \leq \dot{\epsilon} \leq 100 s^{-1}$	
$r = 0\%$	$a(r, \dot{\epsilon})$	1.28	0.23	-1.787
	$b(r, \dot{\epsilon})$	0.054	1.31	0.893
	$\dot{\epsilon}_t(r, \dot{\epsilon})$	6.65		n/a
$r = 25\%$ for Lu et al. [7] and $r = 30\%$ for Xiao et al. [6]	$a(r, \dot{\epsilon})$	1.19	0.65	-1.504
	$b(r, \dot{\epsilon})$	0.037	10.40	0.825
	$\dot{\epsilon}_t(r, \dot{\epsilon})$	10.4		n/a
$r = 50\%$	$a(r, \dot{\epsilon})$	1.08	0.37	-1.898
	$b(r, \dot{\epsilon})$	0.014	0.26	0.906
	$\dot{\epsilon}_t(r, \dot{\epsilon})$	11.75		
$r = 75\%$ for Lu et al. [7] and $r = 70\%$ for Xiao et al. [6]	$a(r, \dot{\epsilon})$	1.04	0.73	-0.702
	$b(r, \dot{\epsilon})$	0.0074	0.40	0.623
	$\dot{\epsilon}_t(r, \dot{\epsilon})$	6.65		n/a
$r = 100\%$	$a(r, \dot{\epsilon})$	1.03	-0.25	-1.555
	$b(r, \dot{\epsilon})$	0.0071	1.00	0.845
	$\dot{\epsilon}_t(r, \dot{\epsilon})$	19.95		n/a

$\dot{\epsilon}_t(r) = 20 s^{-1}$ . Additionally, Li et al. [174] using the same mix design of Xiao et al. [6] provided the *DIF* at low values of the strain rate, i.e.,  $10^{-5} s^{-1} \geq \dot{\epsilon} \geq 10^{-1} s^{-1}$ .

Recently, Guo et al. [8] investigated the properties of RAC by testing with a 74 mm-diameter SHPB varying the replacement ratio as  $r = \{0, 30, 70, 100\} \%$ . They proposed a non-linear predictive equations valid for RAC valid up to  $\dot{\epsilon} = 60 s^{-1}$ :

$$DIF(r, \dot{\epsilon}) = 1 + \frac{4700 \cdot \eta_0(r)}{\sqrt{f_c(r = 0\%, \dot{\epsilon} \rightarrow 0 s^{-1})}} \cdot \dot{\epsilon}^{(1+n(r))} \quad (2.7)$$

where the elastic modulus of the parent concrete (NAC) can be assumed equal to  $E = 4700 \sqrt{f_c(r = 0\%, \dot{\epsilon} \rightarrow 0 s^{-1})}$  [MPa] and  $\eta_0$  and  $n$  are fitted parameters function of  $r$ :

$$\begin{aligned} \eta_0(r) &= 9.309 \times 10^{-7} (0.730r^2 + 1.012r + 1) \\ n(r) &= -0.817 (0.181r - 1) \end{aligned} \quad (2.8)$$

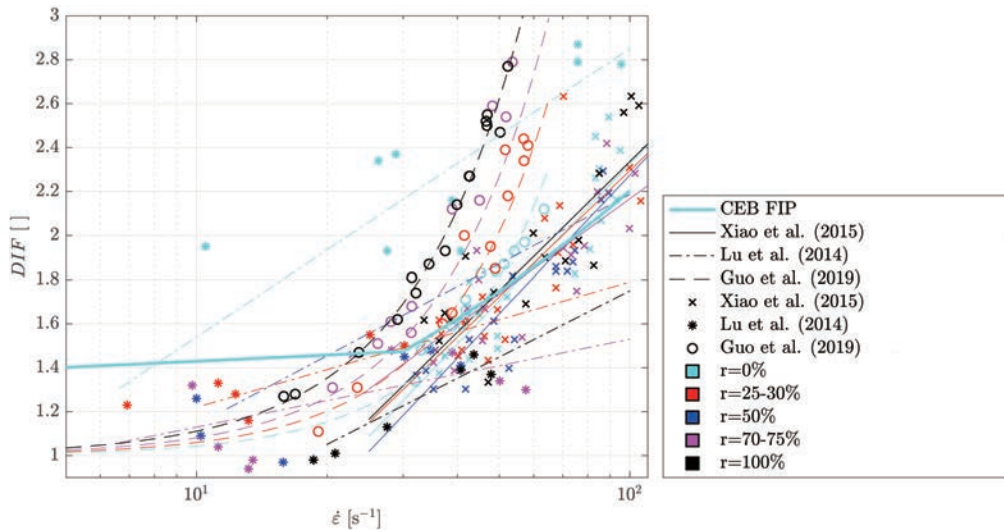


Figure 2.5 Comparison of experimental points and predictive equations of  $DIF$  as a function of  $\dot{\epsilon}$  for different values of  $r$ . Data taken from: CEB-FIP Model Code formula [5], Xiao et al. [6], Lu et al. [7], and Guo et al. [8]. Note that the colors inside the squares in the legend are indicating the substitution level of aggregate,  $r$ , associated to the different lines and markers in the figure.

It is noteworthy that the calibration is performed with only one value of  $f_c(r = 0\%, \dot{\epsilon} \rightarrow 0 \text{ s}^{-1}) = 43.3 \text{ MPa}$  although Eq. 2.7 explicitly refers to the parent concrete.

A comparison of the experimental data and  $DIF$  predictive equations as a function of  $\dot{\epsilon}$  for different values of  $r$  is reported in Figure 2.5. All these studies concluded that RAC is a strain rate dependent material. Xiao et al. [6] found that the strain rate dependency of RAC is quite similar to NAC (i.e.,  $DIF(r, \dot{\epsilon})$  is slightly dependent on  $r$ ) while Guo et al. [8] observed a marked dependency on  $r$ . The experimental data are rather controversial, and there is no general agreement about the exact effect of  $r$  on the  $DIF$ . A large scatter in the results is generally observed (Figure 2.5).

Additional tests on RAC using SHPB were performed to investigate different conditions of mix design [175], confinement and elevated temperatures [176] and aging [177]. Some tests were also performed at structural levels. For instance, Rao et al. [178] carried out some drop weight impact tests on simply supported RAC beams observing a general reduction of the strength increasing  $r$  similar to the case. Guo et al. [179] also conducted drop weight impact tests on the RAC beams discussing that the peak impact force of the beam does not show a significant correlation with the RCA replacement percentage due to the non-monotonicity of



local mechanical properties of RAC, while the mid-span displacement of the beams increases with the increase of RCA replacement percentage.

No experimental tests are available on the high-strain rate compressive behavior of RBC. Only some tests are available on the high-strain rate compressive behavior of brick-based materials. For instance, Larcher et al. [180] tested masonry bricks (adobe, terracotta, clinker) using SHPB in the range of  $\dot{\epsilon}$  from 80 to 160 s<sup>-1</sup> observing a strain rate sensitivity. Zhang et al. [181] carried out a series of tests on clay bricks using SHPB in the range of  $\dot{\epsilon}$  from 10<sup>-2</sup> to 10<sup>2</sup> s<sup>-1</sup>. Results indicate that the compressive strength, strain and Young's modulus are sensitive to strain rate effect. Recently, Piani et al. [182] performed experimental research on adobe brick using SHPB for  $\dot{\epsilon}$  up to 10<sup>2</sup> s<sup>-1</sup> observing a strength enhancement ( $DIF > 1$ ) increasing the strain rate and an almost constant ultimate deformation. In general, these experimental findings demonstrated that  $DIF$  is strongly dependent on the brick composition.

Although the high-strain rate compressive behavior of RAC was investigated by different researchers, the knowledge of dynamic mechanical properties of RBC is still extremely limited. Until recently, there has been no reliable evidence on the quantitative effect of coarse aggregate substitution with recycled aggregates (e.g., RAC or BA) on the high-strain rate compressive behavior. Therefore, the execution of additional investigations on the high-strain rate compressive behavior of concrete made with different levels of substitution and recycled aggregates are crucial for gaining sufficient knowledge on their behavior under rapid varying loads for development of Code prescriptions and application to large scale.

To this aim, current study presents the results of experimental tests made using a large-scale SHPB apparatus with a diameter of 155 mm of RAC and RBC under high-strain rate compressive loads. Using this apparatus, the diameter of the specimens can be that employed in static standard tests which is normally 150 mm. this thesis is organized as follows. Section 4.2 and Section 4.3 present the experimental program. First, the materials employed and the specimens are described. Two different types of concrete (RAC and RBC) with different substituted coarse aggregate are studied. Then, the quasi-static and SHPB test protocol and test matrix are provided. A total of 63 specimens were cast with a diameter and height of 150 mm of 300 mm, respectively. Specimens were divided in 9 groups with different levels of substitution and types of coarse aggregate ranging from 0% (Natural Aggregate Concrete, NAC) up to 100% (full substitution with recycled crushed concrete or clay bricks). For each



group, three specimens were tested under quasi-static conditions using a traditional universal testing machine. The remaining four were cut to obtain a length to diameter ratio of 0.5 and tested using the SHPB. Section 4.4 and 4.5 report the quasi-static and SHPB results. A large discussion on the compressive behavior is provided mainly focusing on the strength and failure modes. Section 4.6 discusses the results in terms of *DIF* and provides data-driven predictive equations proposed for the compressive strength Dynamic Increase Factor (*DIF*) regressed using the data of this study and collected from the literature. Finally, some conclusions and perspectives are drawn in Section 4.7.

## **2.3 High-strain rate compressive behavior of green concrete made with substituted plastic aggregates**

With the development of the constructional material and the strict limitation of recycled plastic materials, the related researches on static mechanical behaviors of plastic aggregate concrete-based material are extensive, but the studies of dynamic compressive behaviors of plastic aggregate concrete-based material are limited. Chen et al. [183] conducted a series of tests on concrete containing PP fiber with SHPB with a diameter of 50mm, and the results revealed that the addition of PP fiber in concrete can increase the dynamic mechanical properties especially the toughness and energy consumption. Chun et al. [184] investigated the dynamic mechanical behavior of ultra-rapid-hardening mortar (URHM) containing PE fiber by a SHPB with a diameter of 76.2mm and drop weight impact test, the results indicated that the dynamic mechanical strength enhances with increasing strain rate, and flexural strength was more sensitive to the strain rate than the compressive strength of URHM containing PE fiber owing to the higher ductility. Hu et al. [185] studied the dynamic mechanical behavior of concrete substituted by PVC flaky particles ( $r = 5, 10, 15, 20, 30\%$ ) with a 74mm-diameter SHPB, the tests identified that the dynamic compressive strength of the concrete dropped obviously with the increase of  $r$ , under same  $r$ , dynamic compressive strength increase with increasing strain rate. The research also pointed out that when  $r < 20\%$ , the mechanical behavior and workability is accepted to be shotcrete used in tunnel, roadway support owing to the lightweight, elastic, crack resistance and effective energy absorption of PVC plastic particles in concrete under impact loading. Kheyroddin et al. [186] and Lin et al.

[187] used drop weight impact setup to conduct a series of tests on fiber-reinforced concrete with PP fiber and engineered cementitious composites (ECC) with PP and PVA fibers, respectively. Kheyroddin et al. [186] reported that employing polypropylene fibers can improve impact resistance of concrete, and Lin et al. [187] reported that as the increasing of the volume ratio of PP fiber, the impact strength of PP-PVA-ECC increases while the impact resistance of PP-PVA-ECC is lower than that of PVA-ECC at a given total fiber volume ratio. Liu et al. [127] employed SHPB with a diameter of 70 mm to carry out tests on concrete substituted by recycled ABS/PC plastic granules with  $r = 5, 10, 15, 20\%$ . The experimental results presented that the energy absorption of plastic aggregate concrete increases with  $r$  and strain rates and *DIF* of plastic aggregate concrete increases with  $r$  when the specimens are subjected to the same level of  $\dot{\epsilon}$ , plastic aggregate concrete also showed relatively stronger strain rate-enhancing effect than plain concrete. Zhong and Zhang [188] investigated dynamic compressive behaviour of ECC containing PVA adopting SHPB system with a diameter of 100 mm, PVA was added in the concrete mix by volume of 1, 1.5, 2%. The results manifest that the dynamic compressive strength, *DIF*, and energy absorption capacity can be markedly improved by adding PVA fiber, while the possibility of PVA fibre rupture increased at  $\dot{\epsilon}$  of 155.65–164.13  $s^{-1}$ , which can weaken the energy absorption capacity of ECC which offer the possibility of ECC with PVA as structural material.

The previously researches of dynamic tests on cementitious material containing plastic aggregate mainly focus on plastic fine aggregate-sized materials and with single particles size. Researches on the synergistic effect of different plastic aggregate applied in the concrete for substituting fine and coarse aggregate at the same time are relatively deficient, and the researches on the effect of different morphology, e.g. fibrous and granular plastic aggregate used in one concrete mixture are still scarce. However, the availability of this data is crucial for definition of constitutive laws accounting for the morphology effect and synergistic effect of various plastic aggregate substituted in same concrete, which allows for the evaluation of the application of plastic waste in concrete and develops a kind of green concrete. In this study, under good and reasonable graded coarse and fine aggregate in concrete mix design and considering comprehensively the size distribution of plastic aggregate, two different types and morphology of recycled plastic aggregates are applied, namely recycled PET fiber and recycled mixed plastic granule, which is composed by PP and PE are employed to substitute fine and coarse aggregates of

### 2.3 High-strain rate compressive behavior of green concrete made with substituted plastic aggregates **31**

---

plain concrete respectively with  $r = 5, 10, 20, 30\%$ . A series of tests were conducted to measure the workability, quasi-static compressive strength and elastic modulus and then adopting SHPB system to investigating dynamic stress-strain response, failure pattern, dynamic compressive strength, dynamic increase factor (*DIF*) and energy absorption capacity of concrete substituted by plastic aggregates.

## Chapter 3

# Design and calibration of 155-mm Split-Hopkinson Pressure Bar

### 3.1 Working principle of large scale 155-mm SHPB

SHPB is a widely used experimental technique that enables the study of materials under high strain rate conditions. During an SHPB test, a cylindrical specimen is axially compressed between two instrumented bars, known as the incident bar and the transmission bar. These bars are equipped with strain gauges that allow for the measurement of stress waves, which are generated during the impact process. The compression wave in the striker is transferred into the incident bar, reflecting back as a tension wave at the free end, while the remainder of the compression wave is transmitted into the transmission bar after dynamic compression on the specimen. The construction of the stress-strain curve is based on at least one of the three signals that represent the propagation of disturbances along the two bars. The SHPB technique was first introduced by Wu and Gorham [189] and has since become a well-established method for testing materials under high strain rate conditions.

The incident loading and reflected pulse (incident strain  $\epsilon_I$  and reflected strain  $\epsilon_R$ ) can be used to derive the stress  $\sigma_{c1}$  on the front (loaded) interfaces of the specimen. Correspondingly, the stress  $\sigma_{c2}$  on the rear interfaces of the specimen is derived from measuring the transmitted pulse showing as transmitted strain  $\epsilon_T$ . The one or two waves analyses are adopted to describe the stress at the rear interface ( $\sigma_{c2}$ ) and the front (loaded) interface ( $\sigma_{c1}$ ), respectively. Hence, the three-wave analysis represents

the mean stress ( $\sigma$ ). These average values represent the dynamic properties of testing material assuming that the stress equilibrium is satisfied during testing. The expressions of specimen stress are:

1D–wave analysis:

$$\sigma_{c2}(t) = \frac{EA_b}{A_s} \varepsilon_T(t) \quad (3.1)$$

2D–wave analysis:

$$\sigma_{c1}(t) = \frac{EA_b}{A_s} (\varepsilon_I(t) + \varepsilon_R(t)) \quad (3.2)$$

3D–wave analysis:

$$\sigma(t) = \frac{\sigma_{c2}(t) + \sigma_{c1}(t)}{2} = \frac{EA_b}{2A_s} (\varepsilon_T(t) + \varepsilon_I(t) + \varepsilon_R(t)) \quad (3.3)$$

where  $A_b$  and  $A_s$  are the bar and the specimen sections respectively,  $c_b = \sqrt{E/\rho_b}$  is the elastic longitudinal stress wave velocity in the bar,  $E$  is the Young's modulus of the bar,  $\rho_b$  is the mass density of the bar. The subscripts,  $I$ ,  $R$  and  $T$  are referring to incident, reflected and transmitted pulse, respectively. Assuming stress equilibrium in the specimen (i.e.,  $\sigma_{c2}(t) = \sigma_{c1}(t)$ ) yields to  $\varepsilon_T(t) = \varepsilon_I(t) + \varepsilon_R(t)$ .

The strain  $\varepsilon$  and strain rate  $\dot{\varepsilon}$  of specimen are evaluated as:

$$\varepsilon(t) = \frac{-2c_b}{L_s} \int_0^t \varepsilon_R(t) dt \quad (3.4)$$

$$\dot{\varepsilon}(t) = \frac{-2c_b}{L_s} \varepsilon_R(t) \quad (3.5)$$

where  $L_s$  is the specimen length.

## 3.2 SHPB primary design and construction

The SHPB apparatus is mainly designed to test concrete specimens having the same size as standard specimens of quasi-static tests, normally 150 mm in diameter [190]. Therefore, in this study, a SHPB with a large diameter of 155 mm is inves-

tigated. The large diameter of the specimen can reduce the influence of the scale problem and size effect of inhomogeneous materials. However, the SHPB apparatus is appropriate to characterize the dynamic mechanical response of different materials at high-rate tests, such as ductile, brittle, and soft materials.

Following the design described in the following, the construction of the SHPB apparatus in the structural labs of Nanjing Tech University for testing materials under high-strain rates started in 2017 and was successfully completed in 2018. The schematic and photos of the main parts of the large-diameter SPHB are shown in Figure 3.1.

In the following, the main steps of design and construction of the large-scale 155 mm SHPB are described.

### 3.2.1 SHPB data acquisition system

After the impact of the striker bar with the incident bar, the produced stress wave propagates back and forth in the bar system in turn resulting in the specimen to be compressed progressively. However, only the pulses associated with the first loading are generally adopted to calculate the stress-strain response of the specimen tested.

The sensors adopted are two strain gauges attached symmetrically on the bar surface across a diameter of the incident and transmission bars and a laser velocimeter to measure the velocity of the striker. The signals from the strain gauges are conditioned with a half Wheatstone bridge [191] with a low-pass filter 100kHz and acquired using a data acquisition system with a sampling frequency of 2.5MHz. An acquisition system (National Instruments) is used to digitalize the input voltages and convert them to strain. The strain gauge on the incident bar is used as a trigger for the acquisition system specifying the recording point before the trigger instance. Moreover, the gas gun is also provided with additional sensors monitoring the air pressure.

A laser velocimeter system is adopted to record the velocity of the striker bar. The system is composed of a pair of parallel light curtains. When the striker moves in, the light curtain is blocked, and a change of the light intensity is detected and then the corresponding analog signal of the voltage is recorded with a digital oscilloscope. By knowing the distance between the two light curtains and the crossing time then the impact velocity of the striker  $v_I$  is calculated.

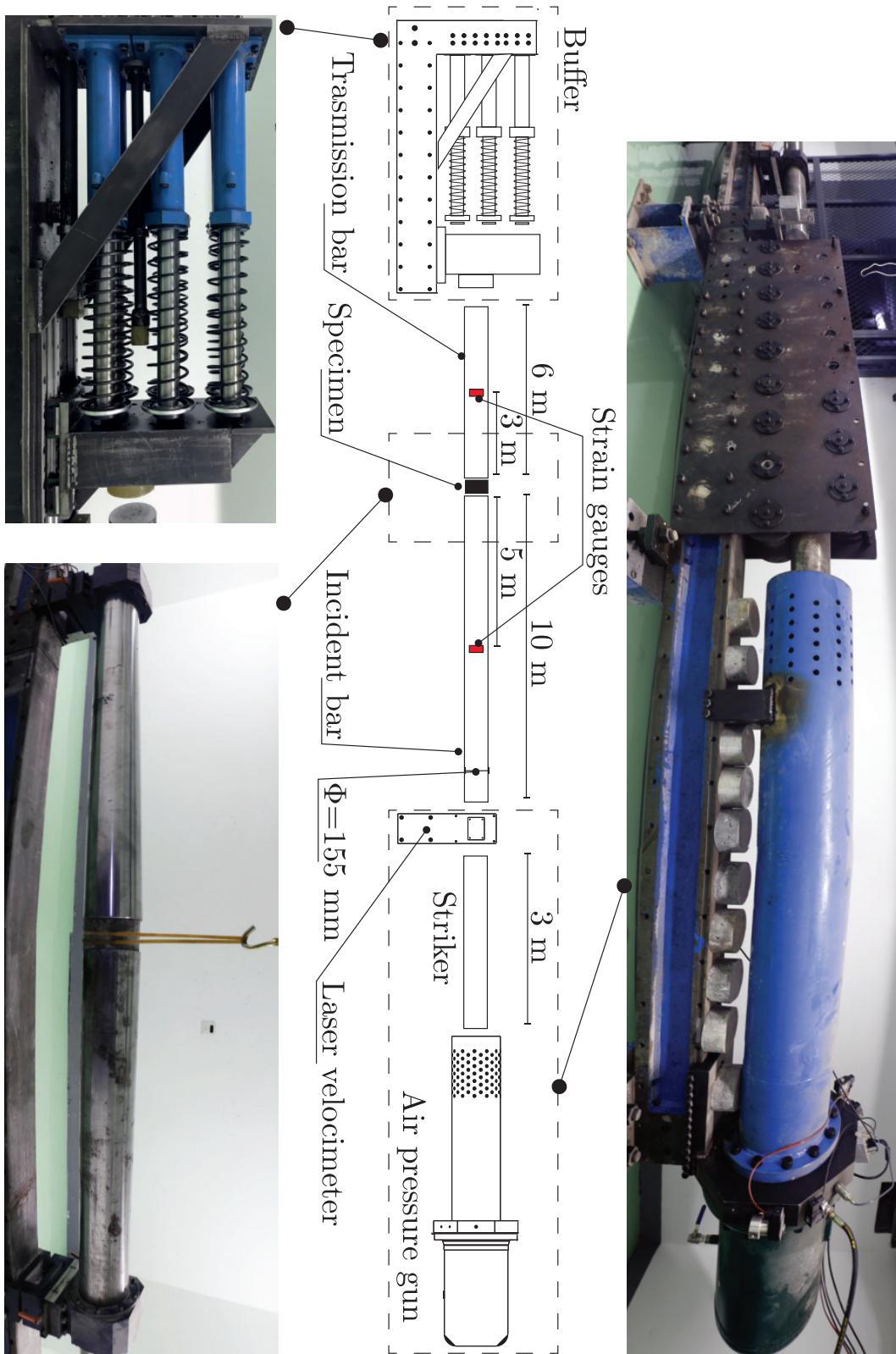


Figure 3.1 Schematic and photos of the main parts of the large diameter SHPB. After Xiong et al. [9].



### 3.2.2 Geometric characteristics of the specimens

The SHPB is mainly composed of three uniform cross-section bars with a diameter of 155 mm. The two interfaces (bar-specimen and specimen-bar) should remain plane during the loading stage. To hold well, the diameters of the specimen and the bar should be equal or closely similar. If the diameters of the bar and the specimen are different, a likely correction of the displacement of the bar end (punching) can be applied [192]. Moreover, negligible effects of the inter-facial friction are required. To limit the radial and longitudinal inertia and friction effects, the diameter of the specimen should be approximately equal to 0.8 of the bar diameter and the aspect ratio of the specimen ranges between 0.5 to 1 [193]. Therefore, bars with a diameter of 155 mm can be used for testing specimens with a diameter larger than 124 mm and less than 155 mm. For non-circular specimens, dimensional limitations are given in Tekalur and Sen [194].

### 3.2.3 Characteristics of the bars

The wave propagation can be represented by the one-dimensional theory. To satisfy this condition, the length-to-diameter ratio of the bar should be higher than 20 [87]. At that distance from the impact, the influence of the spatial variation of load on the peak dynamic strain is drastically reduced [195]. More interestingly, this ratio depends also on the strain that will be conferred to the specimen. For large deformations, the length of the bar should be more than one hundred of the diameter [196]. However, this case is not investigated in this design process. According to the conventional SHPB technique, the length of the input and transmitted bars must be greater than the length of the greatest pulse that will be transmitted by them [197]. Moreover, the length of the incident bar should be more than twice longer than the striker bar to avoid the overlap between the incident and reflected pulses [87]. In this case, the length of the incident, transmission and striker bars are set to be equal to 10 m, 6 m, and 3 m, respectively, complying with all the previous requirements.

The three bars are supported by a bearing support system letting free the expansion due to the Poisson effect (to reduce rotational and axial friction). The bars are perfectly aligned along the straight axis to maintain one-dimensional wave propagation. A laser system is adopted for this alignment. The bearing supports are fully lubricated to minimize friction.





Figure 3.2 Gas gun (left) and air compressor (right).

### 3.2.4 SHPB loading device

In this study, the air gun is designed to provide a controllable, repeatable, and stable device under the challenges of an heavy striker. A high-capacity gas gun is required with stable striker performance. Previous work has used explosive detonations, springs, or even hydraulic systems. According to [87], the loading method can be static or dynamic. In the first type, a pre-load stored is in the tank and the load is released suddenly and directly on the incident bar. The static load method is relatively unstable and difficult to operate. Therefore, in this study, the dynamic type is preferred. Dynamic loading means that a striker bar is launched to impact the incident bar compared with the static loading type. The impulse is produced through a gas gun [198]. Generally, in the design of such a device, an adiabatic model for the gas gun is adopted. The interested reader is referred to Seigel [199], Gallina and Alves [197] for detailed information on this model. The striker bar is launched by the release of compressed air stored in the pressure storage vessel and accelerated in the barrel. The adopted gas gun and air compressor are shown in Figure 3.2. The system adopts dry compressed air to avoid corrosion in the system. The design of the cannon is characterized by several gas venting holes used to balance the pressure and in turn reach a constant velocity of the striker bar.

The way to control the velocity of the sticker is to change the pressure of the compressed air,  $P_g$ .  $v_I$  is is the striker velocity measured from the laser system (Figure 3.1). Preliminary tests were performed to define the velocity given a value of  $P_g$ , see Figure 3.3. According to these tests, an empirical predictive equation of the impact velocity of the striker  $v_I$  as a function of the gun pressure was fitted using the least square method [9]:

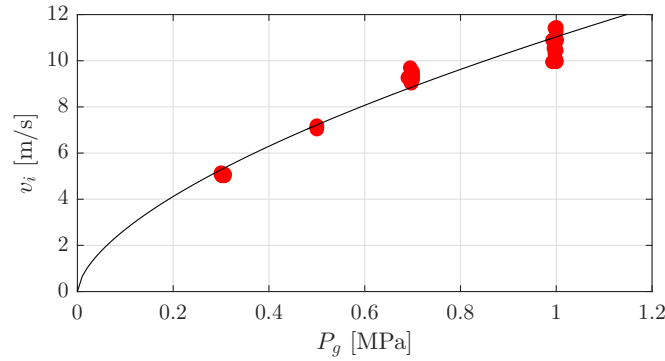


Figure 3.3 Relationship between the pressure and impact velocity with the empirical fitting curve reported in Eq. 3.6. After Xiong et al. [9].

$$v_I = 11.03P_g^{0.613} \quad (3.6)$$

The system is designed to work for a  $P_g \leq 1$  MPa corresponding to  $v_I$  equal to around 11 m/s.

In the test, the specimen is sandwiched between the incident and transmitted bars, then the striker with a flat end hits the end of the incident bar in the axial direction with an initial velocity  $v_I$  and a trapezoidal incident stress impulse is generated. Strain in the specimen is proportional to the wavelength of the incident pulse and its amplitude whereas strain rate is proportional to the incident pulse amplitude [200] and depends on the specific characteristics of the material tested. When the length of the striker is short compared with the total length of the incident and transmitted bars, the incident pulse stress amplitude ( $\sigma_I$ ) is given by Chen and Song [87]:

$$\sigma_I = 0.5\rho_b c_b v_i \quad (3.7)$$

The three bars are made of a 40CrMo alloy with material properties of  $E = 208$  GPa,  $\rho_b = 7800$  kg/m<sup>3</sup> and  $\sigma_{b,y} = 900$  MPa. The choice of 40CrMo alloy for the SHPB apparatus bars is likely due to its high strength and toughness, making it suitable for high-stress applications. This alloy also has good machinability, high hardenability, and good fatigue resistance, which are important properties for the bars in a SHPB apparatus.

During the test, the stress in the three bars should be maintained below their yield strength  $\sigma_{b,y}$  [201]. Using Eq. 3.7, the maximum value of the stress induced in the bar is equal to:

$$\sigma_I = 0.5\rho_b c_b v_I = 0.5 \cdot \sqrt{7800 \text{ kg/m}^3 \cdot 208 \text{ GPa} \cdot 11 \text{ m/s}} = 221 \text{ MPa} \quad (3.8)$$

corresponding to around 25% of the yielding capacity of the material. This indicates that  $P_g$  can be increased without damaging the bars. The stress in the bars could be controlled by adjusting the velocity of the striker as:

$$v_I \leq \frac{2\sigma_{b,y}}{\rho_b c_b} \quad (3.9)$$

Moreover, this limit can be changed by adopting a different material for the bars, for instance, maraging steel has yield strength  $\sigma_{b,y} = 2500 \text{ MPa}$  [202].

During the test when the loading wave is generated, the duration of the trapezoidal incident stress impulse ( $\Delta t$ ) is:

$$\Delta t = 2L/c_b \quad (3.10)$$

where  $L$  is the length of the striker. Accordingly, the strain in the specimen is directly proportional to the intensity of the stress pulse and to the time duration of the incident pulse. Therefore, the system is designed to have a striker with a length is 3 m corresponding to a loading duration of the incident wave of  $1162 \mu\text{s}$  (using Eq. 3.10).

### 3.2.5 SHPB trapping device

A dissipative system is needed to dissipate the kinetic energy at the end of the test. The buffer system here is also known as the unloading control or momentum trapping [87]. The first concept of unloading control of SHPB is proposed in 1960s [203], however, many different designs and applications have been developed. In this system, the buffer system is designed at the end of the transmission bar and is composed of six commercial elevator buffers installed in parallel. An elevator buffer is a device designed to stop a descending car or counterweight beyond its

normal limit and to soften the force with which the elevator runs into the pit during an emergency. The adopted buffers are oil type using a combination of oil and springs to cushion a descending counterweight with a maximum dissipated energy of  $11250 \text{ kg} \cdot \text{m}^2/\text{s}^2$ . At the end of the transmission bar, the six buffers are connected to a thick steel plate configured to distribute the stress to the six elevator buffers. The maximum input energy is equal to:

$$W_k = 0.5 \cdot m \cdot v_I^2 = 0.5 \cdot [\pi \cdot 0.075^2 \text{ m}^2 \cdot 3 \text{ m} \cdot 7800 \text{ kg/m}^3] \cdot 11^2 \text{ m}^2/\text{s}^2 = 25 \text{ kJ} \quad (3.11)$$

The above number is around 2.7 times smaller than the dissipative capacity of the dampers ( $6 \times 11.25 \text{ kJ} = 67.500 \text{ kJ}$ ).

### 3.3 Data processing: validation and test acceptance conditions

#### 3.3.1 SHPB impedance mismatch

In the tests, the compression wave generated by the striker propagates in the incident bar. When it reaches the interface between the incident bar and the specimen, part of it is reflected back into the incident bar as a tension wave while the rest transmits into the specimen and gets reflected back and forth inside the specimen due to wave impedance mismatch between the specimen and bars. Usually, the specimen has a low impedance compared with that one of the bars [204]. In the case of a planar waves, the wave impedance is defining the wave propagation. The bar impedance  $Z_b$  and specimen impedance  $Z_s$  can be calculated as  $Z_b = \rho_b c_b$ ,  $Z_s = \rho_s C_s$ , respectively. The specimen tested should have an impedance less than bar, i.e.,  $Z_s < Z_b = 4 \times 10^7 \text{ kg/m}^2/\text{s}$ .

Due to the effects of different wave impedance between SHPB and specimen tested, the specific SHPB systems were investigated to characterize the dynamic mechanical response validity, such as viscoelastic bars system for rubber [205], aluminum bars system for PMMA [206] and steel bar system for concrete [9, 75]. Especially, the steel bar system was widely used to measure the medium to high

wave impedance materials with high strength and toughness, such as metals [70], limestones [207], ceramic [208], and composite ones [209]. Considering the wave impedance and bar-specimen cross-sectional area ratio, the impedance mismatch  $r_s$  of specimen tested can be expressed as:  $r_s = A_b Z_b / (A_s Z_s)$ . For instance, the impedance mismatch is equal to  $r_s = 3.03$  and  $1.35$  for confined concrete and copper, respectively. Detailed material properties are provided in Section 3.5 and Figure 3.4.

Before processing the data associated with the incident, reflected, and transmitted waves, prominent indications about the specimen could be deduced. If the amplitude of the reflected wave is slightly less than the amplitude of the incident wave, it indicates simply that the impedance mismatch at the bar/specimen interface is important. On the opposite, if the amplitude of the reflected wave is low (near zero) in comparison to the one of the incident wave, it means that the impedance mismatch converges to one.

### 3.3.2 SHPB transmission coefficient

At the front (loaded) interfaces, the reflection and transmission occur inside the incident bar and specimens, so the transmission and reflection coefficients can be expressed as  $\alpha_{R1} = (A_s Z_s - A_b Z_b) / (A_s Z_s + A_b Z_b)$ . and  $\alpha_{T1} = 2A_b Z_s / (A_s Z_s + A_b Z_b)$ , respectively. In contrast, the coefficients including the transmitted pulses in the transmission bar and the reflection one in the specimen at the rear interfaces can be formulated as  $\alpha_{R2} = (A_b Z_b - A_s Z_s) / (A_s Z_s + A_b Z_b)$  and  $\alpha_{T2} = 2A_s Z_b / (A_s Z_s + A_b Z_b)$  [210], respectively. In this case, the transmission coefficient  $\alpha_T$  occurred in transmission bar is a second phase value indicating the wave pulse transmission into the specimen tested, then the rest of it continues to propagation in the transmission bar. Moreover, the reflection coefficient  $\alpha_R$  occurred in the incident bar is one phase value indicating the wave pulse reflected at the bar-specimen surface propagates in the incident bar. Due to the transmission coefficient  $\alpha_T$  and reflection coefficient  $\alpha_R$  being expressed at different pulses phases, the condition  $\alpha_R + \alpha_T \neq 1$  is acceptable corresponding with Al-Maliky [210]. The transmission coefficient  $\alpha_T$  and reflection coefficient  $\alpha_R$  can be calculated as follow [211, 208, 212, 210, 213, 214]:

$$\alpha_R = |\alpha_{R1}| = \left| \frac{1 - r_s}{1 + r_s} \right|, \quad \alpha_T = \alpha_{T1} \cdot \alpha_{T2} = \frac{4}{(r_s + 1) \cdot (1/r_s + 1)} \quad (3.12)$$

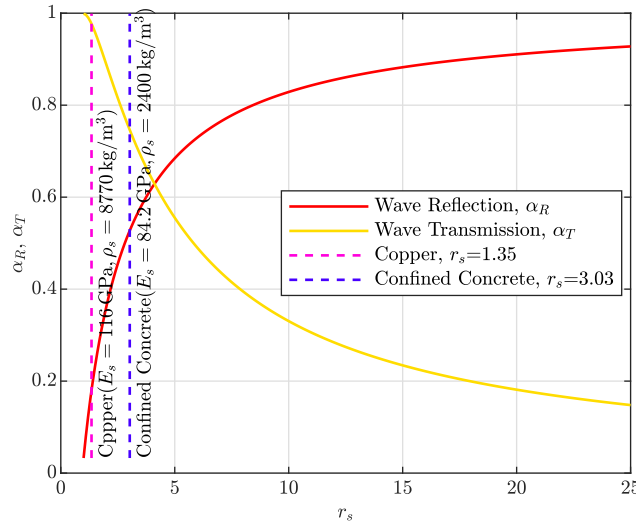


Figure 3.4 Transmission coefficient and reflection coefficient vs. impedance mismatch.

Figure 3.4 shows the evolution of the non-dimensional amplitude of the reflected and transmitted wave as a function of  $r_s$  during the transit time and by assuming an elastic linear response of the specimen without considering effects of the Poisson's ratio. Previous studies show that with a smaller  $r_s$ , a larger portion of the incident pulse would transmit into the specimen tested resulting in a higher signal-to-noise ratio for the specimen stress [206]. While higher values of  $r_s$  can lead to a large percentage of incident pulse reflected causing a higher signal-to-noise ratio for specimen strain rate [206]. With the similar trend between Figure 3.4 and results from Liao and Chen [206], the designed steel bar system can be utilized to test the engineering material with  $r_s$  ranging from more than 1.3 to around 10 indicating the around value of copper and concrete, and the range of  $r_s$  should not be restricted strictly because potential supplementary measures can be used to compensate the influence of  $r_s$ , such as using of rear pulse shaping technique to preserve the deformed state in the soft specimen after high-rate loading ensuring the single loading [87].

### 3.3.3 Strain rate limits

Based on the behavior of ceramics under high strain rate with a conventional SHPB, [208] defined the limit of the strain rate associated with consistent experimental data. The dynamic stress equilibrium and constant strain rate need to be achieved in the specimen test simultaneously. However, the upper strain rate achiev-

ing stress equilibrium is higher than that of constant strain-rate deformation [87]. This indicates that if the input strain rate is high, the specimen tested may deform under equilibrated stress but not ensuring a constant strain rate. The expressions of the upper strain rate under the requirement of stress equilibrium  $\dot{\epsilon}_f$  and of the constant strain-rate deformation  $\dot{\epsilon}_s$  as the main function of a failure strain  $\epsilon_f$  and the impedance mismatch  $r_s$  are as follow:

$$\dot{\epsilon}_f = \frac{\epsilon_f C_s}{\alpha L_s}, \quad \dot{\epsilon}_s = \frac{\beta \epsilon_f}{\tau(\beta/\eta - 1)} \quad (3.13)$$

where  $\epsilon_f$  is the failure strain, and  $\beta = 2\tau C_s/(L_s r_s)$ ,  $\eta = 1 - e^{-\beta}$ ,  $\tau$  is the empirical value indicating the the assigned time started from instant time  $\tau$  to the specimen fails when defining the measured constant strain rate. In this case  $\tau$  is the rising time  $T_{rg}$  (see Figure 3.8b). The non-dimensional parameter  $\alpha$  is of great importance, and was derived from the analysis of one-dimensional wave propagation. Therefore, the time necessary to achieve the stress equilibrium within the specimen (with a brittle behavior) is revealed to be  $\alpha$  times the transit time [208, 215]. Generally, the value of  $\alpha$  is taken as 4.

When estimating the upper limit of strain rate in SHPB test,  $\dot{\epsilon}_f$  and  $\dot{\epsilon}_s$  need to be considered simultaneously. Therefore, the upper limit of strain rate  $\dot{\epsilon}_{cr}$  is:

$$\dot{\epsilon}_{cr} = \min \{ \dot{\epsilon}_f, \dot{\epsilon}_s \} \quad (3.14)$$

For a practical example, the limit of the strain rate possible to achieve under the test condition discussed in Section 3.5 for a confined concrete is  $\dot{\epsilon}_{cr} = 199 \text{ s}^{-1}$  ( $\dot{\epsilon}_f = 474 \text{ s}^{-1}$ ,  $\dot{\epsilon}_s = 199 \text{ s}^{-1}$ , and , where  $\epsilon_f = 2.4\%$ ,  $E_s = 84.2 \text{ Gpa}$ ,  $\rho_s = 2400 \text{ Kg/m}^3$ ,  $C_s = \sqrt{E_s/\rho_s} = 5923 \text{ m/s}$ ,  $L_s = 0.075 \text{ m}$ ,  $\alpha = 4$ ,  $\tau = 139.6 \mu\text{s}$ ).

In this study, the average strain rate (ASR) derived in the dynamic load is assessed to indicate the consistent experimental data when reaching the condition of the upper limit of strain rate as  $ASR < \dot{\epsilon}_{cr}$ . ASR is defined as the total strain accumulated during the loading divided by the assigned time ( $L_s/c_b$ ):

$$ASR = \frac{-2c_b}{L_s} \int_{\tau}^t \epsilon_R(t) dt \quad (3.15)$$

### 3.3.4 SHPB calibration

The calibration process is performed whenever any changes occurred in the SHPB apparatus (e.g., change of the strain gages, bar or striker replacement, etc.). The purpose behind performing a calibration test is the compensation of errors coming from measurements and transmission [193]. The calibration process involves the calculation of correction factors to equalize the effect of a likely gauges misalignment or an undesirable effect of gauges bonding operation on the bar surface [216]. The calibration consists in checking that the amplitude of the generate impulse wave is consistent with the the theoretical one. Using Eq. 3.7, the theoretical strain amplitude of the incident pulses  $\varepsilon_p$  depending on the striker velocity can be calculated as:

$$\varepsilon_p = \frac{v_I}{2c_b} \quad (3.16)$$

where  $v_I$  is is the striker velocity measured from the laser system (Figure 3.1).  $v_I$  could also be determined theoretically or deduced from the signal propagation along the bar by using available techniques [217, 218]. Figure 3.5a shows a collection of incident waves and the gray rectangle indicate the time range ( $700 \mu s \leq t \leq 1000 \mu s$ ) used for the calculation of the mean of the measured incident wave  $\varepsilon_I$ . This range is taken as a range where the trapezoidal wave is sufficiently stable. Figure 3.5b indicates that the predicted amplitude according to Eq. 3.16 has a good agreement with the measured one. The strain correction factor  $K_\varepsilon$  can be calculated as:

$$K_\varepsilon = \frac{\varepsilon_p}{\varepsilon_I} \quad (3.17)$$

Limiting errors of measurement using this approach results in reducing strongly the uncertainty on the stress-strain curve [219], by evaluating  $K_\varepsilon$  nearly to 1.

### 3.3.5 Test validation

The validation of a compression test performed with an SHPB apparatus imposes a checking of the deformation during the loading history. Inhomogeneous deformations of the specimen will cause an inconsistency in the stress-strain curve. Consequently, stress and strain are both not representatives of the actual dynamic responses of the numerous interfaces of the short-length specimen. The condition



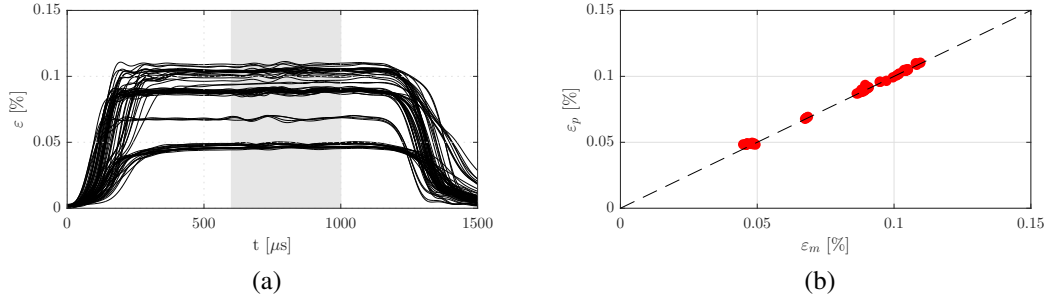


Figure 3.5 Collection of the incident waves adopted for the calibration (a). The gray rectangle indicate the time range ( $700 \mu s \leq t \leq 1000 \mu s$ ) used for the calculation of the mean of the measured incident wave. Comparison of the predicted and measured amplitude of the incident wave (b). After Xiong et al. [9].

to obtain reliable results is to put the specimen under a uniform state of stress or in other words to be under stress equilibrium. Along with the specimen thickness, the axial stress is evenly distributed. The relative stress equilibrium  $\zeta(t)$  between  $\sigma_{c1}(t)$  and  $\sigma_{c2}(t)$  is used to quantify the stress equilibrium process. Practically, the specimen is deemed to be under dynamic equilibrium if [220]:

$$\zeta(t = t^*) = \frac{\Delta\sigma(t = t^*)}{\sigma(t = t^*)} \times 100\% \leq 5\% \quad (3.18)$$

where  $t^*$  corresponds to the ultimate strength time instance and  $\Delta\sigma = |\sigma_{c1} - \sigma_{c2}|$ .

The second condition is referring to the delineation of the rate dependency of the materials behavior. To this end, the specimen needs to be deformed at a constant strain rate [206]. A Constant Strain Rate Factor (*CSRF*) is defined to evaluate the rate constancy [221]:

$$CSRF = \frac{\int_{t_{70\%}}^{t^*} (\dot{\epsilon}(t) - \bar{\epsilon}) dt}{t^* - t_{70\%}} \quad (3.19)$$

where  $t^* - t_{70\%}$  is the effective test period and  $t_{70\%}$  is the time corresponding to the 70% of the ultimate failure strength of the specimen and  $\bar{\epsilon}$  is the average of the strain rate in the effective test period. According to Hassan and Wille [221], the constant strain rate is reached if *CSRF* is less than 0.3.

## 3.4 Dispersion correction

Various countermeasures have been developed to reduce the effect of the dispersion but two physical methods are mainly used. Firstly, the introduction of a pulse shaper to change drastically the rising time of the waveform [222–224, 221, 225, 226]. Secondly, the design of a specific striker, such as a spindle-shaped striker [227, 87, 223, 228]. The pulse shaper technique consists of inserting a disk at the beginning of the incident bar. During the impact, the disk is deformed plastically and the incident wave is adjusted with a modification of the rising time and the pulse duration, meanwhile minimizing the dispersion effects. Nevertheless, to the author's knowledge, there is no admitted and appropriate theoretical method to design a pulse shaper. The utilization of a specific striker is to generate the half-sine stress wave, which eliminates the phenomenon of wave dispersion during the tests, and there are few oscillations in the stress-strain curves. Moreover, the specific geometry of the striker causes difficulties to design and fabrication for a general case.

However, the stress wave will disperse as it propagates along a cylindrical bar, particularly if the signal contains higher-frequency components [83]. Numerically, the dispersion effect in the bars can be corrected from the strain gauge records. Dispersion wave correction in the bar is conducted by two main numerical methods. Firstly, the frequency domain method can be adapted to shift the measured pulses by strain gauges mounted in the middle of the bar into bar/specimen surface pulses [229, 230, 215, 231–235]. Secondly, the radial correction method for non-uniform distribution of stress and particle velocity radial is also adapted [236–238]. In this case, the dispersion correction including frequency domain and radial non-uniform distribution methods was conducted simultaneously.

### 3.4.1 Theory of wave propagation

Considering one dimensional wave propagation, the wave propagates at a constant sonic speed and the bars expand and contract without lateral displacement of the bar axis. However, it is necessary to verify the latter assumption as the exact solution of the propagation of harmonic waves has been addressed for an infinite bar [239, 240].

The relation between the phase velocity of the wave and the wavelength is given by the frequency equation, presented in details by [241]. The phase velocity of the

Table 3.1 Roots of the Pochhammer-Chree frequency equation (Eq. 3.20).

	$\nu$	$a/\lambda$	$C_n/c_b$	$C_n/c_b$	$C_n/c_b$
			mode 1	mode 2	mode 3
This study	0.30	0.50	0.69	1.08	1.34
[238]			0.69	1.08	1.34
This study	0.29	0.36	0.81	1.18	1.59
[83]			0.81	1.02	1.64

$n$ -th frequency components,  $C_n$ , is generally traced as a function of Poisson's ratio  $\nu$ , the radius of the bar  $a$ , and the wavelength  $\lambda$ . The frequency equation, often termed as the Pochhammer-Chree equation, takes the following form [238]:

$$(x-1)^2\Phi(ha) - (\beta x - 1)[x - \Phi(ka)] = 0 \quad (3.20)$$

where  $x = (C_n/c_b)^2(1 + \nu)$ ,  $\beta = (1 - 2\nu)(1 - \nu)$ ,  $h = \gamma\sqrt{(\beta x - 1)}$ ,  $k = \gamma\sqrt{(2x - 1)}$ ,  $\Phi(y) = yJ_0(y)/J_1(y)$ , being  $\lambda$  the wavelength and  $\nu$  the Poisson's ratio,  $J_n(y)$  a Bessel function of the first kind, order  $n$ , and  $\gamma = 2\pi/\lambda$  is the wave number. This equation can be solved either numerically by implementing a suitable root finding algorithm such as the bisection or Newton–Raphson method [238], or graphically following the method introduced by Honarvar et al. [242]. An approach to solve numerically the frequency equation according to [243] was adopted and results are in a good agreement as shown in Figure 3.6a.

Tables listing roots of the dispersion equation at specific Poisson's coefficient of the medium are available in [238], [244], and [83]. For completeness and validation, some of the non-dimensional forms of the second and third roots differing from zero are listed in Table 3.1. The contribution of the second mode (mode 2) has been reported first by [245] and [246] and the smaller wavelengths are known to propagate at a lower speed. With higher modes of propagation, it is currently not known exactly the proportion of energy propagation in each mode at a particular frequency, therefore the accurate correction for dispersion beyond mode 2 is not available. Instead, Follansbee and Frantz [229] demonstrated that the dispersive behavior of the longitudinal waves in a bar is determined by the the first oscillation mode (mode 1).

Conveniently, some authors recognize to use of fitting curves to get the correct phase velocity [247]. Given a root of the Pochhammer-Chree equation (Eq. 3.20) for a particular value of  $a/\lambda$  and  $\nu$ , the normalized group velocity is determined describ-

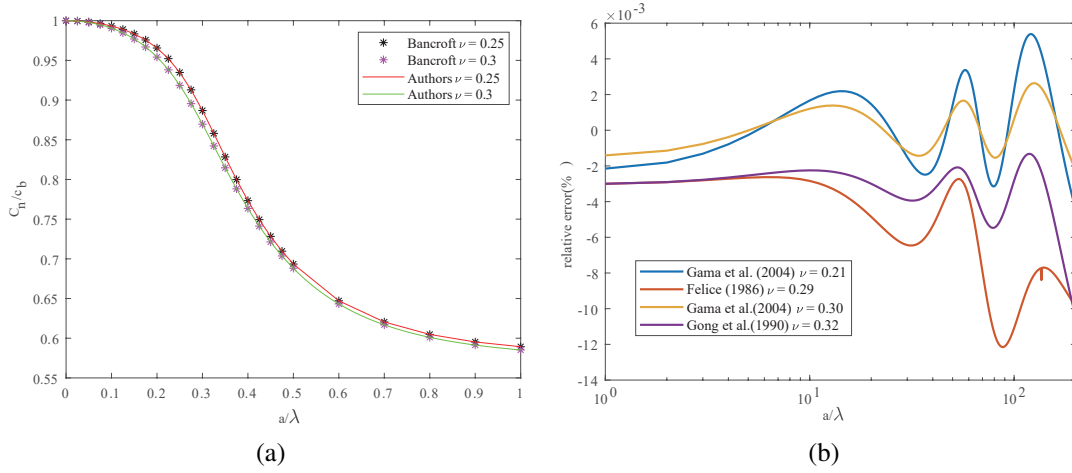


Figure 3.6 Phase velocity: exact numerical solutions,  $\nu = 0.25$  and  $0.30$  (a) and relative uncertainties generated by the fitting curves (b).

ing as  $C_n/c_b = f(a/\lambda, \nu)$ . Therefore, the non-dimensional relationship between the velocity of the bar and the phase velocity of the wave takes the present form [211]:

$$\frac{C_n}{c_b} = A_i + \frac{B_i}{C_i \left(\frac{a}{\lambda}\right)^4 + D_i \left(\frac{a}{\lambda}\right)^3 + E_i \left(\frac{a}{\lambda}\right)^2 + F_i \left(\frac{a}{\lambda}\right)^{1.5} + 1} \quad (3.21)$$

where the value of the factors  $A_i$  to  $F_i$  varies from one medium to another as the coefficient of Poisson changes. The numerical values of the factors given in Eq. 3.21 are reported in [216]. Figure 3.6b shows the relative error of this approach with respect of exact solution.

### 3.4.2 Dispersion correction in the frequency domain

The main effect of the dispersion remains on the generation of a peak with a high-frequency oscillation. This is due to the fact that large wavelengths (low-frequency) travel faster than short wavelengths. Thus, the high-frequency components of the waveform are lagging behind the low frequencies (see Fig. 3.6a).

The contribution of the dispersion in the distortion of a periodic disturbance has been demonstrated by [83]. The algorithm for the phase correction assuming trapezium-shaped wave traveling along elastic bars was separately proposed by Follansbee and Frantz [229] and [248] catering frequency domain correction. The phase angle referring to the geometrical dispersion is:

$$\delta = \delta_0 + \frac{nw_0\Delta z}{c_b} \left( \frac{c_b}{C_n} - 1 \right) \quad (3.22)$$

where  $\delta$  and  $\delta_0$  are the phase angles satisfying Eq. 3.20 at a distance of  $z$  and  $z_0$  ( $z = z_0 + \Delta z$ ) with propagation distance  $\Delta z$ ,  $w_0 = 2\pi/T_0$  being  $T_0$  the pulse period. Based on the same principle, variant and revisited methods were also developed by Lee and Crawford [249], Lifshitz and Leber [250], Li and Lambros [215].

$\Delta z$  and  $c_b$  should be experimentally determined. In a conventional SHPB installation, the strain signal of the incident wave is shifted forward to the bar-sample interface whereas those of the reflected and transmitted waves are moved backward. Consequently,  $\Delta z$  in Eq. 3.22 could either be positive or negative. The waveform is associated with the striker-bar impact. The last important parameter necessary to predict the phase dispersion is the calculation of the different values of  $C_n$ . These values could be obtained by solving numerically the frequency equation [244, 83] or assessed from available approximative solutions [211, 230, 216].

### 3.4.3 Dispersion correction about radial non-uniform distribution

Phase dispersion is not the only issue to foresee for the purpose to reconstruct the signals at the bar-sample interfaces. Tyas and Watson [251], Merle and Zhao [237] emphasized the contribution of two additional phenomena associated with wave propagation. Even though the cross-section of the SHPB is subjected to a uniform forcing function, the displacement of the particles is non-uniform over the bar radius. It implies that the stress and strain at the surface of the bar could be biased by the difference between the surface and axial displacement. Primarily, the lateral inertia is yielding to have the reading from the strain gauges mounted in the bar perimeter somewhat scattered from the average strain over the bar cross-section. Whilst, the elastic modulus at any point on the cross-section of the bar is not constant.

The compensation of these effects has been suggested by Tyas and Watson [236] by adding two correction factors labeled  $M1$  and  $M2$ .  $M1$  is referring to the issue of reading the surface displacement defined as the correction factor to convert surface axial strain to average axial strain over the cross-section, and  $M2$  represents the effect of dynamic elastic modulus defined as the correction factor to convert average

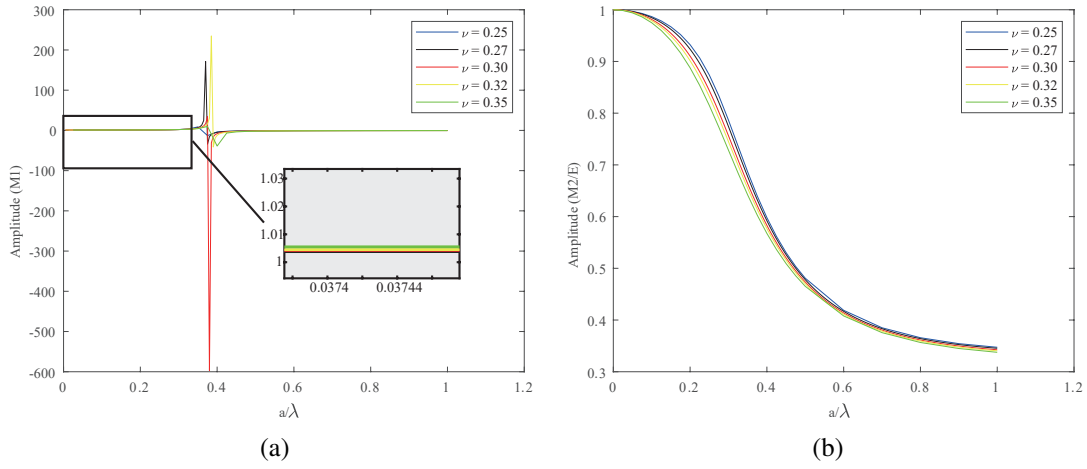


Figure 3.7 Correction factors for  $M_1$  with  $\nu = 0.25, 0.27, 0.30, 0.32, 0.35$  (a) and  $M_2/E$  (b).

axial strain to average axial stress. The mathematical expression of the factors  $M_1$  and  $M_2$  is [251, 237]:

$$M_1 = g\left(\frac{a}{\lambda}, \nu\right) = \frac{2[1 + (1 - \beta x)/(x - 1)]}{\Phi(ha) + [(1 - \beta x)/(x - 1)]\Phi(ka)} \quad (3.23)$$

$$M_2 = E f\left(\frac{a}{\lambda}, \nu\right) = E \left(\frac{C_n}{c_b}\right)^2 \quad (3.24)$$

Figures 3.7a and 3.7b are showing  $M_1$  and  $M_2/E$  as a function of the non-dimensional parameter  $a/\lambda$ , respectively.  $M_1$  and  $M_2/E$  are equal to 1 for low frequencies. Notice that  $M_1$  blows up and down dramatically at the critical frequency as a cut frequency, which is the cause in the procedure of the denominator being near zero when Eq. 3.23 is solved for this non-dimensional frequency.

### 3.4.4 Dispersion correction procedure

In the application of the dispersion correction procedure to correct the signals in SHPB bars with the property of  $\nu = 0.3$ , the time-domain function of the wave pulses  $f(t)$  recorded by strain gauges is known, then the procedure used to correct the dispersion is briefly summarized [251, 237]:

1. convert the wave pulses  $f(t)$  into the frequency  $w$  domain using Fourier Transform Algorithm ( $FFT$ ), the lengthy description of  $FFT$  is described in Follansbee and Frantz [229], Gong et al. [230], Li and Lambros [215], Guo et al. [231], Bragov et al. [232], Brizard and Jacquelin [233], Shin [234, 235];
2. derive the amplitude  $A(w)$  and the phase angle  $\delta_0(w)$  of each frequency component;
3. calculate the phase velocity  $C_n(w)$  of each frequency component;
4. arrange the phase angle according to Eq. 3.22;
5. calculate the new amplitude ( $A'(w) = A(w) \times M1 \times M2$ ) following Tyas and Watson [251], Merle and Zhao [237], where  $M1$ ,  $M2$  according to Eq. 3.23 and Eq. 3.24, respectively;
6. convert the signal back by using the new amplitudes  $A'(w)$  and phase angles  $\delta(w)$  into the time domain using an inverse  $FFT$ .

## 3.5 Results and discussion

### 3.5.1 Brittle material: concrete

The following discussion aims to describe the response of the concrete specimen to dynamic loading. A confined and unconfined concrete specimens are considered herein. The diameter of the specimen is 150mm with an aspect ratio of 0.5 (length 75mm). The specimens are subjected to  $P_g = 1.0\text{MPa}$  for confined specimens, respectively. The confined specimen is wrapped into two layers of Carbon Fiber Reinforced Polymer (CFRP). The mean quasi-static compressive strengths of the wrapped concrete specimens are 82MPa.

Figure 3.8a shows the time histories of the voltage measured by the Wheatstone bridge installed on the incident bar surface. The curve is tracing the disturbance recorded as the incident and reflected waves are traveling along the incident bar. The rising time ( $T_{rg}$ ) which corresponds to the period separating the location of the peak of the principal lobe ( $Amp$ ) and the time instance at 2% of  $Amp$  is also reported.

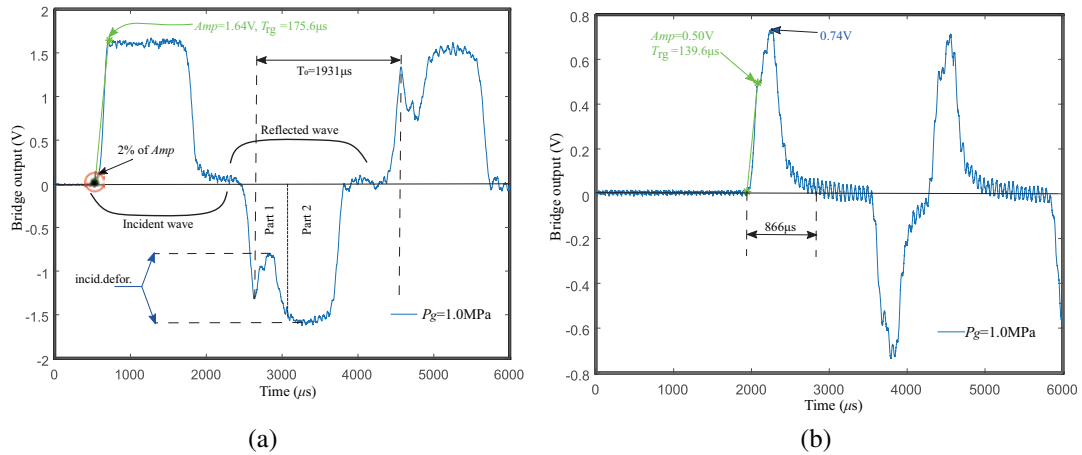


Figure 3.8 Bridge output at the incident and transmitted bars for confined concrete specimen (a) incident (b) transmitted.

The time history of the reflected wave could be split into two parts labeled as Part 1 and Part 2 shown in Figure 3.8a. It can be observed that the duration and the amplitude of the signals referring to Part 1 are less than those identified to be corresponding to the incident wave. In Part 1, the concrete continues to absorb the energy of the loading coming from the incident bar and the deformation of the specimen is elastic and plastic (discussed later). In Part 2, the amplitude of the reflected wave is equivalent to the amplitude of the incident wave confirming that there is no contact with the specimen at the end of the incident bar. No contact indicates that failure occurs. Another information could be deduced from the signal assigned to Part 1. The difference picture as *incid.defor.* in Figure 3.8a between the value of the bridge output at the limit of Part 1 and the voltage value at the deepest point in the concave area, illustrates the amount of energy transmitted (absorbed). Additionally, the time instance corresponding to the location of the deepest point describes the deformation. In this case, the wrapped specimen is experiencing much more deformation (see *indic.defor.*). The bar velocity could also be checked experimentally. From the period corresponding to one round trip of the wave (noted  $T_0$ ), the bar velocity is around 5178 m/s, corresponding with  $c_b = 5164$  m/s.

Figure 3.8b shows the evolution of the voltage measured in the transmitted bar. The useful time interval assigned to the specimen response is around 886  $\mu$ s. This time interval is somewhat higher than the half period of the incident wave (estimated approximately to 1600  $\mu$ s). At  $P_g = 1.0$  MPa, the peaks of the voltage are 0.74 V.



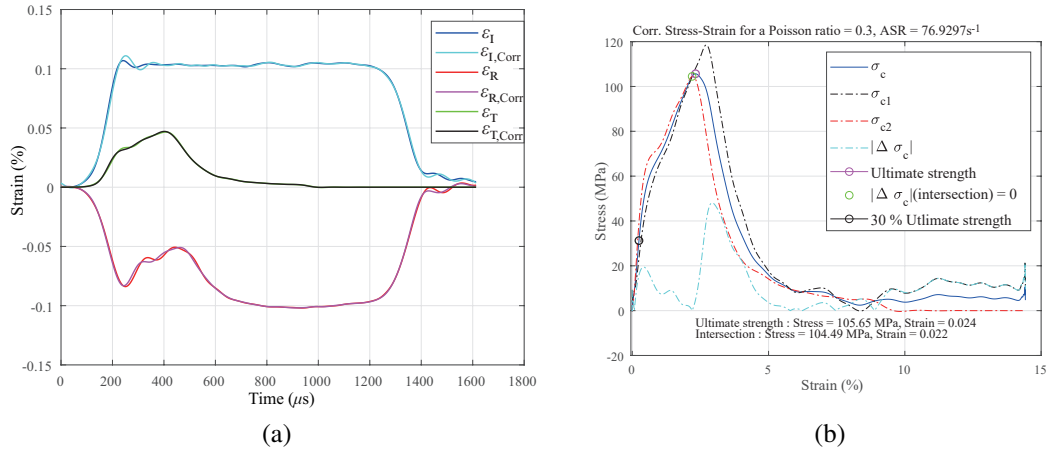


Figure 3.9 Delimitation and correction of the dispersion for confined specimens:  $P_g = 1.0\text{MPa}$  (a) and stress-strain diagram (b).

The next step is the delimitation of the incident, reflected, and transmitted waves. The delimitation consists of defining the start and the end of each pulse. In this paper, a new algorithm was developed to execute automatically the delimitation. The peaks of the principal lobes have been used to determine both the start and the end of the incident and reflected pulses. The start and the endpoint of the pulses represent a very low percentage of the first peak (2% of  $Amp$ ). However, a zero-crossing algorithm has been used to delimit the transmitted pulse [252]. The next step is to perform the correction of the dispersion. In this Section, the sample of confined concrete was selected to indicate the wave pulse delimitation and stress-strain construction for context simplification (see Figure 3.9). Figure 3.9a shows the results of both delimitation and the dispersion correction of the incident, reflected, and transmitted waves for confined specimen. Corrected waves are plotted and the subscript Corr is indicating the modified strains. It is noteworthy that as a pulse shaper is used, adopting by a copper disk with the size of  $\Phi 35\text{mm} \times 3\text{mm}$ , the influence of the dispersion is reduced.

The construction of the stress-strain curve is then accomplished according to 1D, 2D, and 3D– waves analysis. The results are plotted in Figure 3.9b. The wave attenuation is detected from the evolution of the stress at the bar-sample and sample-bar interfaces respectively labeled by  $\sigma_{c1}$  from 2D–wave analysis and  $\sigma_{c2}$  from 1D–wave analysis. During the loading stage, a negligible difference of the stress as a function of strain is observed at the second interface (in comparison to the stress at the first interface) [253]. It means that the sample is deformed uniformly from each side

and the consistency of the experimental data could be confirmed. For the confined concrete specimen, the evolution of the stress-strain curve is showing acceptable stress equilibrium conditions. At the elastic domain, a small difference between the 1D, 2D, and 3D–waves analysis is noticed. According to Sercombe [254], the evolution of the response of the concrete as a function the mean compressive stress under uniaxial loading in compression could be divided in three regimes. (i) The elastic domain (reversible deformation) is in the range of  $0 - 0.3\sigma_{us}$ . (ii) Plastic domain characterized by stable cracking with slow propagation of micro-cracks until their coalescence to form macroscopic cracks in the range of  $0.3 - 0.75...0.9\sigma_{us}$ . (iii) Plastic domain characterized by unstable cracking with a rapid propagation of macro-cracks inducing the drop of the stiffness in the range of  $0.75...0.9-1.0\sigma_{us}$ . Even though the plastic deformation capacity of the concrete is dominating, the stress uniformity along the length of the specimen is observed.

From the test validation procedure which imposes to verify three conditions: (i)  $\zeta(t = t^*) < 5\%$  (relative stress equilibrium); (ii)  $CSR F < 0.3$  (constant strain rate factor); (iii)  $ASR < \dot{\epsilon}_{cr}$  (consistent experimental data). The values of  $\zeta(t = t^*)$ ,  $CSR F$  and  $ASR$  are 4.7%,  $6.72 \times 10^{-8}$  and  $86 \text{ s}^{-1}$ , respectively. The dynamic compressive strength of the confined concrete specimen is 105.65 MPa for a  $DIF$  of 1.28. The confined concrete specimen experiences a deformation up to 2.4% at the ultimate stress value.

### 3.5.2 Ductile material: copper

A copper specimen subjected to a compression test performed with the SHPB setup is discussed in this Section. Figure 3.10 shows the evolution of the bridge outputs as the incident and the reflected waves are traveling along the incident bar. The incident compression wave has been generated with gun pressure of  $P_g = 0.6 \text{ MPa}$ . The sandwiched specimen is made from copper with a density of  $8770 \text{ kg/m}^3$  and an elastic modulus of 116 GPa. The quasi-static tensile strength of the copper is 238.7 MPa for a deformation of around 25%. The diameter of the specimen is 150 mm with an aspect ratio of 0.5 (length 75 mm). Thus, the impedance mismatch is around 1.35. The design of the pulse shaper used to perform the dynamic compressive has been modified. The rising time of the loading stage of the incident pulse is around  $387.6 \mu\text{s}$ .

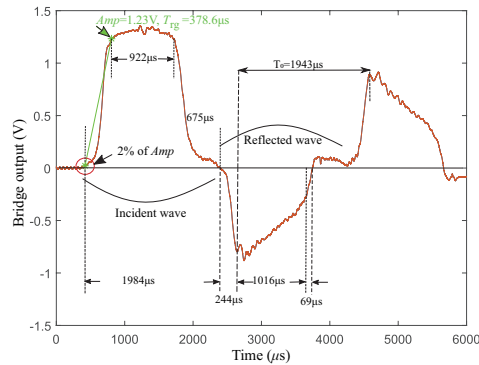


Figure 3.10 Bridge output of the incident bar for copper at  $P_g = 0.6$  MPa.

The evolution of the reflected wave as a function of time is completely different in comparison to the one assigned to concrete (reported in Figure 3.8a). In this case, one part is representing the entire response of copper. The elastic behavior could be identified as the absolute value of the voltage is increasing progressively in a quasi-linear trend (interval of  $244 \mu s$ ). After that stage, the specimen experiences irreversible deformation. The ductile behavior of the specimen could be pointed out as the time range referring to plastic deformation is larger (about  $1016 \mu s$ ).

The results of the delimitation and the correction of the dispersion are depicted in Figure 3.11a. The initiation of the work hardening (also known as the strain hardening) is also circled in the same Figure. Strain hardening is the strengthening of metal by plastic deformation. The derived stress-strain curve of the copper is depicted in Figure 3.11b. The stress-strain curve shows that the ultimate strain reached by applying the loading incident pulse is about 5.8%. This value of strain is largely dispersed from the deformation of the copper under the quasi-static tensile test at the ultimate strength because the sample experienced plastic deformation but no complete failure in the SHPB test. The values of  $\zeta(t = t^*)$ ,  $CSR_F$  and  $ASR$  indicating ultimate failure properties are not reached with the condition of the incomplete failure of the copper specimen in the SHPB test.

This result can be explained by two test conditions. The first condition is that the amplitude of the maximum loading generated by the incident wave at the bar-sample interface is around 190 MPa which is under the stress limit of the copper. To get the required stress to confer a larger deformation to the copper specimen, higher gun pressure is necessary. The second condition is the rising time. Reducing that

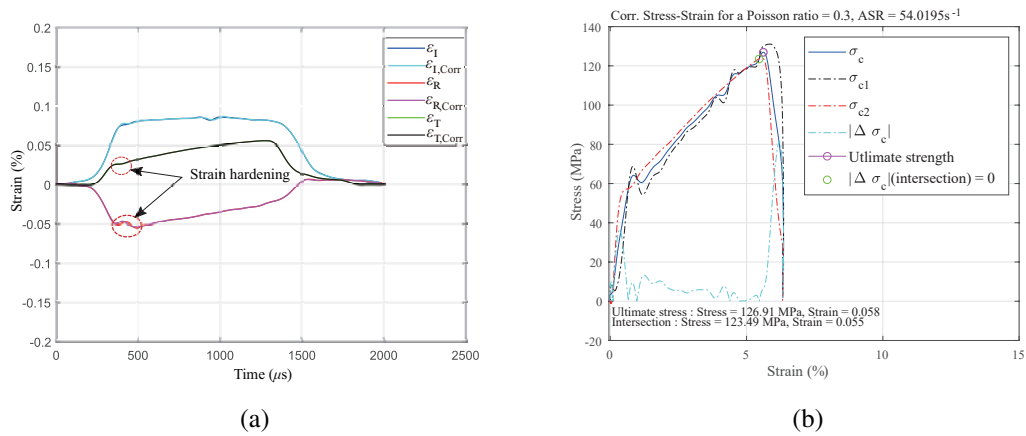


Figure 3.11 Delimitation and correction of the dispersion for copper test (a) and stress-strain diagram for copper under  $ASR = 54 \text{ s}^{-1}$  (b).

time will provide the possibility to obtain larger deformation of the specimen and an important average strain rate. To do so, the design of the pulse shaper should be reconsidered.

### 3.6 Conclusions

This chapter retraces the different steps of the design, construction, and validation of a large-scale SHPB. In the construction of that largest 155 mm SHPB setup, to meet the demand of challenges caused by heavy bars, a special buffer system is adopted as a trapping device. Moreover, a high-capacity gas gun motivated by the air compressor is equipped to attain controllable, repeatable, and stable striker performance. As the component of the data acquisition system, the strain gauges attached symmetrically on the bar surface of the incident and transmission bars and a laser velocimeter measuring the velocity of the striker are adapted. The loading device can reach the capacity of impact velocity of the striker of 11 m/s, the maximum value of the stress induced in the bar of 221 MPa, and a loading duration of the incident wave of 1162  $\mu\text{s}$ .

To verify the characteristic of the large-scale SHPB, the validation and test acceptance conditions were studied. The impedance mismatch of bars can be utilized to test the dynamic response of engineering material with  $r_s$  ranging from more than 1.3 to around 10 without adopting a specific device to adjust the apparatus when

the specimen tested has a diameter of 150 mm. Meanwhile, the upper limit of strain rate indicating the dynamic stress equilibrium and constant strain-rate deformation need to be achieved in the specimen test, which can be confirmed considering the material properties. The predicted and measured amplitude of the incident wave were approved with good agreement by conducting a number of primary tests. To validate the stress equilibrium process and constant strain rate factor during the test, relative stress equilibrium and *CSR*F less than 5 % and 0.3 respectively were conducted as an indicator of the desired test condition.

A proven dispersion correction method combined the frequency domain correction and radial non-uniform distribution method was conducted simultaneously, where the correction factor to convert surface axial strain to average axial strain over the cross-section was used to correct the surface displacement, and the factor to convert average axial strain to average axial stress was calculated to eliminate the effect of dynamic elastic modulus. After the application of the dispersion correction procedure, the dispersed signals in the SHPB bar can be corrected to show the real signals in the bar/specimen interface in the data progress, which can be a more accurate description of the dynamic properties of the specimen tested.

To demonstrate the proper specimen for different materials on the large-scale SHPB test, the brittle material (confined concrete) and ductile material (copper) were tested with the assessment on the result of completely valid data. After signals processing using the delimitation to adjust the start and the endpoint of pulse waves, the dispersion correction of the interpretation of the stress-strain curve will be seriously compromised, while the oscillations still are negligible because of the utilization of the pulse shaper. In the assessment of valid test of brittle material, the values of  $\zeta(t = t^*)$ , *CSR*F and *ASR* are derived from *1D*, *2D*, and *3D*– waves analysis to verify relative stress equilibrium, constant strain rate factor, and consistent experimental data. The confined concrete can be characterized in the test using a large-scale SHPB approach, occupying the result of dynamic compressive strength of 105.65 MPa for a *DIF* of 1.28, and a deformation up to 2.4 % at the ultimate stress. However, in the test of ductile material, the bridge output signals of the reflected wave represent the entire response of copper having elastic behavior and plastic deformation, which is completely different from the brittle material (confined concrete).

The work presented here allows drawing a related conclusion: the largest 155 mm SHPB setup can be used to experimentally evaluate the dynamic properties of large-diameter specimens, directly inferred from test data obtained from confined concrete samples and copper.

# Chapter 4

## Compressive behavior of concrete made with recycled crushed concrete and recycled clay bricks under different strain rate

### 4.1 Materials and methods

#### 4.1.1 Materials

The raw materials used in this study are: Ordinary Portland cement of grade 42.5R, river sand fine aggregates, gravel (NCA), recycled crushed concrete aggregate (RCA), crushed clay brick aggregate (BA), and tap water. The RCA and BA were crushed by an impact crusher. The size of all coarse aggregates was controlled to be in the fraction size of 5 – 12.5 mm. Physical properties and photos of coarse aggregates (NCA, RCA and BA) are reported in Table 4.1.




The bulk density was measured according to BSI [255]. The water absorption of three coarse aggregates was measured following this procedure [255, 256]: (i) samples of three aggregates (NCA, RCA and BA) were taken and their surface was washed and cleaned; (ii) the prepared samples were submerged in the water for 24 hours; (iii) the surface water of aggregates was removed until saturated surface-dried conditions were reached and their weight,  $m_{24}$ , measured; (iv) oven-dried mass of

aggregate  $m_0$  was then obtained after drying in an oven at  $105 \pm 5^\circ\text{C}$  for  $24 \pm 0.5\text{ h}$ ; (v) the water adsorbed,  $\Delta m_a$ , was calculated as the difference of  $m_0$  and  $m_{24}$ , i.e.,  $\Delta m_a = m_{24} - m_0$ . Finally, the water absorption ( $A_c$ ) of the tested aggregates is calculated as:

$$A_c = \frac{\Delta m_a}{m_0} = \frac{m_{24} - m_0}{m_0} \quad (4.1)$$

Table 4.1 Physical properties and photos of the different coarse aggregates employed.

	Natural coarse aggregate	Recycled crushed concrete aggregate	Crushed clay brick aggregate
Tag	NCA	RCA	BA
Bulk density [ $\text{Kg}/\text{m}^3$ ]	1435	1194	811
Water absorption [%]	0.71	2.83	17.33

Photo

#### 4.1.2 Test specimens: mix design and casting

The mass continuity equation of the concrete mixture can be expressed as:

$$W + C + \Delta_w(r) + FA + CA(1 - r) + RA(r) = W_{1\text{m}^3} \quad (4.2)$$

where  $W$  is the mass of water,  $C$  is the mass of cement,  $\Delta_w(r)$  is the additional mass of water due to the different water absorption of substituted aggregates (EEW method),  $FA$  is the mass of fine aggregate,  $CA(1 - r)$  is the mass of NCA ( $CA$  is the mass of NCA of the parent concrete),  $RA(r)$  is the mass of substituted coarse aggregate (RCA or BA), and  $W_{1\text{m}^3}$  is the total mass for  $1\text{ m}^3$  of the concrete mixture.

The mass continuity equation can be expressed as a function of weight fractions as:

$$\frac{W}{\rho_w} + \frac{C}{\rho_w} + \frac{\Delta_w(r)}{\rho_w} + \frac{FA}{\rho_{FA}} + \frac{CA}{\rho_{CA}}(1 - r) + \frac{RA(r)}{\rho_{RA}} = 1\text{ m}^3 \quad (4.3)$$



Table 4.2 Mix proportion and dry density for concrete made with different levels of substitution and types of coarse aggregate tested in this study. Symbols are reported following Eq. 4.3.

Type	$r$	$C$	$W$	$W/C$	$FA$	$CA(1-r)$	$RA$	$\Delta_w$	Dry density of concrete
[-]	[%]	[Kg/m <sup>3</sup> ]	[Kg/m <sup>3</sup> ]	[-]	[Kg/m <sup>3</sup> ]	[Kg/m <sup>3</sup> ]	[Kg/m <sup>3</sup> ]	[Kg/m <sup>3</sup> ]	[Kg/m <sup>3</sup> ]
NAC	0	467	210	0.45	574	1082	0	0	2366
RAC20	20	467	210	0.45	574	866	216	6.1	2317
RAC40	40					649	433	12.2	2389
RAC60	60					433	649	18.4	2351
RAC80	80					216	866	24.5	2283
RAC100	100					0	1082	30.6	2298
RBC20	20	467	210	0.45	574	866	216	37.5	2253
RBC60	60					433	649	112.5	2058
RBC100	100					0	1082	187.5	1934

where  $\rho_i$  is the density of each component (in kg/m<sup>3</sup>).

The mass and volume of substituted coarse aggregate as a function of  $r$  (Eq. 2.2) can be determined as:

$$RA(r) = CA \cdot r \quad (4.4)$$

The additional mass of water due to the different water absorption of substituted aggregates using the EEW method [145] can be determined as:

$$\Delta_w(r) = \rho_w \cdot A_{nc} \cdot RA(r) \quad (4.5)$$

where  $A_{nc}$  is the water absorption ratio of NCA.

Eqs. 4.3, 4.4 and 4.5 are controlling the mix design of the concrete mixture.

Table 4.2 reports a summary of the mix proportion for concrete made with different levels of substitution and types of coarse aggregate. The NAC mix design was done according to JGJ [257] to obtain a C35 concrete class. The coarse aggregate substitution was made following the EEW method as in Eqs. 4.3, 4.4 and 4.5. Designation of the mixture and specimen is given by the following ID tag, NAC-RAC-RBC/#, where the first value denotes the coarse aggregate type (NAC: only gravel; RAC: substitution with RCA; RBC: substitution with BA) and the number, #, represents  $r$  in percentage.

The control of mixing order and time is reported as followed: the coarse and fine aggregates were poured in the flat concrete mixer and mixed for 30s to 60s. Then the cement and tap water were added and mixed together for 30s. PVC molds with the standard size of  $\Phi 150 \times H 300$  mm were used for specimens cast. Specimens were taken from the molds after 24h and then kept in the moisture room at a temperature of  $20^\circ C$  and humidity of 95% for 28 days. The dry density of the hardened concrete was measured after 28 days. The dry density of concrete was evaluated according to MOCO [258]. Before tests, the weight of each specimen was measured to verify the consistency finding a maximum difference of 3% within each type of concrete.

For each concrete type, a total of 6 specimens were cast (54 specimens): 3 of them were used directly for quasi-static tests (see Section 4.2) while the remaining four were cut into 9 small specimens with a size of  $\Phi 150 \times H 75$  mm for SHPB testing (see Section 4.3). The same procedure adopted by Xiong et al. [9] was employed for specimen cutting.

## 4.2 Quasi-static test program

The two end faces of specimens adopted in quasi-static tests were cleaned by sandpaper and brush before testing. Then, to ensure parallel surfaces, one face was capped with high-strength gypsum.

The quasi-static tests were carried out at 28 days curing time using a universal testing machine [259, 260] on three standard specimens at the constant loading rate of 0.6 mm/min (corresponding to a strain rate of  $\dot{\epsilon} = 3.33 \times 10^{-5} s^{-1}$ ). The quasi-static compressive strength (see Eq. 2.4) for each concrete type was defined as the expected value of the three repetitions:

$$f_c(r, \dot{\epsilon} \rightarrow 0 s^{-1}) = \text{mean}_i \left[ \frac{\max_t (F(t, i, r))}{A} \right] \quad (4.6)$$

where  $F(t, i, r)$  is the force as a function of the testing time,  $t$ , measured by the universal testing machine on the  $i$ -th specimen with a certain  $r$ , and  $A = \pi (D/2)^2$  is the cross-section area of the specimen being  $D = 150$  mm. After the test, the failure of the specimen was photographed.

## 4.3 High-strain rate tests program

### 4.3.1 Large diameter SHPB: apparatus and working principle

The apparatus and working principle are basically introduced in Chapter 3. The stress and strain conditions of the specimen can be calculated using Eqs. 4.7 based on the following assumptions [e.g., 87]: (i) one dimensional planar elastic wave propagation; (ii) interfacial friction and inertia effects can be negligible; (iii) constant strain rate deformation and (iv) stress equilibrium between the two ends of the specimens. The validity of these conditions for the tests performed in this study will be discussed in Section 4.3.3. Under these assumptions, the front and back axial stresses ( $\sigma_1$ ,  $\sigma_2$ ), the averaged axial stress ( $\sigma$ ), the strain ( $\varepsilon$ ) and the strain rate ( $\dot{\varepsilon}$ ) can be derived as follows [e.g., 87], which are derived from Eq.3.3-3.5:

$$\sigma_1(t) = \frac{A_B}{A_S} \cdot E_B [\varepsilon_i(t) + \varepsilon_r(t + \tau_1)] \quad (4.7a)$$

$$\sigma_2(t) = \frac{A_B}{A_S} \cdot E_B \varepsilon_t(t + \tau_2) \quad (4.7b)$$

$$\sigma(t) = \frac{\sigma_1(t) + \sigma_2(t)}{2} = \frac{A_B}{2A_S} \cdot E_B [\varepsilon_i(t) + \varepsilon_r(t + \tau_1) + \varepsilon_t(t + \tau_2)] \quad (4.7c)$$

$$\varepsilon(t) = -\frac{C_B}{L_S} \int_0^t [\varepsilon_i(t) - \varepsilon_r(t + \tau_1) - \varepsilon_t(t + \tau_2)] d\tau \quad (4.7d)$$

$$\dot{\varepsilon}(t) = -\frac{C_B}{L_S} [\varepsilon_i(t) - \varepsilon_r(t + \tau_1) - \varepsilon_t(t + \tau_2)] \quad (4.7e)$$

where  $t$  is the time,  $A_B$  and  $A_S$  are the cross-sectional areas of the bars and the specimens, respectively,  $L_S$  is the original length of the specimens and  $\tau_1$  and  $\tau_2$  are the time delays of  $\varepsilon_r$  and  $\varepsilon_t$  with respect to  $\varepsilon_i$ .  $\tau_1$  and  $\tau_2$  were calculated following the procedure adopted by Xiong et al. [9] and Zhou et al. [261].

Table 4.3 Summary of the SHPB tests.

Type	$r$	$P_g$	Repetitions
[-]	[%]	[MPa]	[-]
NAC	0	0.3; 0.7; 1.1	3
RAC	20; 40; 60; 80; 100	0.3; 0.7; 1.1	3
RBC	20; 60; 100	0.3; 0.7; 1.1	3

The strain rate is a function of time, see Eq. 4.7e. Henceforth, the representative strain rate is defined as the ultimate strain rate which is the strain rate corresponding to the peak stress [9]:

$$\dot{\epsilon} = \dot{\epsilon}(t^*) \quad (4.8)$$

where  $t^*$  is the time corresponding to the peak stress.

### 4.3.2 Test matrix and protocol

The test matrix of the high-strain rate test program is reported in Table 4.3. Tests were performed on cut specimens (see Section 4.1.2, i.e., NAC, RAC, and RBC) for all the cases reported in 4.3 at three gun pressures,  $P_g = \{0.3; 0.7; 1.1\}$  MPa. For each case, four repetitions of the tests were done. The three tests with more homogenous responses respecting the conditions discussed in Section 4.3.3 were taken.

The test protocol is the same adopted by Xiong et al. [9] and is briefly summarized in the following. Before each test, the alignment of bars was checked and the bar ends were cleaned using sandpaper. Then, a layer of vaseline was applied on the two interfaces of specimen and interfaces of incident and transmission bars to minimize interfacial friction [221]. The specimen was sandwiched between the incident and transmission bars. Afterwards, a copper disc pulse shaper was stucked on the end face of the incident bar on the contact side with the striker bar. During the test, the striker was launched at a prescribed gun pressure corresponding to a certain impact velocity. The acquisition system triggered by the laser is recording the signals from the two strain gauges (see Figure 3.1) at a sampling frequency of 2.5 MHz. After tests, the debris were collected and photos taken. The data were processed using Eqs. 4.7. All the data coming from the strain gauges are first numerically filtered

using a low-pass filter with a frequency of 10kHz [262, 263, 9]. In the following, the validity of Eqs. 4.7 is discussed with reference to the tests performed.

### 4.3.3 Validation of the tests

The validation of the tests performed herein requires the checking of dynamic stress equilibrium and constant strain rate conditions as explained in Section 3.3.5.

However, these two conditions are easily violated in brittle materials such as concrete due to the steeply increasing incident stress wave that induces a premature failure of the specimen before reaching the peak stress [e.g., 173]. The most common solution is the use of pulse shapers, a deformable element (commonly a disk or ring) installed between the striker and the incident bar, to slow down the rate of increase of the incident stress wave and reduce the dispersion effects [264, 265, 87, 266, 223, 267, 6, 9]. Therefore, in order to help the specimen reach the dynamic stress equilibrium state and constant strain rate conditions, H62 copper discs with a thickness of 3 mm and diameter of 35 mm were employed as pulse shaper in this study, as done in Xiong et al. [9]. It is noteworthy that the copper was chosen because of its strain rate independent mechanical properties [224].

In the following, one of the specimen RAC40 tested at a pressure of  $P_g = 0.3$  MPa was taken as example to show the reaching of dynamic stress equilibrium conditions. Figure 4.1a shows typical waveforms from the incident and transmission bars obtained from the strain gauges and the three identified waves ( $\epsilon_i(t)$ ,  $\epsilon_r(t)$  and  $\epsilon_t(t)$ ). The three identified waves are used to predict the stress-strain conditions using Eq. 4.7 that are reported in Figure 4.1b. It can be observed that the dynamic equilibrium condition at the peak stress point is satisfied. The acceptance limit condition,  $R(t) = 0.05$ , is reported as the blue dashed line, i.e.  $\sigma(t) \times 0.05$ . At  $t^*$  (peak stress point),  $\Delta\sigma(t^*)$  (red line) is near to 0 and below the acceptance limit condition. Accordingly, the dynamic equilibrium conditions are considered to be satisfied.

The checking of the dynamic stress equilibrium and constant strain rate conditions was performed for all tests reported in this study. Tests not respecting these conditions are disregarded from the analysis.

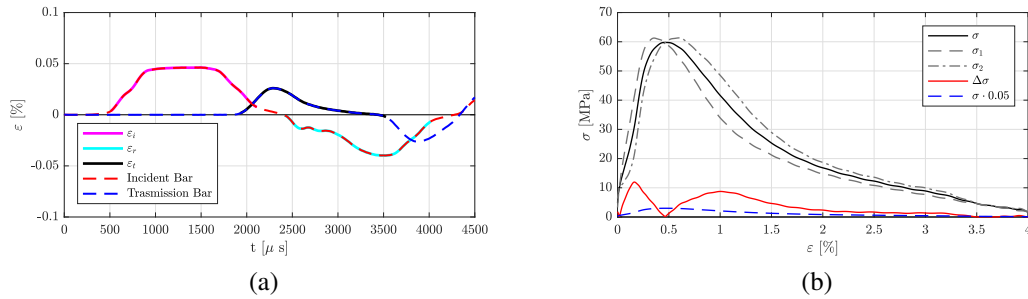


Figure 4.1 Signals obtained for a specimen RAC40 tested at a pressure of  $P_g = 0.3$  MPa: typical waveforms from the incident and transmission bars and the three identified waves ( $\varepsilon_i(t)$ ,  $\varepsilon_r(t)$  and  $\varepsilon_t(t)$ ) (a); stress-strain curve with averaged axial stress (Eq. 4.7c), front and back stresses (Eqs. 4.7a and 4.7b), their difference (Eq. 3.18), and acceptance condition  $R(t) = 0.05$  (b).

## 4.4 Experimental results of quasi-static compressive behavior

### 4.4.1 Compressive strength

The strength of three standard specimens tested at 28 days as a function of  $r$  are summarized in Figure 4.2 for RAC and RBC. In both cases, NAC is reported for  $r = 0\%$ . The black asterisks represent the strength of each of the three repeated tests and grey area is their range. The red asterisks are the average strength on the three repeated tests for each value of  $r$ . The red dashed line indicated the linear trend obtained by joining the average strength at  $r = 0$  and  $100\%$ . The red solid line is the spline interpolation of the average strength as a function of  $r$ .

Generally, the quasi-static compressive strength of RAC and RBC decrease with the increase of  $r$  in a non-linear fashion as showed by the difference with respect to the red solid line. For both RAC and RBC, the final strength loss at  $r = 100\%$  is around  $40\%$  corresponding to  $f_c(r = 100\%, \dot{\varepsilon} \rightarrow 0 \text{ s}^{-1}) \cong 23$  MPa and  $SRF \cong 60\%$ . The coarse aggregate replacement induces a transition between the behavior with NCA to that with RAC or RBC. This transition is not linear and is characterized by a transition point, which shows the dominant coarse aggregate: below this point the behavior is dominated by the NCA and above by the substituted coarse aggregate. This transition point can be roughly identified at  $r = 60\%$  for RAC and  $r = 30\%$

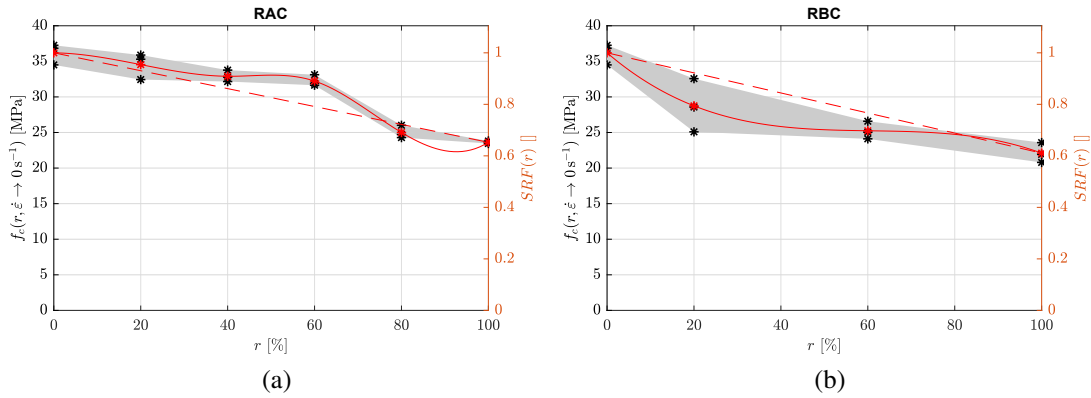


Figure 4.2 Quasi static-strength and  $SRF$  at 28 days,  $f_c(r = 0\%, \dot{\epsilon} \rightarrow 0 \text{ s}^{-1})$ , as a function of  $r$  for RAC (a) and RBC (b).

for RBC. As a matter of fact, the strength loss in the range of  $r$  from 0 to 60% is higher for RBC compared with RAC while for  $r$  above 60% the opposite is true. Generally, a large scatter was observed for RBC. It can thus be suggested that the reduced mechanical performances of BA are very variable thus inducing the observed large strength variability of RBC, especially at  $r = 20\%$ , which can be considered the transition point. Similar trends were previously observed in literature for RAC [144, 268–270, 8] and for RBC [271, 166, 272, 163].

#### 4.4.2 Failure modes

The failure modes of NAC, RAC and RBC cylinder specimens under quasi-static axial compression are presented in Figure 4.3. Only one specimen is shown as representative of the failure mode since similar conditions were observed in the remaining ones.

Generally, the final failure modes for the same type of coarse aggregate are similar. For NAC, a tendency to shear-conic failure is observed. Some major macro-cracks and a large number of micro-cracks eventually coalesced into concrete spalling/crushing near mid-height of the cylinder before final failure occurred, indicating a progressive failure of the specimen, similar to the observations reported in Xiong et al. [9]. On the other hand, the RAC and RBC cylinder specimens are dominated by a column-like failure mode. Major-cracks crossing the whole height

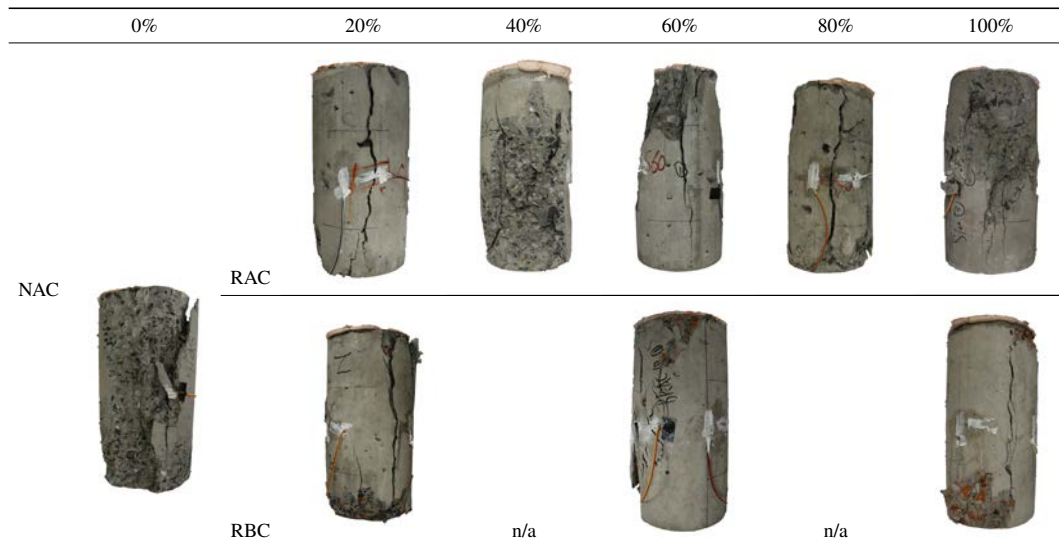


Figure 4.3 Typical failure modes under static loading of standard cylinder specimens for NAC, RAC and RBC with different  $r$ .

of the cylinder were clearly present separating into columnar fragments indicating a sudden failure mode.

It is more difficult to define a clear trend observing the failure modes. However, some qualitative considerations can be provided. Generally, a transition from the shear-conic failure to the column-like failure mode is observed increasing  $r$ . Similarly to the strength (see Figure 4.2), this transition is non-linear with  $r$ . In particular, a similar transition point was observed at  $r = 60\%$  and  $20\%$  for RAC and RBC, respectively. This indicates that coarse aggregate substitution has a marked effect on the final failure mode.

## 4.5 Experimental results of high-strain rate compressive behavior

### 4.5.1 Stress and strain relationship and dynamic strength

Figure 4.4 presents stress-strain curves for different tests corresponding to NAC, RAC and RBC with different values of  $r$ . In each subfigure, different colors correspond to the three different values of  $P_g$ , namely 0.3, 0.7 and 1.1 MPa.



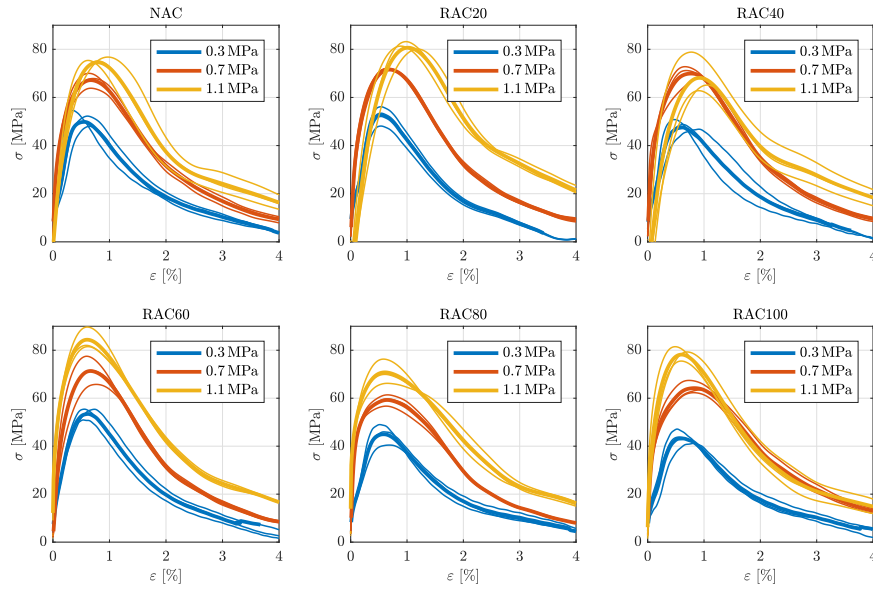
Overall, these results indicate that the strain-stress curves of NAC, RAC and RBC under high strain rate are characterized by the same typical behavior. After an initial linear portion lasting up to about 30 – 40% of the peak stress, the curve becomes non-linear, with larger strains being registered for small increments of stress (stiffness reduction). The non-linearity is primarily a function of the coalescence of micro-cracks at the paste-aggregate interface (Interfacial Transition Zones, ITZs). The peak stress is reached when a large crack network is formed within the concrete, consisting of coalesced micro-cracks and the cracks in the cement paste matrix. The post peak behavior is characterized by a softening behavior typical of brittle materials such as concrete. The softening branch indicates that all specimens failed, as observable in Figure 4.6.

Generally, an increase of the peak stress and its corresponding strain is observed by increasing  $P_g$ . The increase is larger from  $P_g = 0.3$  to 0.7 MPa and less marked from  $P_g = 0.7$  to 1.1 MPa. However, it should be noted that different values of  $P_g$  for the different specimens correspond to different strain rates, as it will be shown in Section 4.6.1. The initial dynamic elastic modulus generally increases by increasing  $P_g$ .

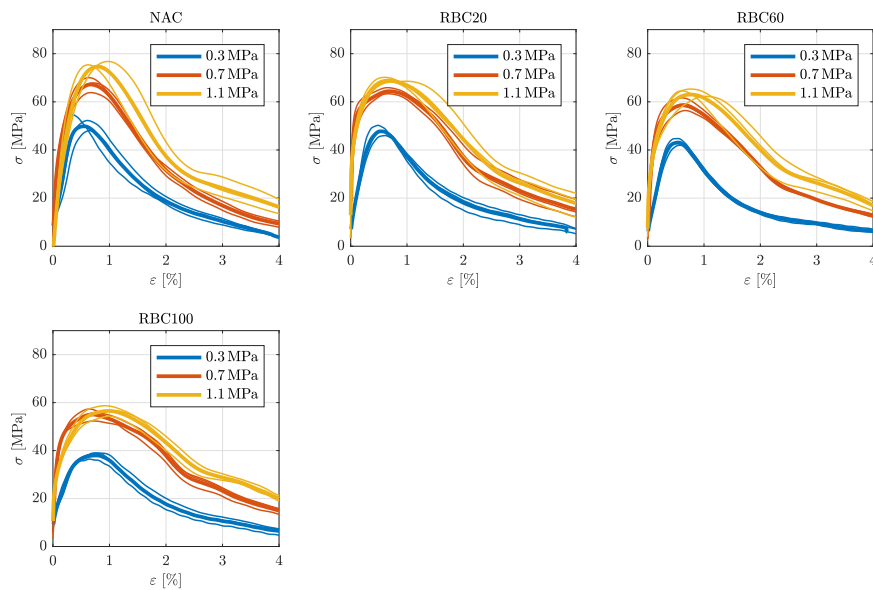
Focusing on RAC (see Figure 4.4a), it can be seen that when  $r \geq 40\%$  the increase of the peak strain is less marked at 1.1 MPa. The increase in the initial dynamic elastic modulus is less marked for  $r \leq 40\%$  (especially for RAC20 and RAC40) and more marked when  $r \geq 40\%$ . Only at  $r = 40\%$  (i.e., RAC40), comparable values of the peak stress at  $P_g = 0.7$  to 1.1 MPa.

The increase of the peak stress from  $P_g = 0.7$  to 1.1 MPa is less marked for RBC (see Figure 4.4b). Lower peak stress and similar peak strain are observed in comparison with RAC. The comparison of the peak stress between RAC and RBC is following the static test results (see Figure 4.2b). Finally, the initial dynamic elastic modulus increase markedly from  $P_g = 0.3$  to 0.7 MPa. On the other hand, the initial dynamic elastic modulus at  $P_g = 0.7$  and 1.1 MPa is almost the same.

The dynamic strength as a function of strain rate is showed in Figure 4.5. It can be seen that an increase of the strength with the strain rate is observed in all cases. This difference in strength is related to different deformation and failure mechanisms. Under high strain rate, the high confining stresses tend to keep the interfaces between the aggregate and matrix (ITZs) under overall compressive loading, retarding the initiation and growth of cracks [273]. The closure effect of the high hydrostatic



(a)



(b)

Figure 4.4 Stress-strain curves for different dynamic tests: RAC (a) and RBC (b). For each gun pressure ( $P_g$ ), the three thin lines are the results of the three repetition tests while the thick line is their average across the axial strain.

stresses causes deformation to occur in both the mortar phase and the aggregate in concrete, allowing the strengthening effect of the aggregate to manifest. The strength increase is more remarkable for RAC than for RBC. The  $r$  increase is generally inducing a reduction of the strength, similar to what observed for the quasi-static case (Figure 4.2).

### 4.5.2 Energy absorption density

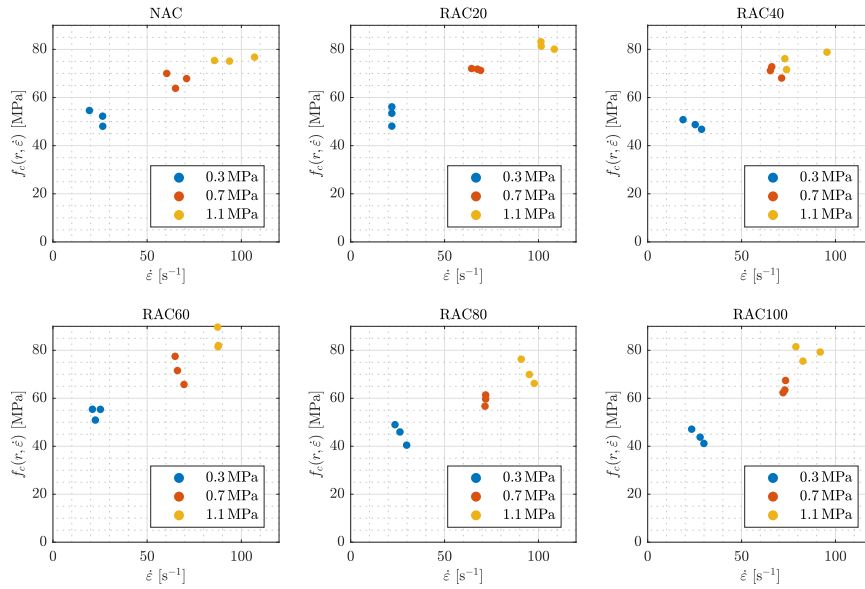
For dynamic loading test, the ability of absorbing impact energy can be expressed in terms of energy accumulated before the failure. The energy absorption density (calculated by the area enclosed by the stress-strain curve) can be defined as [e.g., 274]:

$$\omega(t) = \frac{A_B E_B C_B}{A_S l_S} \int [\varepsilon_i^2(t) - \varepsilon_r^2(t) - \varepsilon_t^2(t)] dt \quad (4.9)$$

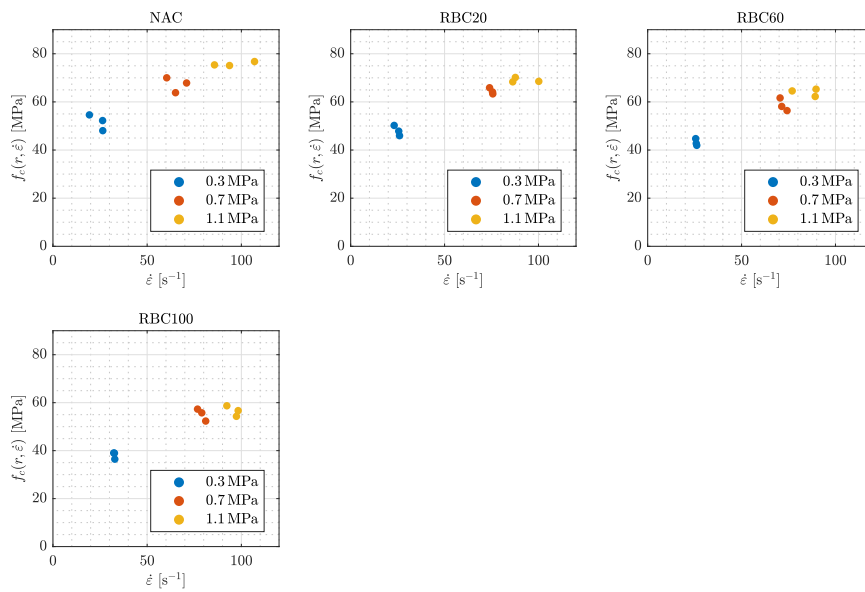
The concrete failure corresponds to the peak stress that in terms of time can be expressed as  $t = t^*$ . Accordingly, Eq. 4.9 is expressed as  $\hat{\omega} = \omega(t^*)$ . The summary of  $\hat{\omega}$  for the different tests is reported in Table 4.4.

For  $P_g = 0.3$  MPa,  $\hat{\omega}$  is almost similar in all cases (NAC, RAC and RBC), with values around  $0.2 \text{ MJ/m}^3$ . Increasing  $P_g$  at  $0.7$  MPa and  $1.1$  MPa,  $\hat{\omega}$  increases with values in the range of  $0.31$  and  $0.52 \text{ MJ/m}^3$  due to the increasing stiffness and strength with the strain rate. It can be observed that  $\hat{\omega}$  increases with increasing  $P_g$  due to increasing stiffness and strength with the strain rate (see Figure 4.4). For RAC, at  $P_g = 0.3$  MPa, the lowest and largest values of  $\hat{\omega}$  are observed in RAC20 and RAC60, respectively, which is in agreement with the difference in the peak stress and ductility in Figure 4.5a. At  $P_g = 0.7$  MPa, the lowest and largest values of  $\hat{\omega}$  are observed in RAC80 and RAC100 respectively (Figure 4.4). At  $P_g = 1.1$  MPa,  $\hat{\omega}$  decreases with increasing  $r$  due to a decrease of the peak stress (Figure 4.4).

For RBC, similar ranges are generally observed comparing with NAC and RBC. The lowest and largest values of  $\hat{\omega}$  are observed in RBC60 and RBC100, respectively, which is the results of the decrease of peak-stress from RBC20 to RBC60 and the increase of peak-strain from RBC60 to RBC100 (Figure 4.4).



(a)



(b)

Figure 4.5 Dynamic strength,  $f_c(r, \dot{\epsilon})$ , as a function of the strain rate,  $\dot{\epsilon}$ , for the different tests: RAC (a) and RBC (b).

Table 4.4 Energy absorption density at failure,  $\hat{\omega}$  [MJ/m<sup>3</sup>], for the different tests. The layout of the data in the cells is the following:  $\hat{\omega}(\hat{\omega}_1, \hat{\omega}_2, \hat{\omega}_3)$ , where  $\hat{\omega}_1, \hat{\omega}_2, \hat{\omega}_3$  are the values of  $\hat{\omega}$  for the three repetitions of tests and  $\hat{\omega}$  their average.

$P_g$	NAC	RAC20	RAC40	RAC60	RAC80	RAC100
0.3MPa	0.19 (0.23; 0.21; 0.13)	0.19 (0.21; 0.18; 0.20)	0.23 (0.22; 0.32; 0.16)	0.24 (0.20; 0.30; 0.22)	0.19 (0.21; 0.20; 0.17)	0.2 (0.18; 0.24; 0.17)
0.7MPa	0.36 (0.36; 0.34; 0.39)	0.38 (0.40; 0.37; 0.37)	0.42 (0.53; 0.37; 0.37)	0.37 (0.36; 0.38; 0.37)	0.33 (0.31; 0.33; 0.34)	0.44 (0.42; 0.49; 0.41)
1.1MPa	0.44 (0.42; 0.34; 0.54)	0.52 (0.55; 0.50; 0.51)	0.49 (0.44; 0.54; 0.48)	0.42 (0.42; 0.41; 0.44)	0.38 (0.39; 0.38; 0.37)	0.37 (0.43; 0.34; 0.35)
$P_g$	NAC	RBC20	RBC60	RBC100		
0.3MPa	0.19 (0.23; 0.21; 0.13)	0.2 (0.20; 0.21; 0.18)	0.16 (0.17; 0.15; 0.17)	0.22 (0.25; 0.18; 0.23)		
0.7MPa	0.36 (0.36; 0.34; 0.39)	0.4 (0.40; 0.41; 0.39)	0.31 (0.32; 0.31; 0.30)	0.34 (0.37; 0.34; 0.31)		
1.1MPa	0.44 (0.42; 0.34; 0.54)	0.46 (0.63; 0.37; 0.40)	0.43 (0.55; 0.42; 0.31)	0.48 (0.46; 0.52; 0.46)		

### 4.5.3 Failure modes

The typical failure modes of NAC, RAC and RBC specimens with different  $r$  after SHPB tests are depicted in Figure 4.6 for different gun pressure. Only one representative specimen is selected from three repeated tests. All photos were taken after the tests. Accordingly, additional damage on the specimen caused by the movement of the bar and/or to its falling may be reported with respect to the damage deriving from the measured propagating wave. However, these photos can provide general information on the final conditions of the specimens after SHPB tests.

Generally, a reduction of the size of fragments is visible with increasing  $P_g$ . Additionally, the increasing of  $P_g$  leads to a more evident breaking of the coarse aggregates and separation of mortar. In fact, as the strain rate increases many more of the inherent flaws are activated and forced to grow into the high strength areas of the mortar and aggregates [275] resulting in increased strength (see Figure 4.5.1), a larger number of much shorter cracks and smaller fragments (Figure 4.6). At much higher rates the fragments are much smaller and the concrete is reduced to rubble. This breaking and separation of the coarse aggregate is particularly observable in RBC specimens due to the minor mechanical performances of BA. For high pressures, BA was partially reduced into a powder.

These results suggest that different strain rates induced by different amplitudes of the incident wave leads to a different crack propagation process which can be related to the observed strength increase (see Section 4.5.1). In particular, higher strain rates correspond to a more extended net of cracks leading to small fragments or sand-like debris, the latter particularly evident for RBC. These features of the the high-strain rate compressive behavior of concrete were observed in different studies [6, 179].



Figure 4.6 Typical failure modes of NAC, RAC and RBC specimens with different  $r$  after SHPB tests.

## 4.6 Discussions

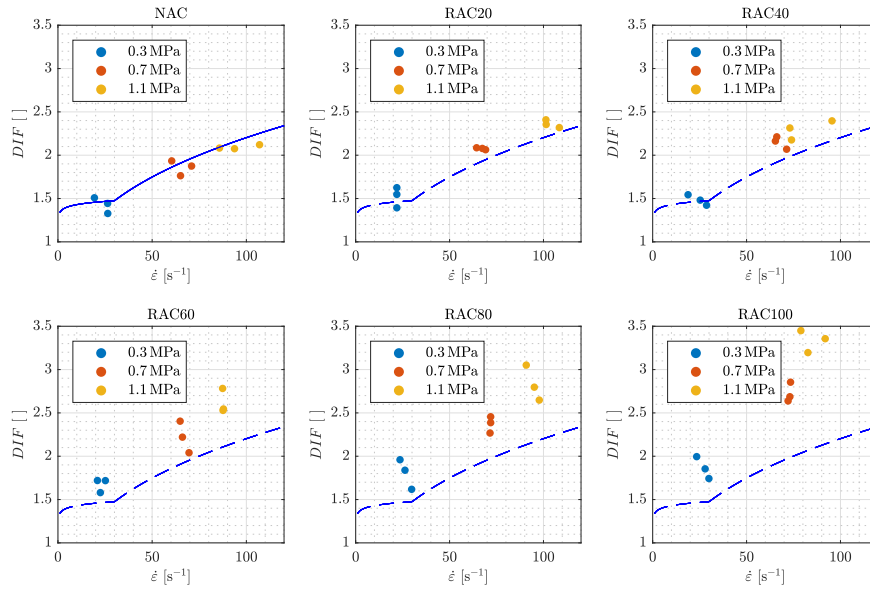
### 4.6.1 Dynamic increase factor

Figure 4.7 shows the *DIF* as a function of strain rate for NAC, RAC and RBC. As indicated in Figure 4.7, each *DIF* of the tests is indicated as asterisk and different air pressures are indicated by different color. The blue solid and dashed line represent the trend of *DIF* for NAC by CEB-FIP code [5] under different strain rates, see Eq. 2.5. A great agreement can be found for the measured *DIF* of NAC with that one proposed in the CEB-FIP code. The *DIF* of all specimens is characterized by a marked increase with the strain rate. It is noted that the *DIF* at a strain rate of  $70s^{-1}$  reaches always values larges 2.

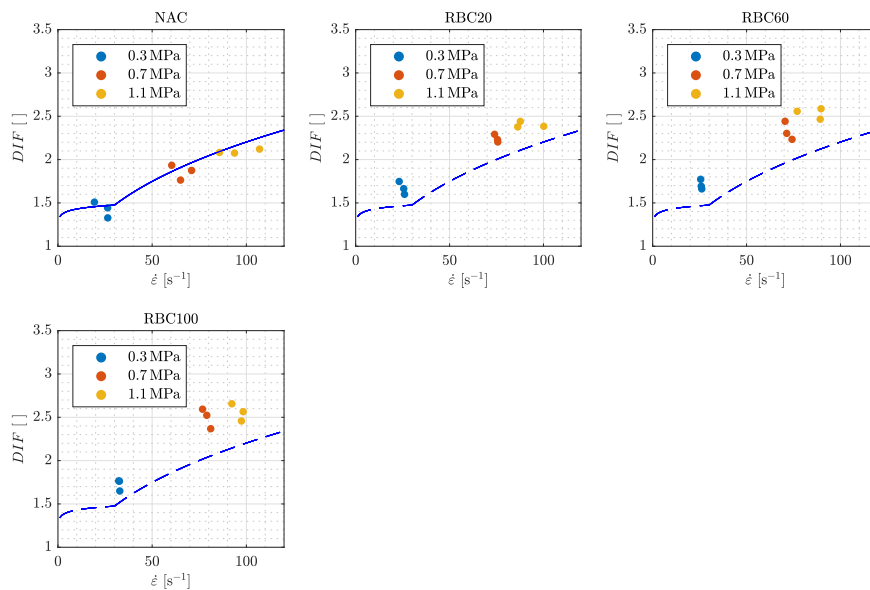
In both cases (RAC and RBC), with increasing  $r$ , the values of *DIF* increases under same air pressure. This is evident by comparing with the blue dashed lines showing the same reference values, valid for NAC. However, different *DIF* values are observed with increasing of  $r$  for RAC and RBC. For RAC, it is observed a slight increase of *DIF* with respect to NAC up to  $r = 60\%$ . Exceeded this value, *DIF* is rapidly increasing compared to NAC. For RAC100, the value of *DIF* is larger than 3 under 1.0MPa. This indicates a different strain rate sensitivity as a function of  $r$  as also observed by Guo et al. [8] (see Figure 2.5). On the other hand, for RBC, a *DIF* increase is observed with increasing  $r$  indicating a strain rate sensitivity function of  $r$ . However, this *DIF* increase is less marked for high values of  $r$  compared with RAC.

The experimental evidence presented in this study are: (i) for both RAC and RBC, an increase of *DIF* is observed with  $r$ ; (ii) the increase of *DIF* with  $r$  is more marked for RAC and particularly marked for  $r > 60\%$ ; (iii) the increase of *DIF* with  $r$  measured in this study is similar to what observed by Guo et al. [8] while independence was observed by Xiao et al. [6] and quite different values for Lu et al. [276] (see Figures 2.5 and 4.8); (iv) the increase of *DIF* with  $r$  is less marked for RBC and negligible for  $r > 60\%$ .

The possible explanation of dynamic increase properties when  $r$  increases is probably related to the differences in the ITZs. When the coarse aggregate is substituted with a recycled one, three ITZs [277]: (i) old natural aggregate with cement paste; (ii) RCA with original cement paste; (iii) new natural aggregate with new cement paste. The cement mortar remains at the ITZ of RCA forming the weak



(a)



(b)

Figure 4.7  $DIF$  as a function of the strain rate,  $\dot{\epsilon}$ , for the different tests: RAC (a) and RBC (b). The blue continuous and dashed lines indicate the CEB-FIP Model Code specification recommendation formula [5], see Eq. 2.5.



Table 4.5 Comparison of the parent concrete mix design among this study, Guo et al. [8] and Xiao et al. [6].

	<i>C</i>	<i>W</i>	<i>W/C</i>	<i>FA</i>	<i>CA</i>	Bulk density of RCA	Apparent density of RCA	Diameter of RCA	Type of cement	$f_c(r=0\%, \dot{\epsilon} \rightarrow 0s^{-1})$
	kg/m <sup>3</sup>	kg/m <sup>3</sup>	-	kg/m <sup>3</sup>	kg/m <sup>3</sup>	kg/m <sup>3</sup>	kg/m <sup>3</sup>	mm	-	MPa
This study	467	210	0.45	582	1082	1290	-	5-12.5	42.5	31.5
Guo et al. [8]	578	231	0.4	559	952	-	2656	5-10	42.5	43.3
Xiao et al. [6]	467	210	0.45	574	1082	1195	2620	5.12.5	42.5R	36.0

link which is composed of many minute pores and cracks, and they critically affect the ultimate strength of RAC [277]. Under static conditions, cracks are generated at these weak links and have the time to propagate inducing early failure of the specimen (observed strength reduction). The dynamic increase properties (i.e., *DIF* increase) are probably related to two main reasons: under high strain rates, (i) the cracks have no sufficient time to propagate in the specimen differently from the quasi-static case; (ii) cement mortar at ITZ of RCA is failing dissipating energy thus reducing the global damage. The latter is confirmed by looking at the typical failure modes of NAC and RAC specimens with different *r* after SHPB tests (Figure 4.6). In fact, this relative increase (in terms of *DIF*) is more evident by increasing *r*, i.e., by enhancing the cement mortar at the ITZ of RCA. This is also confirmed because the difference in terms of *DIF* given *r* is larger for high strain rates. The combination of these two effects is producing a beneficial effect in terms of *DIF*.

The observed differences in the *DIF* among the results reported herein, of Guo et al. [8] and Xiao et al. [6] are potentially related to the different characteristics of the parent concrete used to produce the RCA. In fact, the mix designs of this study, Guo et al. [8] and Xiao et al. [6] are quite similar, see Table 4.5. Unfortunately, Guo et al. [8] and Xiao et al. [6] are not providing specific information on the parent concrete employed (e.g., photos, original mix design, etc.) making impossible any comparison.

For RBC, the observed increase of *DIF* with increasing *r* is less marked and no comparison with previous studies is available. Only some previous experimental tests on bricks [180–182] are indicating that bricks are slightly strain rate dependent. A possible explanation of the reduced dynamic increase properties can be attributed to the minor strength properties of BA compared with RCA. The reduced strength of BA makes the weak link of RBC to be the substituted aggregate. The low strain rate dependency of the bricks makes the global behavior less sensitive to the strain rate.

### 4.6.2 Predictive equations for RAC

In the following, empirical predictive equations for  $DIF$  as a function of the strain rate,  $\dot{\epsilon}$ , and substitution level,  $r$ , are proposed. In particular, the data were fitted using a  $DIF$  linear (in the semi-logarithmic plan) predictive equation:

$$DIF(r, \dot{\epsilon}) = a(r) + b(r) \cdot \log(\dot{\epsilon}) \quad (4.10)$$

where the values of  $a$  and  $b$  are the coefficients. This equation is the same employed by Xiao et al. [6] and reported in Section 2.2. For RAC, data coming from the literature (see Section 2.2) is also employed in the fitting.

Test results presented herein are compared with previous studies [6, 8] and CEB-FIP Model Code [5] in Figure 4.8. Test results of Lu et al. [7] are not reported because very different from this study and Xiao et al. [6], Guo et al. [8], see Figure 2.5. The experimental data from Xiao et al. [6] are shown as cross points, data from Guo et al. [8] are shown as empty circles and experimental results from this study are shown as full circles. Different colors indicate different substitution levels, namely 0%, 20% - 30%, 40% - 60%, 70% - 80% and 100% (the different ranges are chosen to contains the data coming from the different studies). For  $r = 0\%$ , all the studies are in good agreement with CEB-FIP Model Code formula and exhibit similar values. However, for  $r > 0\%$ , the comparison of the data presented herein and by [6, 8] shows some differences. In particular, data from this study and from Guo et al. [8] are generally higher than CEB-FIP code for  $r > 0\%$ . On the other hand, data from Xiao et al. [6] are different and more similar to CEB-FIP Model Code for  $r > 0\%$  indicating independence of the  $DIF$  with respect to  $r$ .

Figure 4.9 illustrates the fitted predictive equations of  $DIF$  as a function of  $\dot{\epsilon}$  for different values of  $r$  for RAC. The fitting of Eq. 4.10 was performed for the following three cases: (i) only using data from this study (continuous thick lines); (ii) data of this study and from Guo et al. [8] (dashed thick lines); (iii) only from Xiao et al. [6] (dotted thin lines). The values of  $a$  and  $b$  of Eq. 4.10 for different  $r$  are listed in Table 4.6 for (i) and (ii).

It can be observed from Figure 4.9 that fitting lines of Xiao et al. [6] is nearly parallel to the CEB-FIP code with values almost independent on  $r$ , confirming results reported in Figure 4.8. Conversely, fitting lines of this study and Guo et al. [8] are steeper than CEB-FIP for  $r > 0\%$  and with increasing values increasing  $r$ . Finally, it

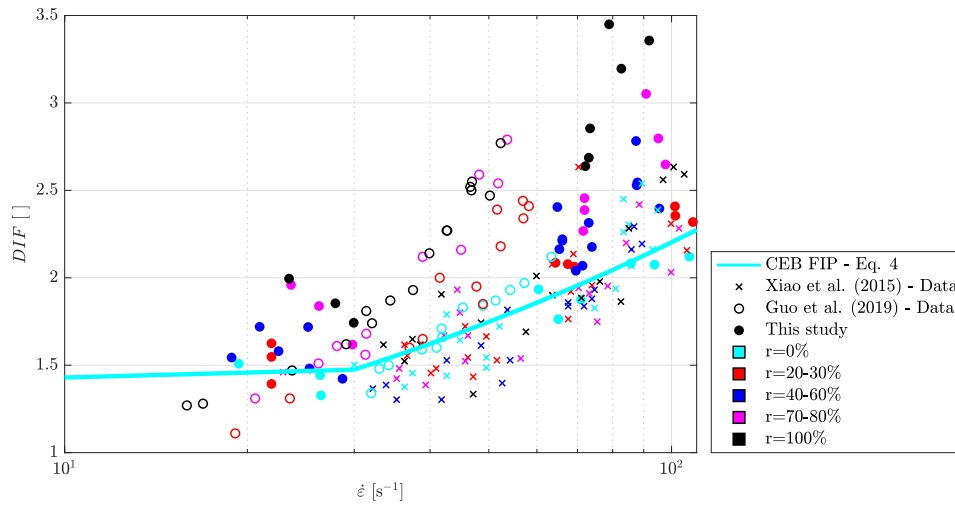


Figure 4.8 Comparison of experimental points of  $DIF$  as a function of  $\dot{\epsilon}$  for different values of  $r$ . Data taken from: CEB-FIP Model Code formula [5] (cyan thick continuous line), Xiao et al. [6] (cross points), Guo et al. [8] (hollow circles) and this study (full circles). Note that the colors inside the squares in the legend are indicating the substitution level of aggregate,  $r$ , associated to the different lines and markers in the figure.

Table 4.6 Coefficients  $a$  and  $b$  in Eq. 4.10 fitted using the experimental data for RAC of this study and this study and Guo et al. [8]. The fitted lines are shown in Figure 4.9.

$r$	$a$	$b$
0%	1.4	0.1
20-30%	1.4	0.1
40-60%	1.4	0.1
70-80%	1.4	0.1
100%	1.4	0.1

can be observed that fitting lines of this study are less inclined than this study and Guo et al. [8] with increasing  $r$ , although this difference is less remarkable.

It can be observed in Table 4.6 that  $a$  decreases with increasing  $r$  while  $b$  increases. The increase of  $b$  indicates that the fitting lines become more inclined ( $b$  is the slope of the curve in the logarithmic plane). The comparison of  $b$  between this study and this study and Guo et al. [8] confirms that fitting lines of this study are less inclined than this study and Guo et al. [8] with increasing  $r$ . However, it can be observed that values of  $a$  in this study are always lower than this study and Guo et al. [8] compensating for the different slope, see Figure 4.9.

### 4.6.3 Predictive equations for RBC

The experimental points for RBC of this study are shown in Figure 4.10 together with the fitting lines (see Eq. 4.10). Also in this case, for  $r = 0\%$ , similar values are observed when comparing experimental points or fitting lines with the CEB-FIP.

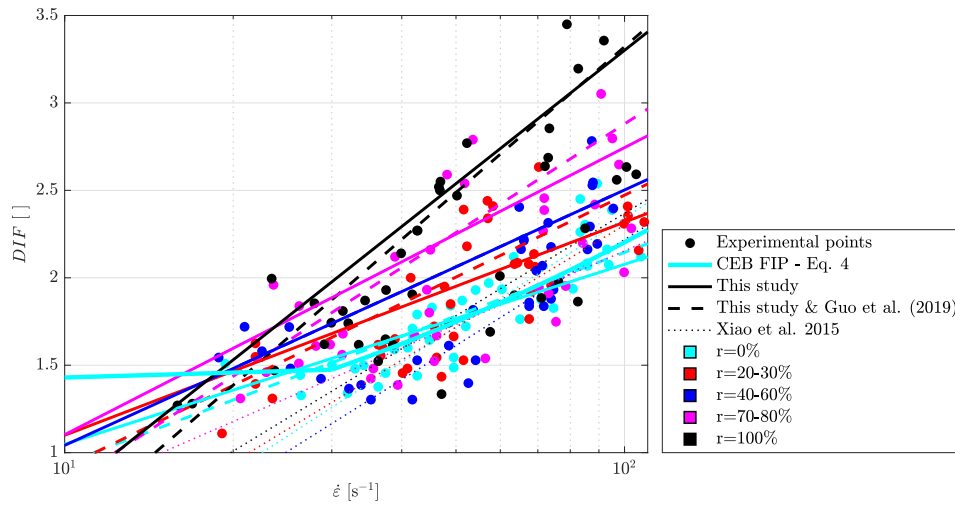


Figure 4.9 Fitted predictive equations of the  $DIF$  as a function of  $\dot{\epsilon}$  (see Eq. 4.10) for different values of  $r$  for RAC. The fitting is reported using different sets of experimental: this study (continuous thick lines), this study and Guo et al. [8] (dashed thick lines), and Xiao et al. [6] (dotted thin lines). The cyan thick continuous line is the CEB-FIP Model Code formula [5] valid for NAC. Note that the colors inside the squares in the legend are indicating the substitution level of aggregate,  $r$ , associated to the different lines and markers in the figure.

Table 4.7 Coefficients  $a$  and  $b$  in Eq. 4.10 fitted using the experimental data for RBC. The fitted lines are shown in Figure 4.10.

$r$	0%	20%	40%	60%	80%	100%
$a$	0.0100	0.0100	0.0100	0.0100	0.0100	0.0100
$b$	0.0100	0.0100	0.0100	0.0100	0.0100	0.0100

When  $r$  is increased, the experimental points or fitting lines becomes larger than CEB-FIP similar to what observed in RAC. This increase can be observed also looking at coefficients  $a$  and  $b$  in Table 4.7. However, comparing RAC (Table 4.6) with RBC (Table 4.7), it can be seen that given  $r$ ,  $b$  is always smaller for RAC than RCB indicating a less marked dependency of  $a$  and  $b$  with respect to  $r$ . Similar considerations applies to  $a$ .

## 4.7 Conclusions

Different experimental studies carried out using SHPB show the strain rate dependency of the dynamic strength of the concrete made with different levels of substitution and types of coarse aggregate. The experimental results available in the literature only refer to recycle aggregate concrete and are rather controversial,

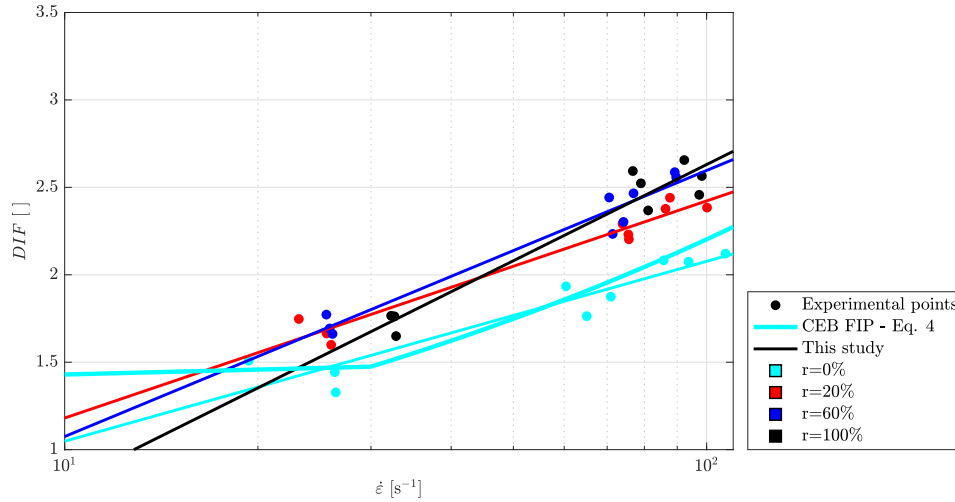


Figure 4.10 Fitted predictive equations of the  $DIF$  as a function of  $\dot{\epsilon}$  (see Eq. 4.10) for different values of  $r$  for RBC. The continuous thick lines are the fitting according to Eq. 4.10. The cyan thick continuous line is the CEB-FIP Model Code formula [5] valid for NAC. Note that the colors inside the squares in the legend are indicating the substitution level of aggregate,  $r$ , associated to the different lines and markers in the figure.

without general agreement about the exact effect of the levels of substitution and types of coarse aggregate on the strength under high strain rate.

In this study, the high-strain rate compressive behavior of concrete made with different levels of substitution and types of coarse aggregate was investigated. Two different types of concrete with different substituted coarse aggregate are studied, namely RAC and RBC. To this end, the compressive behavior was investigated performing standard quasi-static tests and SHPB tests with large bar diameter of 155 mm.

Results from the static tests confirmed the well-known behavior of RAC and RBC concrete. An increase in the levels of substitution leads to a strength decrease. The observed values are comparable with previous findings available in the literature. The strength loss is more marked for RBC rather than RAC. This difference is associated with the minor mechanical performances of the BA compared with RCA.

The results from the SHPB tests indicate that, for both RAC and RBC, an increase of dynamic increase factor,  $DIF$ , is observed with the coarse aggregate level of substitution,  $r$ . The increase of  $DIF$  with  $r$  is more marked for RAC and particularly marked for  $r > 60\%$ . The increase of  $DIF$  with  $r$  is less marked for RBC and negligible for  $r > 60\%$ . The different behavior is attributed to the cement

mortar remains at the ITZ of RCA forming the weak link when the coarse aggregate is substituted with a recycled one. In particular, for RCA, the *DIF* increase is related to two main reasons: (i) under high strain rates, the cracks have no sufficient time to propagate in the specimen differently from the quasi-static case; (ii) under high strain rate, cement mortar at ITZ of RCA is failing dissipating energy thus reducing the global damage. On the other hand, for RBC the reduced strain sensitivity is attributed to the minor strength properties of BA compared with RBC and to their low strain sensitivity. The minor strength properties of BA makes them the weak link of RBC. Using the data of this study and from the literature, data-driven predictive equations were proposed for the compressive strength *DIF*.

Finally, it is noteworthy that for RAC the increase of *DIF* with  $r$  measured in this study is similar to what observed by Guo et al. [8] while independence was observed by Xiao et al. [6] and quite different values for Lu et al. [276]. These differences are potentially attributable to the different characteristics of the parent concrete although this cannot be verified because of the absence of this information in the respective papers.

# Chapter 5

## Quasi-static physical and mechanical properties of mortar with substituted recycled PET powder

### 5.1 Materials and methods

#### 5.1.1 Materials and specimens

The materials adopted in this study to cast mortars are: ordinary Portland cement type 52.5R; natural sand according to European Committee for Standardization CEN [278] with a density of  $2593.5\text{kg/m}^3$ ; tap water; super-plasticizer (SIKA Compactcrete 39T100) with a density of  $1100\text{kg/m}^3$ ; recycled PET powder with a bulk density of  $1370\text{kg/m}^3$ . The mortar specimens were prepared using dry natural sand and recycled PET powder to avoid an increase in the porosity due to the presence of free water released from plastic aggregate [109]. The polyethylene terephthalate (PET) powder, as shown in Figure 5.1, was formed by cleaning, shredding and milling recycled PET bottles. The aggregate is characterized by white color and high reflectance.



Figure 5.1 Recycled PET aggregate (a) and micro-photo (b)

There are many variables that can influence the fresh and hardened behavior of mortar which can be cited as the water/cement ratio ( $w/c$ ) and the aggregate properties as grading and shape [279]. Moreover, grading properties influence the durability of the material as an effect of the different porosity. The micro-photo (Figure 5.1b) clearly shows that the morphology of the PET aggregates is characterized by low sphericity and is very angular.

Particle size distribution of natural sand and recycled PET powder was obtained by mechanical sieving, according to European Standards [280]. The particle size distribution of natural sand and recycled PET powder is reported in Figure 5.2. For both aggregates, continuous grading is observed. Both aggregates are classified as fine aggregates since the main sieve size results lower than 4 mm. The particle size distribution of natural sand and recycled PET are quite similar. In particular, they have a grain size  $< 2$  mm and more than around 70% of the sample passes through 1 mm mesh. The similar particle size distributions of the two aggregates guarantee their interchangeability without changing the packing particles or in other words the mortar skeleton.

Different amounts (0–30% by volume) of recycled PET powder were substituted by the same volume of the sand, to obtain five mortars with different compositions. The mix proportions of five mortars with different compositions are summarized in Table 5.1. All the mixes have  $W/C$  equal to 0.42, fine aggregate to cement ratio equal to 3, and super-plasticizer to cement ratio (by weight) equal to 1%. The natural sand (fine aggregate) was systemically substituted with PET aggregates at 0, 5, 10,



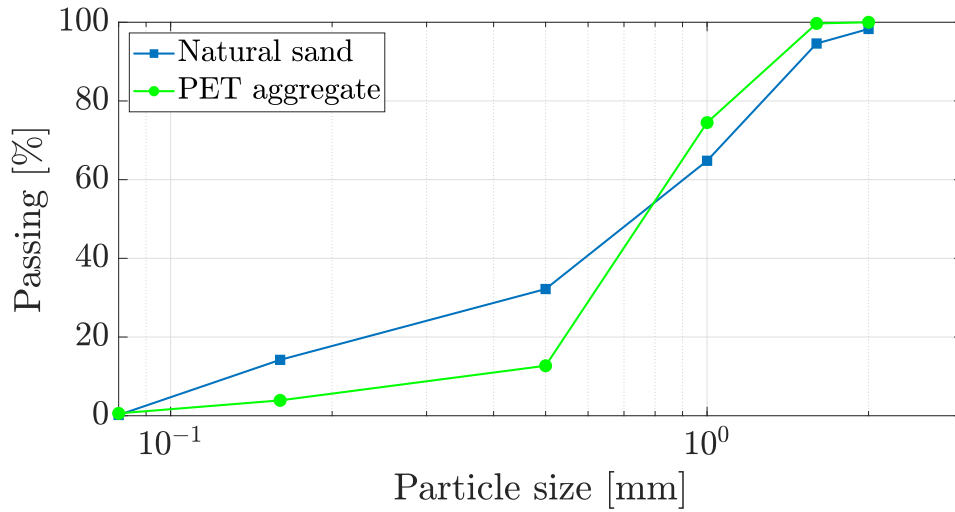


Figure 5.2 Particle size distribution of natural sand and recycled PET powder

Table 5.1 Mix proportion of the different mortars

Type	r	Water	Cement	Water-cement ratio	Natural sand	Super-plasticizer	Recycled PET powder
[-]	[%]	[g]	[g]	[-]	[g]	[g]	[g]
NAM	0				1350		0
PETM5	5				1282.5		35.66
PETM10	10	189	450	0.42	1215	4.5	71.31
PETM20	20				1080		142.63
PETM30	30				945		213.94

20, and 30% by volume. Each mix is defined by the mix proportions of the reference mortar (NAM) and by the volume substitution ratio defined as:

$$r = \frac{V_{PET}}{V_{NS}} \quad (5.1)$$

where  $V_{PET}$  is the volume of substituted recycled PET powder and  $V_{NS}$  is the volume of natural sand of the reference mix (NAM in Table 5.1). It is noteworthy that the density of natural sand ( $2593.5 \text{ kg/m}^3$ ) and recycled PET powder ( $1370 \text{ kg/m}^3$ ) are not the same, therefore the substituted mass in Table 5.1 is different. Designation of the specimen is given by the following ID tag, PETM#, where the numeric value is representing  $r$  expressed in percentage.

The different components of the mortar were accurately weighed, mixed, and dry-homogenized. Mix order and time sequence are as follows: first, super-plasticizer was added into tap water, and this solution and cement were mixed for 30s under low speed; then, natural sand and recycled PET powder were mixed and they were added

and mixed for another 30s; next the mixer was turned to high speed for 30s; after that, the cementitious paste was kept at rest inside the mixer for 90s; finally, the paste was mixed for another 60s with high speed. Completed the mixing phase, the mortar was compacted by means of a jolting apparatus in accordance with CEN [278] for 120s before pouring into molds. One part of the paste was adopted to perform the slump tests and to measure density. Nine  $40 \times 40 \times 160 \text{ mm}^3$  prisms were cast for each mortar type in steel molds. 24 hours after casting, specimens were demolded and stored in the water at a controlled temperature of  $21 \pm 1^\circ\text{C}$ .

## 5.2 Test program

### 5.2.1 Density

Before casting, the mass of the steel mold,  $m_1$ , was measured. The mass of molds and mortar paste just after casting (fresh state),  $m_f$ , and after 24 h,  $m_{24}$ , were recorded. Using these inputs, the fresh density,  $\rho_f$ , and density after 24 h,  $\rho_{24}$ , can be calculated as:

$$\rho_f = \frac{m_f - m_1}{V} \quad (5.2)$$

$$\rho_{24} = \frac{m_{24} - m_1}{V} \quad (5.3)$$

where  $V$  is the volume of one prism ( $40 \times 40 \times 160 = 2.56 \times 10^5 \text{ mm}^3$ ).

Before dry density tests, prisms were placed at a conditioned environment at  $20 \pm 2^\circ\text{C}$  and  $\text{RH } 50 \pm 5\%$ . During this process, drying and water loss continued and the mass were checked and recorded over time until the mass was constant. The density at laboratory condition,  $\rho_l$ , was determined.

For evaluating the dry density at 28 days, prism specimens were dried in the oven with  $100^\circ\text{C}$  for 72 hours (3 days) until the measured mass was constant and then the dry mass,  $M_d$ , and dry density,  $\rho_d$ , were determined. After this, the same prisms were completely immersed in the water for another 72 h at a controlled temperature of  $23 \pm 2^\circ\text{C}$ . After that, the specimens were removed from the water and the extra water on the surface was removed. Weight measurements were repeated with intervals of

24 h until an increase in mass of less than 0.5% of the previous value was observed. The latter value is used to define the saturated-dry mass,  $M_{sd}$ , and density,  $\rho_{sd}$ . The water absorption capacity,  $W_x$ , can be expressed as:

$$W_x = \frac{M_{sd} - M_d}{M_d} \quad (5.4)$$

where  $M_{sd} - M_d$  is the mass of the water absorbed.

### 5.2.2 Slump

The slump is obtained according to JGJ/T 341 [281] by employing a metal cylindrical mold with an internal diameter of 77 mm and a height of 80 mm. The mold is placed on a hard non-absorbent surface. The mortar paste was poured into the cylinder at 1/3 height, then a  $\Phi 8$  mm round steel bar was inserted in the paste to compact. This procedure is repeated again until the end-top was smooth. The mold was carefully lifted vertically upwards, so as not to disturb the mortar. After 1 min of spreading, the slump was recorded [282]. The slump is measured by measuring the distance from the top of the slumped mortar to the level of the top of the mold. Three repetitions were performed.

### 5.2.3 Ultrasonic Pulse Velocity tests

The Ultrasonic Pulse Velocity (UPV) determines the quality of concrete as a non-destructive assessment by a pulse of the ultrasonic wave, which passes through the concrete [283]. UPV can be used to determine the homogeneity, presence of cracks or voids in structures and cement-based materials [e.g., 108, 13]. It measures the velocity of an ultrasonic pulse passing through a concrete structure. The pulse velocity of each specimen,  $V$ , was calculated using the following equation:

$$V = \frac{d}{t} \quad (5.5)$$

where  $d$  is the distance between two transducers, and  $t$  is transmission times. The values of UPV are influenced by the density and elastic properties of mortar and plastic aggregates. UPV tests were carried out based on ASTM 597 [284] at a curing

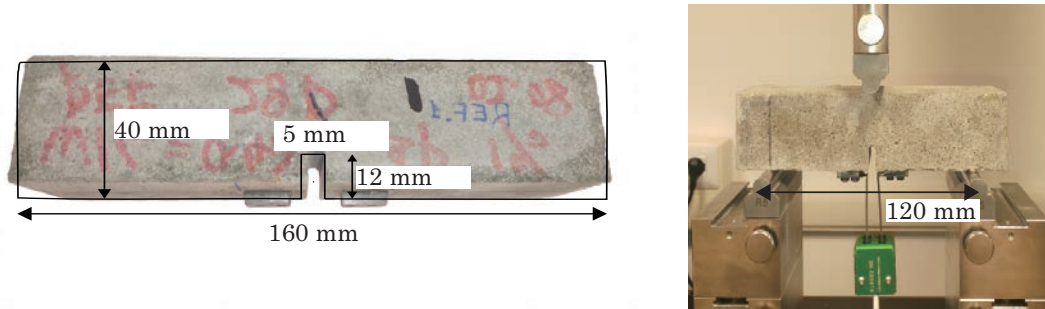


Figure 5.3 Notched specimen (left) and flexural test setup (right)

time of 28 days. In this study, the UPV tests are carried out on the prism specimens with a size of  $40 \times 40 \times 160$  mm before testing using a TICO<sup>®</sup> ultrasonic instrument.

### 5.2.4 Flexural tests

Flexural load-deflection curves and corresponding flexural properties were investigated for each type of mortar. Flexural tests were conducted on notched specimens according to JCI-S-001 [285]. Three of six prisms were tested at 7 days while the remaining three were tested at 28 days. A typical notched specimen is shown in Figure 5.3. The notch in the middle of the specimen (with length of 40 mm, width of 5 mm and depth of 12 mm) was made by using a brick sawing machine. The apparatus for the three-point bending tests on the notched specimens is a Zwick/Roell servo-hydraulic test machine (Figure 5.3), which is operated by a closed loop control system. Tests were performed under displacement control at a rate of 0.03 mm/min and with a support span of  $S = 120$  mm. One extensometer was attached at the middle of the notched surface symmetrically to measure the Crack Mouth Opening Deflection (*CMOD*). Load and deflection are continuously recorded during flexural tests.

Finally, the flexural strength is calculated as:

$$f_f = \frac{3 \cdot F_{\max} \cdot S}{2 \cdot b \cdot h^2} \quad (5.6)$$

where  $F_{\max}$  is the peak load,  $b = 40$  mm and  $h = 28$  mm are the base and height of the notched cross-section.



Figure 5.4 Photo of the compressive test apparatus and specimen

Table 5.2 Fresh density, density after 24h of the mortar, water absorption, and slump. The reported values are the average of three repetitions and the values inside brackets are the standard deviation

Property	Units	NAM	PETM5	PETM10	PETM20	PETM30
Fresh density (Eq. 5.2)	[kg/m <sup>3</sup> ]	2332	2230	2210	2103	2010
Density after 24 h (Eq. 5.3)	[kg/m <sup>3</sup> ]	2321 (10.6)	2217 (15.4)	2204 (11.8)	2098 (11.5)	2004 (10.0)
Density at laboratory condition	[kg/m <sup>3</sup> ]	2324 (6.1)	2221 (14.6)	2210 (9.3)	2078 (11.1)	1995 (10.8)
Dry density at 28 days	[kg/m <sup>3</sup> ]	2205 (5.9)	2103 (13.7)	2088 (9.8)	1963 (9.8)	1873 (9.8)
Saturated-surface dry density at 28 days	[kg/m <sup>3</sup> ]	2343 (6.3)	2238 (12.8)	2229 (9.3)	2106 (9.2)	2026 (9.7)
Water absorption (Eq. 5.4)	[%]	6.26 (0.002)	6.37 (0.061)	6.75 (0.052)	7.29 (0.064)	8.17 (0.045)
Slump	[mm]	23	15	12	10	6

### 5.2.5 Compressive tests

The halves of the prismatic specimens of the flexure test were used for the compression tests. These specimens were cut by using a brick sawing machine into  $40 \times 40 \times 40 \text{ mm}^3$  cubes, using a proper frame to ensure a loading surface equal to  $40 \times 40 \text{ mm}^2$ , according to CEN [278]. Figure 5.4 shows the servo-controlled compressive test machine. Tests were carried out under force control at a constant loading rate of  $0.5 \text{ MPa/s}$  using a universal testing machine. Three specimens were tested at 7 days while the other three were tested at 28 days, similar to flexural tests.

## 5.3 Experimental results

### 5.3.1 Density and slump

The fresh density, density after 24h, water absorption, and slump of the mortar are shown in Table 5.2.

The fresh density and density after 24h of mortars are decreasing with increasing  $r$  as the effect of the light density of PET aggregate (see Sect. 5.1.1). The fresh density loss ratios are 4%, 5%, 10% and 14% for  $r$  in the range 5% to 30%. This is roughly consistent with the ratios of mass densities of sand and PET aggregate which is around 2 (see Section 5.1.1). The same fresh density loss ratio range can be found in several studies [10, 97, 12] although larger ratios were observed when different sizes and types of plastic aggregate are employed [11, 104, 110].

The results of the slump are significantly influenced by  $r$ . Higher values of  $r$  correspond to smaller slumps. A possible explanation for these results may be related to the greater water absorption capacity of PET aggregate compared with that of fine aggregate implying that the water in the cement matrix is reduced and therefore the consistency of fresh mortar is increased. Similar results can be found in Reddy and Gupta [286] and Ghasemi et al. [287]. These studies found that fine plastic aggregates in mortars shows better water retentivity compared to natural sand and a reduction of the slump increasing  $r$ . Differently, studies adopting larger plastic aggregates found an opposite flowability behavior. For instance, Safi et al. [11] used PET recycled as aggregated with a particle size of 1 – 5 mm and found an evident increase of slump. Hannawi and Prince-Agbodjan [104] substituted fine aggregate in the mortar matrix by PC granules with a maximum diameter of 5 mm and also observed an increase in the slump. A similar increase can also be found in Rubio-de Hita et al. [110] with PC flakes.

Results shown in this section have highlighted two pivotal aspects linked to the increase of  $r$ : a decrease in density and an increase in consistency. This paves the way for the design of a lightweight mortar with substituted recycled PET powder to be used in the field of 3D concrete printing. This interesting topic, which combines cutting-edge construction technologies with plastic recycling, will be presented and discussed in a forthcoming study.

### 5.3.2 Ultrasonic Pulse velocity (UPV)

Figure 5.5 shows  $V$  (Eq. 5.5) vs.  $r$ . The results show a linear decrease in UPV values with  $r$  which can be described by the following empirical equation:

$$V = -32.6 \cdot r + 4672 \quad R^2 = 0.99 \quad (5.7)$$

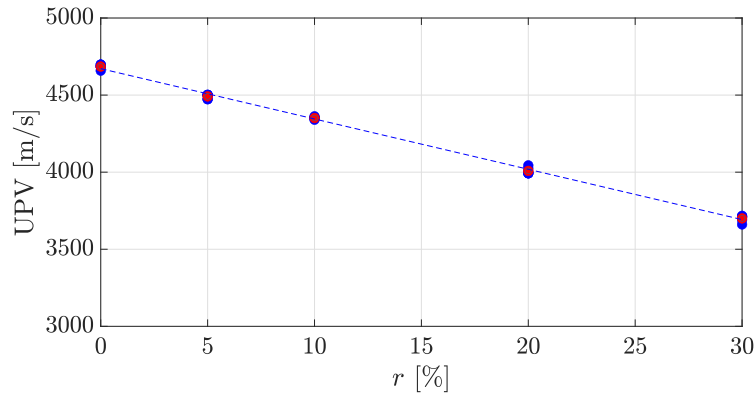


Figure 5.5 Relationship between UPV and  $r$

where  $r$  is expressed in percentage as in Figure 5.5. The reason for the observed reduction in the ultrasonic pulse velocity is ascribed to the reduction of the impedance (i.e.,  $\sqrt{E/\rho}$ ) and to the increase in the porosity of mortar [13]. The pores produced by PET powder affect the UPV by increasing the acoustic impedance. When the incident wave passes through different materials (mortar paste, PET powder, pores), it is partially reflected and only a part is transmitted, which leads to a decrease in its speed [108]. According to IS 13311-1 [288], mortar can be considered as very good to excellent having good homogeneity when  $V \geq 4000$  m/s. Hence, mortars with  $r = 0$  to 20% are falling in this class. Mortars with  $r = 30\%$  can be classified as good to very good with slight porosity mortar according to IS 13311-1 [288].

### 5.3.3 Flexural behavior

The flexural load vs CMOD curves are depicted in Figure 5.6 for the different  $r$  and for two curing times, namely, 7 (Figure 5.6a) and 28 days (Figure 5.6b). The thin colored lines are the results of every single test and the thick black line is the average across CMOD.

Generally, regardless of the substitution level, the peak force (i.e., greater flexural capacity) is higher at 28 days compared with the 7 days. Overall, the flexural load vs. CMOD relationships are characterized by the same behavior. After an initial almost vertical portion lasting up to about 50 – 70% of the peak flexural load, the curve becomes non-linear. This confirms observations by Hannawi et al. [14] setting the crack initiation occurrence at around 60% of the ultimate load. The first part indicates nearly zero CMOD, thus no crack opening at the notched cross-section. The second

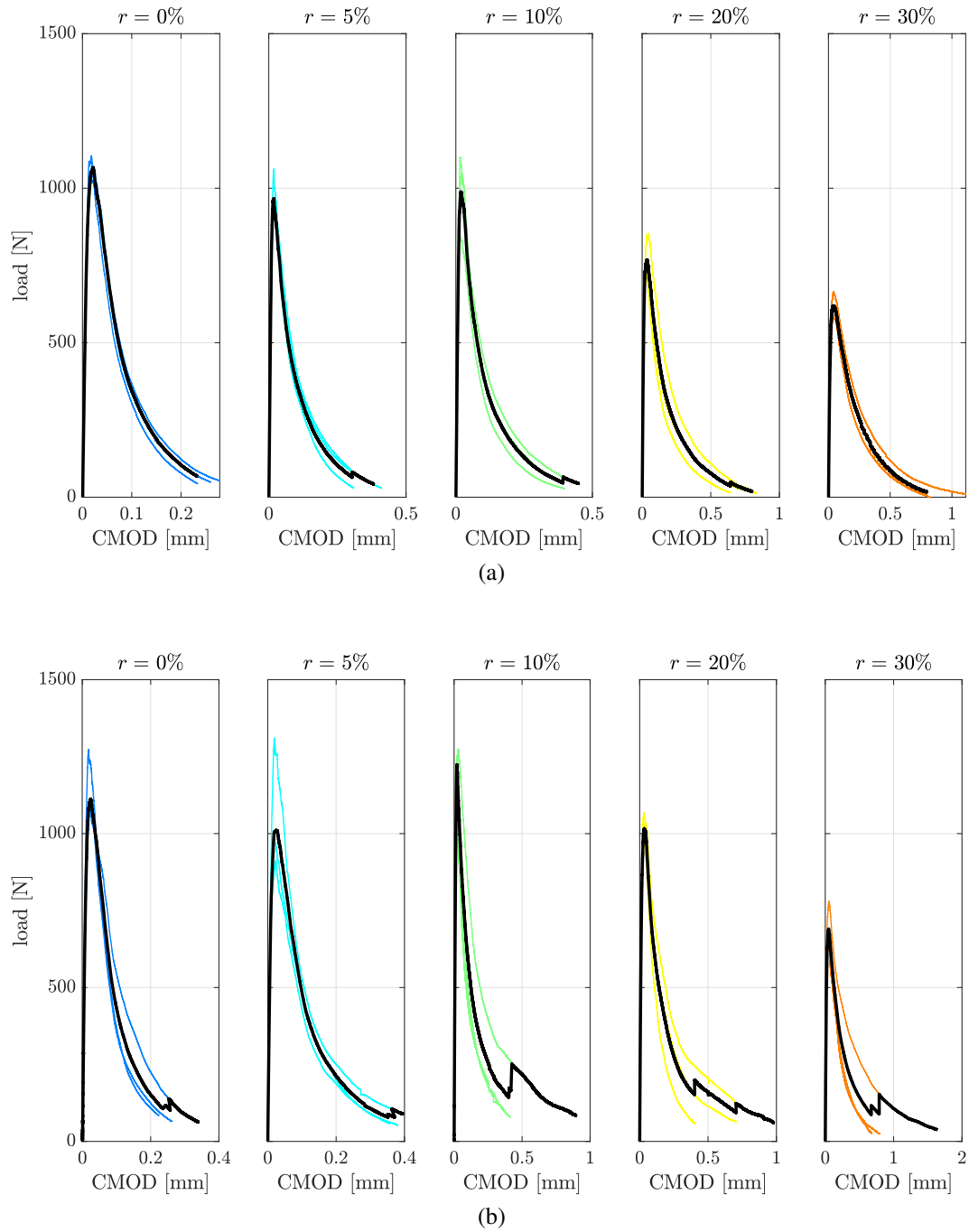


Figure 5.6 Flexural load vs CMOD curves at 7 days (a) and 28 days (b). Note that x axis has different scale



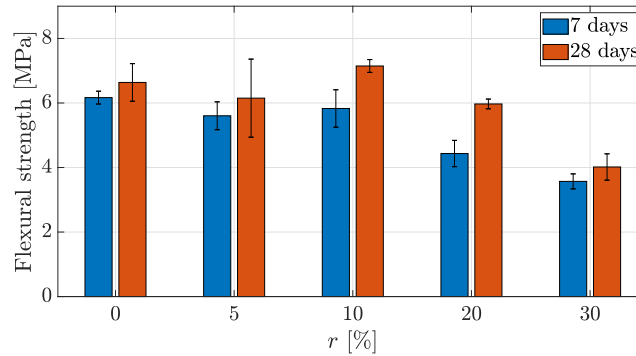


Figure 5.7 Average flexural strength at 7 and 28 days calculated using Eq. 5.6. The standard deviation values are shown with error bars

part is characterized by the evolution of the crack on the notched cross-section. The increase of  $r$  has two different effects on the flexural strength (peak values in Figure 5.6) and post-peak behavior.

The average flexural strength at 7 days and 28 days was calculated using Eq. 5.6 and is summarized in Figure 5.7 for the different values of  $r$ . The PET aggregate has two different and opposite effects on flexural strength. First, the PET aggregate is less performing compared with the natural aggregate in terms of stiffness and Interfacial Transition Zone (ITZ) [125] reducing the tensile strength. Secondly, the elongated shape of the PET aggregates (Figure 5.1b) bridges cracks and prevents the brittle failure of the specimen [20] improving the tensile strength. For the adopted PET aggregates, the first effect is dominant while for recycled PET fibers the second effect dominates [e.g., 289]. Accordingly, for  $r = 10$  and 20%, the influence of  $r$  is generally positive or at least negligible indicating the bridging effect is dominating on the fracture interface (see Figure 5.8). For  $r = 20$  and 30%, the influence of  $r$  on the flexural strength is generally negative indicating that the first effect dominates. For both 7 and 28 days, the final strength loss at  $r = 30\%$  is around 40% compared with reference mortar (6.5 MPa for 7 days and 6.8 MPa for 28 days respectively). However, it can be observed that for  $r = 10\%$ , the flexural strength increase significantly for 28 days compared with reference mortar, the strength increase ratio is near 10%. Similar results can be found in previous studies [10, 112, 108, 12].

The post-peak behavior is highly enhanced in terms of deformation capacity by the addition of PET aggregates (Figure 5.6). Higher substitution levels of PET aggregate substantially improve the ductility of mortar. The flexural load-CMOD

curves can be explained by the ability of PET aggregates to prolong crack propagation interval [10].

Typical failure modes (lateral view, split specimen, crack surface, and micro-photo of crack surface) for flexural tests at 28 days with different  $r$  are presented in Figure 5.8. Only one specimen is shown as representative of the failure mode since similar conditions were observed in the remaining ones.

Generally, the observed final failure modes are similar. In all specimens, only one main crack is observed. Figure 5.8 shows that the PET aggregates at the crack interface were generally pulled out without failure, especially for  $r = 20$  and 30%. The latter observation confirms previous observations on flexural strength and post-peak behavior for different values of  $r$ .

When  $r = 0\%$ , the relatively dense cement matrix and natural sand with smooth surface can be found, resulting in higher strength (Figure 5.6) and lower water absorption capacity (Table 5.2). While with increasing  $r$ , the increased porosity can be observed from corresponding micro-photos, consistently with the physical properties like density, water absorption capacity, and UPV test results. Finally, Figure 5.8 confirms that PET aggregates have a smooth surface characterizing a generally poor interfacial bond between cement matrix and PET aggregates [125]. Moreover, it can be observed the bridging effect of PET aggregates at the interface corroborating the discussion reported in Section 5.3.3. Finally, micro-photos of crack surface indicate that increasing  $r$  induced an increase in the observed porosity.

### 5.3.4 Compressive strength

Figure 5.9 shows average compressive strength at 7 and 28 days for the different values of  $r$ . Regardless  $r$ , the compressive strength is increasing with curing time as the effect of the hydration reaction. For  $r = 10$  and 20%, the increase of strength from 7 to 28 days is more marked. The compressive strength decreases with increasing  $r$ . For the compression case, no increase is observed indicating the ineffectiveness of the bridging action under compression loads. In fact, the shape of PET aggregates is not sufficient to guarantee a behavior similar to fiber-reinforced cementitious materials, differently from what was observed in the flexural case (Section 5.3.3). This provides additional confirmation of previous studies indicating that the negative effect of PET aggregate on compressive strength is caused by the low adhesion effect between the

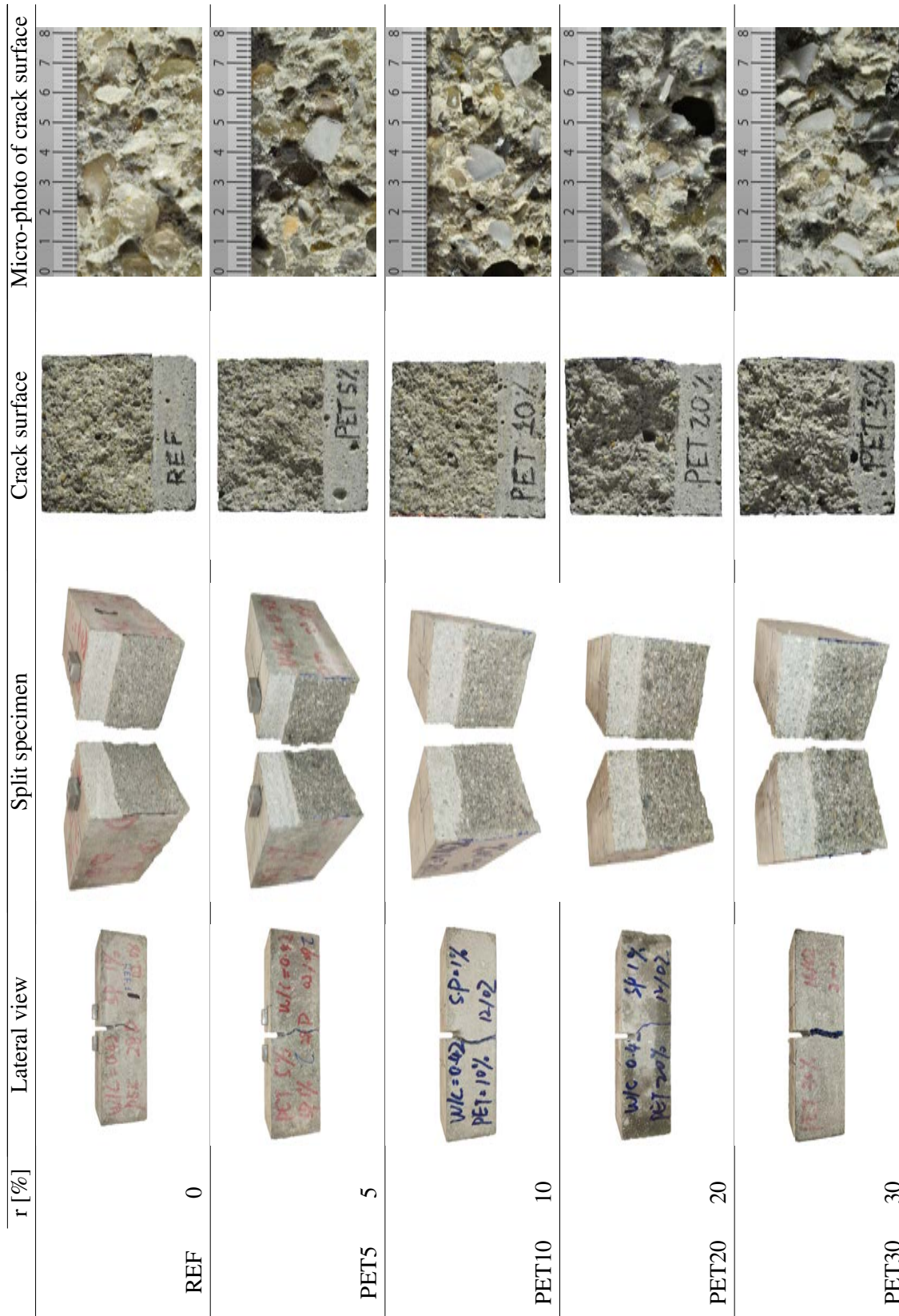


Figure 5.8 Typical failure modes (lateral view, split specimen, crack surface, and micro-photo of crack surface) for flexural tests at 28 days with different  $r$

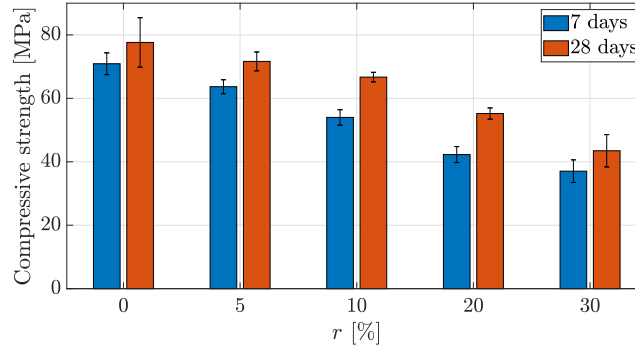


Figure 5.9 Average compressive strength at 7 and 28 days. The standard deviation values are shown with error bars

PET aggregate and cement paste [108], together with the increase in the observed porosity (Figure 5.8). In particular, for  $r = 30\%$ , the strength reduction ratio is around 45% both for 7 and 28 days. For  $r = 10\%$  and  $20\%$ , the strength reduction ratio presents differences for different curing times.

## 5.4 Discussion

### 5.4.1 Fracture energy

The fracture energy can be derived as follows [290]:

$$G_F = \frac{W_0 + W_1}{A_{lig}} \quad (5.8)$$

where  $W_0$  is the area below load vs. CMOD curves (Figure 5.7) up to failure ( $\text{J/m}^2$ );  $A_{lig}$  is the area of broken ligament, and  $W_1$  is additional work performed by gravity:

$$W_1 = \left(\frac{S}{L}m_1 + 2m_2\right) \cdot g \cdot CMOD_r \quad (5.9)$$

where  $m_1$  is the mass of specimen,  $m_2$  is the mass of jig not attached to testing machine but placed on specimen until rupture,  $S = 120\text{mm}$  is the length of load span,  $L = 160\text{mm}$  is the length of specimen,  $g = 9.8\text{m/s}^2$  is the acceleration of the gravity, and  $CMOD_r$  is the crack mouth opening displacement at the time of rupture. The calculated average fracture energy with different  $r$  under 28 days is plotted in Figure 5.10. Generally,  $G_F$  increases non-linearly with the increase of  $r$  and is higher

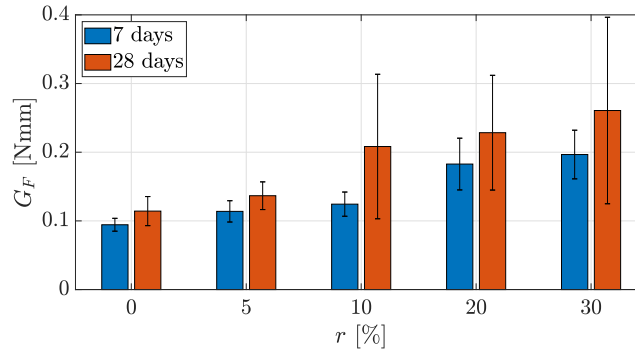


Figure 5.10 Fracture energy of mortar with different  $r$  at 7 and 28 days

at 28 days if compared with 7 days. For  $r = 30\%$ , the average fracture energy at 28 days is about 0.25 Nmm, which is two times the fracture energy of reference mortar ( $r = 0\%$ ). A discontinuity in the growth is found at  $r = 10\%$  for 28 days which shows that the mortar behavior is reasonably dominated by natural aggregate below the transition point and above it by the PET aggregate. This discontinuity is less marked at 7 days.

### 5.4.2 Critical stress intensity factor

Fracture toughness is a fundamental material's property, indicating the strain energy-absorbing ability of materials prior to fracture. Fracture toughness is considered as significant property for brittle or quasi-brittle materials. For brittle materials, the fracture toughness,  $K_{IC}$  can be expressed as:

$$K_{IC} = \sigma \sqrt{\pi a} \quad (5.10)$$

where  $\sigma$  is the applied stress at the tip of the crack and  $a$  the crack length. For quasi-brittle material like mortar, Eq. 5.10 is not valid [291] and the flexural fracture toughness, also known as critical stress intensity factor  $K_{IC}$ , can be calculated as [292]:

$$K_{IC} = Y f_f \sqrt{a} \quad (5.11)$$

where  $f_f$  is the flexural strength (Eq. 5.6),  $a \cong 12$  mm is the crack length, and  $Y$  is a geometrical factor defined as:

Table 5.3 Critical stress intensity factor with different  $r$  at 7 and 28 days. In the table, the average of  $K_{IC}$  is followed by three numbers inside brackets corresponding to the first, second and third tests, respectively

Specimen type	$K_{IC}$ at 7 days	$K_{IC}$ at 28 days
[-]	[MPa√m]	[MPa√m]
REF	2.42 (2.49; 2.43; 2.34)	2.54 (2.40; 2.41; 2.80)
PET5	2.22 (2.15; 2.11; 2.39)	2.35 (2.18; 2.00; 2.88)
PET10	2.30 (2.06; 2.47; 2.35)	2.74 (2.65; 2.75; 2.80)
PET20	1.78 (1.67; 1.71; 1.96)	2.28 (2.34; 2.23; 2.27)
PET30	1.45 (1.38; 1.54; 1.44)	1.53 (1.42; 1.71; 1.47)

$$Y = \frac{1.99 - \alpha(1 - \alpha)(2.15 - 3.93\alpha + 2.7\alpha^2)}{(1 + 2\alpha)(1 - \alpha)^{3/2}} \quad (5.12)$$

where  $\alpha = 28 \text{ mm}/40 \text{ mm} = 0.7$  is the ratio of the notch height to the height of the notched cross-section. The adopted geometrical factor is  $Y = 4.66$ . The flexural toughness of all mixtures with different  $r$  is summarized in Table 5.3. The results show a notable decrease in  $K_{IC}$  increasing  $r$  with larger values found at 28 days in agreement with force vs. CMOD curves (Figure 5.6). A slight increase of  $K_{IC}$  was observed for  $r = 10\%$  at 28 days. The lower fracture toughness can be attributed to a poor bond between cement paste and the PET aggregate. At 28 days,  $r = 10\%$  is the threshold of prolonged crack propagation interval of cement paste and aggregate contributing to better mechanical behavior in flexural tests.

### 5.4.3 Data-driven predictive models

Symbolic regression is the task of identifying a mathematical expression that best fits a provided dataset of input and output values [293, 294]. Two data-driven predictive models for the strength compressive and flexural reduction factors are proposed based on symbolic regression techniques. The strength compressive and flexural reduction factors are defined as:

$$SRF = \frac{f(r)}{f(r = 0\%)} \quad (5.13)$$

Table 5.4 Summary of ranges of input variables (dataset) adopted in the symbolic regression. Additional details are reported in Table 2.3 and Section 5.1.1. \* of the reference mix, i.e., for  $r = 0\%$

Reference	Year	$r$ [%]	$W/C$ [ ]	$FA/C$ * [ ]
Hannawi et al. [10]	2010	0-50	0.5	3
Safi et al. [11]	2013	0-50	0.42	2.07
Kaur and Pavia [12]	2020	0-20	0.5	3
Hacini et al. [13]	2021	0-60	0.5	3
This study	2022	0-30	0.42	3

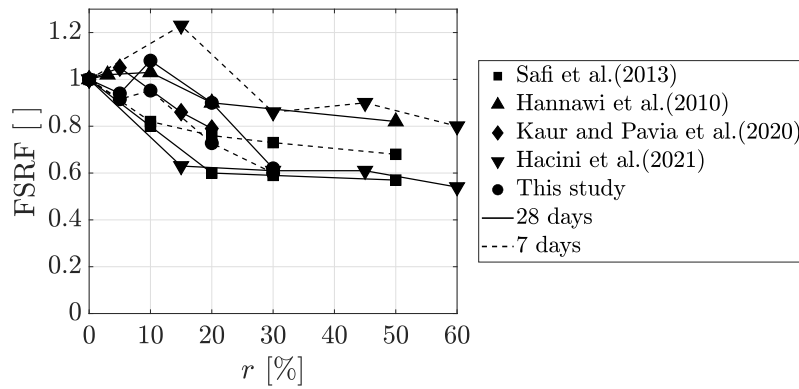
where  $f(r)$  is an index (flexural or compressive strength) for a given value of  $r$  and  $f(r = 0\%)$  is the same index for the reference mix design. In the following,  $FSRF$  refers to the flexural strength reduction ratio (Figure 5.7) while  $CSRF$  refers compressive strength reduction ratio (Figure 5.9).

Figure 5.11 shows  $FSRF$  and  $CSRF$  as a function of  $r$  at 7 and 28 days of mortar containing substituted PET aggregates from this study and literature [10–13] whose additional details are reported in Table 2.3. In Figure 5.11, different colors indicate different studies, and solid lines represent 28 days and dotted lines 7 days. All the studies confirmed experimental observation reported in this study, i.e.,  $FSRF$  and  $CSRF$  decreased with  $r$ . It should be noted that for  $FSRF$  at 7 days reported by Hacini et al. [13], a relatively large increase of  $FSRF$  is observed. A reasonable explanation for this can be that Hacini et al. [13] adopted PET strapping bands with widths between 9 and 19 mm and thicknesses between 0.5 and 1.1 mm, which induces a strong bridge effect when the specimen is bent.

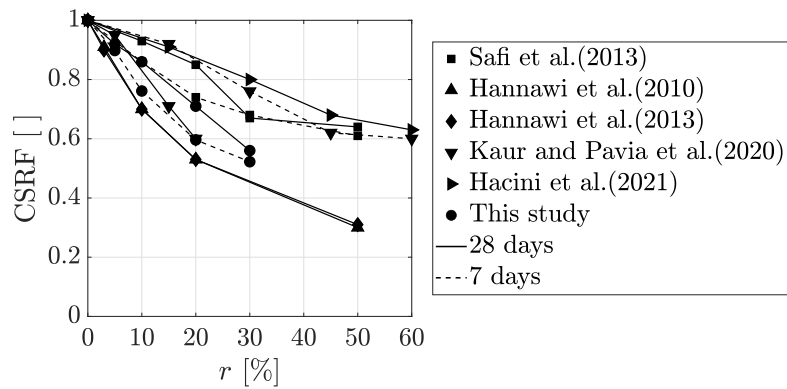
The model inputs adopted are: water to cement ratio ( $W/C$ ), fine aggregate to cement ratio ( $FA/C$ ) and substitution level ( $r$ ). Table 5.4 summarize the database characteristics.

HeuristicLab [295] was used for symbolic regression using genetic programming. The set of function symbols was  $\{+, -, \cdot, /, \exp(), \log(), \text{square}(), \text{sqrt}()\}$ . Numeric constants, as well as variables from the dataset, were allowed as terminal symbols. The presented models were obtained after 50 generations and with a population of 2000 with a mutation probability of 15%. Since the adopted approach is stochastic,





(a)



(b)

Figure 5.11 *FSRF* (a) and *CSRF* (b) as a function of  $r$  at 7 and 28 days of mortar containing substituted PET aggregates from this study and literature [10–13].



Table 5.5 Data-driven predictive models for *FSRF* and *CSRF* at 7 and 28 days

Output	Model	$R^2$	Curing time
<i>FSRF</i>	$(-0.51 - 0.29 \cdot r) \cdot (\frac{W}{C})^{-1} + 2.14$	0.69	7 days
	$0.21 \frac{FA}{C} - 0.14r + 0.41$	0.73	28 days
<i>CSRF</i>	$-0.66 \frac{FA}{C} \cdot r + 1.78 \frac{W}{C} + 0.22$	0.92	7 days
	$-0.71 \frac{FA}{C} \cdot r - 0.55 \frac{W}{C} + 1.26$	0.79	28 days

multiple repetitions were performed with the same settings and selected the best model on the training set identified overall repetitions. Model optimization was based on the coefficient of determination - Pearson  $R^2$ . Different equation forms were derived using the data from this study and used to identify an approximation that better fits their needs in terms of accuracy and simplicity and the final form was selected based on engineering judgment to be sufficiently simple (easy application) and accurate.

The model overall consists of 2-3 parameters and are summarized in Table 5.5. Regarding *FSRF* at 7 days,  $r$  and  $W/C$  are found to be more significant than  $FA/C$  (of the reference mix, i.e., for  $r = 0\%$ ) while 28 days on *FSRF*,  $r$  and  $FA/C$  are the key determination. For *CSRF*, all influence factors, i.e.,  $W/C$ ,  $FA/C$  and  $r$ , have an effect on the results.

Figure 5.12 presents predicted vs. measured values for *FSRF* and *CSRF* using the models summarized in Table 5.5. The data are coming from this study and literature [10–13]. The obtained models are well predicting (considering the simple equation selected) the experimental data with a coefficient of determination of 0.69 and 0.73 for *FSRF* at 7 and 28 days, respectively, and 0.92 and 0.79 for *CSRF*, respectively. Data taken from literature reduces the determination coefficient, which is caused by some intrinsic differences contained in the different studies (e.g., PET aggregate shape and sizes, different cement strength, presence and type of super-plasticizer, etc.) are not considered in the derivation of the models. Additional experimental studies are needed for improving the proposed models by using bayesian update approaches and obtain probabilistic models.

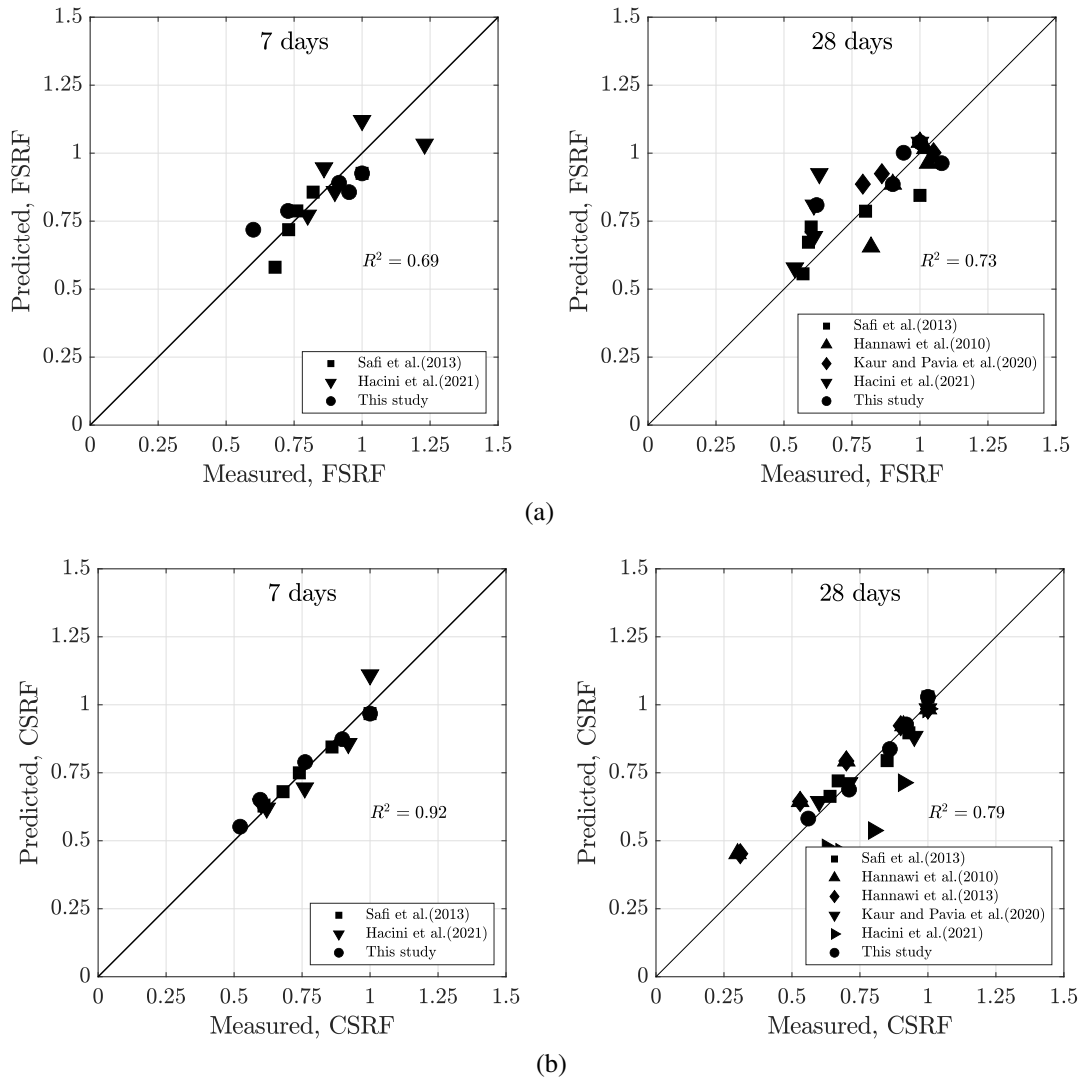


Figure 5.12 Comparison between the measured and predicted *FSRF* (a) and *CSRF* (b) based on proposed model in Table 5.5 at 7 and 28 days. Data from this study and literature [10, 11, 14, 12, 13]

## 5.5 Conclusions

This study presented an experimental investigation to evaluate the effect of PET powder as aggregate on the physical, mechanical, and fracture properties of mortar with mix design  $W/C$  fixed at 0.42 and substitution level of PET aggregate ranging from  $r = 0$  to 30% by volume. In particular, experimental tests to characterize density, slump, water absorption, ultrasonic pulse velocity, flexural and compressive behavior, and micro-structural and interface characterization) were performed. According to the results of this study, the following conclusions can be drawn:

1. The density of the mortar is decreasing with increasing  $r$  as the effect of the reduced bulk density of PET aggregates compared with natural ones ( $2593.5 \text{ kg/m}^3$  vs.  $1370 \text{ kg/m}^3$ ).
2. Higher values of  $r$  correspond to smaller slumps. A possible explanation for these results may be related to the greater water absorption capacity of PET aggregates compared with that of natural fine aggregate.
3. A linear decrease in UPV values with  $r$  is attributable to a reduction of the stiffness, density, and an increase of the porosity.
4. Regardless  $r$ , the flexural strength is increasing with curing time as the effect of the hydration reaction. The PET aggregate has two different and opposite effects on flexural strength. First, the PET aggregate is less performing compared with the natural aggregate in terms of stiffness and ITZ reducing the tensile strength. Secondly, the elongated shape of PET aggregates induces a beneficial bridging effect on the tensile strength. The second effect dominates for low values of  $r$  while the first one dominates for higher ones. The analysis of the crack surface in flexural tests confirms the two effects discussed in this point.
5. Regardless  $r$ , the compressive strength is increasing with curing time as the effect of the hydration reaction. The compressive strength decreases with increasing  $r$  indicating that the second effect discussed in the previous point is not effective under compression loads.

6. Fracture energy is increasing with an increase of  $r$  indicating that the substitution of PET aggregate increases the energy absorption capacity. The opposite tendency is observed for flexural toughness.
7. Data-driven models were established to estimate  $FSRF$  and  $CSRF$  using a parsimonious form found adopting symbolic regression. The relationships take into consideration  $W/C$ ,  $FA/C$  and  $r$  enabling estimates of flexural and compressive properties of mortars with substituted PET.

# Chapter 6

## Physical and mechanical properties of concrete with two different substituted recycled plastic aggregates







### 6.1 Materials and methods

#### 6.1.1 Materials

The materials adopted in this study are tap water, cement, additives, natural aggregates and plastic aggregates. In particular, ordinary Portland cement (CEM II/A-LL 42.5R) made by Buzzi Unicem Group (Casale Monferrato, AL, Italy) according to the European Standards EN 197-1 [296] with Blaine specific surface in the range of 3100 – 4500 cm<sup>2</sup>/g is adopted. The cement has following characteristics: sulfate (SO<sub>3</sub>) content equal to around 4% and chlorides (Cl<sup>-</sup>) content to around 0.1%, containing at least 95% of clinker and up to 5% of minor constituents. Additive of superplasticizer (Sika ViscoCrete -5930) is applied in all mixtures, it is an aqueous solution containing 30% of carboxylic acrylic ester polymer, with a density of 1.08 g/L.

The natural aggregates and plastic aggregates adopted in this study are summarized in Table 6.1. Moreover, the grain-size distribution of these aggregates are conducted with sieve mesh dimensions of 0.063, 0.125, 0.25, 0.5, 1.0, 2.0, 4.0, 8.0,

Table 6.1 Properties and photos of natural aggregates and plastic aggregates adopted in this study

Aggregate	Fine sand	Coarse sand	Coarse aggregate type 1	Coarse aggregate type 2	PET powder	Mix-plastic granules
Density [g/cm <sup>3</sup> ]	2.76	2.73	2.75	2.79	1.38	0.826
Water absorption [%]	1.1	0.9	0.7	0.7		
Fineness modulus	2.62	3.42				
General appearance						

16.0 mm. Figure 6.1 shows the grain size distribution of natural and recycled plastic waste aggregates.

In particular, two types of natural fine aggregates are adopted, namely fine sand with a maximum size of 2 mm and coarse sand with a maximum size of 4 mm. Crushed sandstone coarse aggregates are adopted as natural coarse aggregates with two different granulometries, namely coarse aggregate type 1 with size in the range of 4 – 8 mm and coarse aggregate type 2 with size in the range of 8 – 15 mm. Grain-size distribution curves of fine and coarse aggregates are evaluated according to UNI EN 933-1 [297].

Plastic aggregates include PET powder and mix-plastic granules supplied by *Montello Ltd* (Montello, BG, Italy). Recycled aggregates were checked for proper quality in order to avoid hazardous materials, then ground, cleaned, sieved, and graded. The granulometry of the PET powder is similar to the one of natural fine aggregates (Figure 6.1). The diameter of mix-plastic granules is in the range of 3-5 mm and are mainly composed by PP and PE. The diameter of mix-plastic granules has an average size of 4.2 mm and are obtained by melting and reshaping by PP and PE waste. In particular, mix-plastic granules are obtained from the recycling of post-consumer packaging, coming from urban separate collection, through integrated processes including selection, grinding, washing, drying and related packaging.

According to the sieve analysis, the main size range of PET powder is roughly 0.5-1.0 mm and is slightly different from the fine sand (Figure 6.1). Therefore, PET powder was re-sieved to have the same granulometry of sand aggregates. The mix-plastic granules are not re-sieved since their granulometry is almost constant. Therefore, the concrete skeleton is changed for MIX cases.

The micro-photo of recycled PET powder and mix-plastic granules are shown Figure 6.2. PET powder, as shown in Figure 6.2, was formed by cleaning, shred-

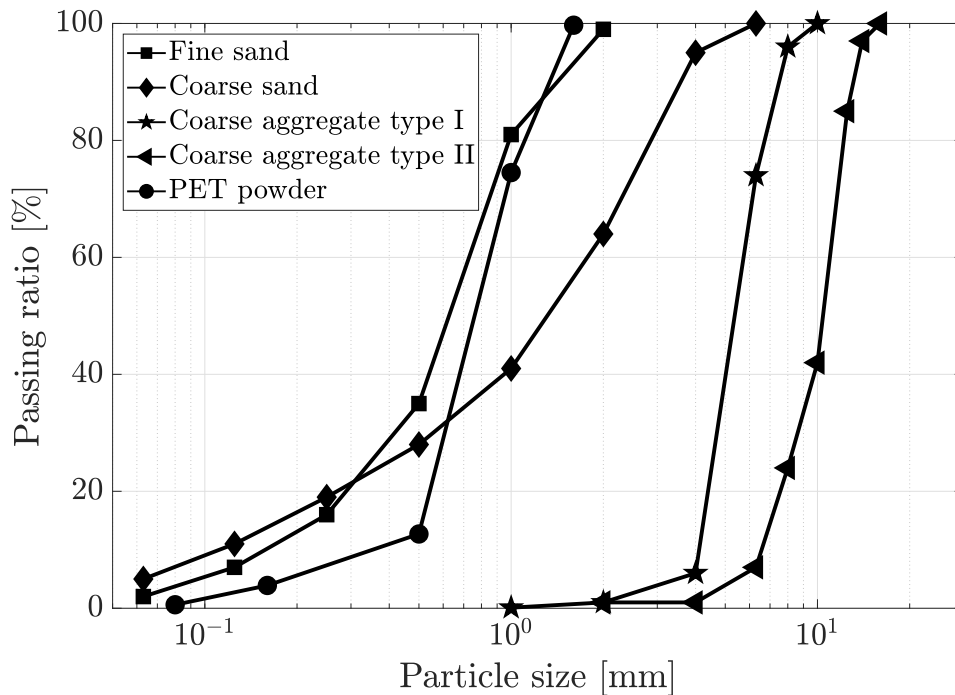


Figure 6.1 Grain-size distribution of adopted materials. The mix-plastic granules are not re-sieved since their granulometry is almost constant

ding and milling recycled PET bottles. The powder is flaky and characterized by white color and high reflectance. The micro-photo in Figure 6.2a shows that the morphology of the PET powder is characterized by low sphericity and medium roundness (Figure 2.4). Mix-plastic granules (Figure 6.2b) was formed by cleaning, milling, melting, extruding and cutting recycled of recycled post-consumer packaging, coming from urban separate collection. Mix-plastic granules have a cylindrical shape with concave bases (Figure 6.2c). The morphology of mix-plastic granules is characterized by low sphericity (cylindrical shape) and medium roundness (Figure 2.4). A similar aggregate shape was employed by Yang et al. [126]. The average diameter is 3.2 mm and the height is 4.2 mm.

### 6.1.2 Concrete mixture proportion and specimens preparation

The mix design of the reference concrete (REF in Table 6.2) was designed to obtain a target compressive strength of standard cubic specimens equal to 60 MPa. The water to cement ratio of 0.45 was maintained for all mixtures, in order to

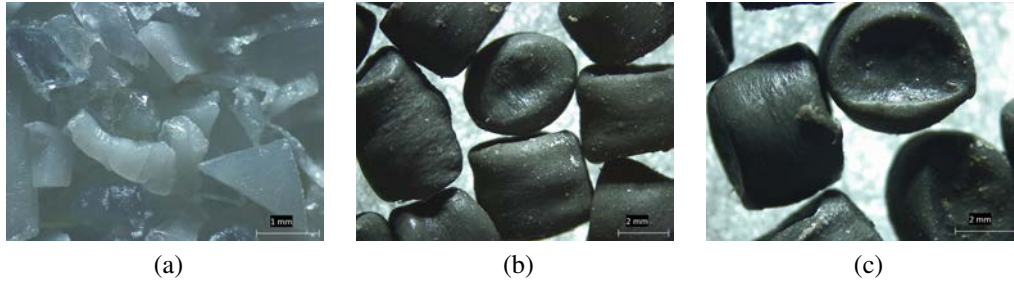


Figure 6.2 Micro-photo of recycled PET powder (a), mix-plastic granules (b), and details of the concave bases (c)

guarantee sufficient workability by varying the kinds of aggregates. The volume of super-plasticizer was always kept same at  $4.2 \text{ kg/m}^3$  (1% of the cement weight).

The volume continuity equation of the concrete mixture can be expressed as:

$$b + w + fa_1(1 - r_{f1}) + fa_2(1 - r_{f2}) + ca_1(1 - r_{c1}) + ca_2 + \overbrace{fa_1 \cdot r_{f1}}^{pet} + \overbrace{fa_2 \cdot r_{f2}}^{mix_2} + \overbrace{ca_1 \cdot r_{c1}}^{mix_1} = 1 \text{ m}^3 \quad (6.1)$$

where  $b$  is the volume of cement,  $w$  is the volume of water,  $fa_1$  and  $fa_2$  are the volumes of fine sand and coarse sand of the reference mix, respectively,  $ca_1$  and  $ca_2$  are the volumes of coarse aggregate type 1 and coarse aggregate type 2 of the reference mix, respectively,  $r_{f1}$  is the substitution level of fine sand by PET powder  $r_{f2}$  is the substitution level of coarse sand by mix-plastic granules,  $r_{c1}$  is the substitution level of coarse aggregate type 1 by mix-plastic granules,  $pet$  is the substituted volume of PET powder, and  $mix_2 + mix_1$  is total substituted volume of mix-plastic granules. The coarse aggregate type 2 is not substituted because of the higher granulometry compared with mix-plastic granules (Figure 6.1).

The substitution is expressed in terms of a total substitution level defined as:

$$r = r_{f1} + r_{f2} + r_{c1} \quad (6.2)$$

Two different substitution were tested: only PET powder substitution of fine aggregates (PET) and simultaneous substitution of PET powder and mix-plastic granules of fine and coarse aggregates (MIX). For the PET case, the substitution is expressed as:



$$r = r_{f1}; \quad r_{f2} = r_{c1} = 0 \quad (6.3)$$

The latter case, implies that the same volume of mix-plastic granules are substituted as fraction of coarse sand and coarse aggregate type I.

For the MIX case, the substitution is expressed as:

$$r = r_{f1} + r_{f2} + r_{c1}; \quad r_{f1} = r_{f2} + r_{c1}; \quad r_{f2} = r_{c1} \quad (6.4)$$

The latter case implies that the same percentage of volume of PET powder and mix-plastic granules are substituted and same fraction of coarse sand and coarse aggregate type I, respectively.

The detailed concrete mix proportions are listed in Table 6.2. A total of 9 concrete mixtures are investigated in this study characterized by different level of substitution with different plastic aggregates (only PET powder or combination of PET powder and mix-plastic granules). In both cases, the following total substitution levels were investigated:  $r = \{5, 10, 20, 30\} \%$ . Designation of the specimen is given by the following ID tag, REF/PET/MIX#, where the first string represents REF/PET/MIX and the second number denotes  $r$ . For REF, the number is omitted since  $r = 0\%$ .

The adopted mixing procedure is: the coarse aggregate type I and coarse aggregate type II were mixed for about 2 minutes with a small amount of water. The coarse sand and more water was added and mixed for 2 minutes. The fine aggregate and cement were added together with remaining water added to control workability and mixed for 3 minutes. Plastic aggregates and SP were added and mixed for 3 minutes. The mixing process was the same for all mixtures.

After mixing, the fresh concrete was immediately tested for the slump (Section 6.2.1). The fresh concrete was poured into cleaned and lubricated moulds. During casting, a compacting rod were adopted for 15 seconds to compact the fresh concrete in the molds. For each mix, the following specimens were prepared: six cubic specimens with a size of 150mm for compressive tests, three prismatic specimens with a dimension of  $150 \times 150 \times 650$ mm for flexural tests, and water-penetration tests. After 48h, all specimens were de-molded, labeled and cured in a water tank with a controlled temperature of  $22^\circ\text{C}$ .

Table 6.2 Mix proportion of the mix investigated. See Figure 6.1 for the definition of the granulometry

ID	Natural aggregate			Plastic aggregate		Cement	Water	Super-plasticizer
	Fine sand	Coarse sand	Coarse aggregate type I	Coarse aggregate type II	PET powder			
REF	475				0			
PET5	451.2				11.88			
PET10	427.5	488	128		23.75			0
PET20	380				47.5			
PET30	332.5			741	71.25	420	185	4.2
MIX5	463.1	481.9	126.4		5.94	2.33		
MIX10	451.2	475.8	124.8		11.88	4.65		
MIX20	427.5	463.6	121.6		23.75	9.3		
MIX30	403.7	451.4	118.4		35.63	13.95		

## 6.2 Test program

### 6.2.1 Fresh concrete properties

The slump test is the most widely used test method to characterize the consistency of fresh concrete. Slump flow value, which is used for the description of the fluidity of a fresh concrete in unconfined conditions, is a sensitive test. It is the primary check for the fresh concrete consistence to meet the specification. Thus, it can normally be specified for all self-compacting concretes. Moreover, additional information about segregation resistance and uniformity of concrete can be achieved from the visual observations during the test [298].

The effect of plastic aggregates on the fresh concrete was evaluated by performing standard slump tests according to BS EN 12350 [299]. Tests were carried out with a standard Abrams cone with an height of 300 mm, a diameter of the opening base of 200 mm and of the opening top of 100 mm. The fresh concrete was poured into the cone filling 1/3 height. Then, a steel rod was used to pound the concrete. This process was repeated two times until the cone was filled. The cone was removed vertically slowly and carefully making the unsupported fresh concrete to collapse. The slump was measured by checking the vertical distance between the original and collapsed positions of the center of concrete top surface. Moreover, the diameter of the final slump flow was measured.

Additionally, the density of fresh concrete was measured using the  $150 \times 150 \times 150 \text{ mm}^3$  cubes. First, the molds were lubricated and weighted. Then, the molds were filled and compacted and the upper surface of the molds cleaned. Finally, the molds filled with concrete were weighted. The density of fresh concrete was determined as the difference of the two weights divided by the volume.

### 6.2.2 Compressive tests

The compressive strength of concrete cubes (three repetitions) was tested at 28 days by a universal testing machine (Galdabini Compression, capacity 3000 kN) with a constant loading rate of 13.5 kN/s [300]. The compressive strength is evaluated as:

$$\sigma_c = \frac{F_{max}}{l^2} \quad (6.5)$$

where  $F_{max}$  is the maximum flexural load and  $l$  the side of the cube tested (150 mm, see Section 6.2). Photos of the final failure modes are taken at the end of the test.

### 6.2.3 Flexural tests

Three prismatic specimens (150 × 150 × 600 mm) were tested at 28-days for three point flexural test to obtain flexural strength and rupture energy absorption capacity adopting a universal testing machine (810, MTS, capacity 100 kN) with a loading rate of 0.05 mm/min according to EN 14651 [301]. Notched mid-point loaded specimen were adopted since crack initiates at the notch-tip and propagates along the notch plane and hence, deformation is always localized at the notch-plane and the rest of the beam does not undergo significant inelastic deformations [302]. The three point flexural test test set-up, geometry and dimensions of notched beam specimen are shown in Figure 6.3. Crack Mouth Opening Displacement (CMOD) is measured using a displacement transducer installed on the mouth of the notch and vertical displacements ( $D$ ) by monitoring the head movement. The flexural strength is calculated as:

$$\sigma_{fl} = \frac{3 \cdot P_{max} \cdot S}{2 \cdot b \cdot (h - 25 \text{ mm})^2} \quad (6.6)$$

where  $\sigma_{fl}$  is the flexural strength;  $P_{max}$  is the maximum flexural load;  $S$  is the distance between the supporting rollers (500 mm, Figure 6.3b);  $b$  is the width of the specimens (150 mm, Figure 6.3b),  $h$  is height of the specimen, ( $h - 25 \text{ mm} = 125 \text{ mm}$  is the distance between the tip of the notch and the top of the specimen, Figure 6.3b). The vertical displacement,  $D_v$ , is the vertical displacement of the head corresponding to  $P_{max}$ . Photos of the final failure modes are taken at the end of the test after marking the crack pattern with a black marker on the surface.

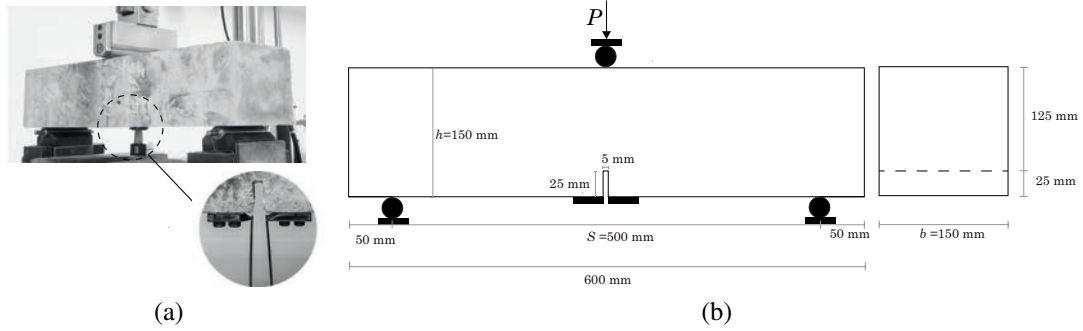


Figure 6.3 Three point flexural test: test set-up (a), geometry and dimensions of notched beam specimen (b).

The fracture toughness for a quasi-brittle material like concrete can be expressed as [303, 304]:

$$K_{IC} = \frac{P_{max} \cdot S}{b \cdot h^{3/2}} f(\alpha) \quad (6.7)$$

where  $P_{max}$  is the peak load during the three point flexural bending tests assumed corresponding to the cracking initiation load, and  $\alpha$  is a geometric factor [303, 304]:

$$f(\alpha) = \frac{1.99 - \alpha(1 - \alpha)(2.15 - 3.93\alpha + 2.7\alpha^2)}{(1 + 2\alpha)(1 - \alpha)^{3/2}} \quad (6.8)$$

where  $\alpha = a_c/h$  being  $a_c$  the critical effective crack length [303, 304]:

$$a_c = \left[ \frac{2}{\pi} (h + H_0) \arctan \sqrt{\frac{b \cdot E_{fl} \cdot CMOD_c}{32.6 \cdot P_{max}} - 0.1135} \right] - H_0 \quad (6.9)$$

where  $H_0$  is the thickness of the screws used connected the specimen to the extensometer (1 mm),  $CMOD_c$  is a critical crack opening displacement corresponding to peak load, and  $E_{fl}$  is the effective modulus based on the load–CMOD curve determined as [305]:

$$E_{fl} = \frac{1}{b \cdot c_i} \left[ 3.7 + 32.6 \cdot \tan^2 \left( \frac{\pi a_0 + H_0}{2 h + H_0} \right) \right] \quad (6.10)$$

where  $c_i = (CMOD)_i/P_i$  can be derived from  $(P, CMOD)$  of the ascent stage of load-CMOD curves.

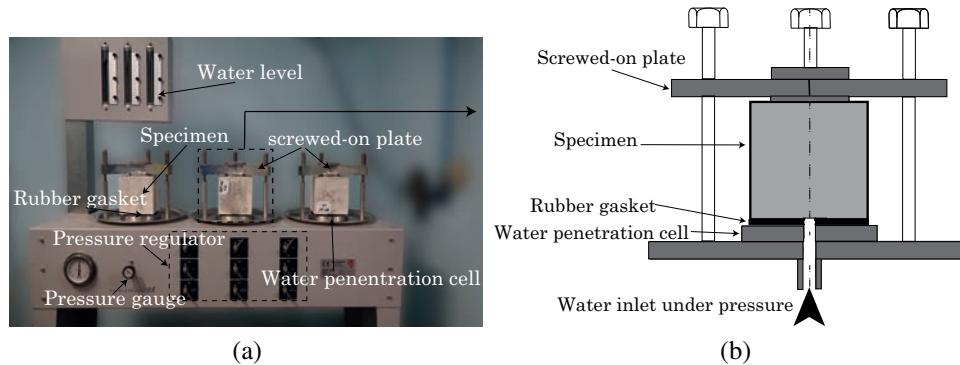


Figure 6.4 Water-penetration test setup: photo (a) and schematic of the specimen (b)

### 6.2.4 Water-penetration tests

The durability of concrete is determined by the resistance to water penetration and possible diluted deleterious substances [306]. The aim of the water penetration tests is to evaluate the water penetration characteristics of concrete specimens. Three cubes with a dimension of 150 mm were tested at 28 days of curing. The three specimens were taken from the curing room. The surfaces of each specimen, especially surfaces in contact with the water inlet (Figure 6.4b), were cleaned using brushes and clothes. After this, the surface with fewer holes and cracks was selected to apply the water pressure. Then the surfaces were cleaned with flowing tap water, and to keep the surface wet. Specimens were rapidly put into the water-penetration test setup (Figure 6.4a). Specimens were subjected to a water pressure of 5 MPa monitored from pressure gauges for 72 h. During the test, a periodic observation of the water level and pressure gauge was done to ensure that the surface is under constant water pressure and to avoid water leakage, according to BS EN 12390-8 [307].

After 72 h, the water inlet and pressure regulator are shut off and releasing the screws the specimens are taken out and rapidly put in the splitting machine (Figure 6.5). A steel rod is used in the splitting tests to make the specimen split into two parts. A clear water penetration front can be observed on each split face (Figure 6.5c). Then, the front was marked and the maximum depth of penetration was measured and digitized. The maximum and average water penetration depth are calculated.

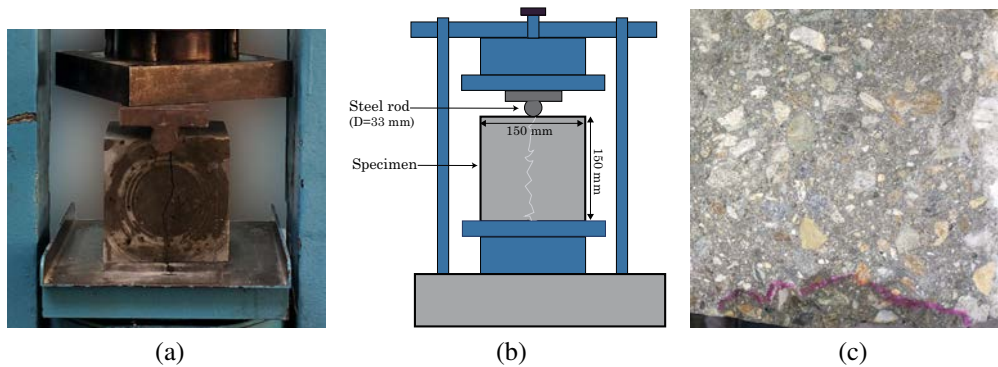


Figure 6.5 Sample splitting apparatus: photo (a), schematic (b), and example of split face of a specimen (c)

## 6.2.5 Micro-scale characterization

The morphology of MIX30 concrete is investigated with a Scanning Electron Microscope (SEM, ZEISS Gemini SEM 300) at a system vacuum pressure of  $4.97 \times 10^{-5}$  mbar and at an accelerating voltage of 10kV. Energy Dispersive X-ray analyses using a Quantax energy-dispersive Electron Probe MicroAnalysis (EPMA) system (EDS) were then performed with an accelerating voltage of 10kV to determine the element components of cement paste, natural and plastic aggregates. Energy dispersive X-ray (EDX) analysis is a method of elemental detection via the collection of characteristic X-rays induced by electron beam radiation. EDX (Oxford Instruments X-Max EDS System) is performed to observe the chemical composition of the natural aggregate and of PET powder and mix-plastic granules.

## 6.3 Experimental Results

### 6.3.1 Fresh concrete properties

Slump, slump flow, visual inspection of slump tests, and fresh density for the different concrete mixtures are summarized in Table 6.3.

The slump values of all mixtures were larger than 180 mm and with a maximum value of about 255 mm (MIX30). For the reference concrete (REF), the slump is 235 mm, and the diameter of slump flow is 410 mm indicating good rheological

Table 6.3 Slump, slump flow, visual inspection of slump tests, and fresh density for the different concrete mixtures.

ID	Slump	Slump flow	Visual inspection	Fresh density
[-]	[mm]	[mm]	[-]	[kg/m <sup>3</sup> ]
REF	235	410	Homogenous and bleeding	2454
PET5	215	370	Homogenous but less consistent	2424
PET10	200	325	Homogenous and bleeding	2428
PET20	205	338	Consistent and homogenous	2412
PET30	180	305	Consistent and homogenous	2389
MIX5	210	335	Homogenous but less consistent	2434
MIX10	240	462	Harsh with bleeding	2442
MIX20	250	450	Harsh with bleeding	2420
MIX30	255	478	Harsh with bleeding	2392

properties. The content, particle size distribution, particle shapes, and surface morphology as well as other properties of aggregates can significantly affect the behavior of fresh mixtures [308, 309]. Table 6.3 indicates that the slump decreases by increasing PET powder. For  $r = 30\%$ , the slump reduction ratio with respect to REF can reach more than 20%. A possible explanation for these results may be related to the sharper edges and more elongated shapes of PET powder grains (Figure 6.2a) which contributes to the reduction of slump and fluidity [126, 125, 1]. In fact, sharp edges of the PET powder decrease the lubrication during the mixing process, which in turn decrease the values of slump and flowability. There are, however, other possible explanations. PET powder induced in a large proportion of very fine particles and powder (Figure 6.1), the surface area to volume ratio increases therefore more free water was surrounded by PET powder [131]. As a matter of fact, larger surface areas of aggregates usually result in higher water demand, possibly leading to faster structural build-up [310].

However, an opposite trend is observed for the concrete with mix-plastic aggregate. The values of slump increased from 210 mm for  $r = 5\%$  (MIX5) up to 255 mm for  $r = 30\%$  with mix plastic granules. An increase in the slump was observed when coarse aggregate was substituted by PET granules in the literature [23, 126, 128]. Combined with observation on PET substituted concrete, results can be explained as follow. Mix plastic granules have a smoother out-surface and smaller surface area to volume ratio (Figure 6.2b) compared with PET powder and their marked hydrophobic characteristic requires less water during mixing in turn contributing to higher slump and better flowability. In MIX cases, having substituted simultaneously PET and mix plastic granules (Table 6.2), the function of mix-plastic granules of lubrication is dominating compared with that of PET powder of decreasing lubri-

ation. It is noteworthy, that increase in the slump and flowability observed in this study is less when compared with other investigations on coarse/fine aggregates only replaced by plastic granules [e.g., 23, 126, 128].

The fresh density of REF is  $2454 \text{ kg/m}^3$ . The increase of  $r$  for both PET and MIX cases induces a reduction of the fresh density with a slightly more marked reduction for PET. The minimum fresh density was observed for PET30 ( $2389 \text{ kg/m}^3$ ). The fresh density loss is less marked when compared with previous studies [120, 118, 132, 121, 124, 128], where, however, only one of the coarse/fine aggregates were substituted by plastic.

### 6.3.2 Compressive behavior

Figure 6.6 compares the mean compressive strength at 28-days curing for different  $r$  and substituted plastic aggregates. The mean compressive strength for REF is 63.7 MPa. When increasing  $r$ , the compressive strength generally decreases with a limited loss (or some gain) for  $r \leq 10\%$  and a more marked reduction for  $r > 10\%$ . The maximum loss of compressive strength is 27% and 18% for PET and MIX, respectively, for  $r = 20\%$ .

When  $r = 5\%$ , a similar compressive strength can be observed for PET and MIX. This result may be explained by the fact that when the plastic content is at a low level, the PET powder and mix plastic are both weakening the interface between aggregate and cement paste. However, for  $r = 5\%$ , a balance exists in PET powder and mix plastic granules [126]. It can be observed that the compressive strength is slightly improved for MIX10, with an average compressive strength of around 65 MPa (slightly larger than REF). The compressive strength of MIX cases is generally higher than PET cases, given  $r$ . The observed increase in the compressive strength could be attributed to the larger size of mix plastic granules (Figure 6.1) inducing more voids and cracks that, however, can be effectively filled by the PET micro-fiber (Figure 6.2a), which in turn enhanced the compressive strength. While the content of plastic is increasing, the function of filling is limited, then the strength decreases. Another possible explanation for this might be that the mix plastic aggregate is inducing an interlocking effect due to its peculiar geometry (Figure 6.2b) which also explains the slightly larger values of the MIX case. When  $r$  is larger



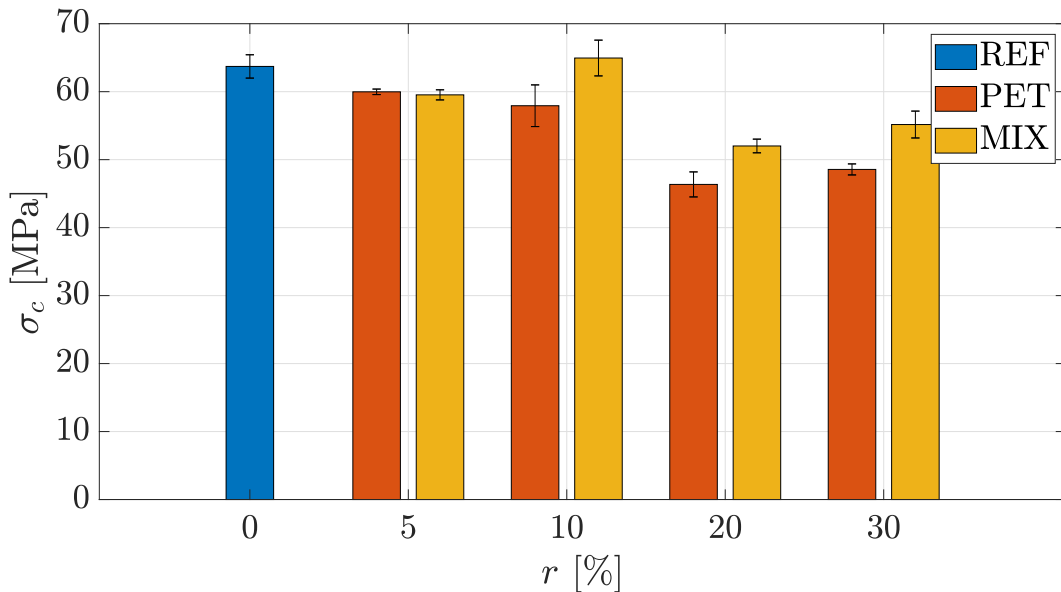


Figure 6.6 Mean compressive strength for different  $r$  and substituted plastic aggregates. Standard deviation values are shown with error bars

than 10%, the negative effect of plastic aggregate on compressive strength can be attributed to the low adhesion effect between plastic aggregate and cement paste.

Figure 6.7 shows failure modes of cubes of different concrete at the end of compressive tests. Since photos are taken after the test is finished, the specimens could have experienced some minor additional damage due to movement. Only one typical failure mode was selected as representative of the three repeated tests since similar conditions were observed in the remaining ones [9].

All tests show non-explosive failure patterns [311]. It can be seen some major macro-cracks and a large number of micro-cracks. The latter generally coalesced near the middle of cubic specimens, and the macro-cracks propagated along  $45^\circ$  from the axis near the ends, especially for PET cases. For MIX cases, similar cracks can be observed on the lateral surfaces, but micro-cracks coalesced near the middle along the height of cubic specimens (e.g., MIX10). For MIX concrete, the black plastic granules can be clearly seen and the granules are expelled from the cement paste. Several concrete debris is fallen off from the cubic specimen along with the location of granules, implying the weakness of the bond between the cement paste and plastic granules.

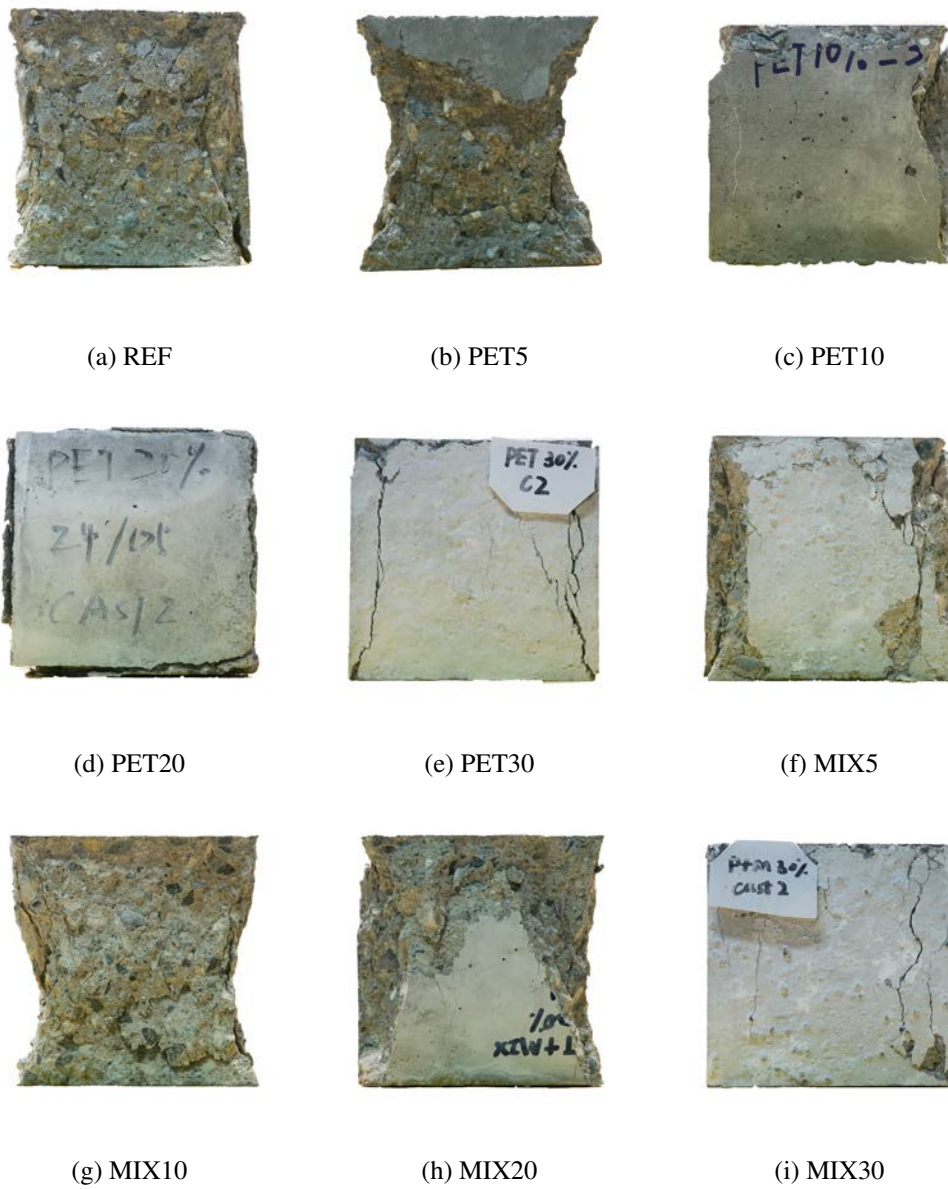


Figure 6.7 Failure modes of compressive tests

### 6.3.3 Flexural behavior

Flexural load-CMOD curves and vertical displacement-load curves for different  $r$  of different mixes are summarized in Figure 6.8. The vertical displacement is the displacement of the mid-span of the beam. A similar behavior is observed for the three bending tests in all cases indicating good test repeatability.

The results show that the general behavior is characterized by a first rise in the force and a sudden decrease characterized by softening with the opening of the cracks. In the first phase, the load-CMOD curves are quasi-vertical since the crack is not opened. For the vertical displacement-load curves, a linear relationship between load and displacement can be observed representing the flexural stiffness of concrete that is undergoing linear elastic deformation.

As the load approaches the peak, however, the linear relationship between load and deflection and the crack initiates and propagates inducing a marked reduction of the forces. This phenomenon is characteristic of brittle behavior and highlights the weakness of concrete under tension. The first cracking point is defined as the point where non-linearity in the load-deflection curve becomes marked or the inclination of the CMOD curve changes noticeably. As the crack opening will cause a reduction in the flexural stiffness of the prism specimen and thereby an increment in the deflection. Nevertheless, the flexural stiffness of the beam specimen may be insensitive to the crack opening and the amount of stiffness loss may be insignificant in the stage of steady-state crack propagation. Compared to REF, the peak load decreases accompanied by displacement increases, which indicates that the opening of the crack induces the decrease of flexural resistance capacity [312].

The average flexural strength was calculated using Eq. 5.6 and is summarized in Figure 6.9 for the different values of  $r$  and substituted plastic aggregates. A similar behavior to the compression case is observed (Figure 6.6) with a more marked increase and less marked reduction with increasing  $r$  of the strength. In particular, an increase of the flexural strength up to  $r = 10\%$  is observed then followed by a decrease. The main explanation for this effect is related to the PET powder having an elongated shape (Figure 5.1) and inducing a bridging effect on the crack surface. The flexural strength is generally slightly larger for the MIX case compared with PET.

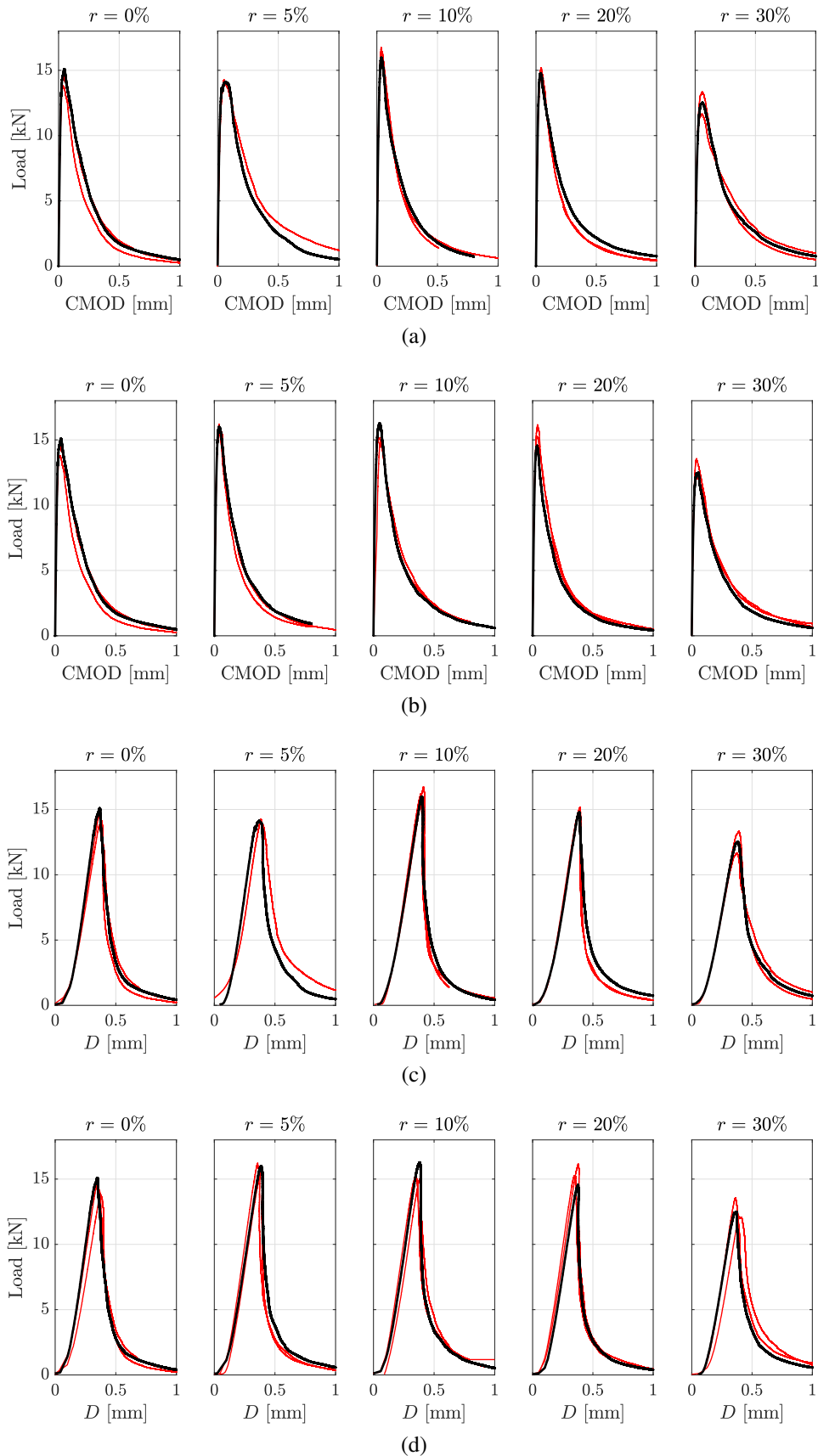


Figure 6.8 Flexural load-CMOD curves (a and b) and vertical displacement-load curves (c and d) for different  $r$ . PET (a and c) and MIX (b and d) cases. Red lines are showing the results of the three repetitions while the black line is their average across CMOD

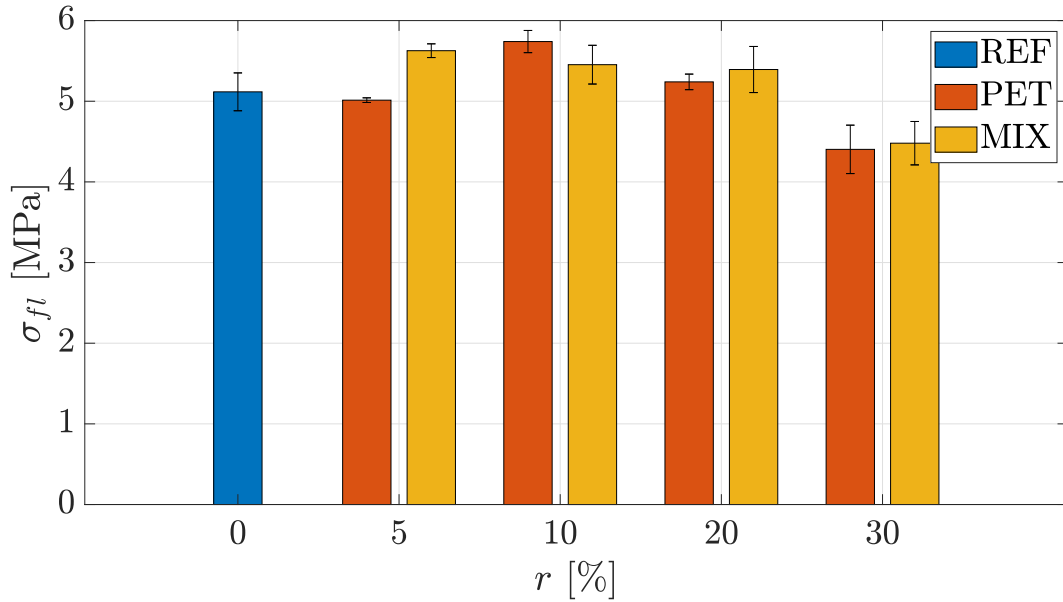


Figure 6.9 Mean flexural strength (Eq. 5.6) for different  $r$  and substituted plastic aggregates. Standard deviation values are shown with error bars

Similar results can be found [313, 140]. Albano et al. [313] utilized two size of PET aggregate (average sizes were 0.26 and 1.14 cm) to replace fine aggregate. Results shows that for  $r = 10\%$ , an increase in flexural strength can be observed, and the flexural strength can be improved with a mix of two sizes of PET aggregate compared with the other case. Thorneycroft et al. [140] used different size of PET aggregate to substitute fine sand. The results shows that a graded PET plastic matched to the size of the sand particles gave the best overall performances.

The failure modes of the three bending tests are shown in Figure 6.10. A main gradual progressive cracks prolonged along the notched part is observed. For the PET cases, a main flexural crack can be observed starting from the notch point with a generally linear trend. For mixed cases, the main crack path is not linear. This difference can be attributed to the large micro size of granules inducing local variation of the stiffness similar to granules expulsions observed in concrete under compression (Figure 6.7).

The cracking initiation load ( $P_{max}$ ), initial crack opening displacement ( $CMOD_c$ ), vertical displacement at peak load ( $D_v$ ), flexural elastic modulus ( $E_{fl}$ ), and fracture toughness ( $K_{IC}$ ) are summarized in Table 6.4.

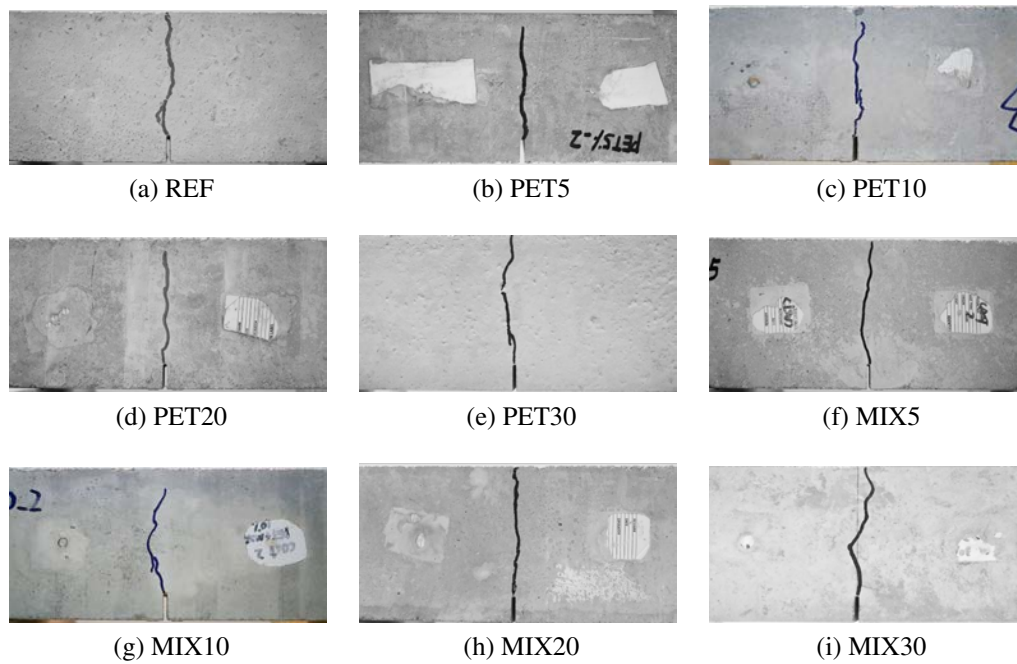


Figure 6.10 Failure modes of flexural tests

The natural aggregate substituted by plastic aggregate can slightly improve  $CMOD_c$  and  $D_v$ , thus the incorporation of plastic aggregates can improve the flexural behavior in terms of brittleness similar to fibers in reinforced concrete [e.g., 314].  $K_{IC}$  has a similar trend with the flexural strength (peak load) increasing for low substitution levels and decreasing for high substitution levels. A possible explanation for this trend can be attributed to the fact that for low substitution levels an optimized grading of aggregate is found which can enhance the bond between aggregate and cement paste. Under flexural load, the PET powder can behave as fiber providing a bridge effect preventing the brittle failure of the specimen [13]. However, when  $r$  is larger than 20%, the bridge effect and ITZ are weakened by more micropores and cracks inducing a reduction in the toughness.

### 6.3.4 Water-penetration tests

The results of water-penetration tests of plastic aggregate concrete are listed in Table 6.5. The maximum and average depth of water penetration can be a significant parameter for evaluating the concrete durability. The maximum depth of

Table 6.4 Cracking initiation load ( $P_{max}$ ), initial crack opening displacement ( $CMOD_c$ ), vertical displacement at peak load ( $D_v$ ), flexural elastic modulus ( $E_{fl}$ ), and fracture toughness ( $K_{IC}$ ). The three numbers are the results of the three tests while the average and standard deviation values are reported inside the parenthesis

ID	$P_{max}$	$CMOD_c$	$D_v$	$E_{fl}$	$K_{IC}$
	[kN]	[mm]	[mm]	[GPa]	[MPa·m <sup>1/2</sup> ]
REF	14.7; 13.8; 15.1 (14.5, 0.67)	0.037; 0.036; 0.046 (0.040, 0.006)	0.35; 0.37; 0.35 (0.36, 0.01)	39.62; 37.69; 36.18 (37.83, 1.73)	1.85; 1.73; 1.97 (1.85, 0.12)
PET5	14.3; 14.3; 14.1 (14.2, 0.12)	0.052; 0.052; 0.067 (0.057, 0.009)	0.36; 0.39; 0.39 (0.38, 0.02)	26.77; 27.22; 33.48 (29.16, 3.75)	1.79; 1.80; 2.21 (1.93, 0.24)
PET10	16.7; 16.2; 16.0 (16.3, 0.36)	0.037; 0.047; 0.040 (0.041, 0.005)	0.34; 0.39; 0.38 (0.37, 0.03)	37.43; 37.45; 36.68 (37.19, 0.44)	2.00; 2.10; 1.96 (2.02, 0.07)
PET20	15.2; 14.7; 14.8 (14.9, 0.26)	0.044; 0.041; 0.040 (0.042, 0.002)	0.35; 0.38; 0.38 (0.37, 0.02)	30.99; 28.73; 30.69 (30.13, 1.23)	1.85; 1.74; 1.77 (1.79, 0.06)
PET30	11.7; 13.3; 12.5 (12.5, 0.8)	0.060; 0.061; 0.061 (0.061, 0.001)	0.40; 0.36; 0.37 (0.38, 0.02)	21.54; 23.23; 20.95 (21.91, 1.19)	1.53; 1.71; 1.59 (1.61, 0.09)
MIX5	16.2; 15.7; 16.0 (16.0, 0.25)	0.040; 0.039; 0.041 (0.040, 0.001)	0.35; 0.39; 0.39 (0.38, 0.02)	37.89; 39.30; 38.13 (38.44, 0.75)	2.00; 1.96; 2.00 (1.99, 0.02)
MIX10	15.2; 15.0; 16.3 (15.5, 0.7)	0.043; 0.063; 0.052 (0.053, 0.01)	0.34; 0.39; 0.38 (0.37, 0.03)	35.58; 32.81; 33.71 (34.04, 1.41)	2.01; 1.73; 2.08 (1.94, 0.11)
MIX20	15.2; 16.2; 14.6 (15.3, 0.81)	0.036; 0.041; 0.039 (0.039, 0.003)	0.35; 0.38; 0.38 (0.37, 0.02)	37.40; 34.72; 33.93 (35.35, 1.82)	1.85; 1.96; 1.79 (1.87, 0.09)
MIX30	12.1; 13.6; 12.5 (12.7, 0.78)	0.036; 0.040; 0.054 (0.043, 0.009)	0.40; 0.36; 0.37 (0.38, 0.02)	29.43; 32.42; 31.04 (30.97, 1.50)	1.47; 1.69; 1.78 (1.64, 0.16)

water-penetration is smaller than 50 mm, therefore the tested material can always be considered as a watertight concrete [315, 316].

For REF concrete, the maximum and average depth is about 17 and 11 mm, respectively. For  $r \leq 10\%$ , the depth of water penetration is similar because the smaller granulometry of PET powder is able to better fill the empty spaces creating a more compact concrete. However, for  $r > 10\%$ , the substitution with plastic aggregates increases micropores and micro-cracks in concrete. In particular, for  $r > 10\%$ , the substitution by plastic aggregates contributes to increasing the depth of water penetration. This is more evident in MIX cases. Combined with the analysis of SEM images (see Figure 6.11), under good mixture design and appropriate aggregate grading, the durability can be slightly improved for low-level substitution of plastic aggregate.

The observed water-penetration levels have a similar trend to the compressive strengths (Figure 6.6). In fact, a considerable increase in the values of water penetration depth indicates a weak bond between plastic aggregate and cement paste and poor adhesion on the ITZ.

### 6.3.5 Micro-scale characterization

Figure 6.11 shows SEM images (at two magnification factors) of the natural aggregate and plastic aggregates. In particular, Figure 6.11a presents SEM images for the REF case. Figure 6.11b reports SEM images for PET30 and Figure 6.11c for MIX30. The specimen in Figure 6.11c was also adopted for point EDX analysis and



Table 6.5 Maximum and average of water penetration depth. The three numbers are the results of the three tests while the average and standard deviation values are reported inside the parenthesis

ID	Maximum water penetration depth	Average water penetration depth
[-]	[mm]	[mm]
REF	15; 21; 17 (17.7, 2.5)	10; 14; 10 (11.3, 1.9)
PET5	26; 14; 13.5 (17.8, 5.8)	13; 10; 8 (10.3, 2.1)
PET10	19; 16; 14 (16.3, 2.1)	11; 11; 10 (10.7, 0.5)
PET20	22; 30; 25 (25.7, 3.3)	15; 19; 16 (16.7, 1.7)
PET30	28; 19; 20 (22.3, 4.0)	17; 14; 13 (14.7, 1.7)
MIX5	22; 19; 18 (19.7, 1.7)	12; 15; 13 (13.3, 1.2)
MIX10	17; 15; 13 (15, 1.6)	8; 8; 9 (8.3, 0.5)
MIX20	21; 20; 23 (21.3, 1.2)	14; 14; 14 (14, 0)
MIX30	47; 20; 22 (29.3, 12.8)	28; 13; 20 (20.3, 6.1)

defined as spectrum 1, 2, and 3. The results of the EDX analyses are provided in Figure 6.12 for the natural aggregate and PET and mix aggregates. The analytical method of EDX was also used to determine the elements (elemental composition) present.

In all SEM images, micropores and micro-cracks can be observed. With the presence of PET powders and mix-plastic granules, more micropores and micro-cracks can be observed. The SEM images at a high magnification factor show the ITZs between the aggregates (natural and plastic aggregates) and the cement matrix. The ITZ reveals a clear gap and a poor bond between the plastic aggregates and the cement paste compared to natural aggregate and cement paste. The failure is along with the granules and the shape of granules is still integral and the surface of granules is relatively smoother after failure while PET powder is pulled off and scratched. Generally, PET powder shows a rough surface with scratches resulting from the manufacturing process. A similar surface was found in previous literature [15]. The presence of these scratches (roughness) on the PET surface slightly enhances the bond with cement paste for a low level of substitution.

EDX analysis was performed on the selected natural aggregates (fine and coarse aggregate) with cement paste and plastic aggregates (PET powder and plastic granules) with a limited amount of cement paste on the surface. Figure 6.12a shows that the major elements are O, Ca, C, Si (see graph on the right side of each subfigure). The observed elemental composition is compatible with sand that is formed by SiO<sub>2</sub>, and coarse aggregate composed of sandstone that is primarily formed by CaCO<sub>3</sub>.



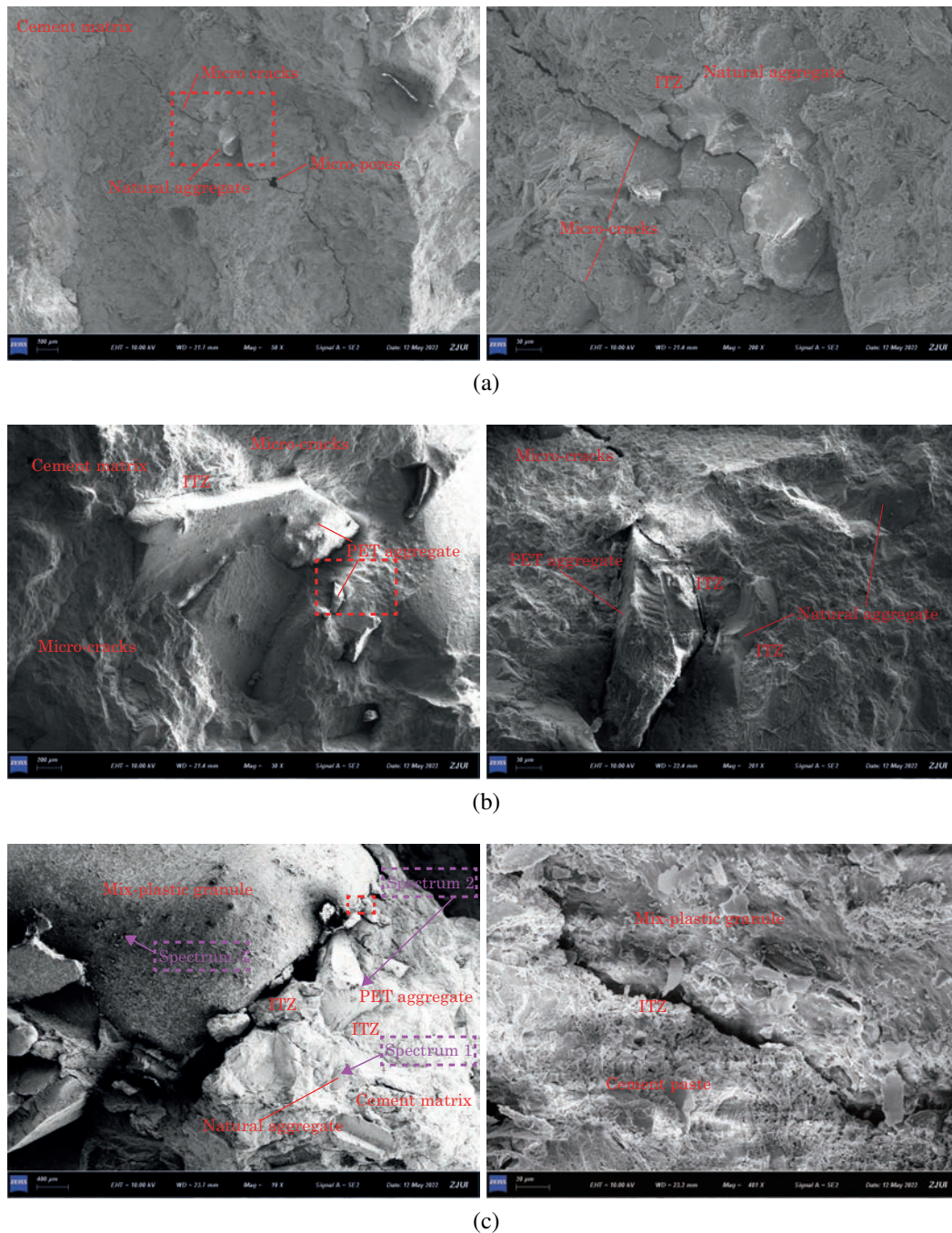
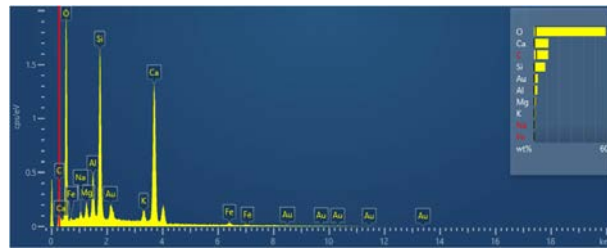
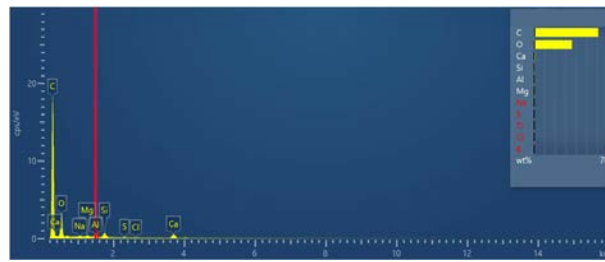


Figure 6.11 SEM scans of: natural aggregate (a), PET powder (b), and MIX aggregate (c). The left scans are large view of the region of interest while right scans are close views of the region inside the rectangle reported on the left side. In MIX aggregate scan (c, left) the location of the spectrum analyses (Figure 6.12) are reported



(a)



(b)



(c)

Figure 6.12 EDX elemental point analysis in terms of spectrum for: (spectrum 1) natural aggregates (a); (spectrum 2) PET powder (b), and (spectrum 3) mix-plastic granules (c).

The presence of Al can be attributed to the presence of  $Al_2O_3$  [317]. The presence of Au was attributed by sputtered gold coat for SEM images.

On the other hand, the major elements shown in Figures 6.12c and 6.12c are O and C. The observed elemental composition is compatible with plastic aggregates (PET or PE). In fact, PET and PE can be identified as a polymer composed of carbon (C) and oxygen (O) (see Table 2.1). The small amount of Ca can be attributed to cement paste coated on the plastic aggregate.

## 6.4 Discussion

This section provides an explanation and interpretation of the results of this study by comparing them with the results of previous studies. The database used herein refers to tests on concrete specimens with substituted aggregates made of PET. The collected tests are compression or flexural ones. Since the compressive or flexural strength of the reference concrete (i.e., only with natural aggregates) is different in the different tests, non-dimensional data are considered. In particular, strength reduction factors (*SRF*) are considered:

$$SRF = \frac{f(r)}{f(r = 0\%)} \quad (6.11)$$

where  $f(r)$  is an index (compressive strength  $f_c(r)$  or flexural  $f_{fl}(r)$ ) for a given value of  $r$ .  $f(r = 0\%)$  is the same index for the reference mix design (only natural aggregates). In the following, *FSRF* refers to the flexural strength reduction ratio while *CSRF* refers compressive strength reduction ratio.

Figures 6.13a and 6.13b show *CSRF* and *FSRF* as a function of  $r$  only substituted by PET, respectively. The details of the studies adopted in the database are provided in Table 2.4. Different colors indicate different studies and different marker and line style represents various factors, like different water/cement ratio [24], and different plastic shape [26]. For this study, the continuous black line refers to the PET case while the dashed black one to the MIX case.

As discussed in Section 2.1, aggregates (type, grading, morphology, and material) have a great influence on the mechanical behaviors, especially for the compressive strength. In particular, Fládr and Bílý [318], Balendran et al. [319], Kozul and Darwin [320] observed that the compressive strength is strongly dependent on the sizes of aggregate, while flexural strength is independent on the aggregate size. Flexural strength is determined by the matrix strength and the strength of ITZs, type of aggregates and surface layer size effect of the specimens. Therefore, *CSRF* database accounts only for micro-plastics (the maximum size of PET powder is smaller than 4.75 mm, see Table ?? for the definition). All the tests show a reduction of *CSRF* with increasing  $r$ . The only exception is for some cases [26, 20, 19] for low  $r$ . In particular, Marzouk et al. [26] used two different maximum sizes of PET powder of 2 (dashed green line) and 4.75 mm (continuous green line) to substitute sand. The results indicated that larger PET aggregates (4.75 mm) performed better

than PET aggregate of 2 mm. The result of Marzouk et al. [26] contrasts with other studies showing an opposite trend. However, several other factors can influence this result. Other studies [19, 21, 22] generally provide similar values of *CSRF* when compared with the results of this study.

Regarding the relationship between *FSRF* and *r*, different trends can be identified (Figure 6.13b). All the studies confirmed experimental observations reported in this study, i.e., *FSRF* decreases for  $r \geq 20\%$  while *FSRF* decreases or slightly increases for  $r \leq 10\%$ . In particular, Dawood et al. [27] and Kangavar et al. [19] reported an increase of *FSRF* for  $r \leq 15\%$ . A possible explanation for this might be that plastic particles can fill some of the voids in concrete more effectively if the plastic content is relatively low. Marzouk et al. [26] demonstrated that aggregates display irregular shape and rough surface texture that can induce an increase in the mechanical characteristics with the enhancement of plastic aggregate “skeleton” effect Wu et al. [321], Dawood et al. [27]. A possible explanation for these results may be the geometry of the substituted aggregate is increasing through the bridging effect and aggregate interlock. The term aggregate interlock describes the possible shear transfer between two opposing crack surfaces, which mainly depends on crack kinematics and crack surface roughness. The particular geometry of the mix aggregate (Figure 6.2c) can explain the observed increase. However, for larger values of *r*, the observed decrease can be attributed to the increased total bond area between neighboring aggregates and weak interfacial bonding between the plastic and cement paste.

Two data-driven predictive models for *SRF* (compressive and flexural) are proposed based on symbolic regression [322, 323] adopting the database provided in Figure 6.13. HeuristicLab which is a common software used for symbolic regression using genetic programming. Model optimization was based on the coefficient of determination - Pearson  $R^2$ . The set of function symbols was  $\{+, -, \cdot, /, \exp(), \log(), \text{square}(), \text{sqrt}()\}$ . Numeric constants, as well as variables from the dataset, were allowed as terminal symbols. Different equation forms were derived using the data from this study and previous studies and used to identify an approximation that better fits their needs in terms of accuracy and simplicity and the final form was selected based on engineering judgment to be sufficiently simple (easy application) and accurate. The so-obtained models consisting of 2-3 parameters are summarized in Table 6.6. In particular, *CSRF* depends on *r*,  $f_{c,r=0}$  and *W/C* while *FSRF* depends only on *r* and *W/C*.

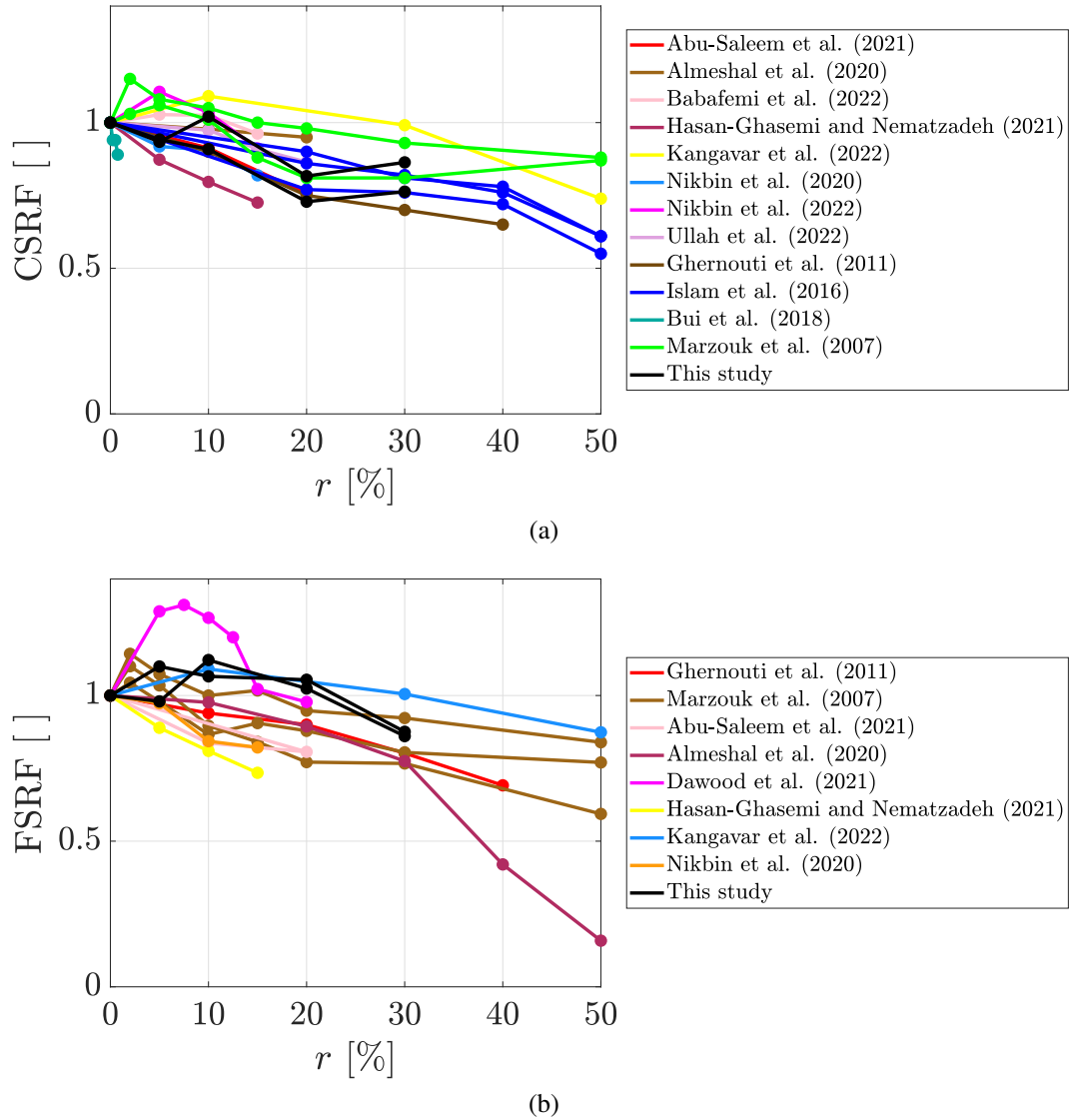


Figure 6.13 *CSRf* (a) and *FSRf* (b) as a function of  $r$  of concrete substituted by plastic aggregates from this study and literature [15–27]. Different colors indicate different studies and different markers and line style represents various factors, see Table 2.4 for details. For this study, the continuous black line refers to the PET case while the dashed black one to the MIX case



Table 6.6 Data-driven predictive models for *CSRF* and *FSRF*

Output	Model	$R^2$
<i>CSRF</i>	$\frac{0.06 \cdot \frac{W}{C} \cdot (2.49 - 2.497 \cdot r)}{0.549 \cdot f_c(r=0) - 6.95} + 0.9968$	0.71
<i>FSRF</i>	$\frac{0.032 \cdot r - 0.075 \left(\frac{W}{C} \cdot r\right)}{1.373 \cdot \frac{W}{C}} + 1.0449$	0.82

Figure 6.14 presents predicted vs. measured values for *CSRF* and *FSRF* using the models summarized in Table 6.6. The data are coming from this study and literature [15–27]. The obtained models are well predicting (considering the simple equation selected) the experimental data with a coefficient of determination of 0.71 for *CSRF* and 0.82 for *FSRF*.

The analysis reported in this discussion demonstrates that *CSRF* and *FSRF* of concrete with plastic aggregates strongly depend on different factors such as type and geometry (width, length, and thickness) of plastic aggregate and additives. Moreover, the type of aggregate of the mix design can have a strong influence. Further data collection and experimental studies are required to determine exactly how these factors affect *CSRF* and *FSRF*.

## 6.5 Conclusions

this thesis presented a pilot study on the characterization of the physical and mechanical properties of a novel green concrete with two different substituted recycled plastic aggregates. A reference mix with an average compressive strength of around 60MPa is considered. Recycled PET powder and recycled mixed plastic (PP and PET) granules were adopted to substitute fine and coarse aggregates. Two different substitution strategies are employed. In the first one, the PET powder is used to substitute the fine sand by volume. In the second one, the PET powder is used to substitute the fine sand while the recycled mixed plastic granules are used to substitute the coarse sand and fine coarse aggregates by volume (50% for PET powder and 50% for recycled mixed plastic granules). Four total replacement

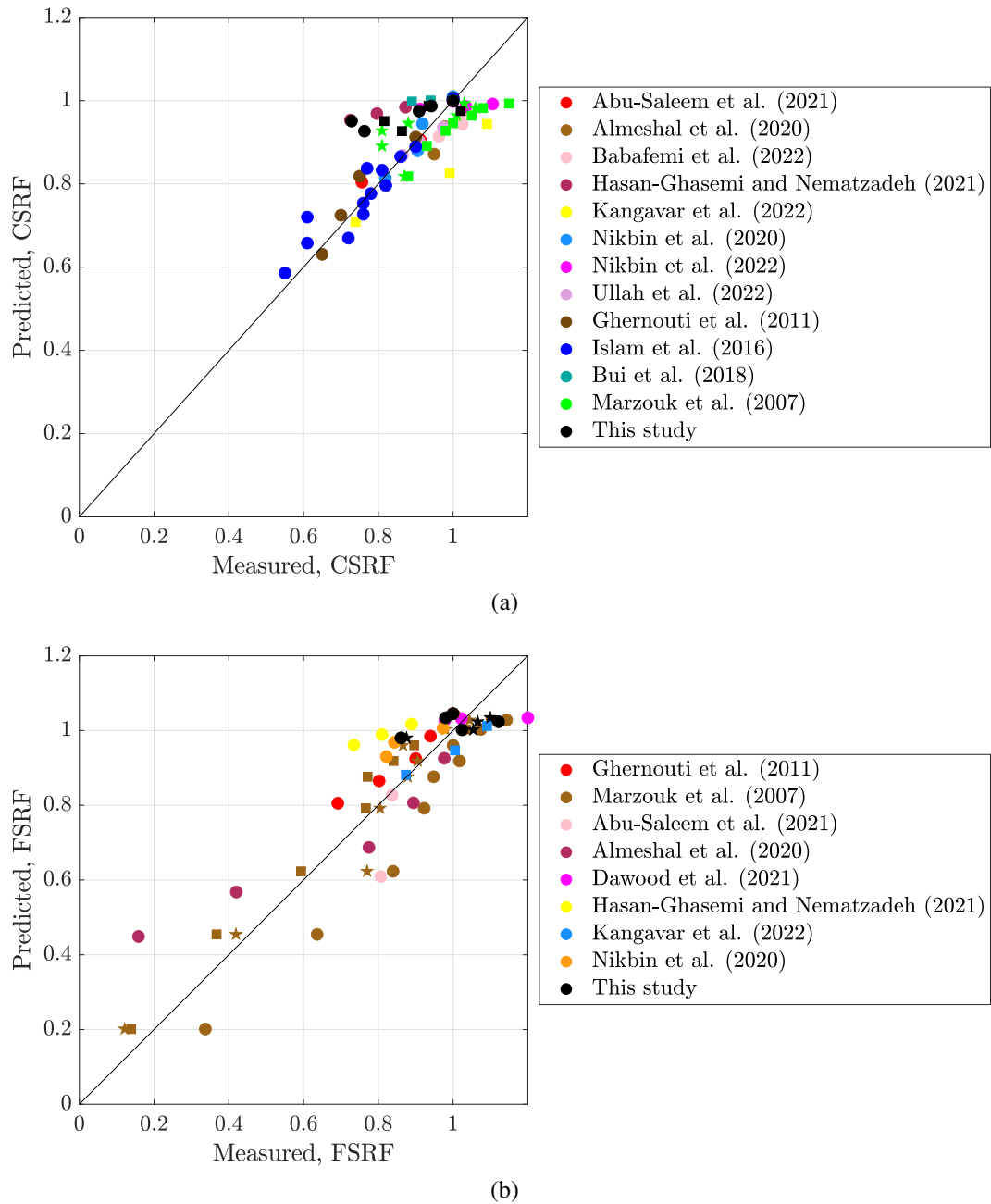


Figure 6.14 Comparison between the measured and predicted  $CSR_F$  (a) and  $FSRF$  (b) based on proposed model in Table 6.6. Data from this study and literature.[15–27]

levels (5%, 15%, 20%, and 30%) by volume were considered. The fresh concrete properties (slump and density), compressive and flexural behavior, toughness, and permeability were investigated. Finally, a micro-scale characterization of the plastic-paste interface is provided. Based on the experimental evidence, the following main conclusions can be drawn:

- The flowability is reduced for PET cases. For  $r = 30\%$ , the slump reduction ratio with respect to REF can reach more than 20%. A possible explanation for these results may be related to the sharper edges and more elongated shapes of PET powder which contribute to the reduction of slump and fluidity. An opposite trend was observed for the concrete with mix-plastic aggregate. The values of slump increased from 235 mm for REF up to 255 mm for  $r = 30\%$  with mix plastic granules. It seems possible that these results are due to the smoother out-surface and smaller surface area to volume ratio compared PET powder and their marked hydrophobic characteristic requiring less water during mixing. The good flowability of the MIX case can be essential in structural applications.
- The compressive strength is slightly reduced by a low substitution level ( $r \leq 10\%$ ) for both PET and MIX cases. For  $r \geq 20\%$ , the compressive strength reduction is more marked. Generally, slightly better performances were found for MIX cases. A possible explanation for this might be that the mix plastic aggregate is inducing an interlocking effect due to its peculiar geometry.
- The flexural strength is slightly improved for  $r \leq 20\%$  while it shows a sudden drop for  $r = 30\%$  for both PET and MIX cases. Relatively low substitution levels by plastic aggregate can fill up the micropores and enhance the interfacial bonding between the plastic aggregates and cement paste. Pet powder and mix plastic granules can induce a bridging effect similar to fibers which can improve the flexural strength. For high substitution levels, the reduction of the water absorbed by the aggregates increases the free water weakening the interfacial bonding between the plastic aggregate and cement paste. A similar trend is observed in terms of fracture toughness.
- The permeability of the novel green concrete was investigated through water penetration tests. The water penetration depth is slightly decreased for  $r \leq 10\%$  while it shows a sudden drop for  $r = 30\%$  for both PET and MIX cases. This



trend is similar to compressive strength. In fact, a considerable increase in the values of water penetration depth indicates a weak bond between plastic aggregate and cement paste and poor adhesion on the ITZ.

- The micro-scale analysis highlighted that presence of PET powder and mix-plastic granules can enhance micropores and micro-cracks. The ITZs analysis reveals a clear gap and a poor bond between the plastic aggregates and the cement paste compared to natural aggregate and cement paste. The observations reported on the micro-scale are consistent with the physical and mechanical properties observed at the mesoscale.
- An interpretation of the results of this study is done by comparing them with the results of previous studies. The results provided in this study are in agreement with the available literature. Taken together, these results suggest that the substituted plastic aggregates (type, grading, morphology, and material) have a great influence on mechanical behavior. Simple and at the same time reliable predictive equations were defined to estimate  $FSRF$  and  $CSRF$  making use of the symbolic regression technique. The relationships take into consideration  $W/C$ ,  $FA/C$  and  $r$  enabling estimates of flexural and compressive properties of concrete with two different substituted recycled plastic aggregates.

The results indicate generally good physical and mechanical performances of the proposed new green concrete. In light of this positive evidence, this novel green concrete appears a promising material for real application in structural engineering, and thus it is appropriate to move toward full-scale application.

# **Chapter 7**

## **Dynamic mechanical properties of concrete with two different substituted recycled plastic aggregates**

### **7.1 Materials and method**

#### **7.1.1 Materials**

The all materials adopted in this Chapter are same as the materials in Chapter 6. The details are shown in Section 6.1.

#### **7.1.2 Test specimens: mix design and cast**

9 different concrete mix design characterized by different substitution level and two types of plastic aggregate are conducted in this study. Four groups of mix design are only related to PET sand, fine sand is substituted by PET sand by volume at 5, 10, 20 and 30%. Another four mixtures adopted PET sand and mix-plastic granules. Considering the sieve results from 6.1 in previous chapter, PET sand replace fine sand and mix-plastic granules replace fine gravel. Keeping the total substitution level as before, here, the substitution level is 2.5, 5, 10. 15% substituted by PET sand and 2.5, 5, 10. 15% substituted by mix-plastic granules. The target compressive strength of standard cylindrical specimen for plain concrete (NAC) is 70 MPa. Concrete mix

design are listed in Table 7.1. The control of mixing order and time is adopted as following: First step, fine gravel (mix-plastic granules) and medium gravel were mixed together for about 30 seconds with a little water. Then the coarse sand was added and another a little water was also added for another 1 minute; After this, the fine sand mixed with PET sand firstly, then fine sand, PET sand and cement were added into mixer, in the meanwhile the water added intermittently with a small amount to control workability for another 2 minutes. Later superplasticizer was also added the material were mixed together for another 2 minutes, in this step, the workability should be observed carefully to avoid segregation. In this study, for each mix , three standard cylindrical molds with diameter of 150mm, height of 300mm were cast, and three small PVC cylinders with diameter of 79mm, height of 160mm for SHPB test were also cast. Before casting, the molds were cleaned and lubricated and mass were weighted. After mixing, the mixtures were immediately conducted with slump tests and then mixtures were poured into the cleaned and lubricated cylindrical molds, when the molds were filled at 1/3 location of height, a compacting rod was adopted for 15 seconds to compact the specimens, this procedure were repeated another two times until end of cast. After casting, the outer surface of specimens were cleaned and the weight of specimens were measured again.

Specimens were taken from the molds after 48 hours and then kept in the curing basin at a temperature of 20°C for 28 days. Before compressive tests, the weight of each specimen was checked to verify consistency. For each concrete type, a total of 6 specimens were cast namely 27 standard cylindrical specimens were used for quasi-static tests directly, 27 cylindrical specimens with a size of  $\Phi 79 \times H 160$ mm were cut into 3 smaller cylindrical specimens with a size of  $\Phi 79 \times H 39$ mm for SHPB testing. The cutting procedure are same with Xiong et al. [9, 75]. Regarding aspect ratio (ratio of the height to the diameter) of SHPB specimens should be sufficiently small to reduce inertial and friction effects in turns guaranteeing equilibrium conditions. Here the aspect ratio is 0.5 is adopted.

Table 7.1 Concrete mix proportion

Mix code	Natural aggregate				Plastic aggregate		Cement	Water	Superplasticizer
	Fine sand	Coarse sand	Fine gravel	Medium gravel	PET sand	Mix-plastic granule			
					kg/m <sup>3</sup>				
NAC	475	488	128	741	0	0			
PET5	451.25	488	128	741	11.88	0			
PET10	427.50	488	128	741	23.75	0			
PET20	380	488	128	741	47.5	0			
PET30	332.5	488	128	741	71.25	0	420	185	4.2
MIX5	463.13	481.90	126.40	741	5.94	2.33			
MIX10	451.25	475.80	124.80	741	11.88	4.65			
MIX20	427.50	463.60	121.60	741	23.75	9.3			
MIX30	403.75	451.4	118.40	741	35.63	13.95			

## 7.2 Quasi-static test program

### 7.2.1 Ultrasonic pulse velocity (UPV) test

The Ultrasonic pulse velocity (UPV) test is employed to examine the durability properties of concrete substituted by PET fiber and mix-plastic granules aggregates. UPV test is a non-destructive test used to estimate the quality of cementitious material like mortars and concrete. For concrete substituted by plastic aggregate, the micro cracks and pores can be more than plain concrete Ahmad et al. [324]. To improve the accuracy of the results of UPV tests, three cubic specimens with  $150 \times 150 \times 150 \text{ mm}^3$  and each symmetrical surface was detected and the results are determined by ASTM C597 [325]. A TICO<sup>®</sup> ultrasonic instrument is adopted in this study. The pulse velocity ( $V$ ) of each specimen, was calculated using the following equation:

$$V = \frac{S}{t} \quad (7.1)$$

where  $S$  is the distance between two transducers, and  $t$  is transmission times of an ultrasonic pulse passing through a concrete.

### 7.2.2 Quasi-static compressive test program

The two end-faces were cleaned and brushed before quasi static tests. The top end face is grinded by a grinder to guarantee the parallel between two end faces and reduce the static compressive stress concentration. The loading rate is  $0.6 \text{ mm/min}$  (corresponding to static strain rate at  $\dot{\epsilon}_s = 3 \times 10^{-5} \text{ S}^{-1}$ ) on the standard

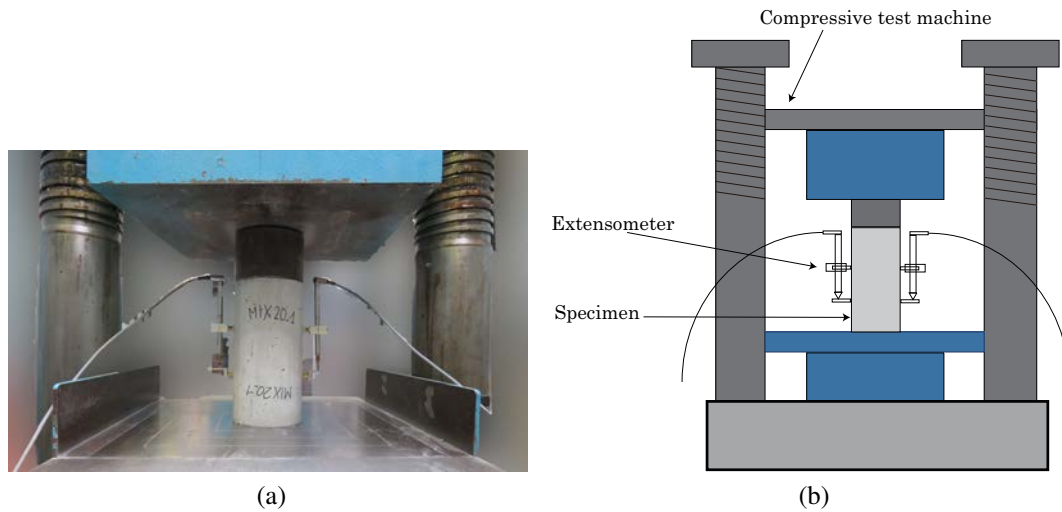


Figure 7.1 Quasi-static test apparatus

specimens by an universal test machine. Two linear variable displacement transducers (LVDTs) were fixed symmetrical to measure the axial deformations of the cylinders as shown in Figure 7.1. The deformation and loads are recorded automatically collected by a data acquisition system during static compressive tests in turn the static axial stress and strain curves can be achieved of concrete containing plastic aggregate.

### 7.2.3 Micro-scale characterization

The morphology of MIX30 concrete is investigated with a Scanning Electron Microscope (SEM, ZEISS Gemini SEM 300) at a system vacuum pressure of  $4.97 \times 10^{-5}$  mbar and at an accelerating voltage of 10kV. Energy Dispersive X-ray analyses using a Quantax energy-dispersive Electron Probe MicroAnalysis (EPMA) system (EDS) were then performed with an accelerating voltage of 10kV to determine the element components of cement paste, natural and plastic aggregates. Energy dispersive X-ray (EDX) analysis is a method of elemental detection via the collection of characteristic X-rays induced by electron beam radiation. EDX (Oxford Instruments X-Max EDS System) is performed to observe the chemical composition of the natural aggregate and of PET powder and mix-plastic granules.

## 7.3 High-strain rate test program

### 7.3.1 Apparatus and working principle

In this study, an 80 mm bar diameter SHPB apparatus was adopted. A schematic and photo of the SHPB are shown in Figure 7.2. The integrated SHPB system includes loading systems, bar system, data acquisition and recording system.

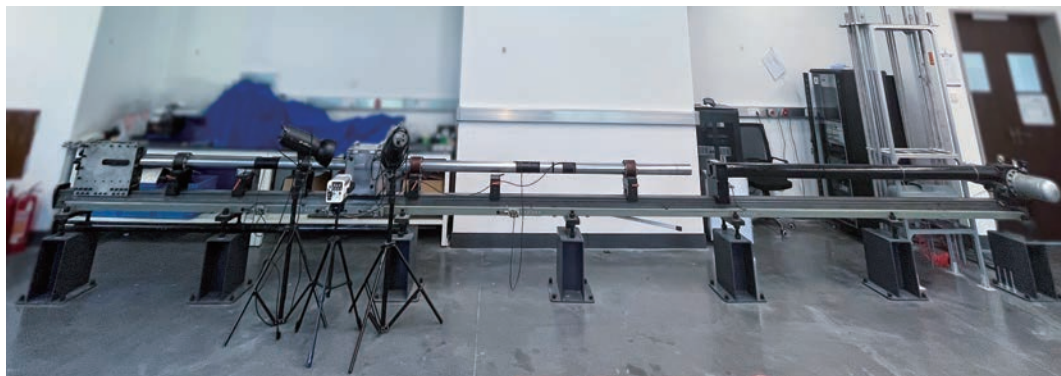
Loading system is component of striker and an air pressure gun, the striker is accelerated using a compressed air gun controlled in terms of air pressure,  $P_g$ . The minimum air pressure is  $P_g=0.02$  MPa while the maximum is  $P_g=1.6$  MPa for this loading system.

The SHPB bar system is mainly component of three same cross-section steel bar, namely  $\Phi = 80$  mm. The three bars are striker bar with length of 0.6 m, incident bar with length of 3 m and transmission bar with length of 2 m. To avoid stress wave overlapping at the strain gauge location, the incident bar should be at least twice as long as the striker, on the other hand, locations of the strain gauges should be far from the bar ends, particularly, they are mounted at least 10 bar diameters from both ends [87].

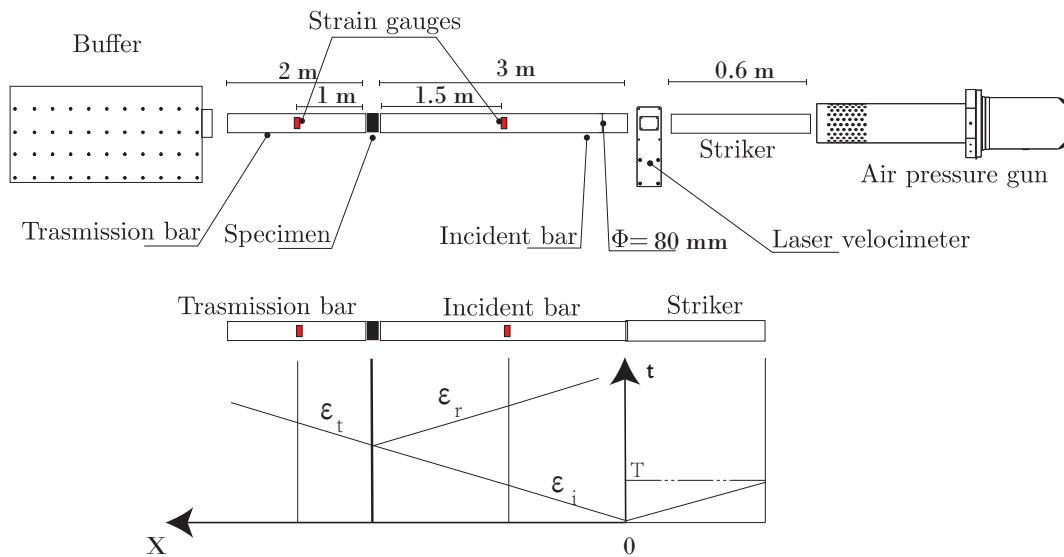
The three bars are made of 40CrMn hardened steel similar with [9, 75]. Young's modulus of bars is  $E_B = 208$  GPa and density is  $\rho = 7800$  kg/m<sup>3</sup> and yield strength is  $\sigma = 900$  MPa. The longitudinal speed of sound in the bar material,  $C_B$ , can be calculated as:

$$C_B = \sqrt{\frac{E_B}{\rho}} = 5164 \text{ m/s} \quad (7.2)$$

7.2 shows clearly that a laser velocimeter is located near at end of the incident bar to measure the impact velocity of the strike with the incident bar,  $v_i$ . The specimen is sandwiched between incident and transmission bar. A transparent cubic box with opening are surrounded the specimen in order to take a video for the destroy of specimen and easy to collect the fragments. At the end of the transmission bar, a buffer system made of two commercial elevator buffers installed in parallel to slow down and stop the transmission bar.



(a)



(b)

Figure 7.2 Photo (a) and schematic (b) of 80mmdiameter SHPB apparatus

Data acquisition and recording system is main component by strain gauges on the bars , a signal amplifier, an oscilloscope. Two strain gauges are usually attached symmetrically on the incident and transmission bar surface across a bar diameter.

The strain gauges are conditioned with a half-Wheatstone bridge with a low-pass filter 100kHz to pre-amplifier. Regarding the data acquisition system, a sampling frequency of 50MHz are adopted in this apparatus.

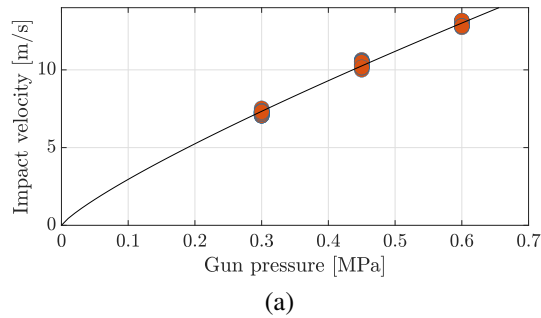


Figure 7.3 Relationship between the gun pressure and impact velocity

### 7.3.2 Calibration for the SHPB system

Before dynamic tests, a series of preliminary tests were carried out to validate and calibrate the signals from the SHPB apparatus. (1) The repeatability and controllability of impact system should be validated, the impact velocities ( $v_i$ ) under different air pressures ( $P_g$ ) were checked by repeating preliminary tests. The results are reported in Figure 7.3. A good repeatability of  $v_i$  can be observed from Figure 7.3,

Based on the repeating preliminary tests, an empirical predictive equation of the impact velocity as a function of the gun pressure was fitting by the least square method:

$$v_i = 19.85 \cdot P_g^{0.8271} \quad (7.3)$$

$v_i$  then can be applied to estimate the predicted amplitude of the incident wave  $\epsilon_p$  [87]:

$$\epsilon_p = \frac{1}{2} \frac{v_i}{C_B} \quad (7.4)$$

while the tested incident wave can be calculated from the strain gauges on the incident bar. Figure (b) reports the incidents wave adopted in this study.

The loading duration of the incident wave can be calculated by the length of striker bar,  $L_o$ :



$$T = \frac{2L_o}{C_B} = 232 \mu s \quad (7.5)$$

### 7.3.3 Test matrix and protocol

Dynamic compressive tests were conducted on cut specimens for 9 different types of concrete under three different gun pressure,  $P_g = 0.3, 0.45$  and  $0.6$  MPa, for each case, three repetitive tests were performed. The three tests with homogenous responses respecting the conditions discussed in 7.3.4 were taken.

Similar test protocol is adopted by [9, 75]. Before each test, the basically alignment between incident bar and transmission bar was checked by hand, and the end surfaces of striker, incident bar and transmission bar were cleaned by sandpaper. Then vaseline was applied on the two surface of specimen and the interfaces of transmission and incident bar contacted with specimen. The the concrete specimen was sandwiched between the incident and transmission bar. Then an agreeable rubber disc pulse shaper was guled on the end face of the incident bar on the contact side with the striker bar using vaseline which is easy to remove and avoid to destroy the end surface of the bar. The selection of rubber disc pulse shaper for different air pressure discussed in 7.3.5 were taken. During the test, the striker was launched at a prescribed gun pressure, the tank cannot hold the compressed air, the difference of the gun pressure is about  $\pm 0.05$  MPa. Then impact velocity was record. After tests, the debris was collected and photos were taken.

In this study, a high-speed camera (FASTCAM Nova S12, Photron Ltd.) was applied to monitor the deformation and failure progress of specimens. The camera is equipped a sampling frequency of 64000 fps and a resolution of  $512 \times 336$  pixels. The setting and trigger method are same with [73].

### 7.3.4 Validation of the tests

In this study, the variations of the engineering stress, strain and strain rate with time as well as the engineering stress–strain relation obtained by 3-wave formulate as follow:

$$F_1(t) = A_B \cdot E_B \cdot [\varepsilon_i(t) + \varepsilon_r(t + \tau_1)] \quad (7.6)$$

$$F_2(t) = A_B \cdot E_B \cdot \varepsilon_t(t + \tau_2) \quad (7.7)$$

$$\sigma_S(t) = \frac{F_1(t) + F_2(t)}{2A_S} \quad (7.8)$$

$$\dot{\varepsilon}(t) = -\frac{C_B}{L_S} [\varepsilon_i(t) - \varepsilon_r(t + \tau_1) - \varepsilon_t(t + \tau_2)] \quad (7.9)$$

$$\varepsilon(t) = -\frac{C_B}{L_S} \int_0^t [\varepsilon_i(t) - \varepsilon_r(t + \tau_1) - \varepsilon_t(t + \tau_2)] d\tau \quad (7.10)$$

where  $F_1$  and  $F_2$  are the forces acting on the two interfaces between the specimen and the incident/transmitter bars, the average stress of the specimens is  $\sigma_S$ , the strain ( $\varepsilon$ ) and the strain rate ( $\dot{\varepsilon}$ ) can be calculated.  $t$  is the time,  $A_B$  and  $A_S$  are the cross-sectional areas of the bar and the specimen, respectively,  $L_S$  is the length of the specimens and  $\tau_1$  and  $\tau_2$  are the time delays of  $\varepsilon_r$  and  $\varepsilon_t$  with respect to  $\varepsilon_i$  at two end face of the specimens.  $\tau_1$  and  $\tau_2$  were calculated following the procedure  $\tau_1$  and  $\tau_2$  can be calculated as following:

$$\tau_1 = \frac{L_I}{C_B} = \frac{3}{5164} = 581 \mu s \quad (7.11)$$

$$\tau_2 = \frac{L_I + L_T}{2C_B} + \frac{L_S}{C_S} = \frac{3 + 2}{2 \times 5164} + \frac{0.039}{C_S} = 484 + \frac{0.039}{\sqrt{E_C/\rho_C}} \quad (7.12)$$

where  $L_I$  and  $L_T$  are the length of the incident and transmission bars, respectively. The strain rate here is characterized as the values corresponding to the time when peak dynamic stress is reached [9]:  $\dot{\varepsilon} = \dot{\varepsilon}(t^*)$ .

Regarding the validation of the tests, the most significant step is to check the dynamic stress equilibrium condition [326], it can be simplified as  $\sigma_S A_S = \sigma_t A_B$  under perfect condition. Generally it is accepted that the dynamic stress equilibrium is achieved when the difference of dynamic stress between two ends of the specimen is less than 5% of the average axial stress at the time that the stress reached its peak values namely  $t = t^*$ .

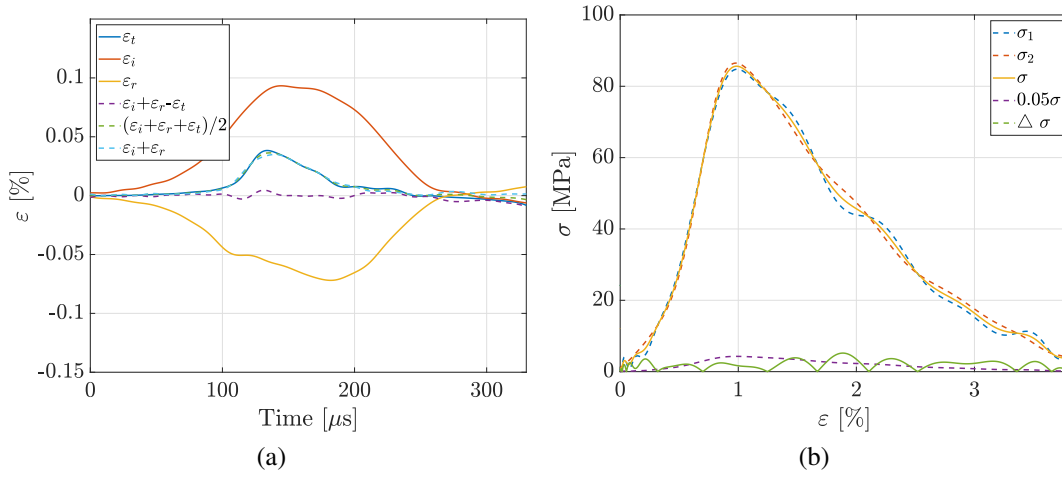


Figure 7.4 Three aligned waves ( $\varepsilon_i$ ;  $\varepsilon_r$  and  $\varepsilon_t$  aligned and equilibrium condition checking (a); stress-strain curve with averaged axial stress, the stress on the back and forth faces of specimen, stress equilibrium condition and their difference (b).

$$\Delta \sigma(t^*) = |\sigma_1(t^*) - \sigma_2(t^*)| = \left| \frac{F_1(t^*)}{A_s} - \frac{F_2(t^*)}{A_s} \right| \leq 0.05 \sigma_S(t^*) \quad (7.13)$$

### 7.3.5 Selection of pulse shaper

Pulse shaping technique is an universal method to achieve dynamic stress equilibrium and constant strain rate, minimize wave dispersion by modifying the square incident pulse into relatively ramp ones according to the response of the specimens [87, 9]. The selection of appropriate pulse shaper is affected by factors like striking velocity, material, and geometry of the striker [87], and the pulse shaper can be diversely varied from materials, geometry and dimensions. Common materials like copper or brass [75, 9, 73], aluminum [221], composite materials [327], rubber [328, 329] and paper [330] have been selected as pulse shaper for brittle materials. During the tests, the striker bar impacts on the soft pulse shaper disc first, due to the characterization of low strength and high ductility for pulse shaper materials, the disc is extensively compressed in turn producing a nearly linear but low-amplitude pulse, which is helpful to shape the incident waves. Previous researches [331, 332] have concluded that thickness and cross sectional area of the pulse shaper should be changed proportional to the gun pressure namely the strain rates, which means

the velocity of the striker bar holds significant function on selection of pulse shaper. Compared with copper, rubber is much cheaper and the easy to change the geometry. So in this study, the rubber disc is selected as the pulse shaper. Combined the pulse shape used in the research of Lai et al. [73], in this study, a rubber disc with diameter of 30 mm and thicknesses of 3mm for tests under  $P_g = 0.6$  MPa and  $P_g = 0.45$  MPa, while a rubber disc with diameter of 20 mm and thicknesses of 2mm for tests under  $P_g = 0.3$  MPa.

Figure 7.5 depicted the procedure on selection of pulse shaper under gun pressure at  $0.3 \pm 0.06$  MPa, here only incident waves were shown. For the gun pressure of 0.45 and 0.6 MPa, the similar procedure is conducted for choosing appropriate pulse shaper. It shows that without pulse shaping technique, the incident wave is relatively square, which means rising time of the incident waves can not ensure the time needed by specimen to satisfy stress equilibrium state. And a relatively large high-frequency component produced by the striker bar directly impacting can be seen. After the pulse shaping, the incident waves tends to be a ramp one and the rising time tends to be longer. Under same diameter, the thicker of rubber disc, the more apparent of the shaping effect. In this study, a rubber disc with thickness of 2 mm and diameter of 20 mm is selected.

## 7.4 Results

### 7.4.1 Fresh state properties

The slump test is the most widely used test method to characterize the consistency of fresh concrete. Slump flow value, which is used for the description of the fluidity of a fresh concrete in unconfined conditions, is a sensitive test. It is the primary check for the fresh concrete consistence to meet the specification. Thus, it can normally be specified for all self-compacting concretes. Moreover, additional information about segregation resistance and uniformity of concrete can be achieved from the visual observations during the test [298]. The slump values for each of concrete mixtures are shown in the Table 7.2. The values of slump flow diameter with different  $r$  at 0 min are also shown in the Table. 7.2.

It can be observed that the slump values of all mixture were more than 180 mm and with maximum value at about 255 mm. The volume of superplasticizer was

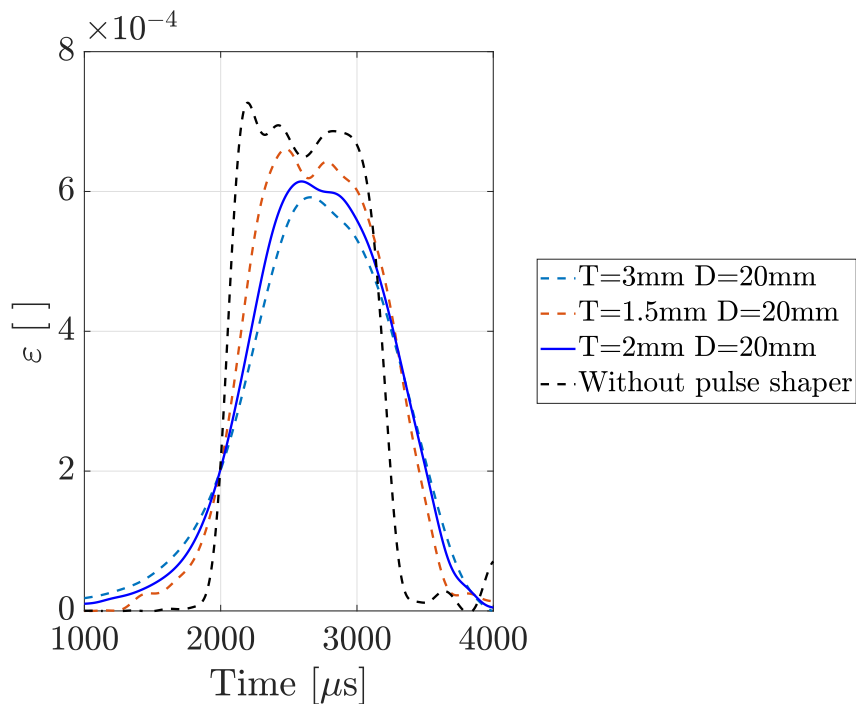


Figure 7.5 Selection of pulse shaper

always kept same at  $4.2 \text{ kg/m}^3$ . For NAC, the slump is 235mm, and diameter of slump flow is 410mm, which concrete can be defined as good workability concrete. Table 7.2 clearly reported that with increasing PET sand, the slump of PET sand decreased, when  $r = 30\%$ , slump reduction ratio can reach more than 20% compared with reference concrete which witnessed a great loss of slump for  $r = 30\%$  although a slightly increase can be observed when  $r = 10\%$  increases to  $r = 20\%$ . Regarding the PET sand replace fine aggregate of concrete, the sharper edges and relatively elongated shapes of PET sand than natural fine and coarse aggregate contributes to the reduction of slump and fluidity [126, 125, 1], sharp edges of the plastic aggregate decrease the lubrication during the mixing process, which in turn decrease the values of slump and flow. Another cause of the workability reduction can be explain as follow. The  $w/c$  ratio, coarse aggregate content and super-plasticizer were kept at constant from  $r = 0$  to  $r = 30\%$  for PET concrete, when the fine aggregate was replace by PET sand, accompanied with the distribution of aggregate 5.2, PET sand induced in a large proportion of very fine particles and sand, the surface area (SA) ratio was increased therefore more free water was surrounded by PET sand [131].

Table 7.2 Slump values of concrete mixture

Mix code [-]	Fine aggregate content	PET sand content [kg/m <sup>3</sup> ]	Mix plastic granules content	Slump [mm]	Slump flow [mm]	Visual inspection [-]	Fresh density [kg/m <sup>3</sup> ]
NAC	475	0	0	235	410	Homogenous and bleeding	2454
PET5	451.25	11.88	0	215	370	Homogenous but less consistent	2424
PET10	427.50	23.75	0	200	325	Homogenous and bleeding	2428
PET20	380	47.5	0	205	338	Consistent and homogenous	2412
PET30	332.50	71.25	0	180	305	Consistent and homogenous	2389
MIX5	463.13	5.94	2.33	210	335	Homogenous but less consistent	2434
MIX10	451.25	11.88	4.65	240	462.5	Harsh with bleeding	2442
MIX20	427.50	23.75	9.3	250	450	Harsh with bleeding	2420
MIX30	403.75	35.63	13.95	255	478	Harsh with bleeding	2392

However, the opposite fashion can be observed in concrete with mix plastic aggregate. The values of slump increased from 235mm of  $r = 0$  to 255mm of  $r = 30\%$  with mix plastic granules. Previous studies [23, 126, 128] observed an apparently increase in slump when coarse aggregate was substituted by PET granules. Combined with observation of PET substituted concrete, the results can be explained as follow. Mix plastic granules have a smoother out-surface than PET sand and the hydrophobic characteristic for plastic required less water during mixing which contributed to a high slump and flow. In this study, with having both PET and mix plastic granules in one same concrete mixture, the function for granules of lubricating are stronger than the function for PET sand of decreasing lubrication. Thence a limited increase in slump and flow can be observed in the study compared with investigation of coarse/ fine aggregate only replaced by plastic granules [23, 126, 128].

Table 7.2 also presented the fresh density. The fresh density of reference concrete is  $2454\text{kg}/\text{m}^3$ , while with  $r = 30\%$ , the fresh density is about  $2390\text{kg}/\text{m}^3$ . The results showed a non-linear fashion decrease on fresh density. Under same  $r$ , the loss of fresh density is slightly lower for concrete with mix plastic than that with PET. Compared with previous studies of [132, 121, 124, 128, 120, 118], the loss of fresh density is less significant. In previous papers, only coarse/fine aggregate was substituted by plastic and the function of two different types and shapes of plastic aggregate is undefined. This studies confirmed the relatively superior properties of PET sand than other plastic granules regarding the fresh density reduction.

## 7.4.2 UPV

UPV tests can be used to determine the casting quality, the consistency and uniformity of the concrete. The values of UPV are determined on the porosity,

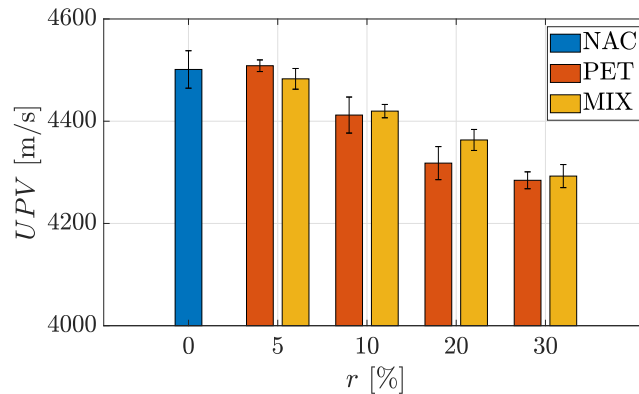


Figure 7.6 Effect of recycled plastic aggregates with  $r$  on UPV tests of different concrete

aggregate type, the density of the concrete in this thesis [333]. The UPV values fall in the range of 3660 – 4575 m/s represent high quality concrete [334], the values of UPV showed in Figure 7.6 of this study are all in range of 4200 – 4575 m/s, which indicates the specimens are high quality concrete specimens. A non-linear decrease with  $r$  can be observed from Figure 7.6. Under low level of substitution, although the density of the specimens is relatively lighter because of the lighter density of plastic aggregate and more free water can volatilize, but the finer flakey PET sands can fill the pores produced by the natural aggregate and cement paste, and the micro cracks are not increasing under low  $r$  (e.g.  $r = 5\%$  in this study). With continuing increasing of  $r$ , the impedance (i.e.,  $\sqrt{E/\rho}$ ) decreases and porosity increase, which in turn attributes to reduction of UPV values. The maximum reduction ratio of UPV compared to NAC are near 5% in  $r = 5\%$ , regardless of the plastic types. Considering the observation in process in mixing, the results showed under good and suitable mix design and application of good graded aggregates, the UPV values not decrease largely. For both case of PET and MIX, when  $r > 10\%$ , the values of UPV belong to MIX are relatively higher than PET, which attributed to the larger size of MIX granule compared to flaky PET sand, longer granule can function as long fiber, which can enhance a dense concrete.

### 7.4.3 Quasi-static compressive behavior

Figure 7.7 depicts static compressive stress strain graphs of concrete with different plastic aggregates and different  $r$ . The data from extensometer was collected until extensometer failure (not concrete failure), herein, the curve just shows the

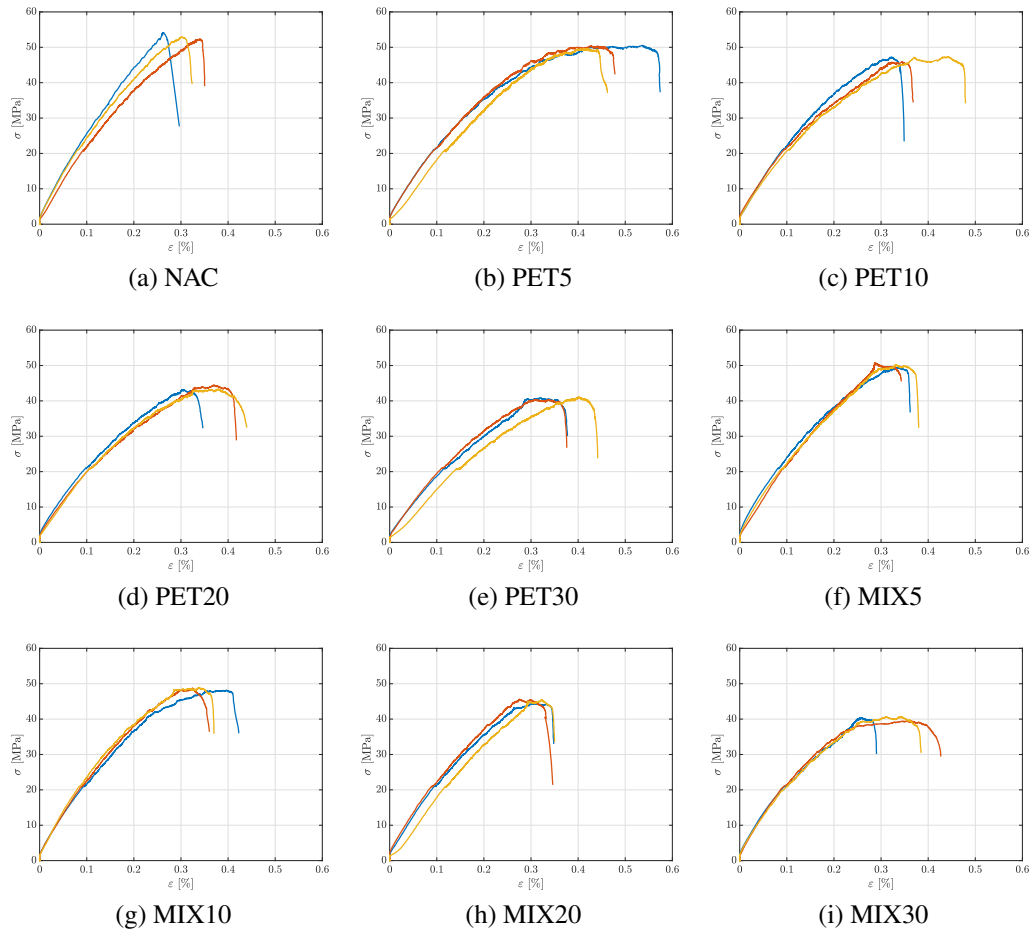


Figure 7.7 Static stress-strain relationship curves

maximum stress and failure strain. From figures, it can be clearly observed that regardless of  $r$  and type, the ultimate stress is lower than the NAC. The highest decrease in static compressive strength is observed at 25% and lowest reduction in static strength is 6% at  $r = 5\%$  irrespective of plastic type. A converse observation can be seen for strain corresponding to the peak stress, with increasing  $r$ , the strain corresponding to the peak stress increases evidently for concrete only replaced by single PET sand, while for concrete containing PET and mix-plastic granules, the strain corresponding to the peak stress not increases with  $r$ . Under same total  $r$ , concrete containing PET shows a higher failure strain than concrete containing two types of plastic aggregate.

The compressive strength reduction factor (SRF) is induced as:



$$SRF = \frac{f_{c,r}}{f_{c,r=0}} \quad (7.14)$$

herein,  $f_{c,r}$  is the compressive strength of concrete substituted by different level of plastic aggregate. The results of compressive strength and elastic modulus are presented in Table 7.3. A noticeable decrease on strength with increasing  $r$  can be seen from table. The decrease in the static compressive strength may be attributed to a weak bond between plastic aggregate and cement mortar resulting in a weak interfacial transition zone (ITZ).

The quasi-static elastic modulus is computed based on ASTM C469 [335] as:

$$E_c = \text{mean} \left( \frac{\sigma_a - \sigma_b}{\varepsilon_a - \varepsilon_b} \right) \quad (7.15)$$

where  $\sigma_a$  and  $\varepsilon_a$  are the quasi-static stress and strain corresponding to 40% of the peak stress and  $\sigma_b$  is the quasi-static stress corresponding to  $\varepsilon_b = 5 \times 10^{-5}$ .

Generally the elastic modulus reduces with increasing  $r$ . As plastic aggregates are less stiff than the natural aggregates, its incorporation in concrete mixture decreases concrete stiffness, the elastic modulus in turn decreases. The elastic modulus is in the range of 19.5 – 22MPa for concrete replaced by PET fiber while it is in the range of 23.5 – 26MPa for concrete substituted by both PET fiber and mix-plastic granules at same time. Concrete containing mix-plastic granules and PET fiber is much stiff than concrete only containing PET fiber. Same finding can be observed in research of 336, where the study depicted that the granule-type plastic aggregate concrete with its regular shape was much stiff compared to the irregular shaped flake- and elongated-shaped fiber-type plastic aggregate concrete. Lower unit weight, elastic modulus, compressive strength of plastic aggregate compared to natural aggregate induce lower elastic modulus of plastic aggregate concrete than NAC. ITZ also is responsible for the elastic modulus, weaker interfacial transition zone (ITZ) and bond funtion decease elastic modulus. when  $r = 10\%$  for two kind of concrete, a slightly increase can be observed compared with  $r = 5\%$ , the increase may arise from that the concrete porosity is filled by the PET sand enhancing the elastic modulus while when  $r$  continuing to increase, a worse bond between cement and aggregate induced, and ten compressive strength and elastic modulus declines.

Table 7.3 Quasi-static compressive properties of different mixes.  $f_c$ : the compressive strength;  $SRF$ : Strength Reduction Factor (see Eq. 5.13);  $E_c$ : Elastic modulus (see Eq. 7.15);  $ERF$ : Elastic modulus Reduction Factor. The number reported in the table are the mean. When the variable is followed by the numbers inside the brackets, e.g.,  $f_c$  (1;2;3), indicates that the results refers to the first, second and third test, respectively.  $SRF$  and  $ERF$  are the mean of the three repetitions.

Specimen tag [-]	$f_c$ (1;2;3) [MPa]	$SRF$ [-]	$E_c$ (1;2;3) [GPa]	$ERF$ [-]
NAC	53.2 (54.2; 52.3; 53.0) (0.78)	1	30.15 (32.45; 27.85; 30.16) (1.88)	1
PET5	50.2 (50.5; 50.4; 49.6) (0.40)	0.94	24.93 (26.10; 26.30; 22.39) (1.80)	0.83
PET10	46.9 (47.2; 46.0; 47.4) (0.62)	0.88	26.90 (28.62; 26.79; 25.29) (1.36)	0.89
PET20	43.7 (43.2; 44.5; 43.3) (0.59)	0.82	24.94 (25.94; 24.10; 24.78) (0.76)	0.83
PET30	40.8 (40.9; 40.4; 41.1) (0.29)	0.77	21.87 (22.53; 24.23; 18.86) (2.24)	0.73
MIX5	50.2 (49.6; 50.8; 50.3) (0.49)	0.94	27.45 (28.46; 27.23; 26.66) (0.75)	0.91
MIX10	48.6 (48.2; 48.8; 48.8) (0.28)	0.91	29.42 (27.79; 29.19; 31.27) (1.43)	0.98
MIX20	45.2 (44.5; 45.6; 45.4) (0.48)	0.85	26.30 (27.52; 28.34; 23.05) (2.32)	0.87
MIX30	40.2 (40.3; 39.5; 40.7) (0.50)	0.76	28.21 (28.20, 29.59; 26.84) (1.12)	0.94

Equations 7.16 and 7.17 show the elastic modulus for various compressive strength calculated by ACI 318-05 and CEB-FIP (2010) [28, 29].

$$E_c = 15.1 \times \left(\frac{f_c}{10}\right)^{1/3} \quad (7.16)$$

$$E_c = 0.043W^{1.5} \cdot \sqrt{f_c} \quad (7.17)$$

where  $E_c$ : Modulus of elasticity of concrete, GPa;  $W$ : Unit weight, kg/m<sup>3</sup>; and  $f_c$ : Compressive strength, MPa.

7.8 present the relationship between elastic modulus and compressive strength from ACI 318-05 and CEB-FIP (2010) [28, 29] and results from this study. For NAC, it fits the curve of CEB-FIP (2010), while for concrete containing plastic aggregate, the values are slightly less than the values computed using the equation proposed by CEB-FIP (2010), which is attributed to the characterize of plastic aggregate like low unit weight, elastic modulus, compressive strength and weak bond between cement paste and plastic aggregate.

The failure modes of all concrete standard cylindrical specimens after quasi-static axial compressive tests are presented in Figure 7.9. Regarding the failure patterns are similar in one same series of concrete, only one representative patterns is selected.

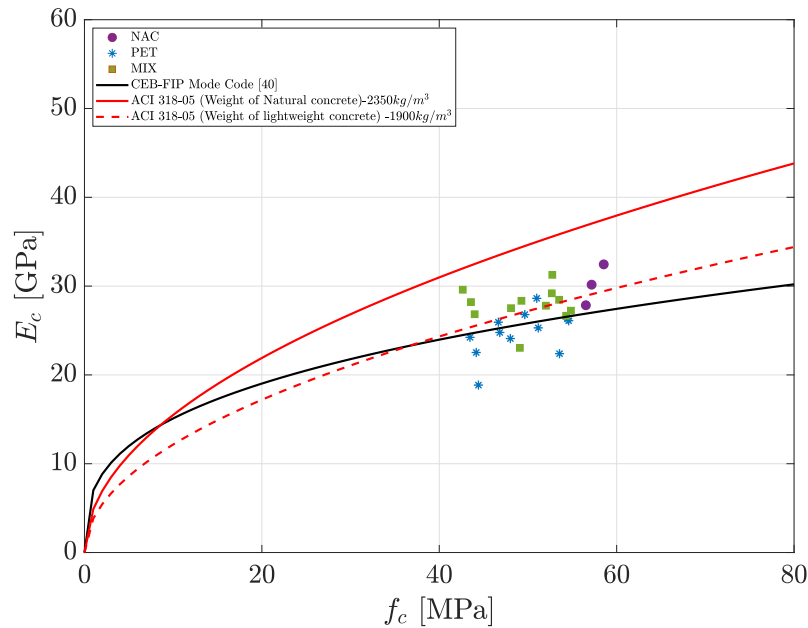


Figure 7.8 Comparison of the elastic modulus calculated using ACI 318-05 [28] and CEB-FIP [29] models and experimental values of concrete from present study.

Generally, the final failure modes for natural and recycled plastic aggregates are quite different. For NAC, it can be characterized as a typical "x" cone-shear shape, some major cracks running along the vertical direction at middle location of the cylinder can be observed. For both two types of plastic aggregate concrete, an increase in width, length, and the number of cracks can be observed with the increase in  $r$ . Regarding concrete only containing PET sand, separation of concrete chunks from the test specimen can be observed in specimens while no such separation was observed in concrete specimens containing PET fiber and mix-plastic granules, which could be related to the collaborative bridging of cracks by plastic granules and PET fiber together [337]. In particular, in case of concrete only containing PET, a major diagonal cracks can be seen through specimens, the failure mode can be characterized as a core and shear shape, while concrete containing both PET fiber and mix-plastic granules, a more diffused micro-crack net characterized by some macro cracks through one end to mid-height of specimens, presenting a more ductile and progressive failure pattern.



Figure 7.9 Typical failure modes under static loading of standard cylinder specimens for NAC, PET and MIX with different r.

#### 7.4.4 High-strain rate compressive behavior

Figure 7.10 presents stress-strain curves for different dynamic tests on concrete substituted by different type of recycled plastic aggregate with different values of  $r$ . In each subfigures, different  $P_g$  namely 0.3, 0.45 and 0.6 MPa are depicted as different color. An initial zero stiffness can be seen in some stress-strain curves which is attributed to the small gap between the bar and specimen [338].

Generally, concrete substituted by recycled plastic namely PET and MIX are characterized by similar typical behavior. Overall, the all dynamic stress-strain consists of two main phrases: 1) an initial linear portion lasting up to about 60–70 of the peak stress; 2) the curves become non-linear as the strain continues to increase and small increments in dynamic stress representing a reduction in stiffness. Especially, in case of  $P_g = 0.3 \text{ MPa}$ , a strain hardening portion at the end can be observed. It indicates that less brittle behavior can be witnessed in case of  $P_g = 0.3 \text{ MPa}$  compared with 0.45 and 0.6 MPa. Combining with high-speed camera videos and 7.10, another observation can be given that one NAC specimen was not total broken and having an evident recovery phase. It also showed that with increasing  $P_g$ , a clearly increase can be obtained in the dynamic compressive while ultimate dynamic strain showed a random fashion, which indicates the concrete substituted by recycled plastic aggregate are the strain rate dependent material.

With increasing  $r$ , different dynamic behaviors can be identified as a function of  $P_g$ . Under same  $P_g$ , with increasing  $r$ , a slightly decrease can be observed in dynamic compressive strength, especially for  $r$  increases from 10% to 30%, when  $r = 5\%$ , the average highest dynamic compressive strength can be obtained. The findings are in good agreement with the results of quasi-static compressive strength. After the stress reaches the peak, the stress start to drop, all cases showed a nonlinear behavior. The reduction attributed to the weak bond of ITZ between cement paste and aggregates including natural and recycled plastic aggregates. Comparing NAC with concrete substituted by recycled plastic aggregate, the curves exhibit a remarked decrease of dynamic stress and increase of final strain. A possible explanation for this might be that recycled plastic aggregates have the characteristics of softness and ductility compared to natural aggregate, which leading to a a better energy absorption.

Energy absorption capacity or toughness is obtained by the stress-strain curve, which can represent the ability of concrete to resist fracture under loading. The

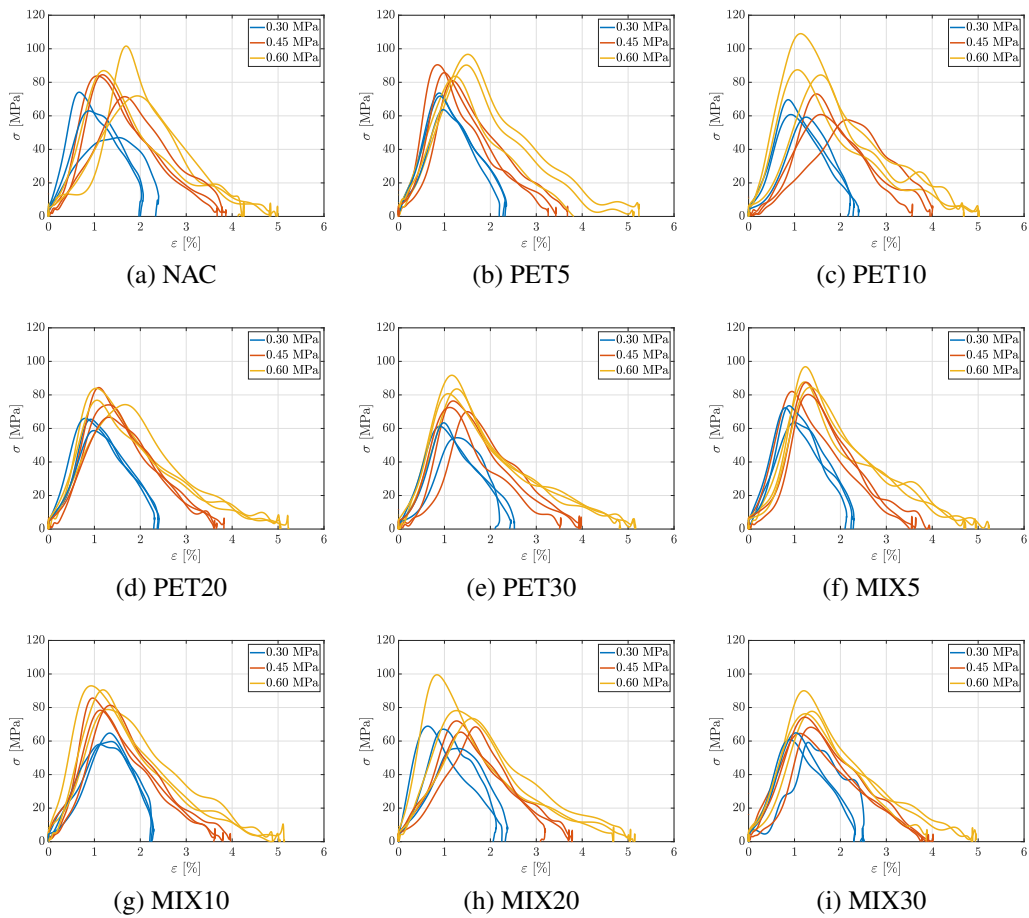


Figure 7.10 Stress–strain curves for different dynamic tests under each gun pressure

energy absorption can be calculated by the area enclosed by the stress-strain curves showed in Figure 7.10. Herein, one specific energy absorption density (per unit of volume of the specimen) are selected to characterize energy absorption capacity. It can be used to measure the absorb impact energy in terms of energy accumulated before the failure.

$$\tilde{\omega} = \int_0^{\varepsilon_*} \sigma(\varepsilon) d\varepsilon \quad (7.18)$$

where  $\varepsilon_*$  is the axial strain corresponding to the peak stress,  $\sigma$  and  $\varepsilon$  are the dynamic stress and strain, respectively.

Figure 7.11 and Table 7.4 exhibit the results of energy absorption density by application of the Eq.7.18 to the dynamic stress-stress curves showed in Figure 7.10. It is noteworthy that  $\tilde{\omega}$  is considered as a benchmark to divide the curves into two regions, namely, pre-peak and post-peak region. Overall, with increasing  $P_g$ , value of  $\tilde{\omega}$  also increases. Especially for NAC, when  $P_g$  increases from 0.3 MPa to 0.6 MPa,  $\tilde{\omega}$  improved 178% compared with 0.37 for  $P_g = 0.3$  MPa. While the maximum increase ratio is 194% and 177% for PET10 and MIX30, respectively. The minimum increase ratio is 167% and 177% for PET30 and MIX10.

Overall, under same  $P_g$ , increasing  $r$  induces different level of reduction of  $\tilde{\omega}$  in case of PET, but it induce a complicated change of  $\tilde{\omega}$  in case of MIX. The observations are similar with study of Hu et al. [185]. Although the soft PET flakes can improve the energy absorption, however, the increment in strain is not enough to compensate for the largely negative effect of the compressive strength reduction, which in the end induce a reduction in  $\tilde{\omega}$ . Under 0.3 MPa, the largest decrease is about 16% for PET30 and MIX30 compared to NAC, while  $\tilde{\omega}$  of MIX10 increase 16%. When  $P_g = 0.45$  MPa, PET10 keep the same value with NAC, while the value improve about 4% for MIX20. When  $P_g = 0.45$  MPa, a relatively decrease can be observation in all case regardless the type of plastic, the maximum decrease is about 20% for PET30 and MIX5. The difference of  $\tilde{\omega}$  induced by PET flakes and mix-plastic granules are attributed to the morphology. PET flakes have a higher aspect ratio than mix-plastic granules, so PET flakes can cause side wall effect of interface bonding Hu et al. [185] which is negative to  $\tilde{\omega}$ , especially in case of  $P_g$  under 0.3 MPa and 0.45 MPa. However, in case of 0.6 MPa, the impact energy is mainly dissipated by the micro cracks and weak ITZs and the major cracks have less relationship with  $\tilde{\omega}$ . Since different specimens obtain different strain rates even



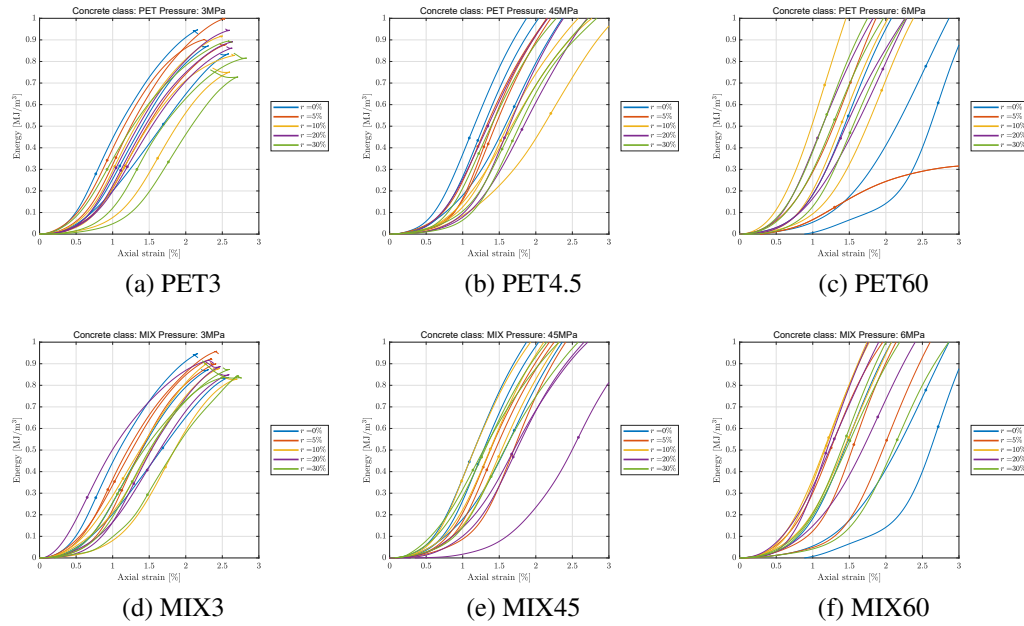


Figure 7.11 Energy absorption density as a function of the axial strain for NAC ( $r = 0\%$ ), PET and MIX tests. The circle mark is representing the point corresponding to the peak stress.

under the same  $P_g$ , the change law is complicated, which may induce the difference of  $\tilde{\omega}$  for different type of plastic. Therefore, the problem needs more research and experimental investigations.

The typical final failure modes of NAC, PET and MIX concrete specimens and pulse shaper with various  $r$  after dynamic tests are shown in Figure 7.12. Only one representative specimen is selected from three repeated tests. It should be noted that photos are taken after finishing tests and additional damage caused by moving debris are produced.

Table 7.4 Energy absorption density at peak stress,  $\tilde{\omega}$  (unit: MJ/m<sup>3</sup>). When the variable is followed by the numbers inside the brackets, e.g., 0.33 (0.35; 0.31; 0.33), indicates that the results refers to the first, second and third test, respectively.

$P_g$ [MPa]	NAC	PET5	PET10	PET20	PET30
0.3	0.36 (0.50; 0.27; 0.31)	0.33 (0.35; 0.31; 0.33)	0.32 (0.31; 0.30; 0.34)	0.30 (0.29; 0.30; 0.30)	0.30 (0.33; 0.29; 0.29)
0.45	0.48 (0.43; 0.42; 0.58)	0.40 (0.40; 0.39; 0.41)	0.47 (0.42; 0.54; 0.45)	0.47 (0.44; 0.49; 0.47)	0.44 (0.36; 0.49; 0.47)
0.6	0.63 (0.59; 0.53; 0.76)	0.69 (0.69; 0.58; 0.80)	0.61 (0.51; 0.67; 0.65)	0.54 (0.43; 0.75; 0.43)	0.51 (0.54; 0.52; 0.46)
$P_g$ [MPa]	NAC	MIX5	MIX10	MIX20	MIX30
0.3	0.36 (0.50; 0.27; 0.31)	0.32 (0.35; 0.31; 0.31)	0.42 (0.49; 0.36; 0.41)	0.33 (0.27; 0.33; 0.40)	0.31 (0.29; 0.29; 0.35)
0.45	0.48 (0.43; 0.42; 0.58)	0.43 (0.41; 0.40; 0.47)	0.44 (0.35; 0.46; 0.50)	0.49 (0.46; 0.55; 0.47)	0.47 (0.40; 0.55; 0.47)
0.6	0.63 (0.59; 0.53; 0.76)	0.51 (0.50; 0.51; 0.53)	0.53 (0.54; 0.51; 0.54)	0.55 (0.47; 0.54; 0.64)	0.54 (0.55; 0.53; 0.53)



Generally, more debris and reduction of the fragments with increasing  $P_g$  can be observed in Figure 7.12. Considering the failure of pulser shaper, after dynamic tests, the rubber disc are falling from the end of incident bar, and it is even with a lightly hot temperature after a short time. The rubber discs are crushed to be larger and thinner with increasing  $P_g$ . The rubber discs used in NAC tests can keep an integral shape after tests, while rubber discs used in other series of concrete tests, a different level of damage can be observed in rubber discs which is related with the energy absorption capacity of different types of concrete. Especially, under  $P_g = 0.3$  MPa, the rubber discs just become thinner and have a slightly damage. When  $P_g$  continues to increase, the rubber discs become thinner and with critically torn and split like in case of PET30 and MIX30.

Regarding NAC specimens, under 0.3 MPa, the specimens break into some main fragments and the major cracks on the fragment can be seen, with increasing  $P_g$ , the smaller fragments are shown and the cracks are shorter and dense. When  $P_g$  reaches 0.6 MPa, many coarse aggregates can be seen. For concrete only substituted by PET, under  $P_g = 0.3$  MPa, the specimens break into some pieces, and on the fragments are accompanied by major cracks, with increasing  $P_g$ , the fragments are smaller and the amount of debris increases, when  $P_g$  increases at 0.6 MPa, the coarse aggregates are also broken and separated, among the fragments, some white and transparent PET flakes can be seen, especially in case of PET30. Similar observation can be obtained in concrete substituted by PET flakes and mix-plastic granules, with increasing  $P_g$ , the black plastic granules are extruded from the specimens, and under  $P_g = 0.6$  MPa, the granules even can be seen crushed and squashed.

### 7.4.5 Micro-scale characterization

Figure 7.13 shows SEM images (at two magnification factors) of the natural aggregate and plastic aggregates. The slices for SEM images and EDS analysis are collected from fragments of NAC, PET30 and MIX30 after static compressive tests. In particular, Figure 7.13a presents SEM images for the NAC. Figure 7.13b reports SEM images for PET30 and Figure 7.13c shows SEM images for MIX30. The specimen in Figure 7.13c was also adopted for point EDX analysis and defined as spectrum 1, 2, and 3. The results of the EDX analyses are provided in Figure 7.14 for the natural aggregate and PET and mix aggregates. The analytical method of EDX was also used to determine the elements (elemental composition) present.

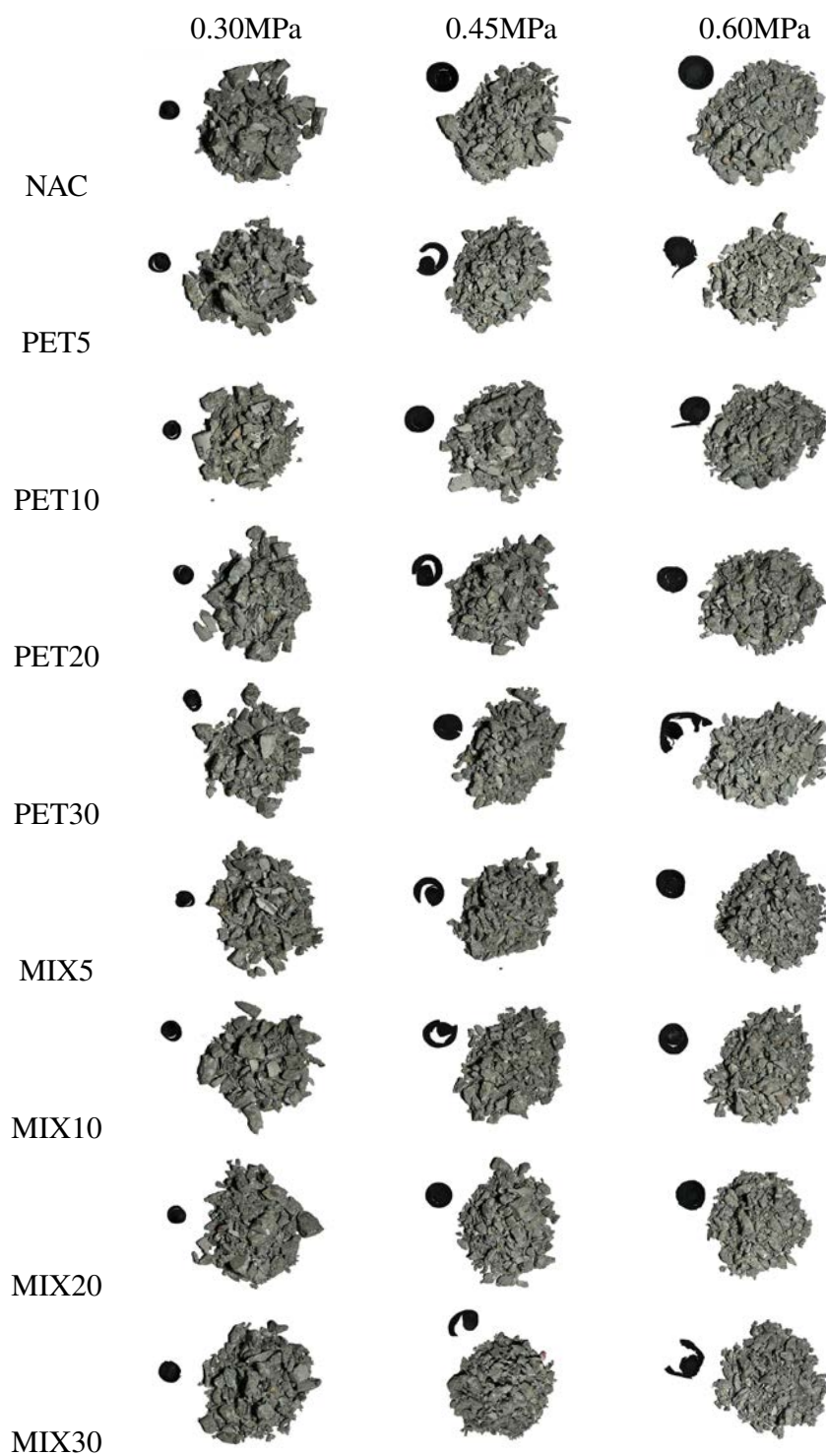


Figure 7.12 Failure modes of SHPB tests

In all SEM images, micropores and micro-cracks can be observed. With the presence of PET fibers and mix-plastic granules, the more micropores, and micro-cracks. The SEM images at a high magnification factor show the ITZs between the aggregates (natural and plastic aggregates) and the cement matrix. The ITZ reveals a clear gap and a poor bond between the plastic aggregates and the cement paste compared to natural aggregate and cement paste. Another clear observation can be seen that the failure is along with the granules and the shape of granules is still integral and the surface of granules is relatively smoother after failure while PET fiber is pulled off and scratched. Generally, PET powder shows a rough surface with scratches resulting from the manufacturing process. A similar surface was found in previous literature [15]. The presence of these scratches (roughness) on the PET surface slightly enhances the bond with cement paste for a low level of substitution.

EDX analysis was performed on the selected natural aggregates (fine and coarse aggregate) with cement paste and plastic aggregates (PET fiber and plastic granules) with a limited amount of cement paste on the surface. Figure 7.14a shows that the major elements are O, Ca, C, Si (see graph on the right side of each subfigure). The observed elemental composition is compatible with sand that is formed by  $\text{SiO}_2$ , and coarse aggregate primarily formed by  $\text{CaCO}_3$ . The presence of Al can be attributed to the presence of  $\text{Al}_2\text{O}_3$  [317].

On the other hand, the major elements shown in Figures 7.14c and 7.14c are O and C. The observed elemental composition is compatible with plastic aggregates (PET or PE). In fact, PET and PE can be identified as a polymer composed of carbon (C) and oxygen (O) (see Table 2.1). The small amount of Ca can be attributed to cement paste coated on the plastic aggregate.

## 7.5 Discussion

### 7.5.1 Dynamic increase factor

Figure 7.15 depicts the DIF (calculated by 5.13) as a function of the strain rate for NAC and concrete substituted by recycled plastic, in each figure, each DIF is represented by an asterisk and different gun pressure is indicated by a different color.

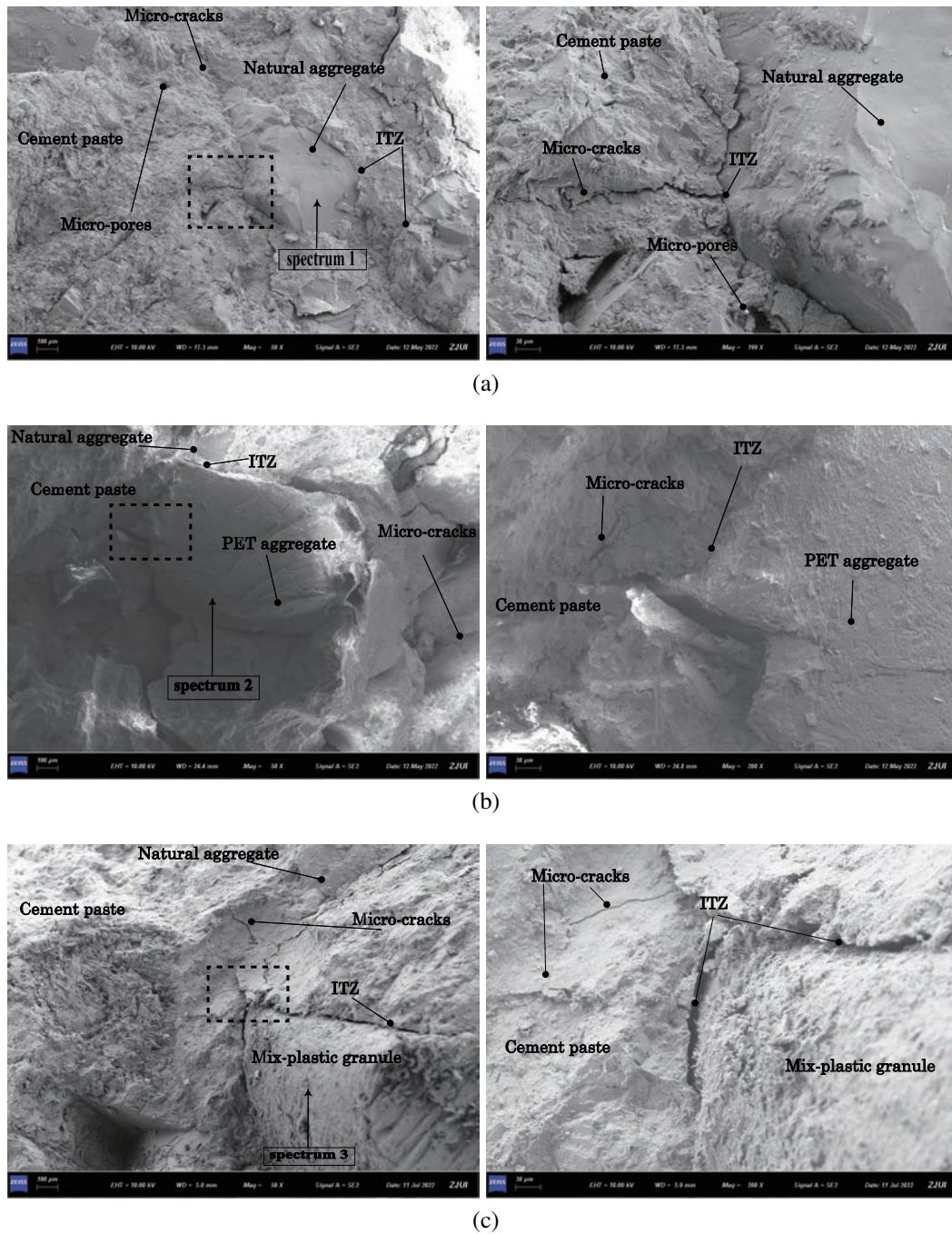
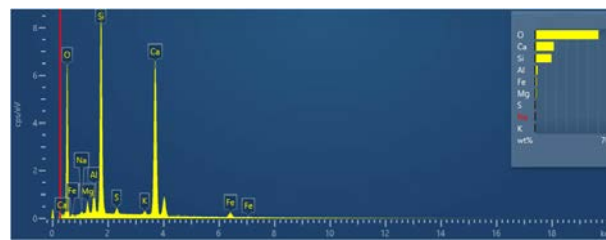


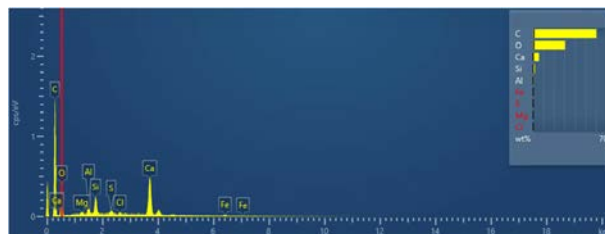
Figure 7.13 SEM scans of: natural aggregate (a), PET aggregate (b), and MIX plastic aggregate (c). The left scans are large view of the region of interest while right scans are close views of the region inside the rectangle reported on the left side. In MIX aggregate scan (c, left) the location of the spectrum analyses (Figure 6.12) are reported.



(a)



(b)



(c)

Figure 7.14 EDX elemental point analysis in terms of spectrum for: (spectrum 1) natural aggregates (a); (spectrum 2) PET powder (b), and (spectrum 3) mix-plastic granules (c).



The black continuous and red dashed lines indicate the different CEB-FIP Model Code specification recommendation formula CEB [5, 30]. It should be noted that when NAC specimens are under 0.3 MPa, one of NAC specimens not failed, which in turn leads to a not real dynamic compressive strength, therefore, the value of DIF of this specimen is even lower than 1.

The difference between the values of DIF in various studies is attributed to many factors. Size effect of specimens including diameter, thickness and aspect ratio and geometry have influence on the results. Other factors like inner characterizes of material difference like aggregate size and type and particle distribution also influence the results of DIF Al-Salloum et al. [339]. In these study , the same SHPB system with Lai et al. [73] are conducted, a significant difference can be observation in the size of specimens of static compressive tests, according to Wang et al. [340], the different sizes of static compressive strength have a relatively large influence in the values of DIF, larger specimens size of static compressive tests than it of SHPB tests will have negative effect on the values of DIF. The studies in Hu et al. [185], Chen et al. [183], Wang et al. [340] applied smaller size of SHPB specimens compared to static tests obtained lower DIF than CEB-FIP Model code. In the meanwhile, Xiong et al. [9, 75], Lai et al. [73], Zhong and Zhang [188], Wang et al. [340] conducted same specimen sizes in both dynamic and static tests and obtained a higher DIF, which is more fitting CEB-FIP Model code Xiong et al. [75] or even higher than the codes Zhong and Zhang [188].

Regarding this studies, in general, almost all the values of DIF of different tests are smaller than the two versions of CEB-FIP Model codes. But similar findings are available in other studies Hu et al. [185], Chen et al. [183]. For NAC, although the specimens under 0.3 MPa are not totally broken and the variability is relatively large but with increasing  $P_g$ , the variability showed a moderate trend. Compared with NAC, the variability is smaller in case of PET and MIX. For case of PET and MIX, a visible increment in  $\dot{\epsilon}$  compared with NAC given same  $P_g$ . While regarding the DIF, a similar or a slightly increase can be observed, especially in case of PET10 and MIX20, which has a good agreement with the results of UPV tests. Under high  $r$ , especially  $r = 30\%$ , the DIF can exceeding the CEB-FIP Model code of 2010 CEB [30]. Combined with the results of UPV tests, with increasing  $r$ , more micro cracks and pores present in concrete and specimens are less dense, which in turn lead to a higher strain-rate sensitively and a higher DIF. The special dynamic behavior of concrete replaced by palstic aggregates can attribute to that the plastic aggregates

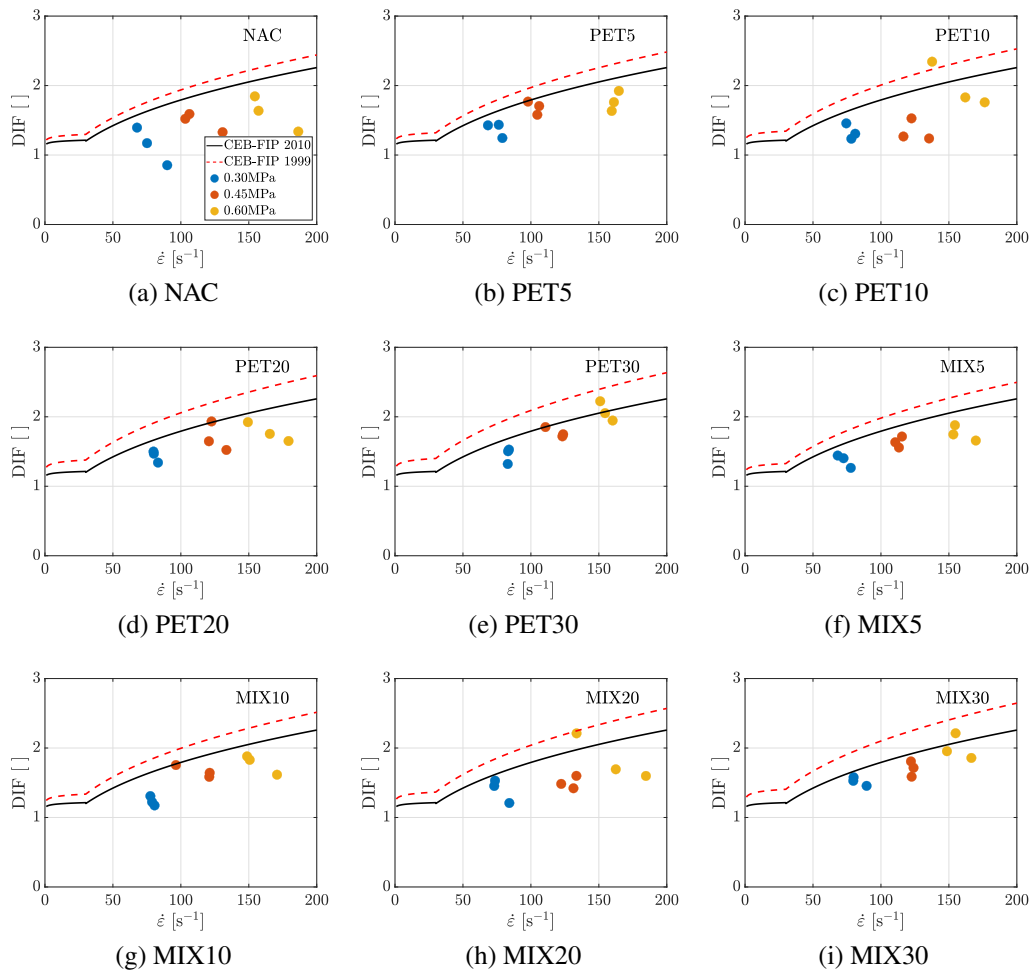


Figure 7.15 DIF as a function of the strain rate,  $\dot{\epsilon}$ , for different tests. The black continuous and red dashed lines indicate the CEB-FIP Model Code specification recommendation formula CEB [5, 30].

have a weaker adhesion with the cement paste than natural aggregate, and more pores and cracks make the processing of cracks propagating time consuming.

### 7.5.2 Image-based waveform analysis of SHPB tests

This section is aimed to the main features of the three waves with the qualitative observations from the high-speed camera showed in Figure 7.16-7.24. Four characteristic points were selected from incident, transmission and reflected waves showed in left column of Figure 7.16-7.24. The first point (A) is half peak value of

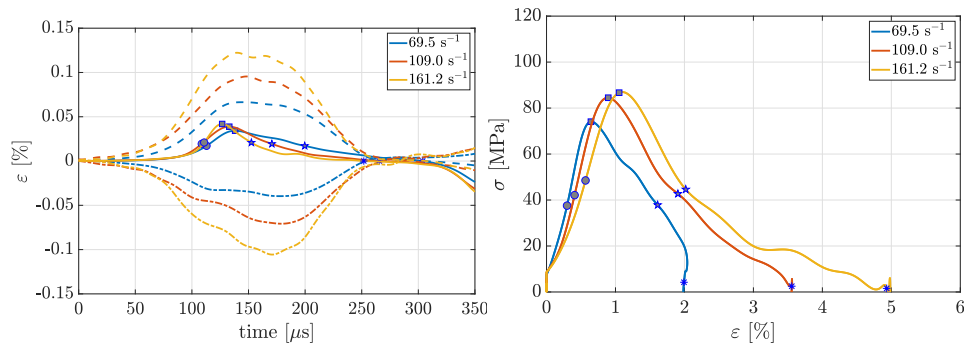


Figure 7.16 Dynamic behavior of NAC in terms of characteristic points. Transmitted and reflected waveform curves (left); Stress–strain curve (right);

transmission wave, marker showed as blue circle, which can be used to represent the pre-peak point; the second point (B) is the peak value of transmission wave, marker showed as blue square, which can be used to represent the important threshold point to divide the pre-peak and post-peak region, the third point (C) is the peak value of reflected point, marker showed as blue pentagram, which can be used to represent the post-peak point; the fourth point (D) is the point when transmission wave is zero, marker showed as blue star, which represents the finish of the first impact. It needs to note that all the characteristic points are showed on the transmitted wave, reported in left column of Figure 7.16-7.24. Right columns of Figure 7.16-7.24 show the characteristic points on the dynamic stress–strain curves. Especially, the small gap between the bar and specimen can be observed clearly from second images of Figure 7.25- 7.33, large amount of vaseline was squeezed out under impact loading at pre-peak stage.



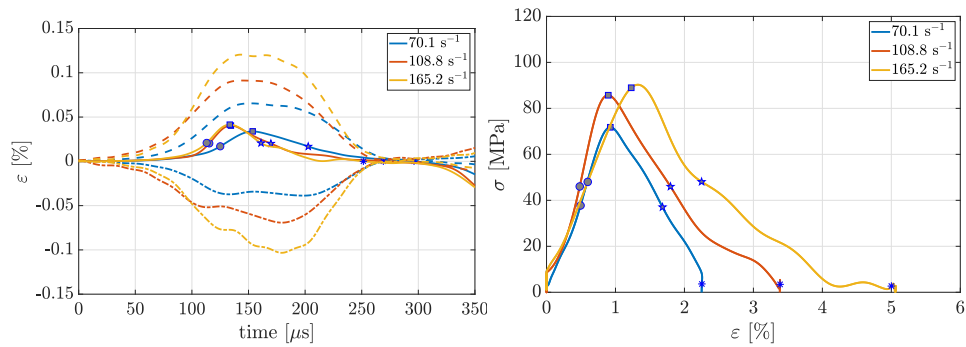


Figure 7.17 Dynamic behavior of PET5 in terms of characteristic points. Transmitted and reflected waveform curves (left); Stress–strain curve (right);

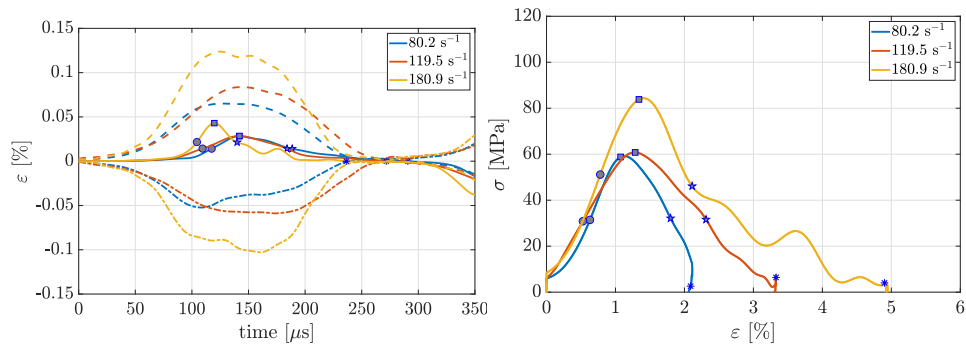


Figure 7.18 Dynamic behavior of PET10 in terms of characteristic points. Transmitted and reflected waveform curves (left); Stress–strain curve (right);

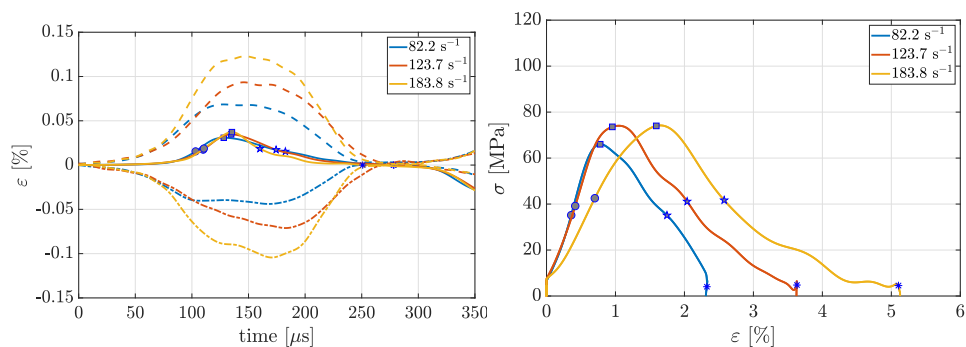


Figure 7.19 Dynamic behavior of PET20 in terms of characteristic points. Transmitted and reflected waveform curves (left); Stress–strain curve (right);

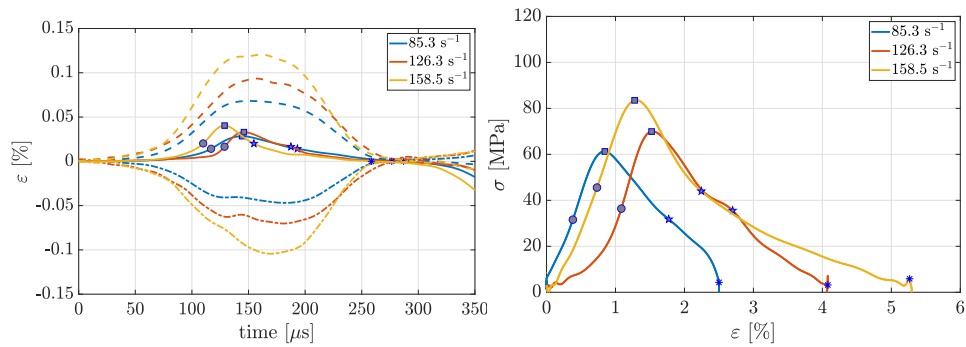


Figure 7.20 Dynamic behavior of PET30 in terms of characteristic points. Transmitted and reflected waveform curves (left); Stress–strain curve (right);

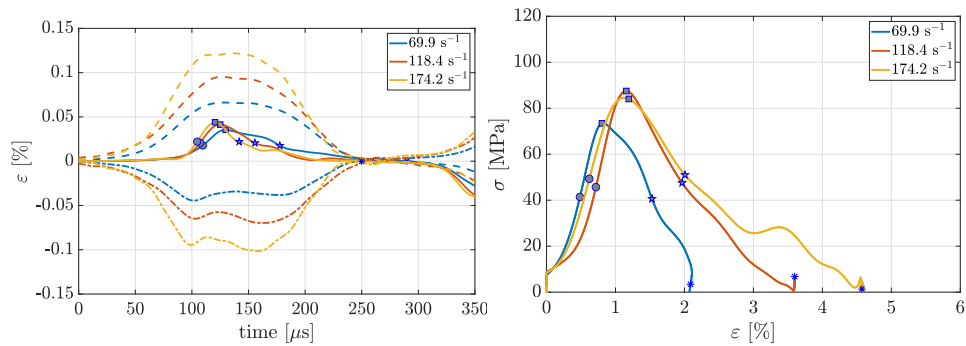


Figure 7.21 Dynamic behavior of MIX5 in terms of characteristic points. Transmitted and reflected waveform curves (left); Stress–strain curve (right);

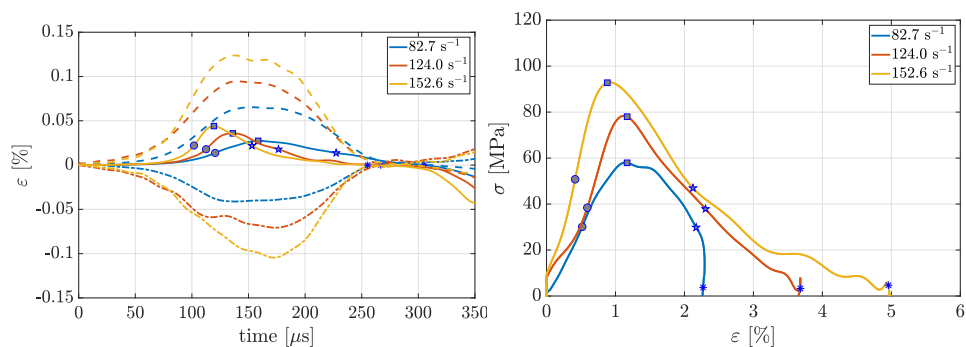


Figure 7.22 Dynamic behavior of MIX10 in terms of characteristic points. Transmitted and reflected waveform curves (left); Stress–strain curve (right);

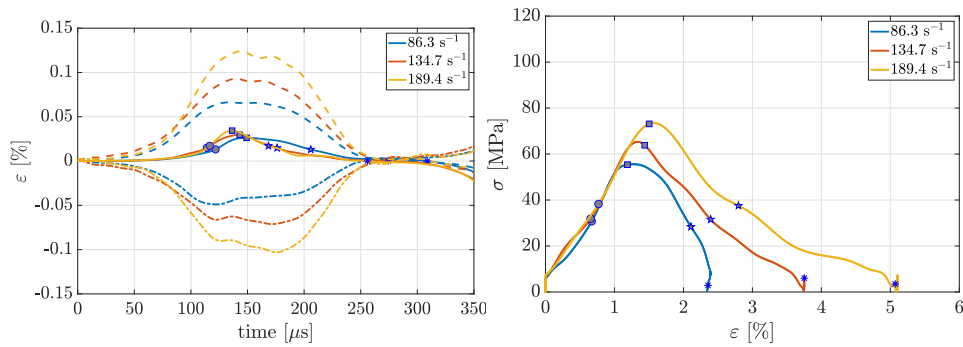


Figure 7.23 Dynamic behavior of MIX20 in terms of characteristic points. Transmitted and reflected waveform curves (left); Stress–strain curve (right);

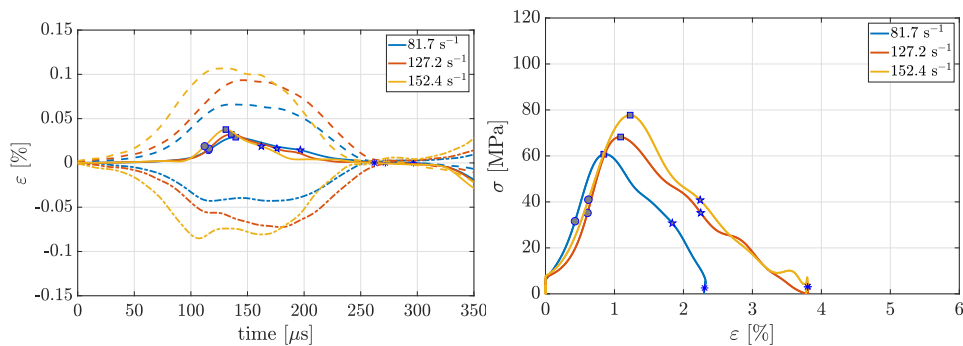


Figure 7.24 Dynamic behavior of MIX30 in terms of characteristic points. Transmitted and reflected waveform curves (left); Stress–strain curve (right);

In this part, the photos from high-speed camera are correlated with features based on the three waves, namely transmission, incident and reflect waves. The four characteristic points ( $A - D$ ) were selected,  $C$  is defined as the peak of transmission wave, and  $A$  is corresponding to half of the peak of transmission wave.  $B$  and  $D$  are corresponding to post peak behavior,  $B$  is the zero of the transmission wave after  $C$ ,  $D$  is corresponding to the peak of the reflected wave. Figure 7.25- 7.33 showed the qualitative observations from high-speed camera correspond to the characteristic points described in section 7.5.2. The high speed camera is aligned by considering the delay between the trigger point and the arrival of the incident wave on the

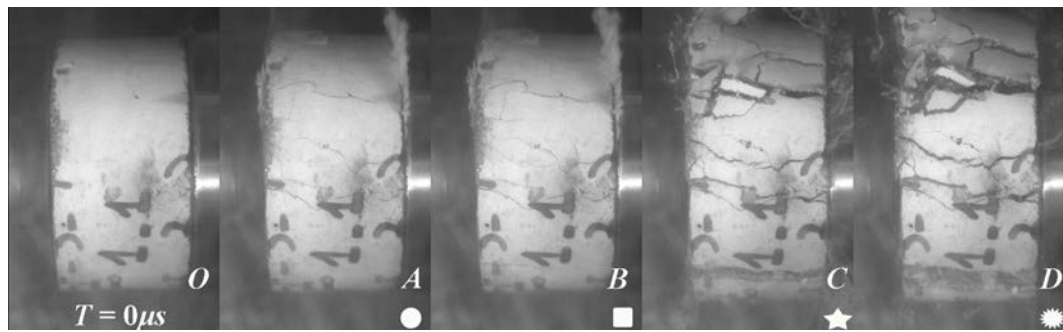
specimen. Figure 7.25 refers to NAC under different  $P_g$ . The first image is the photo comes from the beginning of the tests. Under 0.3 MPa, until NAC reaches at peak values of stress (the third image), no large cracks, although after post-peak (from fourth image), visible large cracks and the specimen start to crush into some pieces. With increasing  $P_g$ , a few visible major cracks start to present during pre-peak stage, after peak stress, the specimens tends to have significantly damage. Compared with NAC, more cracks can be seen at pre-peak stage under 0.3 MPa, with increasing  $r$ , the major cracks run through the specimen, and when it arrives at peak stress, the cracks tend to be width and some small cracks continue to coalescence, at post-peak stage, the separation of fragments can be seen clearly and fall down of the debris.

## 7.6 Conclusion

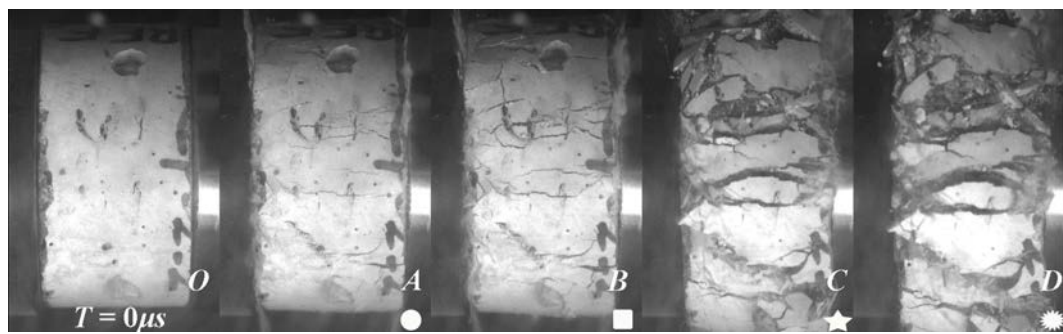
In this study, the quasi-static and high-strain rate compressive behaviors of NAC, PET, and MIX concrete were investigated using a comprehensive experimental test program. Substitution levels of PET powder up to  $r = 30\%$  and substitution levels of mix-plastic granules and PET powder up to  $r = 30\%$  were considered. Tests were performed using traditional quasi-static tests with a compressive testing machine and high-strain rate tests with a  $\Phi 80$ -mm SHPB for strain rates up to  $200 \text{ s}^{-1}$ . Moreover, a characterization of the microstructure was performed using SEM and EDS scans. The high-strain rate behavior damage evolution was monitored by a high-speed camera. Based on the test results, data-driven models for DIF are proposed for different types of concrete replaced by plastic.

The primary outcomes of this research are:

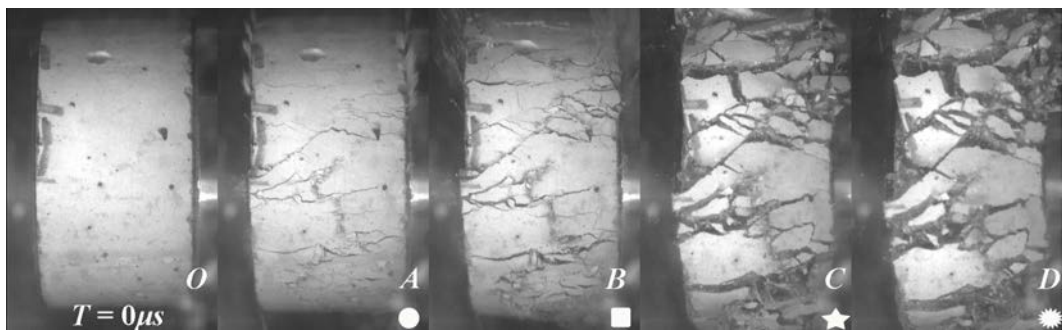
- The flowability is reduced for PET cases. When  $r = 30\%$ , the slump reduction ratio with respect to NAC can reach more than 20%, while an opposite fashion can be observed in cases of MIX, the slump increases from 235mm of NAC to 255mm of  $r = 30\%$ . A possible explanation for these results may be related to the sharper edges and more elongated shapes of PET powder which contribute to the reduction of slump and fluidity. Mix-granules have a smoother out-surface and smaller surface-area-to-volume ratio compared to PET powder.
- SEM and EDS revealed observations of ITZ of different plastic aggregates and cement paste. More micropores and micro-cracks are generally observed



(a)



(b)



(c)

Figure 7.25 NAC: 0.3MPa (a); 0.45MPa (b); 0.6MPa (c)

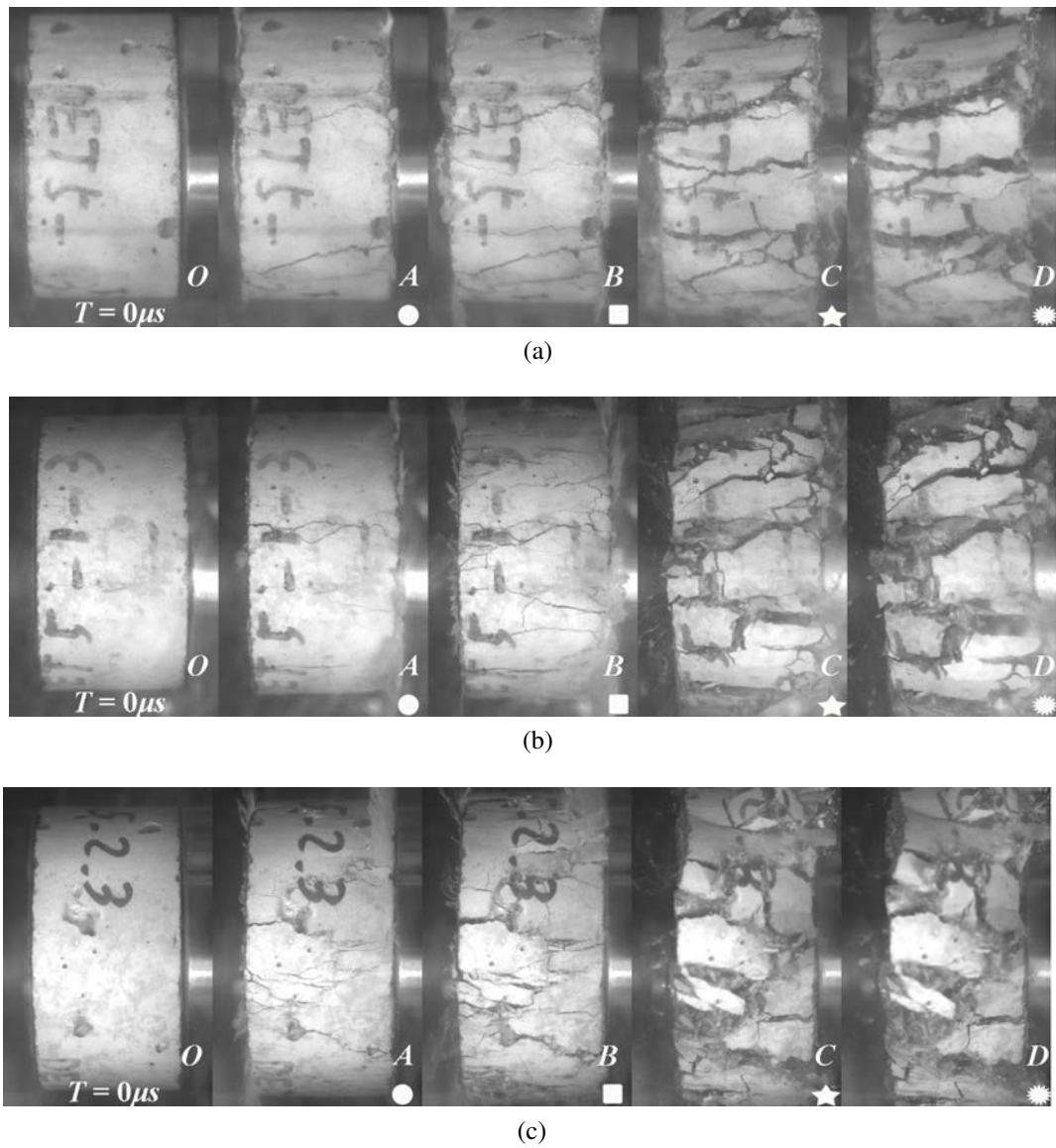


Figure 7.26 PET5: 0.3MPa (a); 0.45MPa (b); 0.6MPa (c)

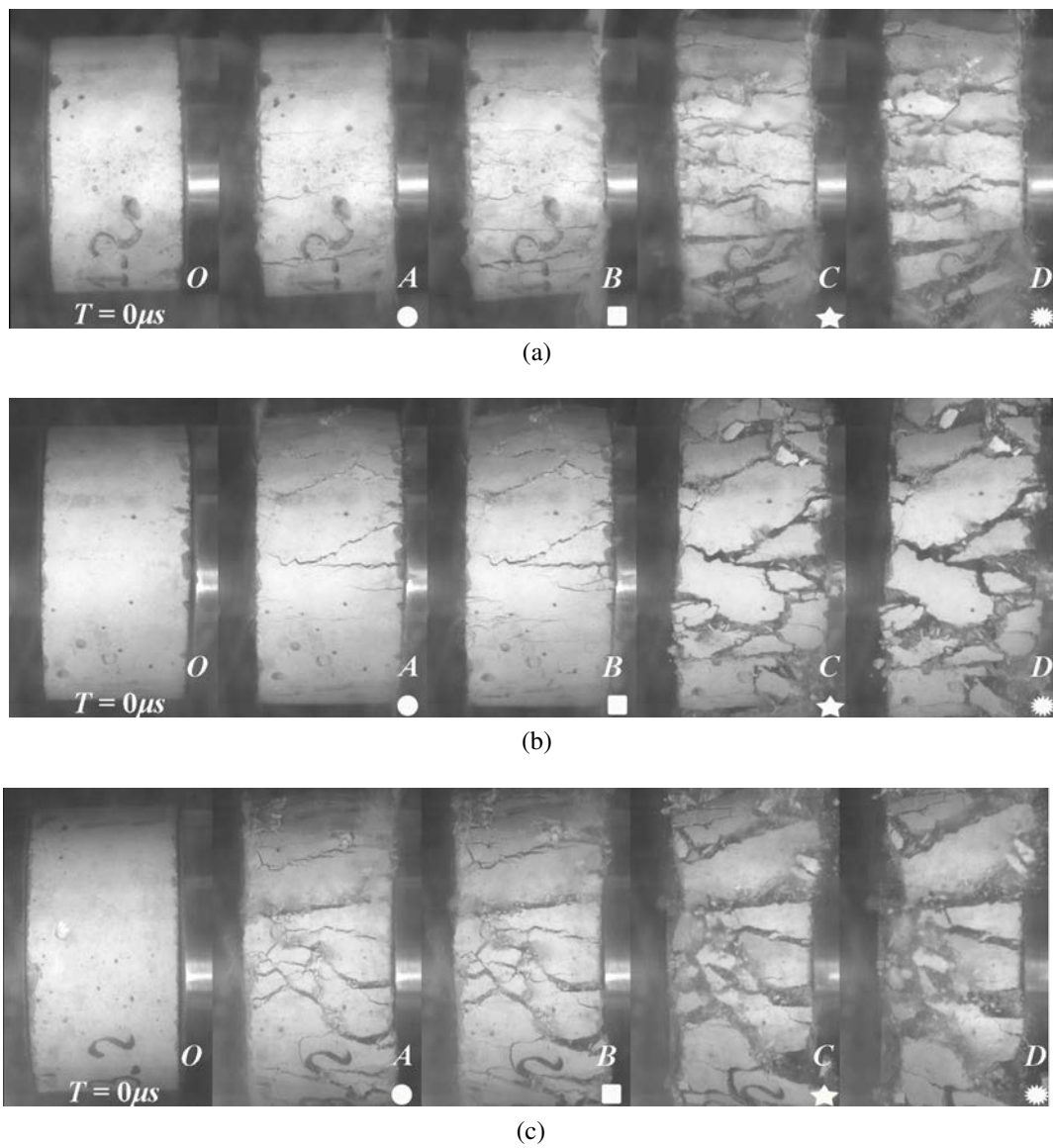


Figure 7.27 PET10: 0.3MPa (a); 0.45MPa (b); 0.6MPa (c)



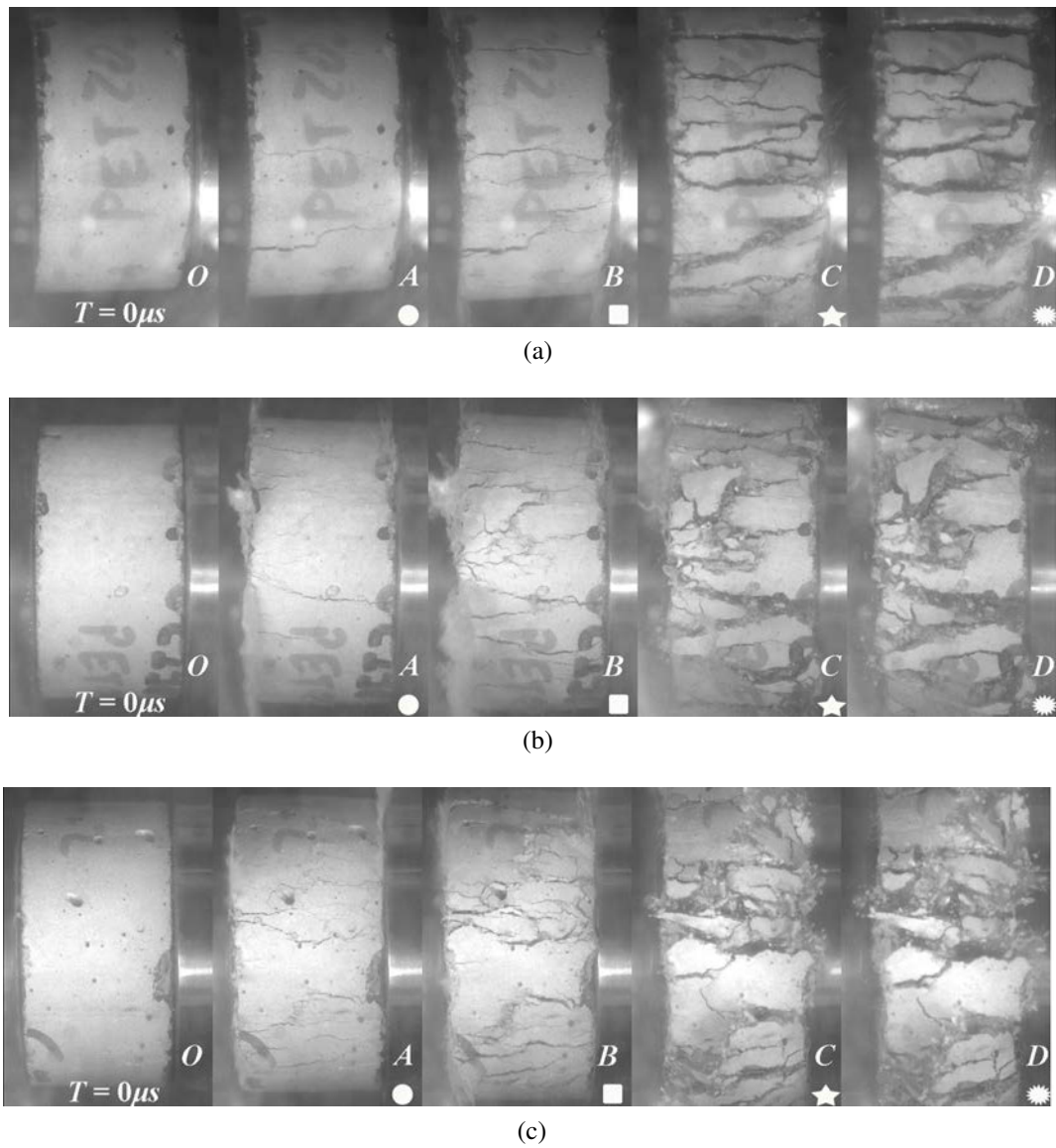


Figure 7.28 PET20: 0.3MPa (a); 0.45MPa (b); 0.6MPa (c)



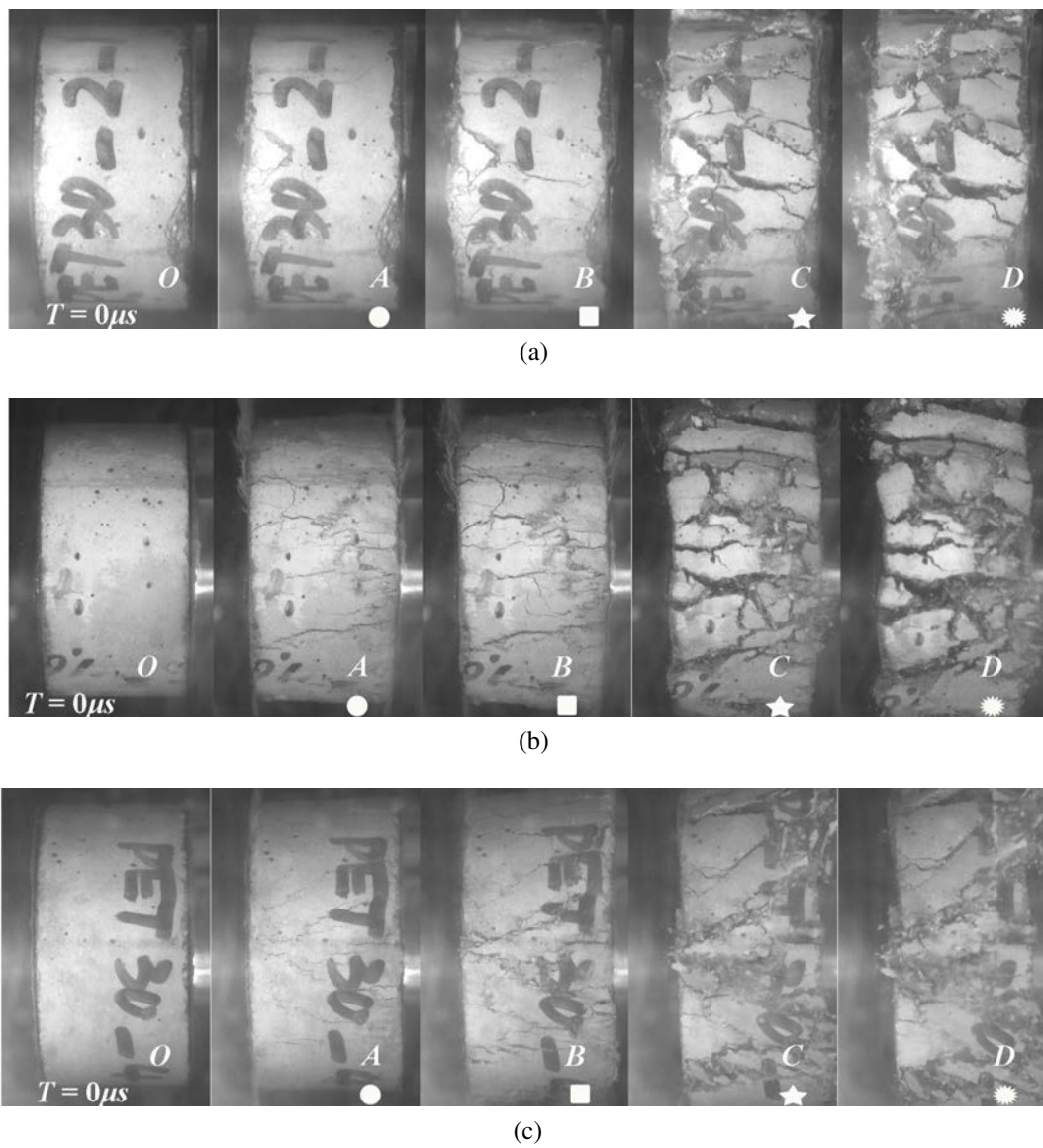
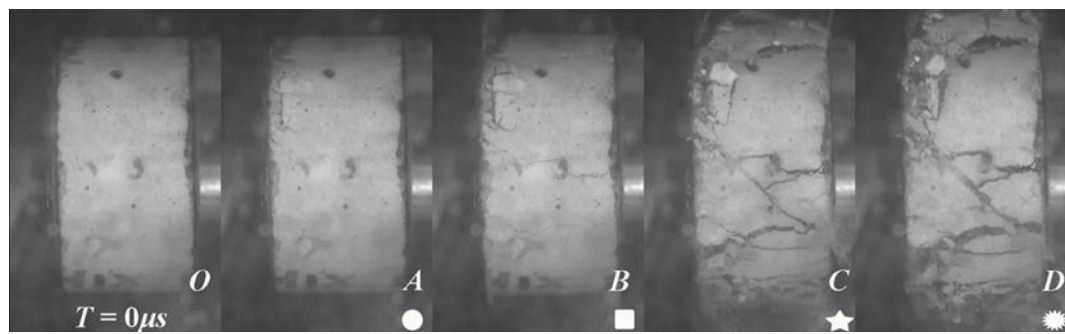
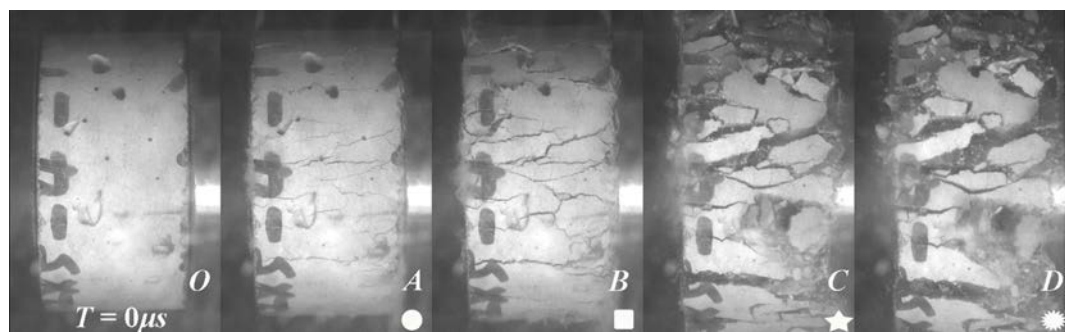


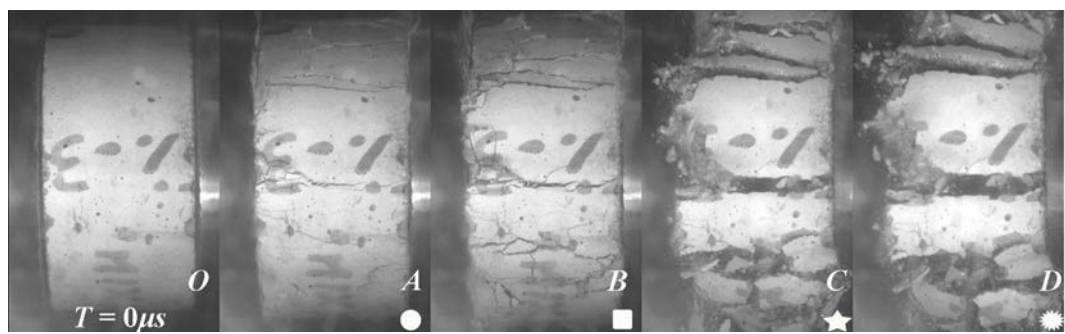
Figure 7.29 PET30: 0.3MPa (a); 0.45MPa (b); 0.6MPa (c)



(a)



(b)



(c)

Figure 7.30 MIX5: 0.3MPa(a); 0.45MPa(b); 0.6MPa(c)

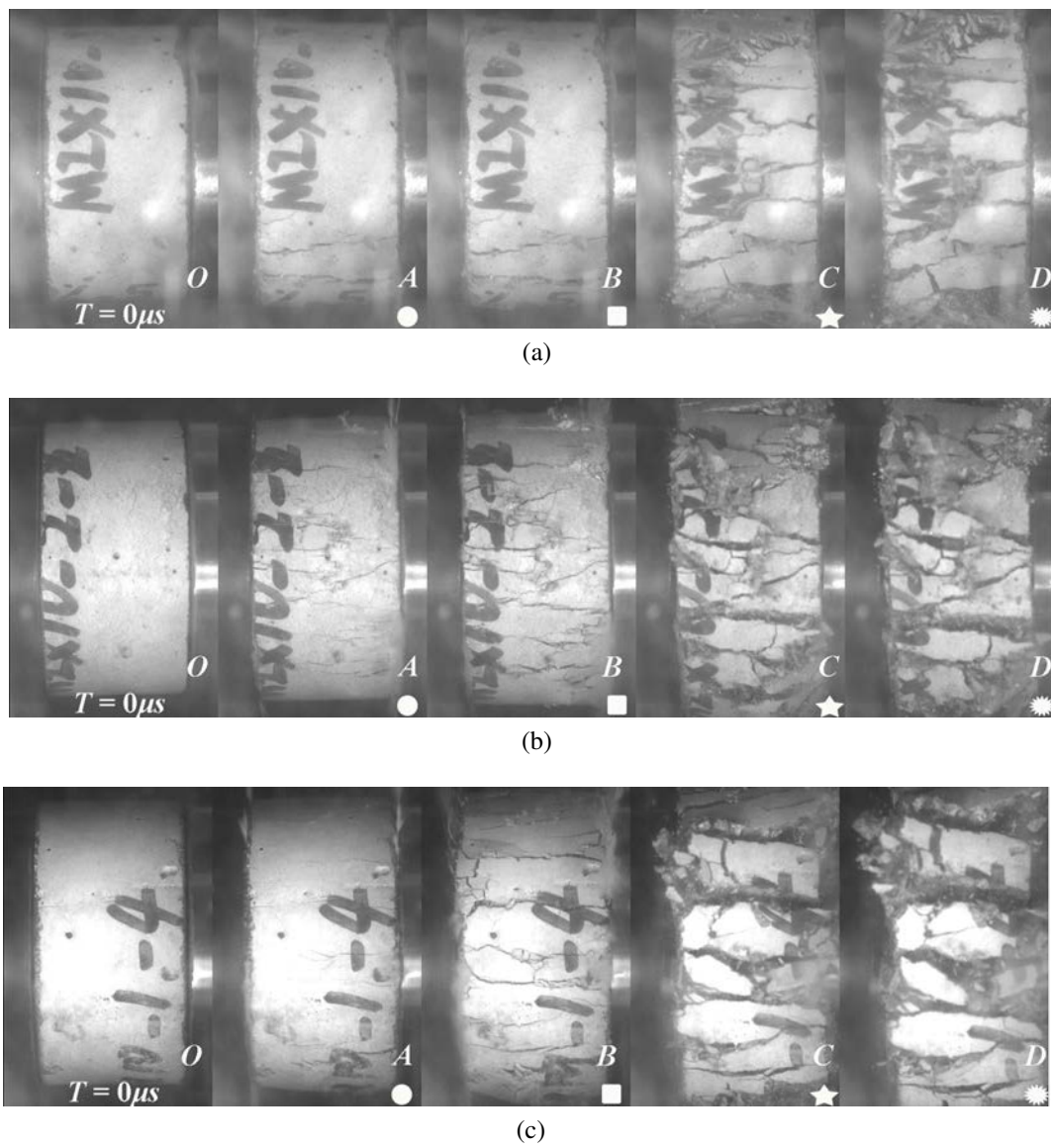


Figure 7.31 MIX10: 0.3MPa (a); 0.45MPa (b); 0.6MPa (c)

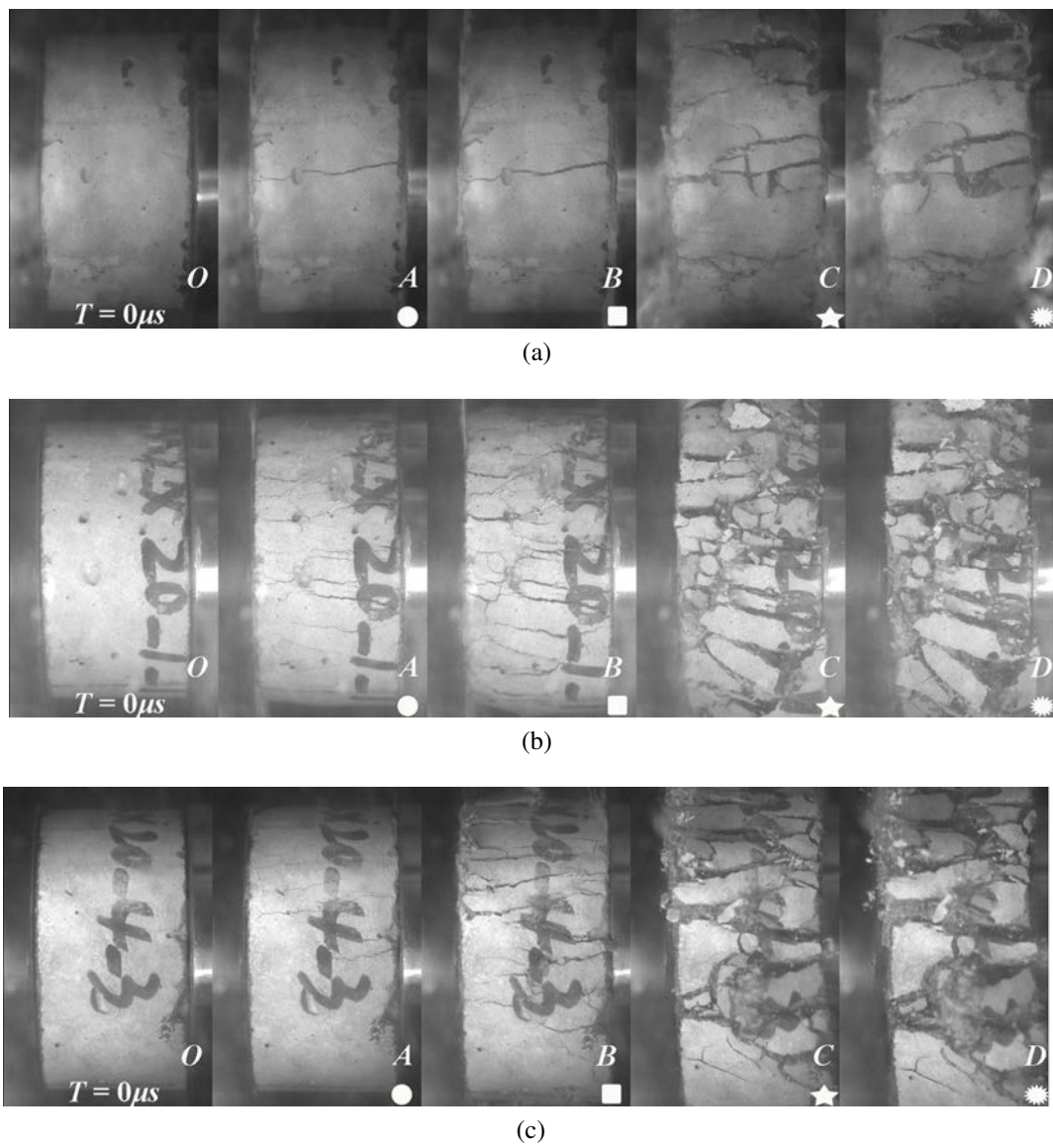


Figure 7.32 MIX20: 0.3MPa (a); 0.45MPa (b); 0.6MPa (c)

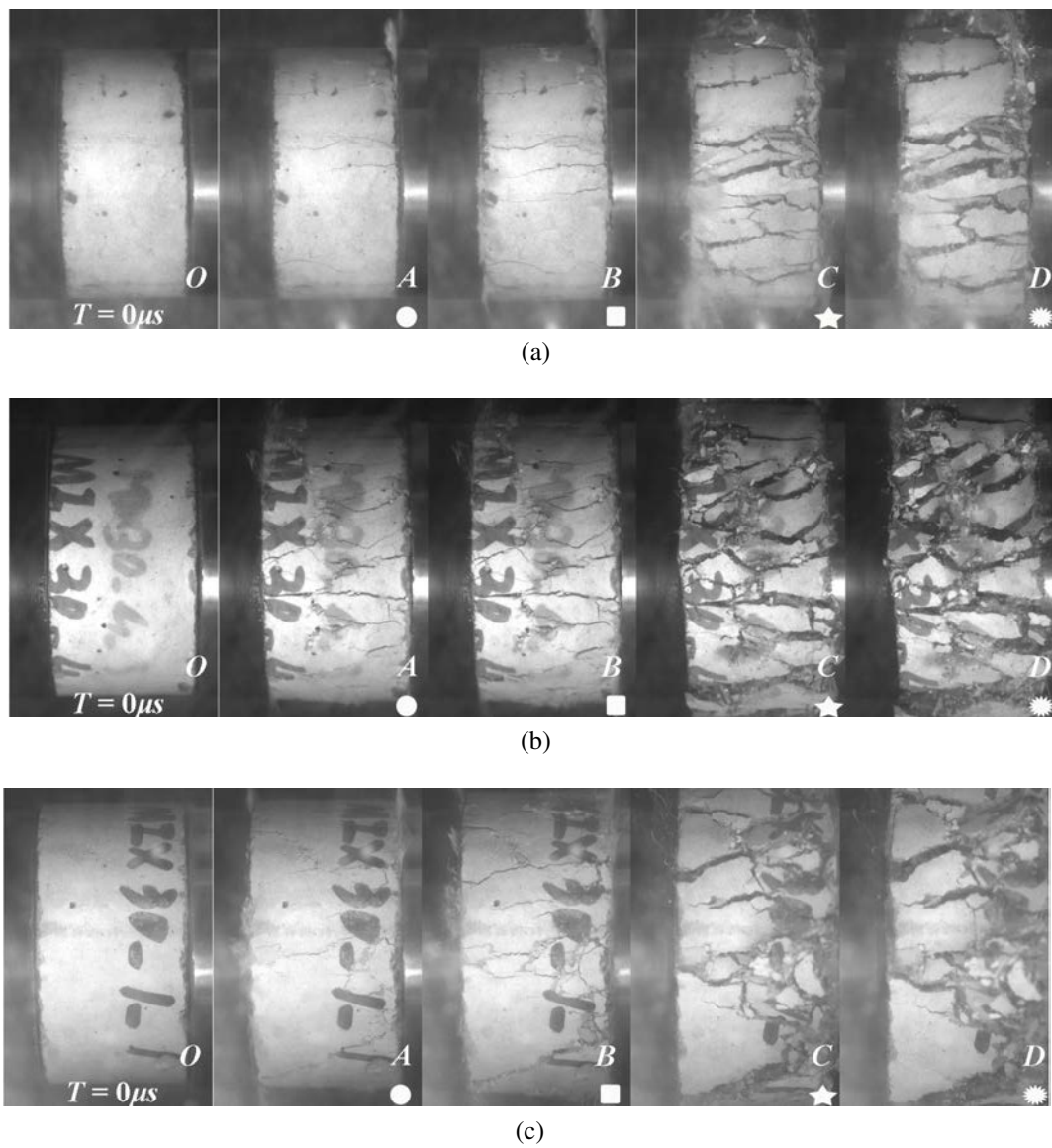


Figure 7.33 MIX30: 0.3MPa (a); 0.45MPa (b); 0.6MPa (c)



with the presence of PET and mix-plastic aggregate. The weaker ITZ and lower adhesion of plastic aggregates are the main explanation for the observed compressive strength reduction.

- Quasi-static tests indicate a reduction of compressive strength and elastic modulus with increasing  $r$ . Generally, at given  $r$ , the reduction of the strength is similar for PET and MIX indicating that the compressive strength is mainly dominated by the total substitution volume. MIX concretes have a higher elastic modulus compared with PET. This result may be contributed to the higher hardness of granules and stiffness of mix-plastic granules.
- SHPB tests indicate that the increase in the strain rate induces an increase in compressive strength. The damage pattern is depending on the strain rate. When concrete is substituted by plastic aggregates, more diffuse micro-cracks due to the different ITZ is observed. The specific energy absorption density before the peak stress decreases with increasing  $r$ . Having fixed  $r$ , the specific energy absorption density increases with increasing  $P_g$ . Similarly, an increase in  $DIF$  is observed by increasing  $r$ . These observations are attributable to the more diffused micro-cracks explaining the larger strain sensitivity of PET and MIX compared with NAC.
- The image-based waveform discussion illustrates the different features of the observed signals and damage evolution in the specimens. The dynamic tests show increased damage with increasing the strain rate (or air gun pressure). The failure of NAC is induced by the sudden propagation of cracks along the direction of the wave in region post-peak region. The failure of PET and MIX is induced by the continuing propagation of cracks along the specimens and a more diffused crack net is observed providing a residual capacity in the post-peak region.

The results indicate generally good physical and mechanical performances of the proposed new green concrete. Under this positive evidence, this concrete appears a promising material for real application in protecting structures against rapidly varying loads.

# Chapter 8

## Conclusions and future perspectives

### 8.1 Conclusions

The reuse and recycled of solid waste in concrete aimed to develop a novel concrete and the mechanical properties, especially the static and dynamic mechanical properties were investigated in this thesis. This was done since recycle CDW in concrete mixture has been proposed as a promising strategy to solve the disposal of it, which constitute the vast majority of the municipal solid waste. Taking into consideration the advantages and limitations of each type of CDW, finally the recycled crushed concrete, recycled brick aggregate, recycled PET powder and recycled mix-plastic granules were selected as the objective of this thesis.

Regarding the large-scale SHPB (diameter of 155 mm) takes big challenges of designing and calibrating and it is the first time to be adopted for experimental investigation. Therefore, before conducting formal tests, the validation and calibration of the large-diameter SHPB are the most significant steps. In the first part, the design and construction of the apparatus were described and its data processing, including wave pulse dispersion correction, was assessed to ensure accurate representation of stress and deformation conditions. The apparatus was validated through experiments on both brittle (confined concrete) and ductile (copper) specimens. The preliminary test results demonstrated the ability of SHPB to characterize the dynamic properties of large-scale specimens and to correct dispersed signals in the bar, allowing for the accurate determination of specimen surface pulses. The validity of the results was confirmed through 1D, 2D, and 3D wave analyses. Which means the 155 mm

diameter SHPB setup has shown excellent performance in deriving the dynamic properties of large-diameter specimens.

The good repeatability and stability of the 155mm-diameter SHPB provides possibility to step further to use it for investigation of inhomogeneous materials like concrete substituted by recycled crushed concrete, recycled brick aggregate. In the second part, different experimental studies carried out by 155mm-diameter SHPB showed the strain rate dependency of the dynamic strength of the concrete made with different levels of substitution and types of coarse aggregate. The experimental results available in the literature only refer to recycled aggregate concrete and are rather controversial, without general agreement about the exact effect of the levels of substitution and types of coarse aggregate on the strength under high strain rate. In this part, the quasi-static tests confirmed the typical behavior of RAC and RBC which means increasing in the levels of substitution leads to a strength decrease and the strength loss is more marked for RBC rather than RAC. This difference is associated with the minor mechanical performances of the BA compared with RCA. And similar results can be seen in dynamic tests. It is interesting that an increase of DIF, is observed with the coarse aggregate level of substitution,  $r$ . The increase of DIF with  $r$  is more marked for RAC and particularly marked for  $r > 60\%$ . The increase of DIF with  $r$  is less marked for RBC and negligible for  $r > 60\%$ . The ITZs between cement and the recycled concrete aggregates leads to the difference and another reasons can be the essential differences between BA and RCA.

Then the thesis focus on the application of recycled plastic aggregates in cementitious materials. This framework is mainly composed of mortar and concrete. To confirm the possibility and researchability, the preliminary experimental investigation to evaluate the effect of PET powder as aggregate on the physical, mechanical, and fracture properties of mortar with substitution level of PET aggregate ranging from  $r = 0$  to 30% by volume of standard natural sand. When  $r$  is under low values, a beneficial bridging effect can be induced, which can improve the flexural strength while it witnessed a continuous decrease on compressive strength, while  $r$  is under low values, the strength loss can be accepted.

The static tests on mortar substituted by PET aggregates confirm the possibility of recycling plastic aggregates in cementitious materials. Afterwards, the relatively research step towards to next stage, namely, the mechanical and physical properties of concrete substituted by recycled plastic aggregates should be investigated. Therefore,



a pilot study on the characterization of the physical and mechanical properties of a novel green concrete with two different substituted recycled plastic aggregates was investigated. Herein, recycled PET powder and recycled mix-plastic granules were adopted to substitute fine and coarse aggregates. Two different substitution strategies were employed. In the first one, the PET powder was used to substitute the fine sand by volume, the concrete tag is PET. In the second one, the PET powder was used to substitute the fine sand while the recycled mixed plastic granules were used to substitute the coarse sand and fine coarse aggregates by volume (50% for PET powder and 50% for recycled mixed plastic granules), the concrete tag is MIX. Four total replacement levels (5%, 15%, 20%, and 30%) by volume were considered. The results shows that compressive strength is slightly reduced by a low substitution level ( $r \leq 10\%$ ) for both PET and MIX cases attributed by an interlocking effect of mix plastic aggregate while flexural strength is slightly improved for  $r = 20\%$ . Relatively low substitution levels by plastic aggregate can fill up the micropores and enhance the interfacial bonding between the plastic aggregates and cement paste. This part indicates generally good physical and static mechanical performances of the proposed new green concrete.

In order to facilitate the comparison with RAC and RBC under high strain rate, the high-strain rate compressive behaviors of PET, and MIX concrete should be investigated. A  $\Phi 80\text{mm}$  SHPB for strain rates up to  $200\text{s}^{-1}$  is adopted. The results of SHPB tests showed that the increase in the strain rate induced an increase in compressive strength. When concrete is substituted by plastic aggregates, more diffuse micro-cracks due to the different ITZ is observed. The specific energy absorption density before the peak stress decreases with increasing  $r$ . Having fixed  $r$ , the specific energy absorption density increases with increasing strain rates. Similarly, an increase in  $DIF$  is observed by increasing  $r$ . These observations are attributable to the more diffused micro-cracks explaining the larger strain sensitivity of PET and MIX compared with NAC.

Overall, the all test results indicate generally good physical and mechanical performances of the proposed new green concrete including RAC, RBC, PET and MIX. Under this positive evidence, these new green concretes appear a promising material for real application in protecting structures against rapidly varying loads.

## 8.2 Future perspectives

Even though the thesis allowed to obtain good mechanical performances both on static and dynamic mechanical properties of novel green concrete substituted by CDW aggregate and plastic aggregate, However, on the basis of current research outcomes, the following areas of research remain unexplored:

- A good understanding of high-strain rate compressive behavior of concrete substituted by different types of CDWs is fundamental to establish the protective system for new or existing structures. Therefore, an extensive experimental program needs to be conducted to investigate the dynamic behaviors of concrete substituted by other types of CDWs, such as glass, wood.
- The existing results from experiments of RAC and RBC show that characteristics of the parent concrete have potentially attribution to inducing difference of increasing in  $DIF$  and  $r$  for RAC which requires additional tests on concrete made with different levels of substitution and types of coarse aggregate under high-strain rate would allow a greater understanding of the implications of the strain rate effects on the strength.
- Regarding the green mortar substituted by plastic aggregates, increased attention should be paid to the further development of comprehensive application of 3D printing mortar. On other hand, considering the novel green concrete substituted by plastic aggregates, full-scale application should be taken into consideration.
- The novel green concrete substituted by CDWs appears a promising material for real application. Consequently, the relative investigation in protecting structures against rapidly varying loads is under urgent need.
- This thesis has established different probabilistic data-driven models to estimate the dependency between different factors ( $W/C$ ,  $r$ , curing time,  $\dot{\epsilon}$ ) and the results ( $SRF$ ,  $DIF$ ). However, a comprehensive probabilistic models with high accuracy should be proposed considering the  $\dot{\epsilon}$  which can establish technical and performance standards for the various application.
- A comparative study on concrete substituted by CDWs and plastics with NAC should be investigated regarding the  $CO_2$  emission, the  $CO_2$  emission of

different concretes should be quantified and it will offer a better understanding of 'green'.

# Bibliography

- [1] M. Batayneh, I. Marie, I. Asi, Use of selected waste materials in concrete mixes, *Waste management* 27 (2007) 1870–1876.
- [2] J. Zheng, S. Suh, Strategies to reduce the global carbon footprint of plastics, *Nature Climate Change* 9 (2019) 374–378.
- [3] ASTM, Astm d7611 / d7611m- standard practice for coding plastic manufactured articles for resin identification, American Society for Testing and Materials (ASTM) (2013).
- [4] U. Ulusoy, Quantifying of particle shape differences of differently milled barite using a novel technique: Dynamic image analysis, *Materialia* 8 (2019) 100434.
- [5] CEB, Concrete structures under impact and impulsive loading, CEB Bulletin CEB Bulletin d'information, vol. 187. Committee Euro-International du Beton Lausanne, France. (1998).
- [6] J. Xiao, L. Li, L. Shen, C. S. Poon, Compressive behaviour of recycled aggregate concrete under impact loading, *Cement and Concrete Research* 71 (2015) 46–55.
- [7] Y. Lu, X. Chen, X. Teng, S. Zhang, Dynamic compressive behavior of recycled aggregate concrete based on split hopkinson pressure bar tests, *Latin American Journal of Solids and Structures* 11 (2014) 131–141.
- [8] J. Guo, Q. Chen, W. Chen, J. Cai, Tests and numerical studies on strain-rate effect on compressive strength of recycled aggregate concrete, *Journal of Materials in Civil Engineering* 31 (2019) 04019281.

- [9] B. Xiong, C. Demartino, Y. Xiao, High-strain rate compressive behavior of cfrp confined concrete: Large diameter shpb tests, *Construction and Building Materials* 201 (2019) 484–501.
- [10] K. Hannawi, S. Kamali-Bernard, W. Prince, Physical and mechanical properties of mortars containing pet and pc waste aggregates, *Waste management* 30 (2010) 2312–2320.
- [11] B. Safi, M. Saidi, D. Aboutaleb, M. Maallem, The use of plastic waste as fine aggregate in the self-compacting mortars: Effect on physical and mechanical properties, *Construction and Building Materials* 43 (2013) 436–442.
- [12] G. Kaur, S. Pavia, Physical properties and microstructure of plastic aggregate mortars made with acrylonitrile-butadiene-styrene (abs), polycarbonate (pc), polyoxymethylene (pom) and abs/pc blend waste, *Journal of Building Engineering* 31 (2020) 101341.
- [13] M. Hacini, A. S. Benosman, N. K. Tani, M. Mouli, Y. Senhadji, A. Badache, N. Latroch, Utilization and assessment of recycled polyethylene terephthalate strapping bands as lightweight aggregates in eco-efficient composite mortars, *Construction and Building Materials* 270 (2021) 121427.
- [14] K. Hannawi, W. Prince, S. K. Bernard, Strain capacity and cracking resistance improvement in mortars by adding plastic particles, *Journal of materials in civil engineering* 25 (2013) 1602–1610.
- [15] M. Abu-Saleem, Y. Zhuge, R. Hassanli, M. Ellis, M. Rahman, P. Levett, Evaluation of concrete performance with different types of recycled plastic waste for kerb application, *Construction and Building Materials* 293 (2021) 123477.
- [16] I. Almeshal, B. A. Tayeh, R. Alyousef, H. Alabduljabbar, A. M. Mohamed, Eco-friendly concrete containing recycled plastic as partial replacement for sand, *Journal of Materials Research and Technology* (2020).
- [17] A. J. Babafemi, N. Sirba, S. C. Paul, M. J. Miah, Mechanical and durability assessment of recycled waste plastic (resin8 & pet) eco-aggregate concrete, *Sustainability* 14 (2022) 5725.

- [18] A. Hasan-Ghasemi, M. Nematzadeh, Tensile and compressive behavior of self-compacting concrete incorporating pet as fine aggregate substitution after thermal exposure: Experiments and modeling, *Construction and Building Materials* 289 (2021) 123067.
- [19] M. E. Kangavar, W. Lokuge, A. Manalo, W. Karunasena, M. Frigione, Investigation on the properties of concrete with recycled polyethylene terephthalate (pet) granules as fine aggregate replacement, *Case Studies in Construction Materials* 16 (2022) e00934.
- [20] I. M. Nikbin, M. Farshamizadeh, G. A. Jafarzadeh, S. Shamsi, Fracture parameters assessment of lightweight concrete containing waste polyethylene terephthalate by means of sem and bem methods, *Theoretical and Applied Fracture Mechanics* 107 (2020) 102518.
- [21] I. M. Nikbin, S. Dezhampanah, S. Charkhtab, S. Mehdipour, I. Shahvareh, M. Ebrahimi, A. Pournasir, H. Pourghorban, Life cycle assessment and mechanical properties of high strength steel fiber reinforced concrete containing waste pet bottle, *Construction and Building Materials* 337 (2022) 127553.
- [22] K. Ullah, M. I. Qureshi, A. Ahmad, Z. Ullah, Substitution potential of plastic fine aggregate in concrete for sustainable production, in: *Structures*, volume 35, Elsevier, 2022, pp. 622–637.
- [23] Y. Ghernouti, B. Rabehi, B. Safi, R. Chaid, Use of recycled plastic bag waste in the concrete, *Journal of International Scientific Publications: Materials, Methods and Technologies* 8 (2011) 480–487.
- [24] M. J. Islam, M. S. Meherier, A. R. Islam, Effects of waste pet as coarse aggregate on the fresh and harden properties of concrete, *Construction and Building Materials* 125 (2016) 946–951.
- [25] N. K. Bui, T. Satomi, H. Takahashi, Recycling woven plastic sack waste and pet bottle waste as fiber in recycled aggregate concrete: An experimental study, *Waste Management* 78 (2018) 79–93.
- [26] O. Y. Marzouk, R. Dheilily, M. Queneudec, Valorization of post-consumer waste plastic in cementitious concrete composites, *Waste management* 27 (2007) 310–318.

- [27] A. O. Dawood, A.-K. Hayder, R. S. Falih, Physical and mechanical properties of concrete containing pet wastes as a partial replacement for fine aggregates, *Case Studies in Construction Materials* 14 (2021) e00482.
- [28] A. Committee, Building code requirements for structural concrete (aci 318-05) and commentary (aci 318r-05), American Concrete Institute, 2005.
- [29] M. Code, International federation for structural concrete (fib). federal institute of technology lausanne–epfl, section génie civil, 2010.
- [30] CEB, Ceb-fip model code 2010, 2010.
- [31] M. Eriksen, L. C. Lebreton, H. S. Carson, M. Thiel, C. J. Moore, J. C. Borerro, F. Galgani, P. G. Ryan, J. Reisser, Plastic pollution in the world's oceans: more than 5 trillion plastic pieces weighing over 250,000 tons afloat at sea, *PloS one* 9 (2014) e111913.
- [32] M. Ghose, A. K. Dikshit, S. Sharma, A gis based transportation model for solid waste disposal—a case study on asansol municipality, *Waste management* 26 (2006) 1287–1293.
- [33] M. O. Saeed, M. N. Hassan, M. A. Mujeebu, Assessment of municipal solid waste generation and recyclable materials potential in kuala lumpur, malaysia, *Waste management* 29 (2009) 2209–2213.
- [34] W. Lu, V. W. Tam, Construction waste management policies and their effectiveness in hong kong: A longitudinal review, *Renewable and sustainable energy reviews* 23 (2013) 214–223.
- [35] F. La Mantia, Handbook of plastics recycling, iSmithers Rapra Publishing, 2002.
- [36] J. R. Jambeck, R. Geyer, C. Wilcox, T. R. Siegler, M. Perryman, A. Andrady, R. Narayan, K. L. Law, Plastic waste inputs from land into the ocean, *Science* 347 (2015) 768–771.
- [37] R. Becerril-Arreola, R. E. Bucklin, Beverage bottle capacity, packaging efficiency, and the potential for plastic waste reduction, *Scientific reports* 11 (2021) 1–11.

- [38] S. Hohn, E. Acevedo-Trejos, J. F. Abrams, J. F. de Moura, R. Spranz, A. Merico, The long-term legacy of plastic mass production, *Science of the Total Environment* 746 (2020) 141115.
- [39] T. S. Vadivel, M. Doddurani, K. Shobana, An experimental study on waste plastic aggregate based concrete-an initiative towards cleaner environment, *Middle-East Journal of Scientific Research* 24 (2016) 552–556.
- [40] S. Al-Salem, P. Lettieri, J. Baeyens, Recycling and recovery routes of plastic solid waste (psw): A review, *Waste management* 29 (2009) 2625–2643.
- [41] R. V. Moharir, S. Kumar, Challenges associated with plastic waste disposal and allied microbial routes for its effective degradation: a comprehensive review, *Journal of Cleaner Production* 208 (2019) 65–76.
- [42] X. Li, T.-C. Ling, K. H. Mo, Functions and impacts of plastic/rubber wastes as eco-friendly aggregate in concrete—a review, *Construction and Building Materials* 240 (2020) 117869.
- [43] D. Lazarevic, E. Aoustin, N. Buclet, N. Brandt, Plastic waste management in the context of a european recycling society: Comparing results and uncertainties in a life cycle perspective, *Resources, Conservation and Recycling* 55 (2010) 246–259.
- [44] G. Scarascia-Mugnozza, E. Schettini, G. Vox, M. Malinconico, B. Immirzi, S. Pagliara, Mechanical properties decay and morphological behaviour of biodegradable films for agricultural mulching in real scale experiment, *Polymer Degradation and Stability* 91 (2006) 2801–2808.
- [45] R. Geyer, J. R. Jambeck, K. L. Law, Production, use, and fate of all plastics ever made, *Science advances* 3 (2017) e1700782.
- [46] P. Awoyera, A. Adesina, Plastic wastes to construction products: Status, limitations and future perspective, *Case Studies in Construction Materials* 12 (2020) e00330.
- [47] J. Ferguson, *Managing and minimizing construction waste: a practical guide*, Thomas Telford, 1995.



- [48] D. Broitman, O. Ayalon, I. Kan, One size fits all? an assessment tool for solid waste management at local and national levels, *Waste management* 32 (2012) 1979–1988.
- [49] G. Churkina, A. Organschi, C. P. Reyer, A. Ruff, K. Vinke, Z. Liu, B. K. Reck, T. Graedel, H. J. Schellnhuber, Buildings as a global carbon sink, *Nature Sustainability* (2020) 1–8.
- [50] J. Skocek, M. Zajac, M. Ben Haha, Carbon capture and utilization by mineralization of cement pastes derived from recycled concrete, *Scientific Reports* 10 (2020) 1–12.
- [51] P. K. Mehta, Greening of the concrete industry for sustainable development, *Concrete international* 24 (2002) 23–28.
- [52] S. Marinković, V. Radonjanin, M. Malešev, I. Ignjatović, Comparative environmental assessment of natural and recycled aggregate concrete, *Waste management* 30 (2010) 2255–2264.
- [53] T. Armstrong, An overview of global cement sector trends, in: FICEM-APCAC 30th Technical Congress. Lima, Peru, 2013.
- [54] K. L. Scrivener, V. M. John, E. M. Gartner, Eco-efficient cements: Potential economically viable solutions for a low-co<sub>2</sub> cement-based materials industry, *Cement and Concrete Research* 114 (2018) 2–26.
- [55] M. Schneider, M. Romer, M. Tschudin, H. Bolio, Sustainable cement production—present and future, *Cement and concrete research* 41 (2011) 642–650.
- [56] C. Fisher, M. Werge, EU as a Recycling Society; ETC, Technical Report, SCP Working Paper 2/2009, 2009.
- [57] D. Hoornweg, P. Bhada-Tata, C. Kennedy, Environment: Waste production must peak this century, *Nature News* 502 (2013) 615.
- [58] P. Nixon, Recycled concrete as an aggregate for concrete—a review, *Matériaux et Construction* 11 (1978) 371.
- [59] T. Hansen, The second rilem state of the art report on recycled aggregates and recycled aggregate concrete, *Materials and Structures* 1 (1986) 201–204.

- [60] T. C. Hansen, *Recycling of demolished concrete and masonry*, CRC Press, 1992.
- [61] I. Page, The rise and fall of claddings, *Build*, June/July 2007 (2007) 68–69.
- [62] M. Adamson, A. Razmjoo, A. Poursaei, Durability of concrete incorporating crushed brick as coarse aggregate, *Construction and building materials* 94 (2015) 426–432.
- [63] S. T. Deresa, J. Xu, C. Demartino, Y. Heo, Z. Li, Y. Xiao, A review of experimental results on structural performance of reinforced recycled aggregate concrete beams and columns, *Advances in Structural Engineering* (2020) 1369433220934564.
- [64] J. Xiao, J. Shen, M. Bai, Q. Gao, Y. Wu, Reuse of construction spoil in china: current status and future opportunities, *Journal of Cleaner Production* (2020) 125742.
- [65] R. Clifton, *High strain rate behavior of metals* (1990).
- [66] P. H. Bischoff, S. H. Perry, Compressive behaviour of concrete at high strain rates, *Materials and structures* 24 (1991) 425–450.
- [67] T. Ngo, P. Mendis, A. Gupta, J. Ramsay, Blast loading and blast effects on structures—an overview, *Electronic journal of structural engineering* (2007) 76–91.
- [68] A. Nghiem, C. Demartino, Y. Xiao, T. H.-K. Kang, Impact behavior of unbonded post-tensioned concrete beams., *ACI Structural Journal* 118 (2021).
- [69] B. Hopkinson, X. a method of measuring the pressure produced in the detonation of high, explosives or by the impact of bullets, *Philosophical Transactions of the Royal Society of London. Series A, Containing Papers of a Mathematical or Physical Character* 213 (1914) 437–456.
- [70] H. Kolsky, An investigation of the mechanical properties of materials at very high rates of loading, *Proceedings of the Physical Society. Section B* 62 (1949) 676.
- [71] G. Taylor, et al., The testing of materials at high rates of loading, *J. Inst. Civil Eng* 26 (1946) 487–501.

- [72] A. Abou-Sayed, R. Clifton, L. Hermann, The oblique-plate impact experiment, *Experimental Mechanics* 16 (1976) 127–132.
- [73] D. Lai, C. Demartino, Y. Xiao, High-strain rate compressive behavior of fiber-reinforced rubberized concrete, *Construction and Building Materials* 319 (2022) 125739.
- [74] D. Lai, C. Demartino, Y. Xiao, High-strain rate tension behavior of fiber-reinforced rubberized concrete, *Cement and Concrete Composites* 131 (2022) 104554.
- [75] B. Xiong, C. Demartino, J. Xu, A. Simi, G. C. Marano, Y. Xiao, High-strain rate compressive behavior of concrete made with substituted coarse aggregates: Recycled crushed concrete and clay bricks, *Construction and Building Materials* 301 (2021) 123875.
- [76] T. D. Rossing, D. A. Russell, Laboratory observation of elastic waves in solids, *American Journal of Physics* 58 (1990) 1153–1162.
- [77] S. Park, M. Zhou, Separation of elastic waves in split hopkinson bars using one-point strain measurements, *Experimental Mechanics* 39 (1999) 287–294.
- [78] H. Wu, Q. Zhang, F. Huang, Q. Jin, Experimental and numerical investigation on the dynamic tensile strength of concrete, *International Journal of Impact Engineering* 32 (2005) 605–617.
- [79] A. Hasan, R. Hamid, A. Ariffin, R. Gani, Normal strength concrete subjected to high strain rate, *Asian Journal of Applied Sciences* 3 (2010) 145–152.
- [80] M. Pająk, The influence of the strain rate on the strength of concrete taking into account the experimental techniques (2011).
- [81] S.-C. Woo, J.-T. Kim, C.-H. Cho, J.-Y. Kim, T.-W. Kim, The dynamic compressive behavior of armor structural materials in split hopkinson pressure bar test, *The Journal of Strain Analysis for Engineering Design* 48 (2013) 420–436.
- [82] J. Field, S. Walley, W. Proud, H. Goldrein, C. Siviour, Review of experimental techniques for high rate deformation and shock studies, *International journal of impact engineering* 30 (2004) 725–775.

- [83] R. Davies, A critical study of the Hopkinson pressure bar, *Philosophical Transactions of the Royal Society of London. Series A, Mathematical and Physical Sciences* 240 (1948) 375–457.
- [84] U. Lindholm, *High strain rate tests, techniques of metals research, measurement of mechanical properties*, 1971.
- [85] L. Malvern, T. Tang, D. Jenkins, J. Gong, Dynamic compressive strength of cementitious materials, *MRS Online Proceedings Library (OPL)* 64 (1985).
- [86] C. Albertini, M. Montagnani, Study of the true tensile stress-strain diagram of plain concrete with real size aggregate; need for and design of a large hopkinson bar bundle, *Le Journal de Physique IV* 4 (1994) C8–113.
- [87] W. Chen, B. Song, *Split Hopkinson (Kolsky) bar: design, testing and applications*, Springer Science & Business Media, 2010.
- [88] A. Jenet, *Open access to jrc research infrastructures* (2021).
- [89] A. Tukker, *Plastics waste: feedstock recycling, chemical recycling and incineration* (2002).
- [90] R. Siddique, J. Khatib, I. Kaur, Use of recycled plastic in concrete: A review, *Waste management* 28 (2008) 1835–1852.
- [91] N. Saikia, J. De Brito, Use of plastic waste as aggregate in cement mortar and concrete preparation: A review, *Construction and Building Materials* 34 (2012) 385–401.
- [92] L. Gu, T. Ozbakkaloglu, Use of recycled plastics in concrete: A critical review, *Waste Management* 51 (2016) 19–42.
- [93] R. Sharma, P. P. Bansal, Use of different forms of waste plastic in concrete—a review, *Journal of Cleaner Production* 112 (2016) 473–482.
- [94] I. Mercante, C. Alejandrino, J. Ojeda, J. Chini, C. Maroto, N. Fajardo, Mortar and concrete composites with recycled plastic: A review, *Science and Technology of Materials* 30 (2018) 69–79.

- [95] I. Almeshal, B. A. Tayeh, R. Alyousef, H. Alabduljabbar, A. M. Mohamed, A. Alaskar, Use of recycled plastic as fine aggregate in cementitious composites: A review, *Construction and Building Materials* 253 (2020) 119146.
- [96] A. Al-Manaseer, T. Dalal, Concrete containing plastic aggregates, *Concrete international* 19 (1997) 47–52.
- [97] A. M. da Silva, J. de Brito, R. Veiga, Incorporation of fine plastic aggregates in rendering mortars, *Construction and Building Materials* 71 (2014) 226–236.
- [98] A. Merlo, L. Lavagna, D. Riera-Suarez, M. Pavese, Mechanical properties of mortar containing waste plastic (pvc) as aggregate partial replacement, *Case Studies in Construction Materials* (2020) e00467.
- [99] A. Aattache, R. Soltani, A. Mahi, Investigations for properties improvement of recycled pe polymer particles-reinforced mortars for repair practice, *Construction and Building Materials* 146 (2017) 603–614.
- [100] L. A. P. de Oliveira, J. P. Castro-Gomes, Physical and mechanical behaviour of recycled pet fibre reinforced mortar, *Construction and Building Materials* 25 (2011) 1712–1717.
- [101] R. Wang, C. Meyer, Performance of cement mortar made with recycled high impact polystyrene, *Cement and Concrete Composites* 34 (2012) 975–981.
- [102] Y. Ghernouti, B. Rabehi, Strength and durability of mortar made with plastics bag waste (mpbw), *International Journal of Concrete Structures and Materials* 6 (2012) 145–153.
- [103] F. Iucolano, B. Liguori, D. Caputo, F. Colangelo, R. Cioffi, Recycled plastic aggregate in mortars composition: Effect on physical and mechanical properties, *Materials & Design* (1980-2015) 52 (2013) 916–922.
- [104] K. Hannawi, W. Prince-Agbodjan, Transfer behaviour and durability of cementitious mortars containing polycarbonate plastic wastes, *European Journal of Environmental and Civil Engineering* 19 (2015) 467–481.
- [105] B. Al-Tulaian, M. Al-Shannag, A. Al-Hozaimy, Recycled plastic waste fibers for reinforcing portland cement mortar, *Construction and Building Materials* 127 (2016) 102–110.

- [106] B. Coppola, L. Courard, F. Michel, L. Incarnato, L. Di Maio, Investigation on the use of foamed plastic waste as natural aggregates replacement in lightweight mortar, *Composites Part B: Engineering* 99 (2016) 75–83.
- [107] C. Aciu, D.-A. Ilutiu-Varvara, D.-L. Manea, Y.-A. Orban, F. Babota, Recycling of plastic waste materials in the composition of ecological mortars, *Procedia Manufacturing* 22 (2018) 274–279.
- [108] A. Badache, A. S. Benosman, Y. Senhadji, M. Mouli, Thermo-physical and mechanical characteristics of sand-based lightweight composite mortars with recycled high-density polyethylene (hdpe), *Construction and Building Materials* 163 (2018) 40–52.
- [109] B. Coppola, L. Courard, F. Michel, L. Incarnato, P. Scarfato, L. Di Maio, Hygro-thermal and durability properties of a lightweight mortar made with foamed plastic waste aggregates, *Construction and Building Materials* 170 (2018) 200–206.
- [110] P. Rubio-de Hita, F. Pérez-Gálvez, M. J. Morales-Conde, M. A. Pedreño-Rojas, Reuse of plastic waste of mixed polypropylene as aggregate in mortars for the manufacture of pieces for restoring jack arch floors with timber beams, *Journal of Cleaner Production* 198 (2018) 1515–1525.
- [111] Y. Senhadji, H. Siad, G. Escadeillas, A. S. Benosman, R. Chihaoui, M. Mouli, M. Lachemi, Physical, mechanical and thermal properties of lightweight composite mortars containing recycled polyvinyl chloride, *Construction and Building Materials* 195 (2019) 198–207.
- [112] E. A. Ohemeng, S. O. Ekolu, Strength prediction model for cement mortar made with waste ldpe plastic as fine aggregate, *Journal of Sustainable Cement-Based Materials* 8 (2019) 228–243.
- [113] M. Martínez-López, G. Martínez-Barrera, R. Salgado-Delgado, O. Gencel, Recycling polypropylene and polyethylene wastes in production of polyester based polymer mortars, *Construction and Building Materials* 274 (2021) 121487.
- [114] P. Górak, P. Postawa, L. N. Trusilewicz, A. Łagosz, Lightweight pet based composite aggregates in portland cement materials-microstructure and physicochemical performance, *Journal of Building Engineering* 34 (2021) 101882.

- [115] Y. W. D. Tay, Y. Qian, M. J. Tan, Printability region for 3d concrete printing using slump and slump flow test, *Composites Part B: Engineering* 174 (2019) 106968.
- [116] S. Kumar, R. C. Gupta, S. Shrivastava, L. Csetenyi, B. S. Thomas, Preliminary study on the use of quartz sandstone as a partial replacement of coarse aggregate in concrete based on clay content, morphology and compressive strength of combined gradation, *Construction and Building materials* 107 (2016) 103–108.
- [117] M. Belmokaddem, A. Mahi, Y. Senhadji, B. Y. Pekmezci, Mechanical and physical properties and morphology of concrete containing plastic waste as aggregate, *Construction and Building Materials* 257 (2020) 119559.
- [118] D. S. Babu, K. G. Babu, W. Tiong-Huan, Effect of polystyrene aggregate size on strength and moisture migration characteristics of lightweight concrete, *Cement and Concrete Composites* 28 (2006) 520–527.
- [119] A. M. Ghaly, M. S. Gill, Compression and deformation performance of concrete containing postconsumer plastics, *Journal of materials in civil engineering* 16 (2004) 289–296.
- [120] B. Chen, J. Liu, Properties of lightweight expanded polystyrene concrete reinforced with steel fiber, *Cement and Concrete Research* 34 (2004) 1259–1263.
- [121] S. Kou, G. Lee, C. Poon, W. Lai, Properties of lightweight aggregate concrete prepared with pvc granules derived from scraped pvc pipes, *Waste Management* 29 (2009) 621–628.
- [122] A. M. Al Bakri, S. M. Tamizi, A. Rafiza, Y. Zarina, et al., Investigation of hdpe plastic waste aggregate on the properties of concrete, *Journal of Asian Scientific Research* 1 (2011) 340–345.
- [123] L. Ferreira, J. de Brito, N. Saikia, Influence of curing conditions on the mechanical performance of concrete containing recycled plastic aggregate, *Construction and Building Materials* 36 (2012) 196–204.

- [124] R. V. Silva, J. de Brito, N. Saikia, Influence of curing conditions on the durability-related performance of concrete made with selected plastic waste aggregates, *Cement and Concrete Composites* 35 (2013) 23–31.
- [125] N. Saikia, J. de Brito, Mechanical properties and abrasion behaviour of concrete containing shredded pet bottle waste as a partial substitution of natural aggregate, *Construction and building materials* 52 (2014) 236–244.
- [126] S. Yang, X. Yue, X. Liu, Y. Tong, Properties of self-compacting lightweight concrete containing recycled plastic particles, *Construction and Building Materials* 84 (2015) 444–453.
- [127] F. Liu, Y. Yan, L. Li, C. Lan, G. Chen, Performance of recycled plastic-based concrete, *Journal of Materials in Civil Engineering* 27 (2015) A4014004.
- [128] Y. Senhadji, G. Escadeillas, A. Benosman, M. Mouli, H. Khelafi, S. Ould Kaci, Effect of incorporating pvc waste as aggregate on the physical, mechanical, and chloride ion penetration behavior of concrete, *Journal of Adhesion Science and Technology* 29 (2015) 625–640.
- [129] J. L. Ruiz-Herrero, D. V. Nieto, A. López-Gil, A. Arranz, A. Fernández, A. Lorenzana, S. Merino, J. A. De Saja, M. Á. Rodríguez-Pérez, Mechanical and thermal performance of concrete and mortar cellular materials containing plastic waste, *Construction and Building Materials* 104 (2016) 298–310.
- [130] F. Colangelo, R. Cioffi, B. Liguori, F. Iucolano, Recycled polyolefins waste as aggregates for lightweight concrete, *Composites Part B: Engineering* 106 (2016) 234–241.
- [131] A. A. Mohammed, I. I. Mohammed, S. A. Mohammed, Some properties of concrete with plastic aggregate derived from shredded pvc sheets, *Construction and Building Materials* 201 (2019) 232–245.
- [132] Z. Z. Ismail, E. A. Al-Hashmi, Use of waste plastic in concrete mixture as aggregate replacement, *Waste management* 28 (2008) 2041–2047.
- [133] K. Ramadevi, R. Manju, Experimental investigation on the properties of concrete with plastic pet (bottle) fibres as fine aggregates, *International journal of emerging technology and advanced engineering* 2 (2012) 42–46.



- [134] N. L. Rahim, S. Sallehuddin, N. M. Ibrahim, R. C. Amat, M. F. Ab Jalil, Use of plastic waste (high density polyethylene) in concrete mixture as aggregate replacement, in: *Advanced Materials Research*, volume 701, Trans Tech Publ, 2013, pp. 265–269.
- [135] R. Saxena, S. Siddique, T. Gupta, R. K. Sharma, S. Chaudhary, Impact resistance and energy absorption capacity of concrete containing plastic waste, *Construction and Building Materials* 176 (2018) 415–421.
- [136] E. Del Rey Castillo, N. Almesfer, O. Saggi, J. M. Ingham, Light-weight concrete with artificial aggregate manufactured from plastic waste, *Construction and Building Materials* 265 (2020) 120199.
- [137] D. P. Bentz, E. J. Garboczi, C. J. Haecker, O. M. Jensen, Effects of cement particle size distribution on performance properties of portland cement-based materials, *Cement and concrete research* 29 (1999) 1663–1671.
- [138] M. Gesoglu, E. Güneyisi, O. Hansu, S. Etili, M. Alhassan, Mechanical and fracture characteristics of self-compacting concretes containing different percentage of plastic waste powder, *Construction and Building Materials* 140 (2017) 562–569.
- [139] Y. Ghernouti, B. Rabehi, T. Bouziani, H. Ghezraoui, A. Makhloufi, Fresh and hardened properties of self-compacting concrete containing plastic bag waste fibers (wfscc), *Construction and Building Materials* 82 (2015) 89–100.
- [140] J. Thorneycroft, J. Orr, P. Savoikar, R. Ball, Performance of structural concrete with recycled plastic waste as a partial replacement for sand, *Construction and Building Materials* 161 (2018) 63–69.
- [141] C. Jacob-Vaillancourt, L. Sorelli, Characterization of concrete composites with recycled plastic aggregates from postconsumer material streams, *Construction and Building Materials* 182 (2018) 561–572.
- [142] J.-J. Xu, Z.-P. Chen, T. Ozbakkaloglu, X.-Y. Zhao, C. Demartino, A critical assessment of the compressive behavior of reinforced recycled aggregate concrete columns, *Engineering Structures* 161 (2018) 161–175.

- [143] J. De Brito, N. Saikia, *Recycled aggregate in concrete: use of industrial, construction and demolition waste*, Springer Science & Business Media, 2012.
- [144] J. Xiao, J. Li, C. Zhang, Mechanical properties of recycled aggregate concrete under uniaxial loading, *Cement and concrete research* 35 (2005) 1187–1194.
- [145] J. Xu, Z. Chen, X. Zhao, C. Demartino, T. Ozbakkaloglu, J. Xue, Seismic performance of circular recycled aggregate concrete-filled steel tubular columns: Fem modelling and sensitivity analysis, *Thin-Walled Structures* 141 (2019) 509–525.
- [146] J. Xu, Y. Chen, T. Xie, X. Zhao, B. Xiong, Z. Chen, Prediction of triaxial behavior of recycled aggregate concrete using multivariable regression and artificial neural network techniques, *Construction and Building Materials* 226 (2019) 534–554.
- [147] J. Xu, X. Zhao, Y. Yu, T. Xie, G. Yang, J. Xue, Parametric sensitivity analysis and modelling of mechanical properties of normal-and high-strength recycled aggregate concrete using grey theory, multiple nonlinear regression and artificial neural networks, *Construction and Building Materials* 211 (2019) 479–491.
- [148] T. Xie, G. Yang, X. Zhao, J. Xu, C. Fang, A unified model for predicting the compressive strength of recycled aggregate concrete containing supplementary cementitious materials, *Journal of Cleaner Production* 251 (2020) 119752.
- [149] J. Xu, Y. Wang, R. Ren, Z. Wu, T. Ozbakkaloglu, Performance evaluation of recycled aggregate concrete-filled steel tubes under different loading conditions: Database analysis and modelling, *Journal of Building Engineering* (2020) 101308.
- [150] M. Etxeberria, E. Vázquez, A. Marí, M. Barra, Influence of amount of recycled coarse aggregates and production process on properties of recycled aggregate concrete, *Cement and concrete research* 37 (2007) 735–742.
- [151] S. Kobayashi, H. Kawano, Properties and usage of recycled aggregate concrete, *Demolition and reuse of Concrete and Masonry* 2 (1988) 547–556.

- [152] J. M. Gómez-Soberón, Porosity of recycled concrete with substitution of recycled concrete aggregate: An experimental study, *Cement and concrete research* 32 (2002) 1301–1311.
- [153] A. Katz, Properties of concrete made with recycled aggregate from partially hydrated old concrete, *Cement and concrete research* 33 (2003) 703–711.
- [154] K. K. Sagoe-Crentsil, T. Brown, A. H. Taylor, Performance of concrete made with commercially produced coarse recycled concrete aggregate, *Cement and concrete research* 31 (2001) 707–712.
- [155] I. B. Topcu, S. Şengel, Properties of concretes produced with waste concrete aggregate, *Cement and concrete research* 34 (2004) 1307–1312.
- [156] C. S. Poon, C. S. Lam, The effect of aggregate-to-cement ratio and types of aggregates on the properties of pre-cast concrete blocks, *Cement and Concrete Composites* 30 (2008) 283–289.
- [157] F. López-Gayarre, P. Serna, A. Domingo-Cabo, M. Serrano-López, C. López-Colina, Influence of recycled aggregate quality and proportioning criteria on recycled concrete properties, *Waste management* 29 (2009) 3022–3028.
- [158] P. Belin, G. Habert, M. Thiery, N. Roussel, Cement paste content and water absorption of recycled concrete coarse aggregates, *Materials and Structures* 47 (2014) 1451–1465.
- [159] V. W. Tam, X. Gao, C. M. Tam, C. Chan, New approach in measuring water absorption of recycled aggregates, *Construction and building materials* 22 (2008) 364–369.
- [160] P. Folino, H. Xargay, Recycled aggregate concrete—mechanical behavior under uniaxial and triaxial compression, *Construction and Building Materials* 56 (2014) 21–31.
- [161] W. H. Kwan, M. Ramli, K. J. Kam, M. Z. Sulieman, Influence of the amount of recycled coarse aggregate in concrete design and durability properties, *Construction and Building Materials* 26 (2012) 565–573.
- [162] S.-C. Kou, C.-s. Poon, Long-term mechanical and durability properties of recycled aggregate concrete prepared with the incorporation of fly ash, *Cement and Concrete Composites* 37 (2013) 12–19.

- [163] P. B. Cachim, Mechanical properties of brick aggregate concrete, *Construction and Building Materials* 23 (2009) 1292–1297.
- [164] T. U. Mohammed, A. Hasnat, M. A. Awal, S. Z. Bosunia, Recycling of brick aggregate concrete as coarse aggregate, *Journal of Materials in Civil Engineering* 27 (2015) B4014005.
- [165] C.-H. Weng, D.-F. Lin, P.-C. Chiang, Utilization of sludge as brick materials, *Advances in environmental research* 7 (2003) 679–685.
- [166] C. S. Poon, D. Chan, Paving blocks made with recycled concrete aggregate and crushed clay brick, *Construction and building materials* 20 (2006) 569–577.
- [167] L. Zong, Z. Fei, S. Zhang, Permeability of recycled aggregate concrete containing fly ash and clay brick waste, *Journal of Cleaner Production* 70 (2014) 175–182.
- [168] G. Carta, F. Stochino, Theoretical models to predict the flexural failure of reinforced concrete beams under blast loads, *Engineering structures* 49 (2013) 306–315.
- [169] C. Demartino, J. Wu, Y. Xiao, Response of shear-deficient reinforced circular rc columns under lateral impact loading, *International Journal of Impact Engineering* 109 (2017) 196–213.
- [170] J. Xu, C. Demartino, B. Shan, Y. Heo, Y. Xiao, Experimental investigation on performance of cantilever cfrp-wrapped circular rc columns under lateral low-velocity impact, *Composite Structures* (2020) 112143.
- [171] A. M. S. Hamouda, M. S. J. Hashmi, Testing of composite materials at high rates of strain: advances and challenges, *Journal of Materials Processing Technology* 300 (1998) 327–336.
- [172] K. Ramesh, High rates and impact experiments, in: *Springer handbook of experimental solid mechanics*, Springer, 2008, pp. 929–960.
- [173] K.-M. Kim, S. Lee, J.-Y. Cho, Effect of maximum coarse aggregate size on dynamic compressive strength of high-strength concrete, *International Journal of Impact Engineering* 125 (2019) 107–116.

- [174] L. Li, J. Xiao, C. S. Poon, Dynamic compressive behavior of recycled aggregate concrete, *Materials and Structures* 49 (2016) 4451–4462.
- [175] W. Li, Z. Luo, C. Long, C. Wu, W. H. Duan, S. P. Shah, Effects of nanoparticle on the dynamic behaviors of recycled aggregate concrete under impact loading, *Materials & Design* 112 (2016) 58–66.
- [176] W. Li, Z. Luo, C. Wu, V. W. Tam, W. H. Duan, S. P. Shah, Experimental and numerical studies on impact behaviors of recycled aggregate concrete-filled steel tube after exposure to elevated temperature, *Materials & Design* 136 (2017) 103–118.
- [177] L. Li, C. S. Poon, J. Xiao, D. Xuan, Effect of carbonated recycled coarse aggregate on the dynamic compressive behavior of recycled aggregate concrete, *Construction and building materials* 151 (2017) 52–62.
- [178] M. C. Rao, S. Bhattacharyya, S. Barai, Behaviour of recycled aggregate concrete under drop weight impact load, *Construction and Building Materials* 25 (2011) 69–80.
- [179] J. Guo, J. Cai, Q. Chen, X. Liu, Y. Wang, Z. Zuo, Dynamic behaviour and energy dissipation of reinforced recycled aggregate concrete beams under impact, *Construction and Building Materials* 214 (2019) 143–157.
- [180] M. Larcher, M. Peroni, G. Solomos, N. Gebbeken, P. Bieber, J. Wandelt, N. T. Tran, Dynamic increase factor of masonry materials: Experimental investigations, *ISIEMS/ICPS* (2013).
- [181] X. Zhang, Y.-W. Chiu, H. Hao, A. Hsieh, N. Salter, J. Cui, Dynamic compressive material properties of clay bricks at different strain rates, *Construction and Building Materials* 192 (2018) 754–767.
- [182] T. L. Piani, J. Weerheijm, M. Peroni, L. Koene, D. Krabbenborg, G. Solomos, L. Sluys, Dynamic behaviour of adobe bricks in compression: The role of fibres and water content at various loading rates, *Construction and Building Materials* 230 (2020) 117038.
- [183] L. Chen, X. Zhang, G. Liu, Analysis of dynamic mechanical properties of sprayed fiber-reinforced concrete based on the energy conversion principle, *Construction and Building Materials* 254 (2020) 119167.

- [184] B. Chun, W. Shin, T. Oh, D.-Y. Yoo, Dynamic compressive and flexural behaviors of ultra-rapid-hardening mortar containing polyethylene fibers, *Archives of Civil and Mechanical Engineering* 21 (2021) 1–17.
- [185] S. Hu, H. Tang, S. Han, Energy absorption characteristics of pvc coarse aggregate concrete under impact load, *International Journal of Concrete Structures and Materials* 15 (2021) 1–16.
- [186] A. Kheyroddin, H. Arshadi, M. R. Ahadi, G. Taban, M. Kioumars, The impact resistance of fiber-reinforced concrete with polypropylene fibers and gfrp wrapping, *Materials Today: Proceedings* 45 (2021) 5433–5438.
- [187] J.-X. Lin, Y. Song, Z.-H. Xie, Y.-C. Guo, B. Yuan, J.-J. Zeng, X. Wei, Static and dynamic mechanical behavior of engineered cementitious composites with pp and pva fibers, *Journal of Building Engineering* 29 (2020) 101097.
- [188] H. Zhong, M. Zhang, Effect of recycled polymer fibre on dynamic compressive behaviour of engineered geopolymer composites, *Ceramics International* (2022).
- [189] X. Wu, D. Gorham, Stress equilibrium in the split hopkinson pressure bar test, *Le Journal de Physique IV* 7 (1997) C3–91.
- [190] B. EN, 206-1: 2000, Concrete, Specification, Performance, Production and Conformity (2001).
- [191] K. Hoffmann, Applying the Wheatstone bridge circuit, HBM Germany, 1974.
- [192] K. Safa, G. Gary, Displacement correction for punching at a dynamically loaded bar end, *International Journal of Impact Engineering* 37 (2010) 371–384.
- [193] G. T. GRAY III, Classic split Hopkinson pressure bar testing, *ASM handbook* 8 (2000) 462–476.
- [194] S. A. Tekalur, O. Sen, Effect of specimen size in the kolsky bar, *Procedia Engineering* 10 (2011) 2663–2671.
- [195] L. Kennedy, O. Jones, Longitudinal wave propagation in a circular bar loaded suddenly by a radially distributed end stress (1969).

- [196] P. S. Follansbee, The hopkinson bar, *Metals handbook* 8 (1985) 198–217.
- [197] F. Gallina, M. Alves, Design of a split hopkinson pressure bar, EPUSP, 2004.
- [198] Z. Rohrbach, T. Buresh, M. Madsen, Modeling the exit velocity of a compressed air cannon, *American Journal of Physics* 80 (2012) 24–26.
- [199] A. E. Seigel, Performance calculations and optimization of gas guns, Technical Report, 1981.
- [200] Z. Wang, L. Meyer, On the plastic wave propagation along the specimen length in shpb test, *Experimental mechanics* 50 (2010) 1061–1074.
- [201] H. Kolsky, *Stress waves in solids*, volume 1098, Courier Corporation, 1963.
- [202] M. Hosur, J. Alexander, U. Vaidya, S. Jeelani, High strain rate compression response of carbon/epoxy laminate composites, *Composite Structures* 52 (2001) 405–417.
- [203] W. E. Baker, C. Yew, Strain-rate effects in the propagation of torsional plastic waves (1966).
- [204] J. S. Rinehart, *Stress transients in solids*, HyperDynamics, 1975.
- [205] B. Song, W. Chen, Dynamic stress equilibration in split hopkinson pressure bar tests on soft materials, *Experimental mechanics* 44 (2004) 300–312.
- [206] H. Liao, W. Chen, Specimen-bar impedance mismatch effects on equilibrium and rate constancy for kolsky bar experiments, *Experimental Mechanics* 58 (2018) 1439–1449.
- [207] D. J. Frew, M. J. Forrestal, W. Chen, A split hopkinson pressure bar technique to determine compressive stress-strain data for rock materials, *Experimental mechanics* 41 (2001) 40–46.
- [208] G. Ravichandran, G. Subhash, Critical appraisal of limiting strain rates for compression testing of ceramics in a split hopkinson pressure bar, *Journal of the American Ceramic Society* 77 (1994) 263–267.
- [209] Y. Pan, W. Chen, B. Song, Upper limit of constant strain rates in a split hopkinson pressure bar experiment with elastic specimens, *Experimental Mechanics* 45 (2005) 440–446.

- [210] N. S. Al-Maliky, Dimension effect on dynamic stress equilibrium in shpb tests, *International Journal of Materials Physics* 5 (2014) 15–26.
- [211] C. W. Felice, The response of soil to impulse loads using the split-Hopkinson pressure bar technique, Technical Report, 1986.
- [212] I. R. Ahmad, D. W. Shu, Effect of specimen diameter in compression at high strain rates, *Journal of engineering mechanics* 137 (2011) 169–174.
- [213] G. Suazo, A. Fourie, J. Doherty, Experimental investigation of propagation and transmission of compressional stress waves in cemented paste backfill, *Journal of Geotechnical and Geoenvironmental Engineering* 143 (2017) 04016104.
- [214] A.-N. Rotariu, E. Trană, L. Matache, Young's modulus calculus using split hopkinson bar tests on long and thin material samples, *Materials* 15 (2022) 3058.
- [215] Z. Li, J. Lambros, Determination of the dynamic response of brittle composites by the use of the split Hopkinson pressure bar, *Composites Science and Technology* 59 (1999) 1097–1107.
- [216] B. A. Gama, S. L. Lopatnikov, J. W. Gillespie Jr, Hopkinson bar experimental technique: a critical review, *Appl. Mech. Rev.* 57 (2004) 223–250.
- [217] J. Klepaczko, A. Brara, An experimental method for dynamic tensile testing of concrete by spalling, *International journal of impact engineering* 25 (2001) 387–409.
- [218] H. Schuler, C. Mayrhofer, K. Thoma, Spall experiments for the measurement of the tensile strength and fracture energy of concrete at high strain rates, *International Journal of Impact Engineering* 32 (2006) 1635–1650.
- [219] D. Brizard, S. Ronel, E. Jacquelin, Estimating measurement uncertainty on stress-strain curves from SHPB, *Experimental Mechanics* 57 (2017) 735–742.
- [220] Z. Fenghua, W. Lili, H. Shisheng, On the effect of stress nonuniformness in polymer specimen of shpb tests, *Experimental Mechanics* 7 (1992) 23–29.
- [221] M. Hassan, K. Wille, Experimental impact analysis on ultra-high performance concrete (uhpc) for achieving stress equilibrium (se) and constant strain rate



- (csr) in split hopkinson pressure bar (shpb) using pulse shaping technique, *Construction & Building Materials* 144 (2017) 747–757.
- [222] T. Jiang, P. Xue, H. Butt, Pulse shaper design for dynamic testing of viscoelastic materials using polymeric shpb, *International Journal of Impact Engineering* 79 (2015) 45–52.
- [223] X. Chen, L. Ge, J. Zhou, S. Wu, Experimental study on split hopkinson pressure bar pulse-shaping techniques for concrete, *Journal of Materials in Civil Engineering* 28 (2016) 04015196.
- [224] Z. Song, Z. Wang, H. Kim, H. Ma, Z. Song, Z. Wang, H. Kim, H. Ma, Pulse shaper and dynamic compressive property investigation on ice using a large-sized modified split hopkinson pressure bar, *Lat.am.j.solids Struct* 13 (2016) 391–406.
- [225] J. Wang, W. Li, L. Xu, Z. Du, G. Gao, Experimental study on pulse shaping techniques of large diameter shpb apparatus for concrete, *Latin American Journal of Solids and Structures* 18 (2021).
- [226] V. M. Deshpande, S. Madan, T. Chakraborty, Experimental and numerical study on designing pulse shapers for testing rocks in large-diameter shpb, *Journal of Materials in Civil Engineering* 35 (2023) 04023012.
- [227] X.-b. Li, L. Hong, T.-b. Yin, Z.-l. Zhou, Z.-y. Ye, Relationship between diameter of split hopkinson pressure bar and minimum loading rate under rock failure, *Journal of Central South University of Technology* 15 (2008) 218–223.
- [228] S. Luo, F. Gong, Experimental and numerical analyses of the rational loading waveform in shpb test for rock materials, *Advances in Civil Engineering* 2018 (2018).
- [229] P. Follansbee, C. Frantz, *Wave propagation in the split hopkinson pressure bar* (1983).
- [230] J. Gong, L. Malvern, D. Jenkins, *Dispersion investigation in the split Hopkinson pressure bar* (1990).

- [231] C. H. Guo, X. H. Shen, F. C. Jiang, G. P. Zou, Effect of stress wave dispersion on hopkinson pressure bar loaded fracture test 577 (2014) 569–572.
- [232] A. M. Bragov, A. K. Lomunov, D. A. Lamzin, A. Y. Konstantinov, Dispersion correction in split-hopkinson pressure bar: theoretical and experimental analysis, *Continuum Mechanics and Thermodynamics* (2019) 1–13.
- [233] D. Brizard, E. Jacquelin, Uncertainty quantification and global sensitivity analysis of longitudinal wave propagation in circular bars. application to shpb device, *International Journal of Solids and Structures* 134 (2018) 264–271.
- [234] H. Shin, Manual for calibrating sound speed and poisson's ratio of (split) hopkinson bar via dispersion correction using excel® and matlab® templates, *Data* 7 (2022) 55.
- [235] H. Shin, Sound speed and poisson's ratio calibration of (split) hopkinson bar via iterative dispersion correction of elastic wave, *Journal of Applied Mechanics* 89 (2022) 061007.
- [236] A. Tyas, A. J. Watson, An investigation of frequency domain dispersion correction of pressure bar signals, *International Journal of Impact Engineering* 25 (2001) 87–101.
- [237] R. Merle, H. Zhao, On the errors associated with the use of large diameter SHPB, correction for radially non-uniform distribution of stress and particle velocity in SHPB testing, *International Journal of Impact Engineering* 32 (2006) 1964–1980.
- [238] S. E. Rigby, A. D. Barr, M. Clayton, A review of Pochhammer-Chree dispersion in the Hopkinson bar, *Proceedings of the Institution of Civil Engineers-Engineering and Computational Mechanics* 171 (2018) 3–13.
- [239] L. Pochhammer, On the propagation velocities of small oscillations in an unlimited isotropic circular cylinder, *J. Reine Angewandte Math* 81 (1876) 324.
- [240] C. Chree, The equation of an isotropic elastic solid in polar and cylindrical coordinates, their solution and application, *Trans. Cambridge Philos. Soc.*–1889.–Pt 3 (1889) 250–369.

- [241] A. E. H. Love, *A treatise on the mathematical theory of elasticity*, Cambridge university press, 2013.
- [242] F. Honarvar, E. Enjilela, A. N. Sinclair, An alternative method for plotting dispersion curves, *Ultrasonics* 49 (2009) 15–18.
- [243] H. Zhao, G. Gary, A three dimensional analytical solution of the longitudinal wave propagation in an infinite linear viscoelastic cylindrical bar. application to experimental techniques, *Journal of the Mechanics and Physics of Solids* 43 (1995) 1335–1348.
- [244] D. Bancroft, The velocity of longitudinal waves in cylindrical bars, *Physical Review* 59 (1941) 588.
- [245] C. Curtis, Propagation of an elastic strain pulse in a semi-infinite bar, in: *International symposium on stress wave propagation in materials*, Interscience Publishers Inc. New York, 1960, pp. 15–43.
- [246] J. Oliver, Elastic wave dispersion in a cylindrical rod by a wide-band short-duration pulse technique, *The Journal of the Acoustical Society of America* 29 (1957) 189–194.
- [247] D. Francis, W. Whittington, W. Lawrimore, P. Allison, S. Turnage, J. Bhattacharyya, Split hopkinson pressure bar graphical analysis tool, *Experimental Mechanics* 57 (2017) 179–183.
- [248] D. Gorham, A numerical method for the correction of dispersion in pressure bar signals, *Journal of Physics E: Scientific Instruments* 16 (1983) 477.
- [249] C. Lee, R. Crawford, A new method for analysing dispersed bar gauge data, *Measurement Science and Technology* 4 (1993) 931.
- [250] J. Lifshitz, H. Leber, Data processing in the split Hopkinson pressure bar tests, *International Journal of Impact Engineering* 15 (1994) 723–733.
- [251] A. Tyas, A. Watson, A study of the effect of spatial variation of load in the pressure bar, *Measurement Science and Technology* 11 (2000) 1539.
- [252] G. Larbi, T. Mostapha, O. Hocine, A. E. M. Alaoui, A practical note for shpb test with new algorithms for delimiting pulses, *Composite Structures* 126 (2015) 145–158.

- [253] N. Naik, K. S. Pandya, J. R. Pothnis, T. A. Gelu, Revisiting kolsky bar data evaluation method, *Composite Structures* 111 (2014) 446–452.
- [254] J. Sercombe, Modelisation du comportement du beton en dynamique rapide application au calcul des conteneurs a haute integrite, Ph.D. thesis, École nationale des ponts et chaussées (France), 1997.
- [255] BSI, Bs en 1744 - tests for chemical properties of aggregates, BSI (British Standards Institution) (1998).
- [256] GB, Gb/t 25177–2010: Recycled coarse aggregate for concrete (in chinese), Chinese Building Press Beijing (China) (2010).
- [257] JGJ, Jgj 55-2011: Specification for mix proportion design of ordinary concrete, Bulletin of the Ministry of Housing and Urban-Rural Development, No. 991 (2011).
- [258] MOCO, Technical specification for lightweight aggregate concrete (in chinese), China Architecture & Building Press: Beijing, China (2002).
- [259] BS, Testing concrete: Method for determination of compressive strength of concrete cubes, 1983.
- [260] GB, Gb/t 50081-2002: Standard for test method of mechanical properties on ordinary concrete( in chinese), GB/T 50081-2002 (2002).
- [261] S. Zhou, C. Demartino, Y. Xiao, High-strain rate compressive behavior of douglas fir and glubam, *Construction and Building Materials* 258 (2020) 119466.
- [262] X. Sun, K. Zhao, Y. Li, R. Huang, Z. Ye, Y. Zhang, J. Ma, A study of strain-rate effect and fiber reinforcement effect on dynamic behavior of steel fiber-reinforced concrete, *Construction and Building Materials* 158 (2018) 657–669.
- [263] S. Lee, K.-M. Kim, J. Park, J.-Y. Cho, Pure rate effect on the concrete compressive strength in the split hopkinson pressure bar test, *International Journal of Impact Engineering* 113 (2018) 191–202.

- [264] D. J. Frew, M. J. Forrestal, W. Chen, Pulse shaping techniques for testing brittle materials with a split hopkinson pressure bar, *Experimental mechanics* 42 (2002) 93–106.
- [265] W. Li, J. Xu, Impact characterization of basalt fiber reinforced geopolymeric concrete using a 100-mm-diameter split hopkinson pressure bar, *Materials Science and Engineering: A* 513 (2009) 145–153.
- [266] O. S. Lee, H. Choi, H. Kim, High-temperature dynamic deformation of aluminum alloys using shpb, *Journal of Mechanical Science and Technology* 25 (2011) 143–148.
- [267] M. Zhang, H. Wu, Q. Li, F. Huang, Further investigation on the dynamic compressive strength enhancement of concrete-like materials based on split hopkinson pressure bar tests. part i: Experiments, *International journal of impact engineering* 36 (2009) 1327–1334.
- [268] S. C. Kou, C. S. Poon, D. Chan, Influence of fly ash as cement replacement on the properties of recycled aggregate concrete, *Journal of Materials in Civil Engineering* 19 (2007) 709–717.
- [269] C.-C. Fan, R. Huang, H. Hwang, S.-J. Chao, Properties of concrete incorporating fine recycled aggregates from crushed concrete wastes, *Construction and Building Materials* 112 (2016) 708–715.
- [270] Z. Zhang, Y. Zhang, C. Yan, Y. Liu, Influence of crushing index on properties of recycled aggregates pervious concrete, *Construction and Building Materials* 135 (2017) 112–118.
- [271] R. Senthamarai, P. D. Manoharan, Concrete with ceramic waste aggregate, *Cement and Concrete Composites* 27 (2005) 910–913.
- [272] F. Debieb, S. Kenai, The use of coarse and fine crushed bricks as aggregate in concrete, *Construction and building materials* 22 (2008) 886–893.
- [273] D. L. Grote, S. W. Park, M. Zhou, Dynamic behavior of concrete at high strain rates and pressures: I. experimental characterization, *International Journal of Impact Engineering* 25 (2001) 869–886.

- [274] H. Yang, H. Song, S. Zhang, Experimental investigation of the behavior of aramid fiber reinforced polymer confined concrete subjected to high strain-rate compression, *Construction & Building Materials* 95 (2015) 143–151.
- [275] C. A. Ross, Fracture of concrete at high strain-rate, in: *Toughening mechanisms in quasi-brittle materials*, Springer, 1991, pp. 577–596.
- [276] Y. Lu, S. Yu, Y. Cai, Experimental study on dynamic splitting of recycled concrete using shpb, in: *EPJ Web of Conferences*, volume 94, EDP Sciences, 2015, p. 01008.
- [277] V. W. Tam, X. Gao, C. M. Tam, Microstructural analysis of recycled aggregate concrete produced from two-stage mixing approach, *Cement and concrete research* 35 (2005) 1195–1203.
- [278] CEN, En 933-1 tests for geometrical properties of aggregates - part 1: Determination of particle size distribution - sieving method, European Committee for Standardization CEN (2016).
- [279] L. D. de Oliveira Haddad, R. R. Neves, P. V. de Oliveira, W. J. dos Santos, A. N. de Carvalho Junior, Influence of particle shape and size distribution on coating mortar properties, *Journal of Materials Research and Technology* 9 (2020) 9299–9314.
- [280] B. Standard, Tests for geometrical properties of aggregates-determination of particle size distribution, 1997.
- [281] C. I. Standard, Technical specification for application of foamed concrete (jgj/t 341–2014) (2014).
- [282] X. Yuanliang, L. Baoliang, C. Chun, Z. Yamei, Properties of foamed concrete with  $Ca(OH)_2$  as foam stabilizer, *Cement and Concrete Composites* 118 (2021) 103985.
- [283] Z. Abdollahnejad, M. Mastali, F. Rahim, T. Luukkonen, P. Kinnunen, M. Ilkainen, Influence of cobinders on durability and mechanical properties of alkali-activated magnesium aluminosilicate binders from soapstone, in: *New Materials in Civil Engineering*, Elsevier, 2020, pp. 877–895.

- [284] ASTM, 597, standard test method for pulse velocity through concrete, ASTM International, West Conshohocken, PA (2009).
- [285] JCI, Method of test for fracture energy of concrete by use of notched beam, JCI-S-001e2003, Japan Concrete Institute (2003).
- [286] B. V. Reddy, A. Gupta, Influence of sand grading on the characteristics of mortars and soil–cement block masonry, *Construction and Building Materials* 22 (2008) 1614–1623.
- [287] Y. Ghasemi, M. Emborg, A. Cwirzen, Exploring the relation between the flow of mortar and specific surface area of its constituents, *Construction and Building Materials* 211 (2019) 492–501.
- [288] I. Standard, Non-destructive testing of concrete, part 1: Ultrasonic pulse velocity, Bureau of Indian Standard, New Delhi (1992).
- [289] S. B. Kim, N. H. Yi, H. Y. Kim, J.-H. J. Kim, Y.-C. Song, Material and structural performance evaluation of recycled pet fiber reinforced concrete, *Cement and concrete composites* 32 (2010) 232–240.
- [290] R. D. Recommendation, Determination of the fracture energy of mortar and concrete by means of three-point bend tests on notched beams, *Materials and structures* 18 (1985) 285–290.
- [291] N. Banthia, J. Sheng, Fracture toughness of micro-fiber reinforced cement composites, *Cement and Concrete Composites* 18 (1996) 251–269.
- [292] R. TC89-FMT, Fracture mechanics of concrete test methods, *Mater Struct* 23 (1991) 54.
- [293] M. Valipour, B. You, M. Panju, A. Ghodsi, Symbolicgpt: A generative transformer model for symbolic regression, *arXiv preprint arXiv:2106.14131* (2021).
- [294] S. Marasco, A. Fiore, R. Greco, G. P. Cimellaro, G. C. Marano, Evolutionary polynomial regression algorithm enhanced with a robust formulation: Application to shear strength prediction of rc beams without stirrups, *Journal of Computing in Civil Engineering* 35 (2021) 04021017.

- [295] S. Wagner, G. Kronberger, A. Beham, M. Kommenda, A. Scheibenpflug, E. Pitzer, S. Vonolfen, M. Kofler, S. Winkler, V. Dorfer, et al., Architecture and design of the heuristiclab optimization environment, in: *Advanced methods and applications in computational intelligence*, Springer, 2014, pp. 197–261.
- [296] E. Standard, *Cement-part 1: Composition, specifications and conformity criteria for common cements* (2000).
- [297] B. EN, 933-1: 2012. tests for geometrical properties of aggregates. determination of particle size distribution. sieving method, British European Standard, UK (2012).
- [298] A. I. Al-Hadithi, N. N. Hilal, The possibility of enhancing some properties of self-compacting concrete by adding waste plastic fibers, *Journal of Building Engineering* (2016) S2352710216300687.
- [299] BS, En 12350 testing fresh concrete. 2 slump test. (2000).
- [300] B. EN, 12390-8. testing hardened concrete, Making and curing specimens for strength tests.(European Standard 2000) part 2 (2009).
- [301] EN, En 14651: 2005; a1: 2007: Test method for metallic fibre concrete—measuring the flexural tensile strength (limit of proportionality (lop), residual) (2007).
- [302] G. H. Mahmud, Z. Yang, A. M. Hassan, Experimental and numerical studies of size effects of ultra high performance steel fibre reinforced concrete (uhpfrc) beams, *Construction and Building materials* 48 (2013) 1027–1034.
- [303] S. Xu, H. W. Reinhardt, A simplified method for determining double-k fracture parameters for three-point bending tests, *International Journal of Fracture* 104 (2000) 181–209.
- [304] J. Xie, L. Huang, Y. Guo, Z. Li, C. Fang, L. Li, J. Wang, Experimental study on the compressive and flexural behaviour of recycled aggregate concrete modified with silica fume and fibres, *Construction and Building Materials* 178 (2018) 612–623.



- [305] Y. Guo, J. Zhang, G. Chen, G. Chen, Z. Xie, Fracture behaviors of a new steel fiber reinforced recycled aggregate concrete with crumb rubber, *Construction and Building Materials* 53 (2014) 32–39.
- [306] M. Hassani, K. Vessalas, V. Sirivivatnanon, D. Baweja, Influence of permeability-reducing admixtures on water penetration in concrete, *ACI Mater. J* 114 (2017) 911–922.
- [307] E. 12390-8, Testing hardened concrete, part 8: depth of penetration of water under pressure, 2009.
- [308] H. Hafid, G. Ovarlez, F. Toussaint, P. Jezequel, N. Roussel, Effect of particle morphological parameters on sand grains packing properties and rheology of model mortars, *Cement and Concrete Research* 80 (2016) 44–51.
- [309] H. Van Damme, Concrete material science: Past, present, and future innovations, *Cement and Concrete Research* 112 (2018) 5–24.
- [310] I. Ivanova, V. Mechtcherine, Effects of volume fraction and surface area of aggregates on the static yield stress and structural build-up of fresh concrete, *Materials* 13 (2020) 1551.
- [311] B. BS EN 12390-5, Testing harden concrete. compressive strength of test specimens; bs en 12390-3, 2009.
- [312] Z. Xie, H. Zhou, L. Lu, Z. Chen, An investigation into fracture behavior of geopolymer concrete with digital image correlation technique, *Construction and Building Materials* 155 (2017) 371–380.
- [313] C. Albano, N. Camacho, M. Hernández, A. Matheus, A. Gutierrez, Influence of content and particle size of waste pet bottles on concrete behavior at different w/c ratios, *Waste Management* 29 (2009) 2707–2716.
- [314] N. Liang, L. Ren, S. Tian, X. Liu, Z. Zhong, Z. Deng, R. Yan, Study on the fracture toughness of polypropylene–basalt fiber-reinforced concrete, *International Journal of Concrete Structures and Materials* 15 (2021) 1–23.
- [315] H. Singh, R. Gupta, Influence of cellulose fiber addition on self-healing and water permeability of concrete, *Case Studies in Construction Materials* 12 (2020) e00324.

- [316] M. A. González-Ortega, S. Cavalaro, G. R. de Sensale, A. Aguado, Durability of concrete with electric arc furnace slag aggregate, *Construction and Building Materials* 217 (2019) 543–556.
- [317] K. De Weerd, H. Justnes, M. R. Geiker, Changes in the phase assemblage of concrete exposed to sea water, *Cement and Concrete Composites* 47 (2014) 53–63.
- [318] J. Fládr, P. Bílý, Specimen size effect on compressive and flexural strength of high-strength fibre-reinforced concrete containing coarse aggregate, *Composites Part B: Engineering* 138 (2018) 77–86.
- [319] R. Balendran, F. Zhou, A. Nadeem, A. Leung, Influence of steel fibres on strength and ductility of normal and lightweight high strength concrete, *Building and environment* 37 (2002) 1361–1367.
- [320] R. Kozul, D. Darwin, Effects of aggregate type, size, and content on concrete strength and fracture energy, Technical Report, University of Kansas Center for Research, Inc., 1997.
- [321] K. Wu, B. Chen, W. Yao, Study of the influence of aggregate size distribution on mechanical properties of concrete by acoustic emission technique, *Cement and Concrete Research* 31 (2001) 919–923.
- [322] E. M. Golafshani, A. Behnood, Estimating the optimal mix design of silica fume concrete using biogeography-based programming, *Cement and Concrete Composites* 96 (2019) 95–105.
- [323] S. Mangalathu, J.-S. Jeon, Classification of failure mode and prediction of shear strength for reinforced concrete beam-column joints using machine learning techniques, *Engineering Structures* 160 (2018) 85–94.
- [324] F. Ahmad, M. I. Qureshi, Z. Ahmad, Influence of nano graphite platelets on the behavior of concrete with e-waste plastic coarse aggregates, *Construction and Building Materials* 316 (2022) 125980.
- [325] A. Standard, C597-09 (2003), Standard Test Method for Pulse Velocity Through Concrete, ASTM International, West Conshohocken, PA (2003).

- [326] X. Q. Zhou, H. Hao, Modelling of compressive behaviour of concrete-like materials at high strain rate, *International Journal of Solids & Structures* 45 (2008) 4648–4661.
- [327] H. Luo, H. Lu, N. Leventis, The compressive behavior of isocyanate-crosslinked silica aerogel at high strain rates, *Mechanics of Time-Dependent Materials* 10 (2006) 83–111.
- [328] S. Huang, K. Xia, L. Qiao, Dynamic tests of cemented paste backfill: effects of strain rate, curing time, and cement content on compressive strength, *Journal of Materials Science* 46 (2011) 5165–5170.
- [329] C. Jiang, G.-F. Zhao, J. Zhu, Y.-X. Zhao, L. Shen, Investigation of dynamic crack coalescence using a gypsum-like 3d printing material, *Rock Mechanics and Rock Engineering* 49 (2016) 3983–3998.
- [330] T. On, P. A. LaVigne, J. Lambros, Development of plastic nonlinear waves in one-dimensional ductile granular chains under impact loading, *Mechanics of Materials* 68 (2014) 29–37.
- [331] A. B. Shemirani, R. Naghdabadi, M. Ashrafi, Experimental and numerical study on choosing proper pulse shapers for testing concrete specimens by split hopkinson pressure bar apparatus, *Construction and Building Materials* 125 (2016) 326–336.
- [332] S. Pang, W. Tao, Y. Liang, Y. Liu, S. Huan, A modified method of pulse-shaper technique applied in shpb, *Composites Part B: Engineering* 165 (2019) 215–221.
- [333] M. J. Islam, M. Shahjalal, Effect of polypropylene plastic on concrete properties as a partial replacement of stone and brick aggregate, *Case Studies in Construction Materials* 15 (2021) e00627.
- [334] V. M. Malhotra, *Testing hardened concrete: nondestructive methods* (1976).
- [335] C. ASTM, et al., Standard test method for static modulus of elasticity and poisson's ratio of concrete in compression, *Annual book of ASTM standards* 4 (2002) 469.

- [336] S. I. Basha, M. Ali, S. Al-Dulaijan, M. Maslehuddin, Mechanical and thermal properties of lightweight recycled plastic aggregate concrete, *Journal of Building Engineering* 32 (2020) 101710.
- [337] Y.-F. Wu, S. M. S. Kazmi, M. J. Munir, Y. Zhou, F. Xing, Effect of compression casting method on the compressive strength, elastic modulus and microstructure of rubber concrete, *Journal of Cleaner Production* 264 (2020) 121746.
- [338] Y. Guo, G. Gao, L. Jing, V. Shim, Response of high-strength concrete to dynamic compressive loading, *International Journal of Impact Engineering* 108 (2017) 114–135.
- [339] Y. Al-Salloum, T. Almusallam, S. M. Ibrahim, H. Abbas, S. Alsayed, Rate dependent behavior and modeling of concrete based on shpb experiments, *Cement & Concrete Composites* 55 (2015) 34–44.
- [340] Wang, Zhang, M.-H, Quek, S.T, Effect of specimen size on static strength and dynamic increase factor of high-strength concrete from shpb test, *Journal of Testing & Evaluation* 39 (2011) 898–907.